

OPTIMIZATION STUDIES ON THE SECONDARY TREATMENTS AND
MECHANICAL BEHAVIOR OF Ti48Al2Cr2Nb ALLOY PRODUCED BY
ELECTRON BEAM MELTING (EBM) METHOD

A THESIS SUBMITTED TO
THE GRADUATE SCHOOL OF NATURAL AND APPLIED SCIENCES
OF
MIDDLE EAST TECHNICAL UNIVERSITY

BY

GÜNEY MERT BİLGİN

IN PARTIAL FULFILLMENT OF THE REQUIREMENTS
FOR
THE DEGREE OF DOCTOR OF PHILOSOPHY
IN
METALLURGICAL AND MATERIALS ENGINEERING

JUNE 2024

Approval of the thesis:

**OPTIMIZATION STUDIES ON THE SECONDARY TREATMENTS AND
MECHANICAL BEHAVIOR OF Ti48Al2Cr2Nb ALLOY PRODUCED BY
ELECTRON BEAM MELTING (EBM) METHOD**

submitted by **GÜNEY MERT BİLGİN** in partial fulfillment of the requirements
for the degree of **Doctor of Philosophy in Metallurgical and Materials
Engineering, Middle East Technical University** by,

Prof. Dr. Naci Emre Altun
Dean, **Graduate School of Natural and Applied Sci., METU** _____

Prof. Dr. Ali Kalkanlı
Head of the Department, **Met. and Mat. Eng., METU** _____

Prof. Dr. Arcan F. Dericioğlu
Supervisor, **Metallurgical and Materials Eng., METU** _____

Prof. Dr. Ziya Esen
Co-Supervisor, **Materials Sci. and Eng. Dept., Çankaya Uni.** _____

Examining Committee Members:

Prof. Dr. Y. Eren Kalay
Metallurgical and Materials Engineering, METU _____

Prof. Dr. Arcan F. Dericioğlu
Metallurgical and Materials Engineering, METU _____

Prof. Dr. Metin Uymaz Salamcı
Mechanical Engineering, Gazi University _____

Assist. Prof. Dr. Eda Aydoğan Güngör
Metallurgical and Materials Engineering, METU _____

Assist. Prof. Dr. Kemal Davut
Materials Sci. and Eng. Dept., İzmir Institute of Technology _____

Date: 27.06.2024

I hereby declare that all information in this document has been obtained and presented in accordance with academic rules and ethical conduct. I also declare that, as required by these rules and conduct, I have fully cited and referenced all material and results that are not original to this work.

Name Last name : Güney Mert Bilgin

Signature :

ABSTRACT

OPTIMIZATION STUDIES ON THE SECONDARY TREATMENTS AND MECHANICAL BEHAVIOR OF Ti48Al2Cr2Nb ALLOY PRODUCED BY ELECTRON BEAM MELTING (EBM) METHOD

Bilgin, Güney Mert
Doctor of Philosophy, Metallurgical and Materials Engineering
Supervisor : Prof. Dr. Arcan F. Dericioğlu
Co-Supervisor: Prof. Dr. Ziya Esen

June 2024, 320 pages

Reducing structural weight is crucial in aviation engine development for lower emissions, enhanced performance, and cost efficiency. Titanium aluminides (TiAl) are potential substitutes for nickel-based superalloys due to their high-temperature strength and low density. However, their low ductility and fracture toughness present challenges for conventional processing methods. In this study, Ti48Al2Cr2Nb alloys were produced using electron beam melting (EBM) additive manufacturing. The as-built samples exhibited extreme brittleness due to coarse γ -bands, aluminum content inconsistencies, and high dislocation density, rendering them impractical for aviation applications. To address these issues three secondary thermal treatments were applied: hot isostatic pressing (HIP) at 1200 °C under 100 MPa, annealing at 1200 °C (HT1), and annealing at 1400 °C (HT2). HIP induced a slight increase in α_2 phase fraction and grain size, while HT1 accentuated the banded structure without significantly increasing α_2 content. HIP and HT1 reduced dislocation density and inherent strain. HT2 transformed the duplex microstructure into a fully lamellar morphology with the highest texture. Room and high-

temperature tensile tests demonstrated that HIP, HT1, and HT2 treatments effectively mitigated brittleness. HIP reduced anisotropy at room temperature, with a 9.53 MPa difference in yield strength between specimens tested perpendicular and parallel to the building direction, compared to a 65.15 MPa variation in HT1 samples. At 800 °C, samples treated with HIP and HT1 exhibited a ductile transition, while HT2 processed samples retained brittleness. Consequently, this study reveals the potential of secondary heat treatments and novel scanning strategies in improving the mechanical characteristics of additively manufactured Ti48Al2C2Nb alloy for high-temperature applications.

Keywords: Additive Manufacturing (AM), Electron Beam Melting (EBM), Ti48Al2Cr2Nb Alloy, Annealing, Hot Isostatic Pressing (HIP)

ÖZ

ELEKTRON IŞIMASI ERGİTME (EIE) YÖNTEMİYLE ÜRETİLEN Tİ-48AL-2CR-2NB ALAŞIMININ İKİNCİL İŞLEMLERİNİN VE MEKANİK DAVRANIŞININ OPTİMİZE EDİLMESİ ÇALIŞMALARI

Bilgin, Güney Mert
Doktora, Metalurji ve Malzeme Mühendisliği
Tez Yöneticisi: Prof. Dr. Arcan F. Dericioğlu
Ortak Tez Yöneticisi: Prof.Dr.Ziya Esen

Haziran 2024, 320 sayfa

Havacılık motorlarının geliştirilmesinde yapısal ağırlığın azaltılması; düşük emisyonlar, iyileştirilmiş performans ve maliyet tasarrufu için hayati öneme sahiptir. Titanyum alüminitler (TiAl), yüksek sıcaklık mukavemeti ve düşük yoğunlukları nedeniyle nikel bazlı süperalaşımlara potansiyel alternatiflerdir. Ancak, düşük süneklikleri ve kırılma toklukları, geleneksel işleme yöntemleri için zorluklar yaratır. Bu çalışmada, Ti48Al2C2Nb alaşımları, elektron ışın ergitme (EIE) eklemeli imalat yöntemi kullanılarak üretildi. Üretilen numunelerin; kaba γ -bantları, alüminyum içeriği tutarsızlıkları ve yüksek dislokasyon yoğunluğu nedeniyle aşırı kırılma sertleştirilerek havacılık uygulamaları için uygunsuz olduğu tespit edildi. Bu sorunları çözmek için üç farklı ikincil ısıl işlem uygulandı: 1200 °C'de 100 MPa altında sıcak eşeksenli basınçlama (SEB), 1200 °C'de tavlama (HT1) ve 1400 °C'de tavlama (HT2). HIP, α_2 faz fraksiyonu ve tane boyutunda hafif bir artışa neden olurken, HT1 bantlı yapıyı belirginleştirip α_2 içeriğini önemli ölçüde artırmadı. SEB ve HT1, dislokasyon yoğunluğunu ve içsel gerilimi azalttı.

HT2, çift fazlı mikro yapıyı tamamen lameller bir morfolojiye dönüştürdü ve en yüksek dokuya yol açtı. Oda ve yüksek sıcaklık çekme testleri SEB, HT1 ve HT2 işlemlerinin kırılma dayanımı etkili bir şekilde azalttığını gösterdi. Dik ve paralel yönde üretilen numuneler arasındaki akma dayanımı farkı SEB sonrasında 9.53 MPa iken HT1 işlemlili numunede bu fark 65.15 MPa oldu. Bu durum SEB'nin mekanik dayanımdaki anizotropiyi azaltmaktaki başarısını gösterdi. 800 °C'de; EIE ile üretilen, SEB ve HT1 işlemlili numuneler sünek özellik gösterirken HT2 işlemlili numuneler gevrek karakterlerini korudu. Sonuç olarak, bu çalışma, eklemeli imalat ile üretilen Ti48Al2C2Nb alaşımının yüksek sıcaklık uygulamalarındaki kullanılabilirliği için mekanik özelliklerini iyileştirmede ikincil ısıl işlemlerin ve yeni tarama stratejilerinin potansiyelini ortaya çıkardı.

Anahtar Kelimeler: Eklemeli İmalat (EI), Elektron Işıması Ergitme (EIE), Ti48Al2Cr2Nb Alaşımı, Tavlama, Sıcak Eşeksenli Basınçlama (SEB)

To my beloved family

ACKNOWLEDGMENTS

I extend my gratitude to my supervisor Prof. Dr. Arcan F. Dericiođlu, for his valuable guidance, suggestions, feedback, advice, and constructive criticism. I would like to express my truthful appreciation to my co-supervisor Prof. Dr. Ziya Esen for his motivation, wise criticism, exceptional advice and knowledge.

I express my sincere gratefulness to TUSAS Engine Industries Inc. (TEI) Technology Programs Manager Gray Akbulut, and Additive Manufacturing Team Leader Akin Orhangl for the opportunity and support they provided for my work. I would like to convey my appreciation to M. Naci Uđur who endured the challenges during the operation and production in Arcam A2X system. He played the role of the unsung hero in this study.

I am also thankful to Assist. Prof. Dr. Eda Aydođan Gngr and Assist. Prof. Dr. Kemal Davut for their precious help, advice, valuable support and encouragement during the development of the study.

I am indebted to my lab mates and friends; Tuđçe Altuntop, Seren zer and Bařar Ser for their assistance, unwavering patience, and insightful suggestions. I cannot thank them enough for generously sharing their knowledge and putting forth tremendous effort in every stage of my study.

I am grateful to my mom Őebnem Gkkuřu, dad Murat Bilgin, and all beloved members of my family for the warm support they have provided, the trust they have shown, and for always making me feel their presence by my side. I wish to express my special appreciation to my mom particularly for standing by me in any condition.

Finally, my deepest gratitude goes to my dear wife Simay, whose patience, respect, and selfless dedication sustained me throughout the extensive years of my thesis. Her unwavering support has been indispensable.

TABLE OF CONTENTS

ABSTRACT.....	v
ÖZ	vii
ACKNOWLEDGMENTS	x
TABLE OF CONTENTS.....	xi
LIST OF TABLES.....	xvi
LIST OF FIGURES	xix
LIST OF ABBREVIATIONS.....	xxxiv
CHAPTERS	
INTRODUCTION	1
LITERATURE REVIEW	7
2.1 Introduction to Titanium Aluminides and Their Applications	7
2.1.1 Introduction and Overview	7
2.1.2 Applications	10
2.2 Properties of Titanium Aluminides.....	14
2.2.1 Binary Ti-Al Phase System.....	14
2.2.1.1 Phase transformation from β to α	19
2.2.1.2 Phase transformation from α to α_2	22
2.2.2 Alloy Design and Multicomponent Alloy Systems	25
2.2.2.1 Effect of Aluminum.....	26
2.2.2.2 Effect of Chromium.....	27
2.2.2.3 Effect of Niobium.....	31
2.2.2.4 Effect of Manganese and Vanadium.....	33
2.2.2.5 Effect of Tungsten, Molybdenum and Tantalum.....	34

2.2.2.6	Effect of Boron.....	34
2.2.2.7	Effect of Carbon.....	36
2.2.2.8	Effect of Silicon	37
2.2.3	Specific γ -TiAl Alloy Systems.....	39
2.2.3.1	Convetional Alloys.....	40
2.2.3.1.1	Ti48Al2Cr2Nb Alloy.....	41
2.2.3.2	High Niobium Containing Alloys	43
2.2.3.3	β - Solidifying Alloys.....	44
2.2.3.4	Massively Transformed Alloys	46
2.3	Conventional Manufacturing of Titanium Aluminides	48
2.3.1	Casting.....	49
2.3.2	Wroughting.....	50
2.3.3	Powder Metallurgy	52
2.4	Additive Manufacturing of Titanium Aluminides.....	53
2.4.1	Directed Energy Deposition	55
2.4.1.1	Laser Beam Directed Energy Deposition.....	55
2.4.1.2	Wire Arc Additive Manufacturing.....	60
2.4.2	Powder Bed Fusion.....	63
2.4.2.1	Laser Beam Powder Fusion	63
2.4.2.2	Electron Beam Powder Bed Fusion	68
2.5	Insights into Electron Beam Powder Bed Fusion Method	88
2.5.1	History of the Technology.....	88
2.5.2	Application Areas in Aviation Industry	90
2.5.3	Powder Characteristics	95

2.5.4	Fundamentals of the Process.....	104
2.5.5	Effects of the Process Variables on Part Quality.....	108
2.5.5.1	Powder Bed Pre-Heating	110
2.5.5.2	Powder Flowability.....	111
2.5.5.3	Layer Thickness.....	111
2.5.5.4	Hatch and Contour Scanning Strategy.....	113
2.5.5.5	Part Location and Orientation.....	124
	EXPERIMENTAL PROCEDURE	127
3.1	Starting Materials.....	127
3.2	Electron Beam Powder Bed Fusion Fabrication	130
3.3	Post Processing: Hot Isostatic Pressing	135
3.4	Post Processing: Conventional Annealing Heat Treatment.....	136
3.5	Structural and Chemical Analysis.....	137
3.5.1	Density Measurement	137
3.5.2	Computed Tomography Scans	138
3.5.3	Thermal Expansion Measurements.....	138
3.5.4	X-ray fluorescence Analysis	139
3.5.5	X-Ray Diffraction Analysis	139
3.5.6	Metallographic Examinations	140
3.5.7	Electron Back Scatter Diffraction	141
3.5.8	Thermodynamic Modelling Studies.....	141
3.6	Mechanical Characterization	142
3.6.1	Microhardness	142
3.6.2	Tensile Tests	142

RESULTS AND DISCUSSION.....	145
4.1 Porosity and Density Investigations	145
4.2 Thermal Expansion Measurements	148
4.3 Chemical Composition Measurements.....	149
4.4 X-Ray Diffraction Analysis.....	150
4.5 Metallographic Examinations.....	153
4.5.1 Microstructural Evaluations on of As-Built Samples.....	153
4.5.2 Microstructural Evaluations on Post Processed Samples.....	159
4.6 Electron Backscattered Diffraction Evaluation.....	167
4.7 Mechanical Evaluations.....	179
4.7.1 Microhardness Measurements	179
4.7.2 Tensile Tests.....	181
4.7.2.1 Tensile Tests of As-Built Samples.....	181
4.7.2.1.1 Tensile Test Results of As-Built Samples	181
4.7.2.1.2 Tensile Test Fracture Surfaces of the As-Built Samples	183
4.7.2.2 Tensile Tests of HIPed Samples	191
4.7.2.2.1 Tensile Test Results of HIPed Samples.....	191
4.7.2.2.2 Tensile Test Fracture Surfaces of the HIPed Samples.....	193
4.7.2.3 Tensile Tests of HT1 Processed Samples	198
4.7.2.3.1 Tensile Tests of HT1 Processed Samples	198
4.7.2.3.2 Tensile Test Fracture Surfaces of HT1 Processed Samples	201
4.7.2.4 Tensile Tests of HT2 Samples	206
4.7.2.4.1 Tensile Test Results of HT2 Processed Samples.....	206
4.7.2.4.2 Tensile Test Fracture Surfaces of HT2 Processed Samples	209

4.7.2.5	Overview of Tensile Tests	214
4.7.2.6	Overview of Fracture Surfaces	222
4.8	Thermodynamic Modelling Studies	227
4.9	Electron Beam Powder Bed Fusion Double-Scan Studies.....	230
4.9.1	Double Scan Partial Overlap #1 Studies	234
4.9.2	Double Scan Complete Overlap Studies	246
4.9.3	Double Scan Partial Overlap #2 Studies	255
4.9.4	Overview of Double-Scan Studies	264
	CONCLUSION	269
	REFERENCES	275
A.	Coefficient of Thermal Expansion of Electron Beam Powder Bed Fusion Fabricated Ti48Al2Cr2Nb	315
	CURRICULUM VITAE	319

LIST OF TABLES

TABLES

Table 2.1: Comparative properties for high temperature alloys [27].	8
Table 2.2: Several properties of titanium, TiAl and Ni-base alloys [37].	10
Table 2.3: Crystallographic data of the phases exhibiting in the binary Ti-Al system [54].	17
Table 2.4: Several specific γ -TiAl alloys with various properties [66].	39
Table 2.5: Chemical composition of the Ti ₄₈ Al ₂ Nb ₂ Cr alloy in wt.% [20].	41
Table 2.6: DED-LB process parameters in the literature to manufacture γ -TiAl [162].	56
Table 2.7: DED-LB process parameters to produce Ti-47Al-2Cr-2Nb alloy [171].	58
Table 2.8: Room temperature tensile properties of DED-LB processed Ti-47Al-2.5V-1Cr and Ti-40Al-2Cr [174], [175].	60
Table 2.9: WAAM process parameters found in the literature to manufacture γ -TiAl [162].	61
Table 2.10: PBF-LB process parameters found in the literature to manufacture γ -TiAl [162].	64
Table 2.11: EB-PBF process parameters found in the literature to manufacture γ -TiAl [162].	69
Table 2.12: Heat treatments according to Yue et al. [191].	80
Table 2.13: The room temperature tensile properties of the PBF-EB manufactured Ti ₄₈ Al ₂ Cr ₂ Nb alloy along the build (Z) direction.	84
Table 2.14: Creep properties of PBF-EB manufactured Ti-48Al-2Nb-0.7Cr-0.3Si alloy [26].	86
Table 2.15: The process parameters used in experimental design [267].	123
Table 3.1: The chemical composition of Ti ₄₈ Al ₂ Cr ₂ Nb powders supplied by Praxair S.T. Technology, Inc.	127

Table 3.2: D10, D50 and D90 values of Ti48Al2Cr2Nb powders.	128
Table 3.3: Powder flow characterization of Ti48Al2Cr2Nb powders.	129
Table 3.4: Arcam A2X technical data [278].	131
Table 3.5: PBF-EB melt theme process variables used in this study.	133
Table 3.6: HIP parameters of Ti48Al2Cr2Nb alloy produced by PBF-EB.	136
Table 3.7: Conventional annealing heat treatment conditions.	137
Table 3.8: The constituents of Kroll's reagent.	140
Table 4.1: XRF measurements (wt.%) of Ti48Al2Cr2Nb as-built sample.	149
Table 4.2: Phase fractions obtained by rietveld refinement.	153
Table 4.3: EDS analysis of as-built sample in parallel to build direction at nine different points showed in Figure 4.7 (a).	159
Table 4.4: Microhardness values of PBF-EB as-built sample.	181
Table 4.5: Tensile test average results of as-built Ti48Al2Cr2Nb samples.	182
Table 4.6: Tensile test average results of HIPed Ti48Al2Cr2Nb samples.	192
Table 4.7: Tensile test average results of HT1 processed Ti48Al2Cr2Nb samples.	200
Table 4.8: Tensile test average results HT2 processed Ti48Al2Cr2Nb samples. .	208
Table 4.9: Eutectoid temperature and phase constituent versus temperature relationship in TiAl and Ti48Al2Cr2Nb systems calculated in ThermoCalc Software.	229
Table 4.10: Double-scan parameters.	234
Table 4.11: Room temperature tensile test results of the double scan partial overlap #1 samples.	245
Table 4.12: Room temperature tensile test results of the complete overlap samples.	254
Table 4.13: Room temperature tensile test results of the double scan partial overlap #2 samples.	263
Table 4.14: Room temperature tensile test results for samples that have highest strength values in double-scan studies.	265

Table A.5.1: Coefficient of thermal expansion of PBF-EB fabricated Ti48Al2Cr2Nb.....	315
--	-----

LIST OF FIGURES

FIGURES

Figure 2.1: Temperature dependent specific strength of various alloy categories [27].	8
Figure 2.2: (a) Last two stages of the GENx made of TiAl and (b) single stage of GENx [40].	11
Figure 2.3: (a) Cast stator vanes at various stages of production. The cast preform, post electrochemical milling, and the final machined stator vane are shown from left to right [47]. (b) GE90 engine transition duct beams [48].	12
Figure 2.4: (a) TiAl turbocharger wheel joined to the shaft and (b) TD05 turbocharger used in Lancer Evolution VI [53].	14
Figure 2.5: Crystal Structures of binary Ti-Al phases; (a) hexagonal α_2 (Ti ₃ Al) phase, (b) tetragonal γ (TiAl) phase, (c) cubic B2 phase [54].	15
Figure 2.6: Ti-Al binary phase diagram according to Schuster and Palm [292].	16
Figure 2.7: Ti-Al binary phase diagram that shows typical range for engineering γ -TiAl base alloys [65].	18
Figure 2.8: The simplified Ti-Al binary phase diagram, along with solidification pathways under different Al contents in equilibrium conditions [66].	19
Figure 2.9: The orientation relationship between the primary β phase and the secondary α phase: (a) Stereographic projection of the $[001]\beta$ [68], (b) the $\{110\}\beta$ planes of the β phase crystal structure and (c) in the Burgers orientation relationship, two potentially distinct growth directions of the α phase parallel to the β phase $(110)\beta$ plane [66].	20
Figure 2.10: The precipitation of γ phase from α_2 phase [66].	23
Figure 2.11: (a) The effect of heat treatment temperature on tensile ductility at room temperature [93] and (b) the effect of Al content on the room - temperature ductility of wrought materials [94].	27
Figure 2.12: The impact of Cr modification on the α transus temperature for; (a) 48 at.% Al alloy and (b) Ti-Al binary and 2 at.% Cr added systems [101].	28

Figure 2.13: (a) Effect of Cr addition on plastic fracture strain and (b) effect of aluminum concentration on plastic fracture strain for Ti-Al binary and 2 at.% Cr added systems [101].	29
Figure 2.14: Isothermal oxidation kinetics of; (a) Ti-50Al and (b) Ti-50Al-10Cr alloys [98].	30
Figure 2.15: (a) Yield strengths in Ti-48Al-xCr alloy at room temperature and 900 °C as a function of Cr percentage. (b) The creep rupture life response to Cr concentration at 800 °C under 240 MPa stress [99].	31
Figure 2.16 (a) Isothermal oxidation at 900 °C and (b) crack length vs. thermal fatigue cycle for Ti-47Al-xNb alloys [108].	32
Figure 2.17: The α transus temperature is affected by the additions of 2Cr, 3V, and 2Mn [94].	33
Figure 2.18: The correlation between boron concentration and grain size in cast Ti47Al2MnX. The data point represented by a plus sign (+) corresponds to the alloy Ti47Al2Mn2Nb1B [111].	35
Figure 2.19: α_2 and γ phase unit cell volumes depending on the carbon content [114].	37
Figure 2.20: (a) The impact of silicon additions on the creep behavior [120] and (b) variation in oxidation scale thickness with Nb and Si contents [122].	38
Figure 2.21: Various microstructures obtained after several heat treatment temperatures corresponding to distinct regions in the binary phase diagram for a 48 at.% Al alloy [20].	43
Figure 2.22: Refined "convoluted microstructure" of previously γ_m contained Ti-46Al-8Nb alloy followed by heat treatment within the $\alpha + \gamma$ region [143].	47
Figure 2.23: Processing routes suggested by Chen et al. [40].	48
Figure 2.24: (a) An investment casted LPT blade and (b) its corresponding X-ray picture [149].	49
Figure 2.25: Centrifugally casted GEnx LPT blade [41].	50
Figure 2.26: Compressor blades of Ti45Al8Nb0.5(B,C) produced using extrusion and forging process; (a) set of blades and (b) an individual blade [3].	51

Figure 2.27: HIP produced; (a) turbine engine compressor rotor and (b) machining preform [159].	53
Figure 2.28: (a) The breakdown of various AM techniques employed for fabricating TiAl parts and (b) the primary techniques highlighted in publications of 2022 for printing TiAl [161].	54
Figure 2.29: Schematic illustration of DED-LB process [40].	56
Figure 2.30: Macrostructure and microstructures of Ti48Al2Cr2Nb alloy manufactured by DED-LB [167].	59
Figure 2.31: Schematic diagram of WAAM setup [166].	61
Figure 2.32: Macro and microstructures of γ -TiAl alloy fabricated by TIG method representing; (a) cross-section (x-z plane) morphology; (b) macro- and (c) micro-structure in the top region; (d) macro- and (e) micro-structure in the middle region; (f) macro- and (g) micro-structure in the bottom region. [166].	62
Figure 2.33: TiAl alloy produced by PBF-LB method that shows; (a) 3D-dodecahedron structures, (b) SEM image of as-built and (c) SEM image of two step heat treated sample [181].	65
Figure 2.34: SEM images of the samples produced at 800 °C (top row and middle row) and 1000 °C (bottom row) preheating temperatures [12].	67
Figure 2.35: SEM images of the surfaces of Ti48Al2Cr2Nb samples produced by the (a) PBF-EB and (b) PBF-LB methods [180].	68
Figure 2.36: PBF-EB manufactured as-built (left) and subsequently machined (right) Ti48Al2Cr2Nb LPT blade [40].	70
Figure 2.37: Microprobe measurements, reflected in the element mappings, reveal an uneven distribution of Al attributed to the evaporation process occurring in the upper region of the melt pool [15].	72
Figure 2.38: a) The schematic representation of the temperature history at different heights of the as-built specimen during PBF-EB, b) changes in the build plate temperature over time and building height [188].	74

Figure 2.39: Microstructure of as-built Ti48Al2Cr2Nb that shows; (a) upper and lower regions, (b) fully-lamellar, (c) near-lamellar, (d) duplex, (e) equiaxed γ microstructures and (f) central portion of the Ti–Al binary phase diagram [23]. .. 75

Figure 2.40: Schematic illustrations that show the evolution of microstructure and the distinctive formation of layered microstructures during the PBF-EB process. (a) Snapshot during the PBF-EB process, (b) powder layer feed, (c) fusion of several layers, (d) next layer feed, and (e) fusion of several layers again [23]. 76

Figure 2.41: The CCT diagram for the Ti48Al2Cr2Nb [190]...... 77

Figure 2.42: EBSD analysis results; (a) band-contrast maps, (b) grain-orientation maps [190]...... 78

Figure 2.43: Micrographs of sample S1 after annealing at; (a) 1310 °C for 3 h and (b) 1370 °C for 2 h and sample S2 after annealing at; (c) 1370 °C for 2 h, followed by furnace cooling (vertical cross section) [191]. 80

Figure 2.44: (a) PBF-EB as-built and (b) HIPed Ti8Al2Cr2Nb SEM-BSE images [192]. 81

Figure 2.45: EBSD phase maps of the as-built and HIPed Ti48Al2Cr2Nb [193]. . 82

Figure 2.46: (a) A pore in PBF-EB Ti48Al2Nb2Cr sample. Microstructures of; (b) as-built, (c) HIPed and (d) HTed samples [20]. 83

Figure 2.47: UTS versus temperature relationship of PBF-EB processed Ti48Al2Cr2Nb alloy in various microstructures [40]. 85

Figure 2.48: Tensile test results of PBF-EB manufactured Ti48Al2Cr2Nb alloy subjected to HIP and heat treatment; (a) yield strength, (b) elongation, (c) UTS and (d) stress-strain curves [196]. 88

Figure 2.49: A tube component redesigned through PBF-EB for the HTF7000 Turbofan engine [215]...... 91

Figure 2.50: A front bearing housing produced by Rolls Royce [216]. 92

Figure 2.51: (a) A rocket engine impeller, (b) a landing gear hinge, (c) an early warning system mixing part produced by CalRAM Inc. [217]. 92

Figure 2.52: γ -TiAl turbine blades produced by Avio Aero [218]...... 93

Figure 2.53: Airbus A320 engine attachment hinge; in the background: geometry produced with traditional methods, in the foreground: geometry produced with PBF-EB and topology optimization [219].	94
Figure 2.54: ELCSS test chamber [220].	94
Figure 2.55: The particle size distribution of metal powder for PBF-LB [221].	96
Figure 2.56: The time-dependent powder spattering behaviors [227].	98
Figure 2.57: (a) Particle size distribution of EOS Ti6Al4V powder, (b) particle size distribution of Arcam Ti6Al4V powder, (c) SEM images of EOS Ti6Al4V powder, (d) SEM images of Arcam Ti6Al4V powder [230].	99
Figure 2.58: (a) Particle size distribution of CMSX-4 powder produced by gas atomization, (b) SEM image of Ti6Al4V powder produced by gas atomization [253].	100
Figure 2.59: Particle size distributions. Dashed lines = new powder, solid line = recycled powder [231].	101
Figure 2.60: SEM images of Inconel 718 produced by; (a), (c) gas atomization and (b), (d) PREP [232].	102
Figure 2.61: TiAl powders used in PBF-EB; (a) SEM image, (b) particle sizes [232].	103
Figure 2.62: Schematic of a PBF-EB system [233].	104
Figure 2.63: Meltpool width and shape in; (left) PBF-EB, (right) PBF-EB [209].	107
Figure 2.64: (a) Part production cycle and (b) Arcam A2X process chamber [253].	109
Figure 2.65: Steps involved in producing a layer in PBF-EB [253].	110
Figure 2.66: The effect of increasing scanning speed and beam power on the production of Ti6Al4V material with different layer thicknesses [27].	112
Figure 2.67: SEM surface images of samples produced with different powder sizes and layer thicknesses; a) 45 - 100 μm powder size distribution and 70 μm layer thickness, b) 45 - 100 μm powder size distribution and 50 μm layer thickness, c) 25	25

- 45 μm powder size distribution and 70 μm layer thickness, d) 25 -4 5 μm powder size distribution and 50 μm layer thickness [27].	113
Figure 2.68: PBF-EB heating and melting stages of; (a) preheating (b) melting: Hatch scanning, (c) melting: Contour scanning with multiple beams [253].	114
Figure 2.69: (a) Single-beam and (b) multi-beam illustration. Arrows indicate the scanning direction [27].	115
Figure 2.70: Pore densities and distributions obtained through 3D XCT scanning in different process modes (coded as C0-C7) [27].	116
Figure 2.71: Support structures; a) without contour scanning and b) when contour scanning is enabled [27].	117
Figure 2.72: a) Support structure example and (b) error rate between the model and the produced part according to the part thickness [27].	117
Figure 2.73: Three-dimensional surface measurement of parts produced with; (a) single beam and (b) multi-beam strategies under the same parameters. The arrow direction indicates the production direction [259].	118
Figure 2.74: The change in the thickness of acicular α plates with scan rate [27].	119
Figure 2.75: The variation in α -lamella thickness with energy input for Ti6Al4V material [253].	120
Figure 2.76: Perpendicular and parallel to the build direction views of samples produced at different scanning speeds [27].	121
Figure 2.77: Process map for Ti6Al4V [249].	122
Figure 2.78: The particle width variation at two different beam diameters (400 and 500 μm) [27].	124
Figure 2.79: Process maps obtained from studies conducted at different scan (deflection) speeds for Inconel 718; (a) defocused electron beam (beam diameter of 500 μm), (b) focused electron beam (beam diameter of 400 μm) [27].	124
Figure 2.80: The schematic representation of samples produced in a study examining part orientation and position [27].	125
Figure 3.1: PSD analyze of Ti48Al2Cr2Nb powders.	128

Figure 3.2: SEM images illustrating: (a) the overall appearance of powders at lower magnification, (b) irregularly shaped powders and satellites, and (c) the XRD pattern of Ti48Al2Cr2Nb powder.....	130
Figure 3.3: Picture of the Arcam A2X machine [278].....	131
Figure 3.4: Arcam A2X temperature log for the mechanical test samples build job.	134
Figure 3.5: (a) Schematics illustrating horizontally and vertically built tensile test samples along with the observation directions for microstructural examinations, and (b) as-built samples on the building plate, with emphasis on the XY-direction samples to indicate the cutting direction.....	135
Figure 3.6: A sketch of XRF measurement sample that shows sectioning planes.	139
Figure 3.7: A picture of room and elevated temperature tensile test specimen. ...	143
Figure 3.8: A technical drawing of room and elevated temperature tensile test specimen.	143
Figure 4.1: XCT reconstructed images that show the spatial distribution of pores in the tensile test samples of; (a) as-built in XY-direction, (b) as-built in Z-direction.	147
Figure 4.2: CTE values varying at different temperatures for XY- and Z-direction samples.....	148
Figure 4.3: XRD patterns obtained from the as-built sample in perpendicular and parallel to build direction sections.	150
Figure 4.4: XRD patterns obtained from the as-built, HIPed, HT1 and HT2 processed samples in parallel to build direction.	151
Figure 4.5: Optical micrographs of as-built Ti48Al2Cr2Nb samples produced via PBF-EB. The images captured in various sections: (a) Upper section in the perpendicular direction, (b) upper section in the parallel direction, (c) middle section in the perpendicular direction, (d) middle section in the parallel direction, (e) lower section in the perpendicular direction, and (f) lower section in the parallel direction, all at a magnification of 500x.	154

Figure 4.6: Optical micrographs of two different observation directions; in cross-sections at 50x; (a) perpendicular and (b) parallel to building direction, at 200x; (c) perpendicular and (d) parallel to building direction. Backscattered electron SEM images at 2500x in cross-sections; (e) perpendicular and (f) parallel to building direction..... 156

Figure 4.7: Secondary electron SEM images taken from parallel observation direction in as-built sample that shows; (a) duplex microstructure at 1500x, (b) fine lamellae + equiaxed grains separated by coarse colonies at 5000x, (c) EDS elemental maps obtained from the coarse and lamellar regions..... 157

Figure 4.8: PBF-EB fabricated Ti48Al2Cr2Nb alloy optical micrographs at 200x magnification. As-built sample in the observation direction of; (a) perpendicular and (b) parallel. HIPed sample in the observation direction of; (c) perpendicular and (d) parallel. HT1 processed sample in the observation direction of; (e) perpendicular and (f) parallel. HT2 processed sample in the observation direction of; (g) perpendicular and (h) parallel..... 161

Figure 4.9: PBF-EB fabricated Ti48Al2Cr2Nb alloy secondary electron SEM images. As-built sample in; (a) perpendicular and (b) parallel observation direction. HIPed sample in; (c) perpendicular and (d) parallel observation direction. HT1 processed sample in; (e) perpendicular and (f) parallel observation direction. HT2 processed sample in; (g) perpendicular and (h) parallel observation direction..... 164

Figure 4.10: Optical microscope images taken from cross-sections parallel to building directions in; (a) as-built, (b) HIPed, and (c) HT1 processed conditions. Secondary electron SEM images taken from identical sections in; (d) as-built, (e) HIPed, and (f) HT1 processed conditions. 165

Figure 4.11: Secondary electron SEM images of parallel observation direction of HT2 processed sample. (a) Less etched surface to represent bright particles, (b) the bright particles located between the γ/α_2 lamellae, (c) EDS point analyses regions, (d) EDS mapping obtained from the lamellar region. 167

Figure 4.12: Phase maps of; (a) as-built, (b) HIPed, (c) HT1 and (d) HT2 processed samples in parallel observation direction. 169

Figure 4.13: IQ-GBs maps of; (a) as-built, (b) HIPed, (c) HT1, and (d) HT2 processed samples in parallel observation direction.....	171
Figure 4.14: IPF maps of; (a) as-built, (b) HIPed, (c) HT1, and (d) HT2 processed samples in parallel observation direction.....	173
Figure 4.15: IPFs of; (a) as-built, (b) HIPed, and (c) HTed samples in parallel observation direction.....	174
Figure 4.16: KAM maps of; (a) as-built, (b) HIPed, (c) HT1 and (d) HT2 processed samples in parallel observation direction.....	176
Figure 4.17: GOS maps of; (a) as-built, (b) HIPed, (c) HT1 and (d) HT2 processed samples in parallel observation direction.....	178
Figure 4.18: Microhardness indentation marks; in γ grains from the; (a) measurement 1, (b) measurement 2, (c) measurement 3, (d) measurement 4 and in $\alpha_2 + \gamma$ lamellae from the; (e) measurement 5, (f) measurement 6, (g) measurement 7, (h) measurement 8.....	180
Figure 4.19: Temperature dependent yield strength, tensile strength and elongation values of as-built samples.	183
Figure 4.20: SEM images of fracture surfaces of as-built PBF-EB fabricated in XY-direction; (a) room temperature, (b) 700 °C, (c) 800 °C and in Z-direction; (d) room temperature, (e) 700 °C, (f) 800 °C tensile test specimens.....	184
Figure 4.21: SEM images of the fracture surface from room temperature tensile tests on the as-built XY-direction specimen at; (a) 250x, (b) 5000x magnification, along with EDS analysis for (c) the left side (marked as 1) and (d) the right side (marked as 2) of the crack.....	185
Figure 4.22: SEM images of the fracture surface from room temperature tensile tests on the as-built Z-direction specimen at; (a) 250x, (b) 5000x magnification, along with EDS analysis for (c) the top side (marked as 1) and (d) the bottom side (marked as 2) of the crack.....	186
Figure 4.23: Cross section optical micrographs of room temperature tensile test fracture surfaces for PBF-EB fabricated Ti48Al2Cr2Nb as-built samples in XY-	

direction at; (a) 50x, (b) 100x, (c) 200x, (d) 500x magnifications and in Z-direction at; (a) 50x, (b) 100x, (c) 200x, (d) 500x magnifications. 187

Figure 4.24: Secondary electron SEM images of the cross section of as-built Z-direction room temperature tensile test specimen revealing; (a) sub-surface crack path at a magnification of 1000x, (b) coarse grains aligned parallel to fracture surface at a magnification of 250x, (c) crack zone at a magnification of 2500x. . 189

Figure 4.25: Cross-sectional optical micrographs of PBF-EB fabricated Ti48Al2Cr2Nb as-built samples in the XY-direction for; (a) 700 °C tensile test fracture surface at 50x, (b) 700 °C tensile test fracture surface at 500x, (c) 800 °C tensile test fracture surface at 50x, (d) 800 °C tensile test fracture surface at 500x, and in the Z-direction for; (e) 700 °C tensile test fracture surface at 50x, (f) 700 °C tensile test fracture surface at 500x, (g) 800 °C tensile test fracture surface at 50x, (h) 800 °C tensile test fracture surface at 500x..... 190

Figure 4.26: Temperature dependent yield strength, tensile strength and elongation values of HIPed XY-direction samples. 193

Figure 4.27: SEM images of the fracture surfaces of XY-direction HIPed samples after tensile tests at; (a) room temperature, (b) 700 °C, (c) 800 °C and Z-direction HIPed samples after tensile tests at; (d) Room temperature, (e) 700 °C, (f) 800 °C tensile test specimens. 194

Figure 4.28: SEM images of the fracture surface from room temperature tensile tests on the HIPed XY-direction specimen at; (a) 250x, (b) 5000x magnification, along with EDS analysis for (c) the right side (marked as 1) and (d) the left side (marked as 2) of the crack. 195

Figure 4.29: SEM images of the fracture surface from room temperature tensile tests on the HIPed Z-direction specimen at; (a) 250x, (b) 5000x magnification, along with EDS analysis for (c) the left side (marked as 1) and (d) the right side (marked as 2) of the crack. 196

Figure 4.30: Cross section optical micrographs of room temperature tensile test fracture surfaces for PBF-EB fabricated Ti48Al2Cr2Nb HIPed samples in XY-

direction at; (a) 50x, (b) 100x, (c) 200x, (d) 500x magnifications and in Z-direction at; (a) 50x, (b) 100x, (c) 200x, (d) 500x magnifications..... 197

Figure 4.31: Cross-sectional optical micrographs of PBF-EB fabricated Ti48Al2Cr2Nb HIPed samples in XY-direction for; (a) 700 °C tensile test fracture surface at 50x, (b) 700 °C tensile test fracture surface at 500x, (c) 800 °C tensile test fracture surface at 50x, (d) 800 °C tensile test fracture surface at 500x and in Z-direction for; (e) 700 °C tensile test fracture surface at 50x, (f) 700 °C tensile test fracture surface at 500x, (g) 800 °C tensile test fracture surface at 50x, (h) of 800 °C tensile test fracture surface at 500x. 198

Figure 4.32: Temperature dependent yield strength, tensile strength and elongation values of HT1 processed samples. 200

Figure 4.33: SEM images of fracture surfaces of XY-direction HT1 samples after tensile tests at; (a) room temperature, (b) 700 °C, (c) 800 °C and Z-direction HT1 samples after tensile tests at; (d) Room temperature, (e) 700 °C, (f) 800 °C tensile test specimens. 202

Figure 4.34: SEM images of the fracture surface from room temperature tensile tests on the HT1 processed XY-direction specimen at; (a) 250x, (b) 5000x magnification, along with EDS analysis for (c) the left side (marked as 1) and (d) the right side (marked as 2) of the crack. 203

Figure 4.35: SEM images of the fracture surface from room temperature tensile tests on the HT1 processed Z-direction specimen at; (a) 250x, (b) 5000x magnification, along with EDS analysis for (c) the left side (marked as 1) and (d) the right side (marked as 2) of the crack. 204

Figure 4.36: Cross section optical micrographs of room temperature tensile test fracture surfaces for PBF-EB fabricated Ti48Al2Cr2Nb HT1 samples in XY-direction at; (a) 50x, (b) 100x, (c) 200x, (d) 500x magnifications and in Z-direction at; (a) 50x, (b) 100x, (c) 200x, (d) 500x magnifications..... 205

Figure 4.37: Cross-sectional optical micrographs of PBF-EB fabricated Ti48Al2Cr2Nb HT1 processed samples in XY-direction for; (a) 700 °C tensile test

fracture surface at 50x, (b) 700 °C tensile test fracture surface at 500x, (c) 800 °C tensile test fracture surface at 50x, (d) 800 °C tensile test fracture surface at 500x and in Z-direction for; (e) 700 °C tensile test fracture surface at 50x, (f) 700 °C tensile test fracture surface at 500x, (g) 800°C tensile test fracture surface at 50x, (h) of 800 °C tensile test fracture surface at 500x.....	206
Figure 4.38: Temperature dependent yield strength, tensile strength and elongation values of HT2 processed XY-direction samples.	208
Figure 4.39: SEM images of fracture surfaces of XY -direction HT2 samples after tensile tests at; (a) Room temperature, (b) 700 °C, (c) 800 °C and Z-direction HT2 samples after tensile tests at; (d) Room temperature, (e) 700 °C, (f) 800 °C tensile test specimens.....	209
Figure 4.40: SEM images of the fracture surface from room temperature tensile tests on the HT2 processed XY-direction specimen at; (a) 250x, (b) 5000x magnification, along with EDS analysis for (c) the left side (marked as 1) and (d) the right side (marked as 2) of the crack.	211
Figure 4.41: SEM images of the fracture surface from room temperature tensile tests on the HT2 processed Z-direction specimen at; (a) 250x, (b) 5000x magnification, along with EDS analysis for (c) the left side (marked as 1) and (d) the right side (marked as 2) of the crack.	212
Figure 4.42: Cross section optical micrographs of room temperature tensile test fracture surfaces for PBF-EB fabricated Ti48Al2Cr2Nb HT2 processed samples in XY-direction at; (a) 50x, (b) 100x, (c) 200x, (d) 500x magnifications and in Z-direction at; (a) 50x, (b) 100x, (c) 200x, (d) 500x magnifications.....	213
Figure 4.43: Cross-sectional optical micrographs of PBF-EB fabricated Ti48Al2Cr2Nb HT2 processed samples in XY-direction for; (a) 700 °C tensile test fracture surface at 50x, (b) 700 °C tensile test fracture surface at 500x, (c) 800 °C tensile test fracture surface at 50x, (d) 800 °C tensile test fracture surface at 500x and in Z-direction for; (e) 700 °C tensile test fracture surface at 50x, (f) 700 °C	

tensile test fracture surface at 500x, (g) 800 °C tensile test fracture surface at 50x, (h) of 800 °C tensile test fracture surface at 500x.	214
Figure 4.44: Temperature dependent line graphs of; (a) UTS, (b) YS, (c) El.% for; as-built, HIPed, HT1 and HT2 processed samples in both XY- and Z-directions.	220
Figure 4.45: Stress-strain curves obtained at; (a) 25 °C, (b) 700 °C, (c) 800 °C for; as-built, HIPed, HT1 and HT2 processed samples in both XY- and Z-directions.	221
Figure 4.46: Mechanical property anisotropy diagrams of XY/Z ratio for; (a) XY_{UTS}/Z_{UTS} and XY_{YS}/Z_{YS} and (b) $XY_{El.\%}/Z_{El.\%}$	222
Figure 4.47: SEM images obtained from 800 °C tensile tests of the fracture surfaces of; (a) as-built sample in XY-, (b) as-built sample in Z-, (c) HIPed sample in XY-, (d) HIPed sample in Z-, (e) HT1 sample in XY-, (f) HT1 sample in Z-, (g) as-built sample in XY-, (h) HT2 sample in XY-, (h) HT2 sample in Z-directions.	226
Figure 4.48: Binary and quaternary phase diagrams of; (a) Ti-Al binary and (b) Nb/Cr modified Ti-Al-Cr-Nb quaternary phase systems. Binary and quaternary phase diagrams at 100 MPa for; (c) Ti-Al binary and (d) Nb/Cr modified Ti-Al-Cr-Nb quaternary phase systems.	228
Figure 4.49: Top view of Z-direction double-scan tensile specimens; (a) partial overlap #1, (b) complete overlap and (c) partial overlap #2.	232
Figure 4.50: Optical micrographs of 01 st sample that shows; (a) inner circle at 50x, (b) overlap region at 50x, (c) overlap region at 200x and (d) overlap region at 500x magnifications.	235
Figure 4.51: Optical micrographs of 02 nd sample that shows; (a) inner circle at 50x, (b) overlap region at 50x, (c) overlap region at 200x and (d) overlap region at 500x magnifications.	236
Figure 4.52: Optical micrographs of 03 rd sample that shows; (a) inner circle at 50x, (b) overlap region at 50x, (c) overlap region at 200x and (d) overlap region at 500x magnifications.	237

Figure 4.53: Optical micrographs of 04th sample that shows; (a) inner circle at 50x, (b) overlap region at 50x, (c) overlap region at 200x and (d) overlap region at 500x magnifications.238

Figure 4.54: Optical micrographs of 05th sample that shows; (a) inner circle at 50x, (b) overlap region and middle ring at 50x, (c) overlap region at 200x and (d) overlap region at 500x magnifications.240

Figure 4.55: Optical micrographs of 06th sample that shows; (a) inner circle at 50x, (b) overlap region and middle ring at 50x, (c) overlap region at 200x and (d) overlap region at 500x magnifications.241

Figure 4.56: Optical micrographs of 07th sample that shows; (a) inner circle at 50x, (b) overlap region and middle ring at 50x, (c) overlap region at 200x and (d) overlap region at 500x magnifications.242

Figure 4.57: Optical micrographs of 08th sample that shows; (a) inner circle at 50x, (b) overlap region and middle ring at 50x, (c) overlap region at 200x and (d) overlap region at 500x magnifications.243

Figure 4.58: Optical micrographs of 09th sample at; (a) 50x, (b) 200x, (c) 500x, (d) 1000x magnifications.247

Figure 4.59: Optical micrographs of 10th sample at; (a) 50x, (b) 200x, (c) 500x, (d) 1000x magnifications.248

Figure 4.60: Optical micrographs of 11th sample at; (a) 50x, (b) 200x, (c) 500x, (d) 1000x magnifications.249

Figure 4.61: Optical micrographs of 12th sample at; (a) 50x, (b) 200x, (c) 500x, (d) 1000x magnifications.250

Figure 4.62: Optical micrographs of; (a) 13th sample at 50x, (b) 13th sample at 1000x, (c) 14th sample at 50x, (d) 14th sample at 1000x, (e) 15th sample at 50x, (f) 15th sample at 1000x, (g) 16th sample at 50x, (h) 16th sample at 1000x magnifications.251

Figure 4.63: Optical micrographs of 17th sample that shows; (a) inner circle at 50x, (b) overlap region at 50x, (c) inner circle at 1000x and (d) outer ring at 1000x magnifications.256

Figure 4.64: Optical micrographs of 18th sample that shows; (a) inner circle at 50x, (b) overlap region at 50x, (c) inner circle at 1000x and (d) outer ring at 1000x magnifications..... 257

Figure 4.65: Optical micrographs of 19th sample that shows; (a) inner circle at 50x, (b) overlap region at 50x, (c) inner circle at 1000x and (d) outer ring at 1000x magnifications..... 258

Figure 4.66: Optical micrographs of 20th sample that shows; (a) inner circle at 50x, (b) overlap region at 50x, (c) inner circle at 1000x and (d) outer ring at 1000x magnifications..... 259

Figure 4.67: Optical micrographs of; (a) inner circle of 21st sample at 50x, (b) inner circle of 21st sample at 1000x, (c) inner circle of 22nd sample at 50x, (d) outer ring of 22nd sample at 1000x, (e) inner circle of 23rd sample at 50x, (f) inner circle of 23rd sample at 1000x, (a) inner circle of 24st sample at 50x, (b) outer ring of 24st sample at 1000x. 260

Figure 4.68: Optical microscopy images in parallel to build direction of; (a) as-built, (b) DS05, (c) DS10, (d) DS17 samples at 50x magnification. 267

Figure 4.69: Optical microscopy images in Z-direction of; (a) as-built, (b) DS05, (c) DS10, (d) DS17 samples at 200x magnification. 268

LIST OF ABBREVIATIONS

ABBREVIATIONS

TiAl	: Titanium Aluminide
AM	: Additive Manufacturing
PBF	: Powder Bed Fusion
DED	: Directed Energy Deposition
WAAM	: Wire Arc Additive Manufacturing
EBM	: Electron Beam Melting
PBF-EB	: Electron Beam Powder Bed Fusion
PBF-LB	: Laser Beam Powder Bed Fusion
DED-LB	: Laser Beam Directed Energy Deposition
HIP	: Hot Isostatic Pressing at 1200 °C under 100 MPa for 2 hour
HT1	: Annealing Heat Treatment at 1200 °C
HT2	: Annealing Heat Treatment at 1400 °C
XCT	: X-Ray Computed Tomography
XRF	: X-Ray Fluorescence
XRD	: X-Ray Diffraction
EBSD	: Electron Backscattered Diffraction
DS	: Double Scanning
RT	: Room Temperature
ET	: Elevated Temperature
UTS	: Ultimate Tensile Strength
YS	: Yield Strength
El.%	: Elongation Percent

CHAPTER 1

INTRODUCTION

Titanium Aluminide (TiAl) alloys belong to the class of ordered intermetallics, characterized by distinct properties such as high specific strength at elevated temperatures, good creep resistance, and notably, low density, particularly when compared to nickel-based superalloys [1]. Their low density, in particular, renders TiAl alloys appealing for aerospace applications, serving as a potential substitute for nickel-based superalloys with the aim of enhancing the efficiency of aero engines through a higher thrust-to-weight ratio [2]. These alloys have already found practical use in commercial applications, such as low-pressure turbine blades in turbofan aero engines and turbochargers in piston automobile engines, owing to their inherent advantages over superalloys [3]. In the near future, the role of TiAl alloys in aerospace applications is expected to expand, notably with the development and certification of the Ti48Al2C2Nb alloy by General Electric for use in the commercial GEnX turbofan engine [4].

On the contrary, the challenges posed by high oxygen reactivity, low ductility, and poor high-temperature deformability make the processing of TiAl alloys difficult, despite their exceptional material properties [5]. Consequently, the casting method has conventionally been perceived as the sole viable manufacturing technology for TiAl alloys [6]. However, the casting process introduces various metallurgical issues in the production of TiAl alloys, such as the oxidation of bulk material from the ceramic crucible and the formation of a coarser resultant microstructure, leading to a decrease in part quality. Moreover, casting technology lacks design flexibility and demands significant effort in terms of pre and post processes [7], [8]. In an effort to mitigate the drawbacks associated with casting, researchers have

explored novel manufacturing routes to produce TiAl parts in a near-net shape, aiming to eliminate process deteriorations inherent in casting [9].

To address the limitations of casting, powder bed additive manufacturing (AM) processes, including both laser beam powder bed fusion (PBF-LB) [10] – [13] and electron beam melting (or more generally known as electron beam powder bed fusion (PBF-EB)) [2], [11], [14] – [23], have emerged as promising fabrication methods for TiAl alloy components. More recent approaches favor PBF-EB due to its high-temperature processing capability and vacuum environment. PBF-EB allows for the production of intricately shaped metallic TiAl parts from pre-alloyed powders, with a higher deposition rate compared to PBF-LB [20]. PBF-EB has garnered greater attention than PBF-LB, especially in the manufacturing of TiAl parts, as its high energy density and hot process nature result in fewer residual stresses during production. This characteristic enables the fabrication of crack-free TiAl components with PBF-EB [16], [17].

Despite the success in TiAl manufacturing, the microstructure and mechanical properties differ from those obtained through casting due to the directional solidification and layered nature of the PBF-EB process. Additionally, TiAl exhibits very low ductility, along with low fracture toughness and pronounced brittleness [10]. The ductility, among other mechanical properties of TiAl alloys, is highly dependent on their microstructure, which can be modified through heat treatments. Particularly for aerospace applications, enhancing the poor ductility of TiAl alloys while ensuring adequate strength and creep resistance is imperative [1].

Structural applications of TiAl alloys involve major phases γ -TiAl and α_2 -Ti₃Al, along with their combinations exhibiting various morphologies and distributions [25]. The microstructure in titanium-rich TiAl alloys typically varies as follows: (i) a fully lamellar structure comprising γ -TiAl and α_2 -Ti₃Al phases, (ii) a duplex structure consisting of γ/α_2 lamellae and fine γ grains, and (iii) a near γ structure where equiaxed γ grains predominate, with a small amount of γ and α_2 lamellae [25]. The duplex microstructure is recommended because of its high strength and

ductility, whereas the fully lamellar microstructure is advantageous for good creep properties. [1], [22], [25]. The microstructure-dependent mechanical properties allow TiAl alloys to be tailored for specific applications through additional heat treatments. This study aims to control the mechanical properties of PBF-EB-manufactured TiAl by secondary processes such as heat treatment and hot isostatic processing.

Previous researches have looked into the effect of the layered process in PBF-EB on the microstructure and mechanical anisotropy of TiAl alloys [20], [23]. The as-built microstructure was identified as two alternating layers, one with a lamellar structure (γ/α_2) and fine equiaxed grains, and the other with coarser equiaxed grains arranged in a chain-like pattern perpendicular to the building direction. The applied load's direction in relation to the layered microstructure determines how the structure responds to stress and deformation. Anisotropy was seen in tensile behavior, with slightly decreased yield strength at a 45° angle compared to vertical and horizontal specimens. Maximum shear stress and higher tensile elongation occurred when the layered structure was at 45° angle to the loading axis [22], [23].

The microstructure and mechanical properties of Ti48Al2Cr2Nb alloy components manufactured through PBF have been the focus of intensive research in recent years. Various publications [11], [17], [21], [23], [24] and [26] have addressed the impact of microstructural anisotropy resulting from the PBF-EB method on mechanical properties. However, a comprehensive exploration underlying the pronounced brittleness observed in as-built Ti48Al2Cr2Nb samples tested parallel to the production direction is still lacking. The significant brittleness observed in relation to the manufacturing direction poses a crucial challenge for the utilization of Ti48Al2Cr2Nb alloy produced by the PBF-EB process in applications such as aviation engines.

This study delves into the excessively brittle behavior of Ti48Al2Cr2Nb alloy fabricated with PBF-EB samples produced parallel to the manufacturing direction (Z-direction). Various methods, including microstructure analysis, EBSD

examinations, microhardness measurements, and room/high-temperature tensile tests, were employed to investigate this behavior. The substantial brittleness observed in specimens manufactured in the Z-direction was primarily attributed to the coarse banding of the γ -TiAl phase, aligned perpendicular to the production direction. In contrast, the coarse γ colonies randomly dispersed in samples oriented in the XY-direction did not induce excessive brittleness due to their lack of a distinct pattern. The extreme brittleness in the Z-direction was comprehensively evaluated in terms of hardness, chemical composition, dislocation density, and recrystallization features, addressing gaps in the cause-and-effect relationship identified in the literature.

The current study employs a materials engineering approach, utilizing post-process thermal treatments to enhance the mechanical properties of the Ti48Al2Cr2Nb alloy under loads parallel to the production direction. Within this framework, the effects of secondary thermal treatments on the microstructural and mechanical properties of the Ti48Al2Cr2Nb alloy produced through PBF-EB were thoroughly investigated. Two conventional annealing methods were implemented at 1200 and 1400 °C, yielding duplex-like and fully lamellar microstructures, respectively. Additionally, the impact of hot isostatic pressing (HIP) at 1200 °C under a pressure of 100 MPa on the material properties was evaluated. Extensive EBSD analyses were conducted to assess the impact of secondary processes on texture.

The study revealed that both HIPing and heat treatment processes conducted at 1200 °C effectively mitigated dislocation density and internal stresses generated by PBF-EB, while preserving recrystallization. Conversely, the heat treatment performed at 1400 °C resulted in a higher amount of α_2 , responsible for the absence of recrystallization and an increased $\langle 001 \rangle$ texture in PBF-EB fabrication. Moreover, this research aims to address gaps in the existing literature through the execution of high-temperature tensile tests and detailed microstructure analyses. These analyses aim to elucidate the effect of secondary processes following PBF-EB and establish correlations between resulting microstructural features and mechanical properties.

In the last part of the study, three distinct groups comprising 24 alternative scanning procedures were assessed with the aim of mitigating the pronounced brittleness in the Z-direction associated with the PBF-EB process, without relying on secondary thermal treatments. The double-scan approach involved the repetitive scanning of sample surfaces with electron beams using specific procedures. As per the study's findings, it is feasible to optimize the mechanical properties of Ti48Al2Cr2Nb produced in the Z-direction through PBF-EB without the need for additional processes that would augment overall manufacturing time and cost. This opens the door to the use of the novel production approach named as double-scan, which has not previously been investigated in the literature, to Ti48Al2Cr2Nb material.

This Ph.D. thesis contains five chapters designed to provide comprehensive information about the primary concepts of secondary thermal treatments on PBF-EB manufactured Ti48Al2Cr2Nb alloy. The Chapter 2, dedicated to the literature review, is divided into several sections to present the theoretical background that illuminates the main study. Initially, the properties of titanium aluminide (TiAl) alloys and their physical metallurgy are explained, emphasizing their relevance to the aerospace industry. Subsequently, before delving into detailed information about additive manufacturing (AM) process routes for TiAl, conventional manufacturing methods such as casting, wroughting, and powder metallurgy are elucidated. The chapter further discusses direct energy deposition (DED) and powder bed fusion (PBF) AM fabrication methods employed for TiAl production, providing comprehensive insights into their impact on microstructure and mechanical characteristics. PBF-EB manufacturing of TiAl is particularly emphasized in detail to offer preliminary information about the study. Additionally, an in-depth literature review is provided for the PBF-EB technology. Chapter 3 presents the production method, along with the physical and chemical properties of initially PBF-EB fabricated samples. The principles of various characterization methods, including computed tomography measurements, thermal expansion measurements, compositional analysis, X-ray diffractions, metallographic

examinations, electron backscattered diffractions, thermodynamic modelings, tensile tests, and hardness measurements, are introduced within this chapter. Chapter 4 covers experimental results and their discussions with respect to structural, microstructural, and mechanical doctrines. Finally, Chapter 5 concludes the thesis, presenting overall findings and suggestions for future work.

CHAPTER 2

LITERATURE REVIEW

2.1 Introduction to Titanium Aluminides and Their Applications

2.1.1 Introduction and Overview

Titanium aluminides (TiAl) have garnered an extensive amount of interest in the last three decades because of their desirable characteristics which have the ability to permit elevated temperatures in power generator, automotive and aerospace applications [27]. In comparison to conventional titanium alloys, the remarkable thermo-physical properties of TiAls stem primarily from their highly ordered structure which includes a high melting point, a high specific strength, a low diffusion coefficient, a low density ranging from 3.9 to 4.2 g/cm³, high structural stability and excellent corrosion resistance [27]. Figure 2.1 shows the temperature dependent specific strength of various alloy categories. Accordingly, TiAl-based alloys surpass titanium alloys, steels, and nickel-based superalloys in terms of specific strength vs temperature characteristics within the temperature range of 500 to 900 °C [27] – [28]. Table 2.1 provides a qualitative assessment of the attributes of advanced high temperature alloys designed for application in the aerospace sector [27], [29].

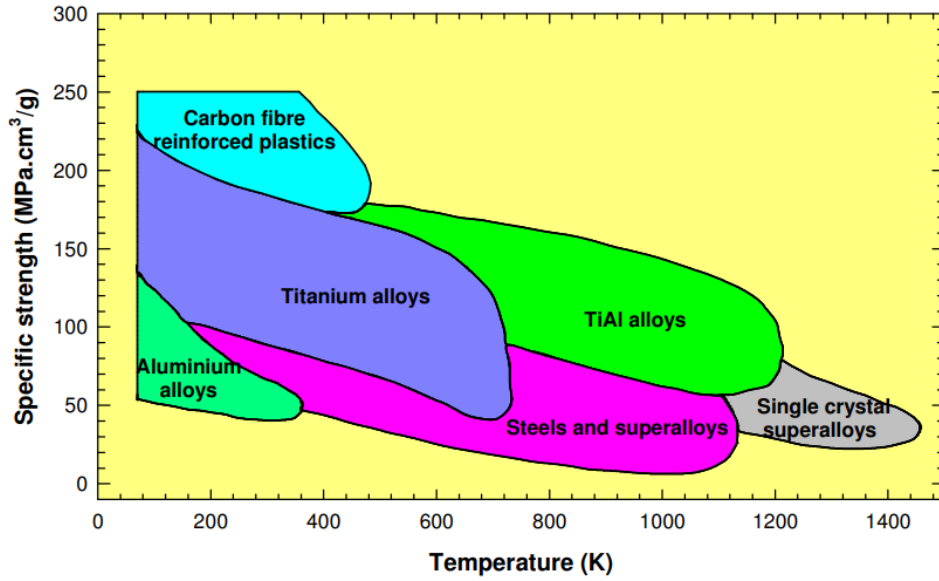


Figure 2.1: Temperature dependent specific strength of various alloy categories [27].

Table 2.1: Comparative properties for high temperature alloys [27].

	Near- α Ti	Ni based	γ TiAl
Density	+	-	++
Specific tensile strength	+	-	+/-
High-temperature Young's modulus	+/-	+	++
Room-temperature ductility	+	+	-
Formability	+	+	-
Creep	-	++	++
Room-temperature fracture toughness	+	++	-
Room-temperature crack growth	+	+	-
Specific fatigue strength	+	-	+/-
Oxidation	-	++	++
High-temperature embrittlement	-	+	+/-

TiAls have emerged as major competitors for replacing nickel based superalloys in gas turbine engines due to their low density and high strength [30], [31]. They have half the density of nickel-based superalloys. Furthermore, TiAls have advantageous properties such as elevated temperature oxidation and creep resistance along with outstanding strength and modulus retention at high temperatures. Especially γ -

TiAls have excellent thermal stability and great strength [30], [31]. It is expected that replacing nickel based superalloy sections with TiAls will reduce the structural weight of high performance gas turbine engines by 20-30% [32]. As a result, using TiAls in gas turbine engines may result in significant improvements in engine performance and fuel efficiency [30].

The long range order characteristic of intermetallics restricts the deformation modes [33]. These constraints typically result in increased strength, especially at high temperatures, as well as decreased ductility and fracture toughness [33]. TiAls have low room temperature ductility and fracture toughness due to their long range order. The fatigue fracture growth rate is also lower than in nickel-based superalloys [33], [34]. TiAls have a limited range of uses due to their brittleness at room temperature [35]. The service temperature limit for TiAl alloys in engineering applications is at 750 °C, owing to low strength and creep resistance above this temperature [35]. Because of their microstructure and complicated structure, TiAls are brittle and difficult to process using standard manufacturing procedures [36]. Table 2.2 lists numerous parameters for titanium alloys, Ti₃Al and TiAl base alloys, and Ni base superalloys [37]. Due to manufacturing restrictions, TiAls are significantly more expensive to produce (about 65 times) than nickel-based superalloys [37], [38]. In the past two decades, significant research efforts have been dedicated to enhancing productivity through the adoption of near-net-shape methods, such as powder metallurgy and additive manufacturing [31].

Table 2.2: Several properties of titanium, TiAl and Ni-base alloys [37].

Property	Ti-base alloys	Ti₃Al-base alloys (α_2 alloys)	TiAl-base alloys (γ alloys)	Ni-base superalloys
Density (g cm⁻³)	4.5	4.1-4.7	3.7-3.9	8.3
Yield strength (MPa)	380-1150	700-900	400-630	850
Tensile strength (MPa)	480-1200	800-1140	450-700	1000
RT modulus (GPa)	96-115	120-145	160-176	206
Oxidation (°C)	600	650	900-1000	1090
Creep limit (°C)	600	750	1000	1090
Ductility (%) at RT	10-20	2-7	1-3	3-5
Ductility (%) at HT	High	10-20	10-90	10-20

2.1.2 Applications

The main motivation for TiAl adoption in the aerospace sector was to replace nickel-based superalloys in order to reduce weight because of TiAl's low density, high modulus and creep strength [39]. TiAl (Ti48Al2Cr2Nb) blades were first integrated in the low-pressure turbine (LPT) of GENx engines in 2006. Figure 2.2 (a) displays the last two stages of the GENx LPT blades, which are made of TiAl, while Figure 2.2 (b) shows a single stage of this engine [40]. The reduced centrifugal stress caused by the lightweight TiAl blades leads to a further reduction in the size of the nickel-based superalloy disc, which provides overall weight reductions. The use of two stages of TiAl LPT blades enables the elimination of about 100 kg of weight per engine [40]. The GENx engine provides a 50% decrease in noise, an 80% decrease in NO_x emissions and a 20% gain in fuel efficiency when compared to previous engines [41].

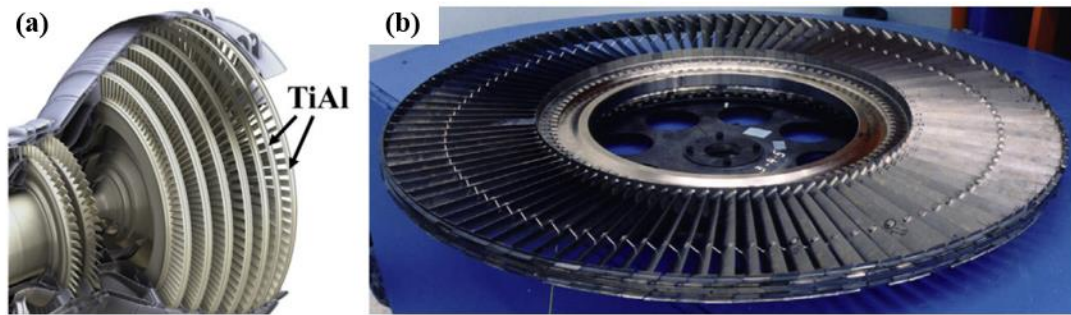


Figure 2.2: (a) Last two stages of the GEnx made of TiAl and (b) single stage of GEnx [40].

TiAl blades are presently employed on Boeing 787 and 747-8 [42]. Furthermore, LEAP engines, developed in collaboration with GE and Snecma, incorporate TiAl for the LPT blades. Furthermore, Pratt & Whitney and GE, in partnership with MTU, use a TiAl alloy known as TNM for the final stage of the PW1100G Geared TurboFan (GTF) engine [42], [43]. The Airbus 320neo aircraft, powered by two GTF engines, demonstrated the use of hot-forged TNM turbine blades in 2014 during its first flight. Furthermore, Rolls-Royce uses TiAl LPT blades in their Advance and Ultra Fan medium-thrust engines [44].

Aside from LPT blades, Volvo and Pratt & Whitney have been manufacturing TiAl components that include blade retainers and turbine dampers, compressor blades and shrouds [45]. A comprehensive engine test was carried out employing TiAl for 76 dampers. The duration of the endurance test was 214 hours. The outcomes revealed that using TiAl dampers at low stimulation frequencies resulted in a considerable 50% decrease in dynamic stress [46]. Meanwhile, Snecma and Turbomeca have completed several studies in order to produce a TiAl high-pressure compressor case using powder metallurgy [40].

There is a considerable opportunity in substituting iron and nickel based stator vanes with TiAl [47]. This substitution could result in significant weight savings and could be used for stator vanes operating at temperatures ranging from 300 to 400 °C to higher temperatures. As shown in Figure 2.3 (a), vanes are expected to

be cast with larger dimensions and then machined to their final shape [47]. GE has experimented with TiAl transition duct beams for GE90 engine, as shown in Figure 2.3 (b) [48]. These beams contribute to the support of a flow-path panel which provides resistance to engine stall loads [48].

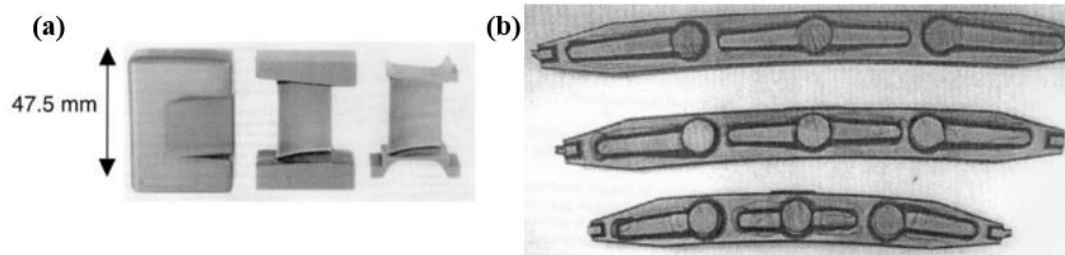


Figure 2.3: (a) Cast stator vanes at various stages of production. The cast preform, post electrochemical milling, and the final machined stator vane are shown from left to right [47]. (b) GE90 engine transition duct beams [48].

TiAl has already found application in automotive combustion engines [46]. The automotive industry actively attempts to minimise the size of conventional combustion engines while increasing their performance and efficiency, with the goal of improving fuel economy and lowering emissions. To achieve these objectives, lightweight and high temperature resistant internal combustion engine components such as turbocharger wheels, engine valves and connecting rods are needed. The second largest application field for TiAl alloys is the manufacture and integration of such components [46].

Lightweight valves in combustion engines provide numerous benefits including higher performance, fuel economy and reduced vibration as well as noise [49]. TiAl is a promising material for both intake and exhaust valves. Intake valves can withstand temperatures of up to 600 °C, while exhaust valves can resist temperatures of over 800 °C. This makes TiAl a possible replacement for conventional exhaust valve steels and nickel-based superalloys. TiAl valves have a significantly lower mass than steel valves by around 49% [49]. Several

corporations including General Motors, Daimler/Chrysler and Ford have conducted engine tests with TiAl valves [50]. The most serious issue appears to be wear. Coating the stem and valve tip has been suggested as a potential solution to mitigate this wear problem [50]. However, it is believed that no TiAl valves are currently in large production [46].

The maximum service temperature for diesel engines is 750 °C and for petrol engines it is 950 °C [51]. An alloy with superior creep resistance and strong oxidation resistance is required when service temperature and high loads are combined [51]. The major turbocharger and diesel engine manufacturers including Toyota, ABB, Daimler/Chrysler, Honeywell Garrett and Mitsubishi has successfully tested TiAl turbochargers [46]. The nickel-based superalloy Inconel 713C is currently the most frequently utilised material to produce turbocharger wheels in diesel engines [51]. Employing TiAl resulted in a 16% faster response time for turbocharger acceleration and a 26% improvement at speeds of 170,000 rpm when compared to Inconel 713C [52]. The TiAl turbocharger exceeded the Inconel 713C turbocharger's maximum speed by 10,000 rpm. Resistance to foreign-object damage (FOD) and erosion are also critical [52]. A high niobium-containing TiAl is more resistant to erosion than a low niobium-containing alloy [52]. Mitsubishi Heavy Industries (MHI) pioneered TiAl turbocharger wheels in the Lancer Evolution series automobiles [53]. Figure 2.4 (a) illustrates a turbocharger wheel joined to the shaft using electron beam welding, while Figure 2.4 (b) provides a cross-sectional view of the TD5 turbocharger [53].

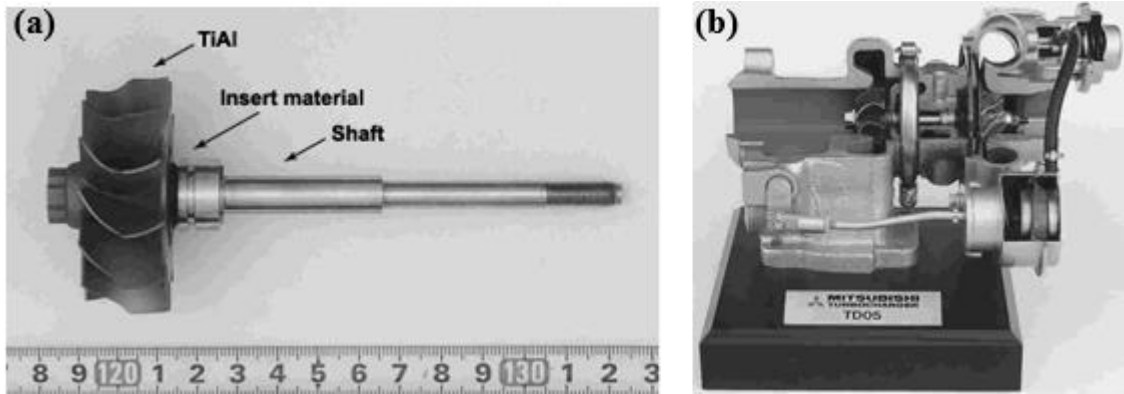


Figure 2.4: (a) TiAl turbocharger wheel joined to the shaft and (b) TD05 turbocharger used in Lancer Evolution VI [53].

2.2 Properties of Titanium Aluminides

2.2.1 Binary Ti-Al Phase System

Several intermetallic phases have been identified as possible foundations for lightweight high-temperature materials in the Ti-Al binary phase system. Extensive studies over many years have shown that only alloys based predominantly on the hexagonal $D0_{19}$ structured α_2 phase (Ti_3Al) or the tetragonal $L1_0$ structured γ phase ($TiAl$) have emerged as feasible structural materials. Significant interest has been focused on γ titanium aluminide alloys, which in technical applications typically contain small amounts of the α_2 phase. Furthermore, the high-temperature β phase, with its body-centered cubic (bcc) B2 structure ordered B2 version is important in certain alloys. Crystal structures of α_2 , γ and B2 are shown in Figure 2.5 (a), (b) and (c), respectively [54].

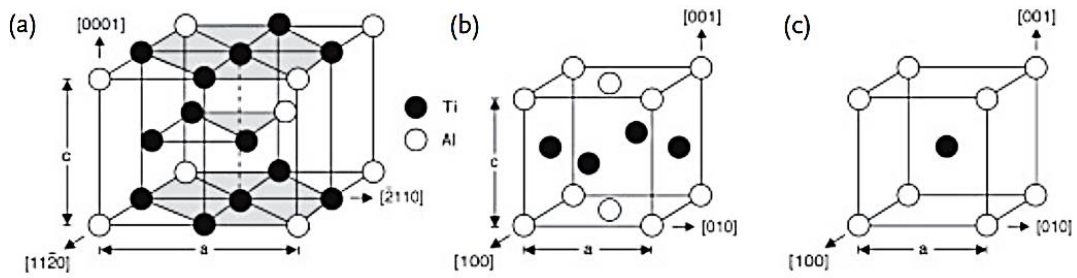


Figure 2.5: Crystal Structures of binary Ti-Al phases; (a) hexagonal α_2 (Ti_3Al) phase, (b) tetragonal γ (TiAl) phase, (c) cubic B2 phase [54].

α_2 - Ti_3Al phase exhibits a hexagonal $D0_{19}$ ordered structure belonging to $P6_3/mmc$ space group and its lattice parameters are $a = 0.5765$ nm and $c = 0.4625$ nm which result 0.8 c/a ratio. α_2 - Ti_3Al phase homogeneous at room temperature for aluminium contents between 21 - 35 at.%. It remains ordered up to 1180 °C before transforming to a disordered hcp α - phase for 32 at.% aluminum content. Hcp α phase transforms to a bcc β Ti phase during further heating [54], [291]. γ - TiAl phase has a face-centered tetragonal (fct) $L1_0$ ordered structure belonging to $P4/mmm$ space group and its lattice parameters are $a = 0.3997$ nm and $c = 0.4062$ nm which result 1.02 c/a ratio. As aluminum content decreases the c/a ratio becomes around 1 and the structure becomes ordered fcc [2]. γ - TiAl phase homogenous at room temperature for aluminium contents between 48 - 53 at.%. [54], [291], [292]. B2 phase has body centered cubic (bcc) B2 ordered structure belonging to $Im\bar{3}m$ space group and its lattice parameters are $a = 0.33065$ nm [54].

At room temperature there is γ - TiAl and α_2 - Ti_3Al two phase region in the phase diagram showing in Figure 2.6 where aluminium content is between 35 and 48 at.%. At 1120 °C the mixture of γ - TiAl and α_2 - Ti_3Al forms into α phase by eutectoid reaction at 38 at.% aluminum. Hcp α phase transforms to β + liquid with a peritectic reaction taking place at 1500 °C and 46 at.% aluminum content [292]. The crystallographic data of the main phase in Ti-Al binary system is given in Table 2.3 [54].

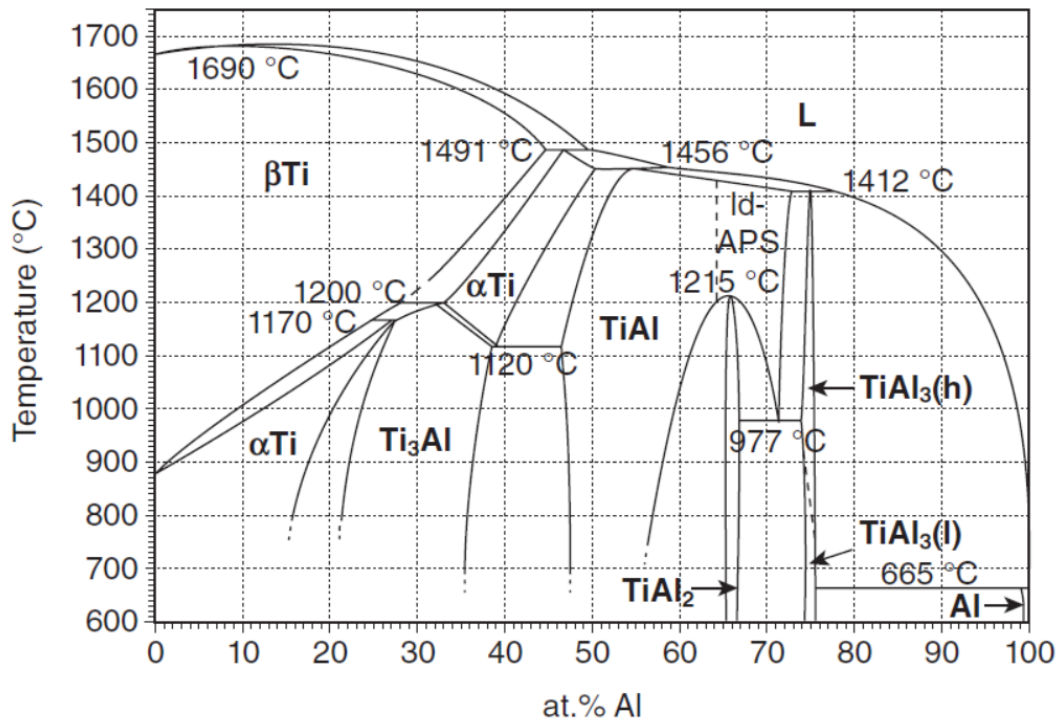


Figure 2.6: Ti-Al binary phase diagram according to Schuster and Palm [292].

The binary Ti-Al phase diagram is still a source of discussion [292] – [60]. The importance of these studies cannot be emphasised because the microstructural development of an alloy is governed by an understanding of the phase equilibria. Nonmetallic impurities, particularly those with a high susceptibility to oxygen, can change phase equilibria, resulting in discrepancies between different versions of the phase diagram [61], [62].

Table 2.3: Crystallographic data of the phases exhibiting in the binary Ti-Al system [54].

Designation	Pearson symbol	Space group	Strukturbericht designation	Prototype	Lattice parameters
L (liquid)					
Al	cF4	Fm $\bar{3}m$	A1	Cu	a = 4.0496 nm
β , β -Ti	cI2	Im $\bar{3}m$	A2	W	a = 0.33065 nm
α , α -Ti	hP2	P6 ₃ /mmc	A3	Mg	a = 0.29504 nm c = 0.46833 nm
α_2 , Ti ₃ Al	hP8	P6 ₃ /mmc	D0 ₁₉	Ni ₃ Sn	a = 0.5765 nm c = 0.4625 nm
γ , TiAl, γ (TiAl)	tP4	P4/mmm	L1 ₀	AuCu	a = 0.3997 nm c = 0.4062 nm a = 0.4000 nm c = 0.4075 nm a = 0.4016 nm c = 0.4068 nm
η , TiAl ₂	tI24	I4 ₁ /amd		HfGa ₂	a = 0.3971 nm c/6 = 0.4052 nm
ϵ (h), TiAl ₃ (h), TiAl ₃ (HT)	tI8	I4/mmm	D0 ₂₂	TiAl ₃ (h)	a = 0.3849 nm c/2 = 0.4305 nm
ϵ (l), TiAl ₃ (l), TiAl ₃ (LT)	tI32	I4/mmm		TiAl ₃ (l)	a = 0.3877 nm c/2 = 0.4229 nm

The intermetallic phases α_2 and γ have the potential to meet the necessary requirements for engineering applications. While the α_2 alloy possesses higher tensile strength compared to γ alloys, it lacks the capability to maintain its mechanical properties at elevated temperatures, unlike γ alloys. Consequently, when comparing these two phases, it becomes clear that the γ phase takes precedence in engineering applications [27], [292]. For the most engineering applications, alloys based on the γ -TiAl phase typically contain aluminum concentrations ranging from 44 to 48 at.%. As highlined in the phase diagram shown in Figure 2.7, γ -TiAls can solidify either through the β phase or peritectically. Two peritectic reactions could take place depending on the chemical composition. Even slight variations in aluminum content can lead to significantly different microstructures and textures. A variety of phase transitions can occur during the cooling process from high temperatures. In basically, this allows for the development of an extensive array of microstructures [63], [64]. The eutectoid

transformation $\alpha \rightarrow \alpha_2 + \gamma$, which occurs during the cooling process, is a common feature in all γ -TiAl alloys. The mechanism of this is similar to that of the reaction $\alpha \rightarrow \alpha + \gamma$, which involves the nucleation and development of γ lamellae. The volume percentage of the γ phase must increase rapidly as the temperature drops below the eutectoid transformation temperature to retain alloy compositions in thermodynamic equilibrium. However, the cooling rates are frequently too high to maintain thermodynamic equilibrium. As a consequence, resulting microstructures may be unstable at the service temperature. It is important to consider a microstructural stabilization treatment or implement appropriate cooling conditions [54].

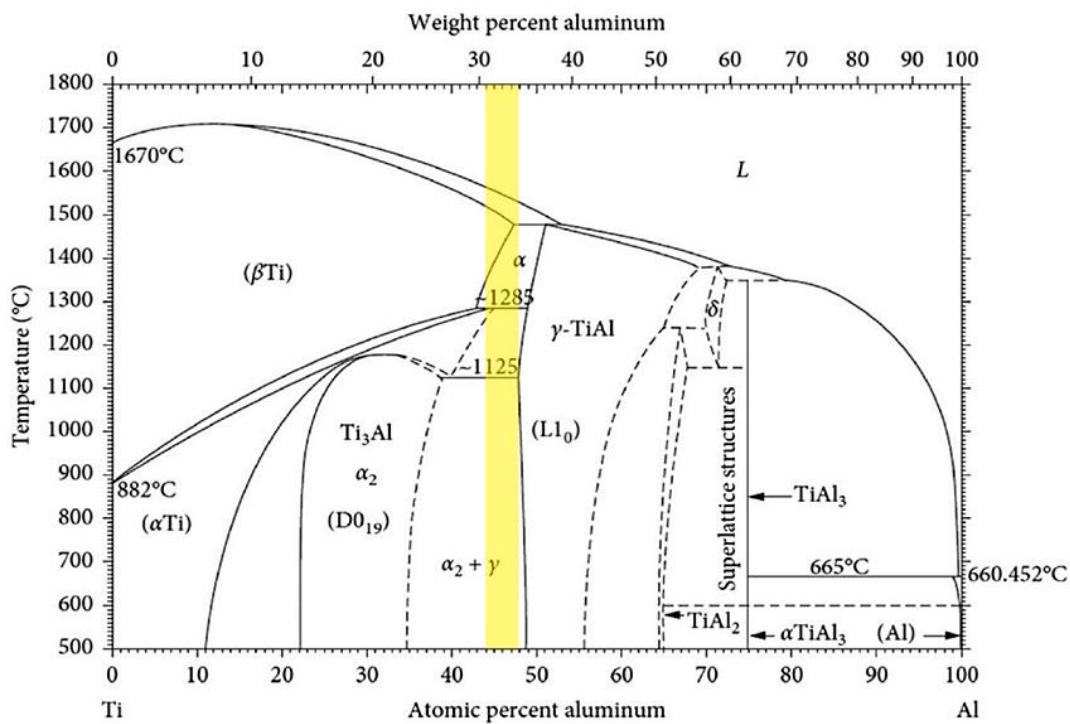


Figure 2.7: Ti-Al binary phase diagram that shows typical range for engineering γ -TiAl base alloys [65].

Figure 2.8 presents a simplified Ti-Al binary phase diagram, delineating the β -solidification pathway as "I" and the peritectic solidification pathways as "II" and "III." In the context of γ -TiAl alloys, two fundamental phase transformations occur: the $\beta \rightarrow \alpha$ or $L + \beta \rightarrow \alpha$ and the $\alpha \rightarrow \alpha_2 + \gamma$. Within these transformations, the composition and cooling rate emerge as pivotal factors [66].

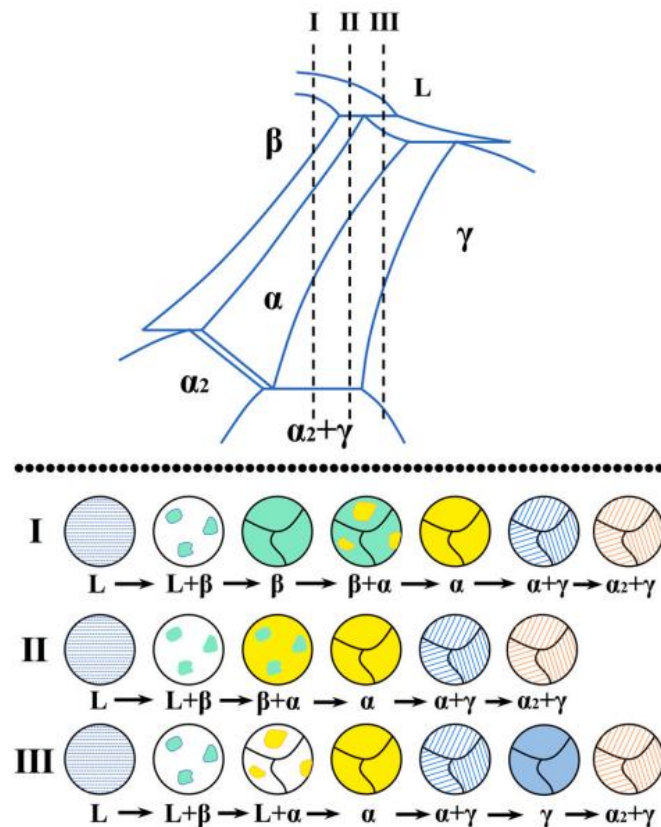


Figure 2.8: The simplified Ti-Al binary phase diagram, along with solidification pathways under different Al contents in equilibrium conditions [66].

2.2.1.1 Phase transformation from β to α

The β phase, characterized by a BCC structure in the $Im\bar{3}m$ space group, displays three equivalent orthorhombic $\langle 001 \rangle$ β growth directions [67]. In the

microstructure, primary arms of β dendrites exhibit secondary and tertiary branches arranged approximately orthogonal to each other [68]. The hexagonal crystal structure of the α phase ($P6_3/mmc$ space group) undergoes transformation from the β phase, adhering to the Burgers orientation relationship ($\{1\bar{1}0\}\beta \parallel (000\bar{1})\alpha$ and $\langle 111 \rangle \beta \parallel \langle 11\bar{2}0 \rangle \alpha$) [69]. Theoretical considerations suggest the generation of 12 distinct α phase orientation variants from the primary β phase, as depicted in Figure 2.9 [68]. Figure 2.9 (a) portrays the $[001] \beta$ stereographic projection, illustrating $\{1\bar{1}0\}\beta \parallel (000\bar{1})\alpha$ planes for the 12 α phase variants [68]. Stereographic projection points of different crystal faces of the β phase lattice are denoted by black solid circles. Figure 2.9 (b) identifies all six $\{1\bar{1}0\}\beta$ planes of the β phase lattice, while Figure 2.9 (c) clarifies that each Burgers-oriented α phase may have two variants with distinct growth directions [66].

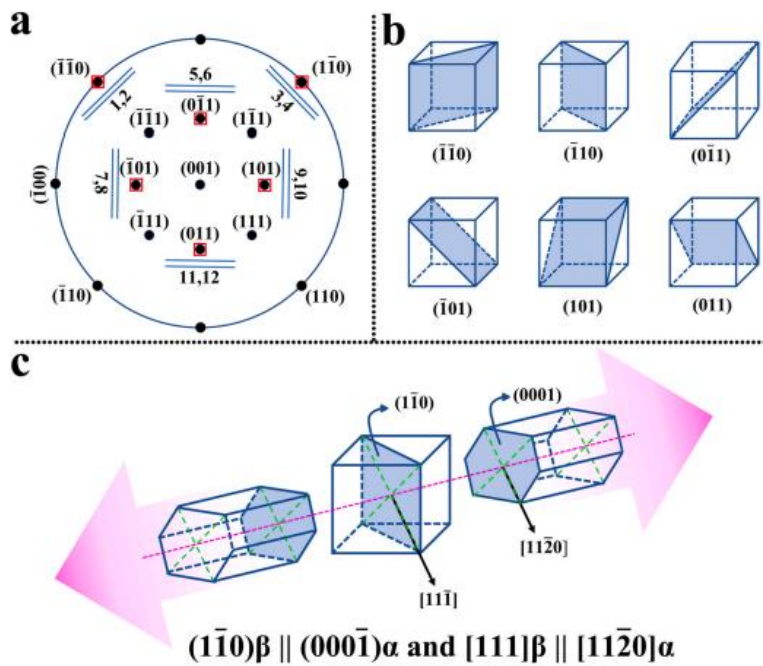


Figure 2.9: The orientation relationship between the primary β phase and the secondary α phase: (a) Stereographic projection of the $[001] \beta$ [68], (b) the $\{110\} \beta$ planes of the β phase crystal structure and (c) in the Burgers orientation relationship, two potentially distinct growth directions of the α phase parallel to the β phase $(1\bar{1}0)\beta$ plane [66].

In peritectic solidified alloys, the β phase acts as the primary phase originating from the liquid phase, experiencing a peritectic reaction following these steps [70]:

1. The primary β dendrites that solidify from the liquid phase typically exhibit preferential growth along the $\langle 100 \rangle$ β direction, aligning parallel to the direction of heat flow.
2. As the temperature decreases, a rapid cooling rate increases the probability of peritectic α phase nucleation at the interface between the primary β phase and the liquid. In contrast, with a slow cooling rate, nucleation may take place within the melt. Consequently, the favored growth direction of the α phase will align either with the c-axis orientation ($\langle 000\bar{1} \rangle$ α) parallel to the heat flow or with the primary β phase through the Burgers orientation relationship.
3. The peritectic reaction is completed through short-range diffusion, resulting in the formation of the α phase.
4. The residual liquid phase or the β phase with incomplete reaction will undergo direct transformation into the α phase.

In the β -solidified alloys, the initial phase during solidification is β , which subsequently transforms into the α phase after the completion of solidification [71], [72]. Two explanations for the distinction in solidification structures between as-cast peritectic solidified and β -solidified alloys are delineated [68], [71], [72]. The initial proposal suggests that, when the α phase nucleates in the melt, the peritectic α phase exhibits preferential growth with an orientation of the c-axis ($\langle 000\bar{1} \rangle$ α direction) parallel to the direction of heat flow. This tendency for growth in a specific direction unavoidably leads to the development of coarse columnar grains. The columnar grains produced by the peritectic α phase exhibit a singular lamellar orientation, specifically perpendicular to the growth direction. Additionally, the primary β phase is marked by enrichment in Ti and β phase stabilizers, contributing to chemical inhomogeneity [71], [72].

The second viewpoint suggests that the peritectic α phase originates at the interface between the primary β phase and the liquid, adopting its orientation from the primary β phase via the Burgers orientation relationship [68]. There are 12 possible α phase variants, each with a different development direction, based on the previously described crystallographic orientation. However, due of the substantial temperature gradient during solidification, it is common for only one of the 12 variants to be selected to envelop a specific β dendrite [68].

Depending on the cooling rate, the transition from β to α may occur in a diffusionless martensitic mode or via a composition-invariant massive transformation that involves short-range diffusion. Additionally, it can occur through the precipitation of the α phase from the β phase [73], [74]. Variable cooling rates give rise to diverse microstructures, such as martensitic transformation at rapid cooling rates, massive transformation at marginally reduced rates, and Widmannstätten plate precipitation at comparatively slower rates [75], [76].

2.2.1.2 Phase transformation from α to α_2

Another significant phase transformation in γ -TiAl alloys leads to the development of a lamellar structure [66]. Referring to the TiAl binary phase diagram shown in Figure 2.7, as the temperature decreases and enters the α single-phase zone upon cooling, the α phase undergoes decomposition, resulting in the formation of a lamellar structure comprising $\alpha_2 + \gamma$ lamellae. Two pathways characterize this reaction: one involves the sequence $\alpha \rightarrow L(\alpha + \gamma) \rightarrow L(\alpha_2 + \gamma)$, and the other follows $\alpha \rightarrow \alpha_2 \rightarrow L(\alpha_2 + \gamma)$, with 'L' representing the laths [66]. The selection between these two paths is dependent upon the cooling rate. A higher cooling rate favors the latter path, wherein the α phase initially transforms into α_2 through an ordered transformation, followed by the precipitation of the γ phase from the α_2 phase [66]. Conversely, a slower cooling rate leads to the first path, where γ lamellae precipitate first from the α phase, and subsequently, the ordered

transformation of the α phase takes place. With a further reduction in cooling rate, increased diffusion time results in the coarsening of γ lamellae into γ grains. The Blackburn orientation relationship leads to the emergence of the γ phase from the α_2 [77]: $(0001)\alpha_2 \parallel \{111\}\gamma$ and $\langle 11\bar{2}0 \rangle_{\alpha_2} \parallel \langle \bar{1}\bar{1}0 \rangle_{\gamma}$, as illustrated in Figure 2.10 [66]. Once the α phase orientation is established, it determines the orientation of following lamellae, with the c-axis of the α phase being perpendicular to the lamellar interface [78]-[81].

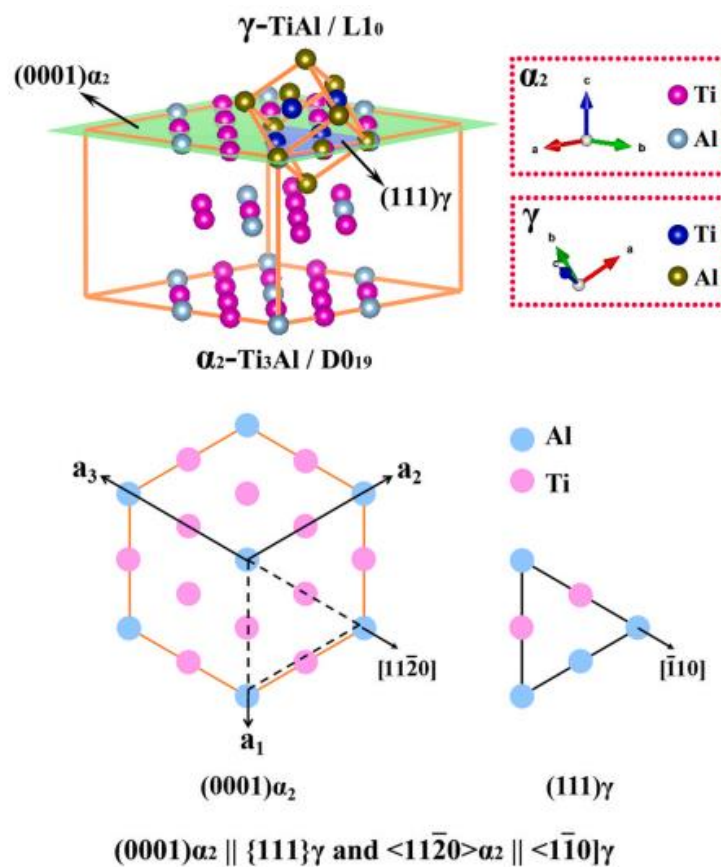


Figure 2.10: The precipitation of γ phase from α_2 phase [66].

When the Al equivalent is below 45 at%, the alloy undergoes complete solidification through the β phase, involving a $\beta \rightarrow \alpha$ transformation following the

Burgers orientation relationship $\{110\}\beta \parallel (0001)\alpha$ and $\langle 111 \rangle \beta \parallel \langle 11\bar{2}0 \rangle \alpha$ [82]. Within a single β grain, the α phase can develop up to 12 orientation variants, resulting in inherent grain refinement. This intrinsic grain refinement is not achievable in peritectic solidification of γ -TiAl alloys. The appeal of low Al-equivalent β -solidified alloys lies in their creation of a homogeneous and fine-grained solidification microstructure, making them particularly attractive when considering elemental segregation and lamellae orientation. Additionally, a lower Al equivalent level corresponds to a higher volume fraction of α_2 phase, leading to reduced lamellar spacing [82].

Apart from composition, the cooling rate is a crucial factor [83]. At slow cooling rates, a fully lamellar microstructure forms from the single α phase field through the phase transformation $\alpha \rightarrow \alpha + \gamma \rightarrow \alpha_2 + \gamma$. Increasing the cooling rate induces a significant transformation from α to γ_m , where the disordered hexagonal α phase undergoes a massive transformation into the γ_m phase, characterized by a high density of internal boundaries and defects [83]. Exceptionally high cooling rates, such as those achieved through water-quenching, inhibit the massive transformation. Instead, the α phase directly undergoes an ordered transformation to produce the α_2 phase, leading to a solidification structure characterized by supersaturated α_2 grains [84].

γ -TiAl alloys can undergo thermal-mechanical processing to yield four types of microstructures:

- Equiaxed (near γ),
- Duplex,
- Nearly lamellar,
- Fully lamellar.

Various microstructural factors including equiaxed grain size, γ volume fraction, α_2/γ lamellae width and α_2/γ colony size, texture exert a substantial influence on mechanical properties. The duplex or equiaxed microstructure displays better

ductility and fatigue properties while the lamellar microstructure demonstrates superior fracture toughness and creep resistance [85][86].

2.2.2 Alloy Design and Multicomponent Alloy Systems

The addition of alloying elements has a considerable impact on phase composition, and hence on the microstructure and mechanical characteristics. A variety of alloying elements are incorporated into TiAl alloys to attain novel properties [87][88]. The TiAl alloys can be defined using the composition formula given in Equation (1.1) [54]:



The elements Cr, Nb, Mn, Mo, V, Zr, Ta, Si, W, Y, C, Y and B denoted by X in the Equation 1.1 can be part of the alloy composition [89], [152]. The α_2 phase is usually present alongside the γ phase and additional phases may appear on occasion. Based on the influence alloying elements on the composition, two distinct alloying design techniques can be determined. Some alloying elements can be incorporated into γ -TiAl alloys in solid solution, altering features such as planar defect energies and phase diffusion coefficients. Certain alloying elements, on the other hand, are designed to stimulate the creation of third (or more) phases. This can result in grain refinement during casting, microstructure stabilization and precipitation hardening [54].

In terms of γ phase solubility, most of the aforementioned alloying elements are soluble to a limited level often about 2 to 3 at.%. The solid solution of β or its ordered variant with a B2 structure frequently forms as a third phase at greater concentrations of alloying elements [90]. Elements of Cr, V, Ta, Mo and W tended to be enriched in the α_2 phase. Nb and Mn elements were distributed evenly between the α_2 and γ phases, however Zr was predominant in the γ phase. Elements such as Cr, Mo, W and Fe showed strong partitioning to the β phase in comparison to both the α_2 and γ phases [90]. The addition of elements like Nb, W and Mo

enhances oxidation resistance. The presence of Cr, Mn and V reduces brittleness and improves mechanical properties by reducing grain size [91].

One of the initial alloys of significant technical interest was developed and patented by Huang of General Electric (GE). This alloy, known as Ti48Al2Cr2Nb, comprises 48 at.% of aluminum. The addition of 2 at.% of chromium was found to be the optimum for enhancing ductility and the inclusion of 2 at.% of niobium was sufficient to provide adequate high-temperature oxidation resistance. A composition level thought to be ideal for room-temperature ductility [92].

2.2.2.1 Effect of Aluminum

The aluminium concentration in binary alloys determines the initial phase to precipitate and then controls phase transformations during solidification. The maximum ductility was reported in the Ti-(46-60)Al range processed by rapid solidification for γ (90%) and α_2 (10%) duplex microstructures with a heat treatment roughly in the middle of the $\gamma + \alpha_2$ phase field [93]. The temperature to obtain peak ductility rises from 1300 °C for Ti-48 to 1400 °C for Ti-51Al, as seen in Figure 2.11 (a) [93]. Previously, it was considered that room-temperature ductility maximised around Ti-48Al, as shown in Figure 2.11 (b) [94]. Engineering TiAls should have both γ and α_2 phases. This allows dislocations near phase boundaries to contribute to deformation and the α/α_2 phase to absorb oxygen [95].

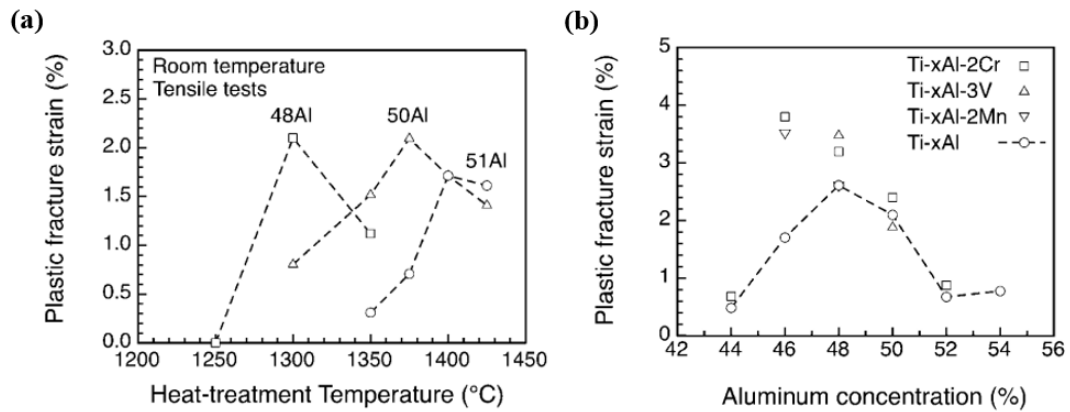


Figure 2.11: (a) The effect of heat treatment temperature on tensile ductility at room temperature [93] and (b) the effect of Al content on the room - temperature ductility of wrought materials [94].

Austen and Kelly's study on the impact of aluminum content in cast Ti-xAl-2Cr-2Nb alloys revealed that maximum ductility is achieved at around 48 at.% Al, while aluminum levels of 45 at.% or lower result in very little to no ductility [48]. It was observed that alloys with lower aluminum content tend to be stronger, as evidenced in cast Ti-xAl-2Cr-2Nb alloys [96]. Paul et al. conducted research on the compression flow stress and attributed the increased strength in alloys with low aluminum content to the higher α_2 phase content [96]. Additionally, Brotzu et al. determined that achieving a good fracture toughness with high oxidation resistance necessitates a ratio of Al/(Al + Ti) of at least 50% [91]. Alloys with higher aluminum content are generally favored for their superior oxidation resistance [97].

2.2.2.2 Effect of Chromium

The inclusion of chromium in TiAl alloys has a positive impact on their mechanical properties. It enhances ductility by decreasing grain size and also shifts the phase boundaries, leading to a reduction in the alpha-transus temperature [91]. Cr lowers oxidation rates at both low (800-900 °C) and high (1000-1100 °C) temperatures

[98]. Furthermore, it acts as a strong B2 stabiliser [99]. It also improves TiAl's plasticity [100].

The α -transus temperature was shown to decrease as Cr addition increased (Figure 2.12 (a)) [101]. For each atomic percentage of Cr added, the decrease rate was around 15 °C. As shown in Figure 2.12 (b), the introduction of Cr reduced the α -transus temperature consistently across all aluminium concentrations ranging from 45 to 50%. This suggested that Cr extends the α -phase field [101].

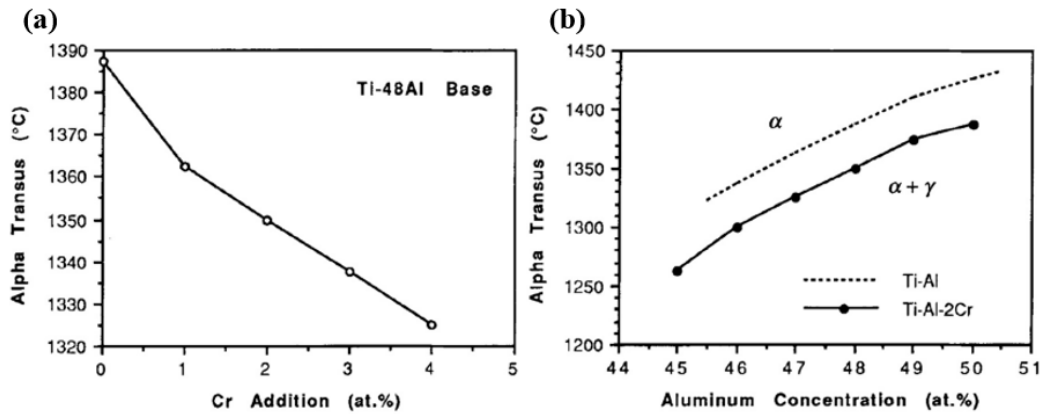


Figure 2.12: The impact of Cr modification on the α transus temperature for; (a) 48 at.% Al alloy and (b) Ti-Al binary and 2 at.% Cr added systems [101].

The addition of Cr significantly enhances the plasticity of duplex alloys characterized by grains of single phase γ and γ/α_2 lamellae. The ductilization effect of Cr arises from its tendency to occupy aluminum lattice sites. As illustrated in Figure 2.13 (a), the plasticity of γ based alloys rises with Cr content, peaking at 2 at.% Cr. However, beyond this limit, plasticity begins to decline, owing mostly to the development of excessive Ti_2CrAl particles, which lowers ductility [101]. Figure 2.13 (b) demonstrates the variation in plasticity as an effect of aluminium content, both with and without the addition of 2 at.% Cr. For alloys with the same aluminium concentration, the addition of 2 at.% Cr leads in significant increases in

ductility (about 1-2 at.%) within the range of 46-50 at.% aluminum. However, Cr additions only improve the plasticity of duplex alloys and an increase in ductility cannot be attained in an alloy with 54 at.% Al and a single γ phase structure [101].

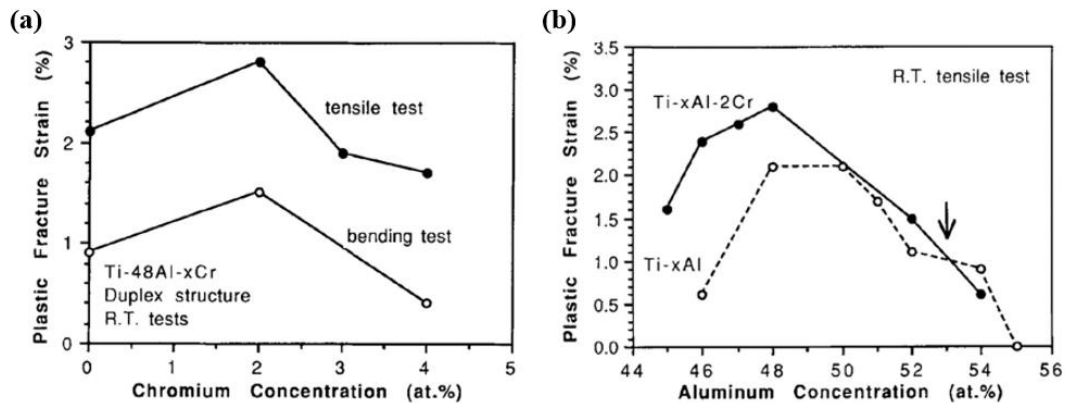


Figure 2.13: (a) Effect of Cr addition on plastic fracture strain and (b) effect of aluminum concentration on plastic fracture strain for Ti-Al binary and 2 at.% Cr added systems [101].

The introduction of Cr is a critical factor in improving the oxidation resistance of TiAl alloys. It was determined that replacing 10 at.% of the Ti in the TiAl alloy with Cr resulted in an approximately 2:1 drop in oxidation rates across all temperatures. The addition of 10 at.% Cr, carried out in order to improve the TiAl alloy's cyclic oxidation resistance. Figure 2.14 displays the isothermal oxidation kinetics of Ti-50Al and Ti-50Al-10Cr alloys in an air environment at temperatures ranging from 800-1100 °C. Notably, at all temperatures, Ti-50Al-10Cr exhibits significantly lower weight gains than Ti-50Al [98].

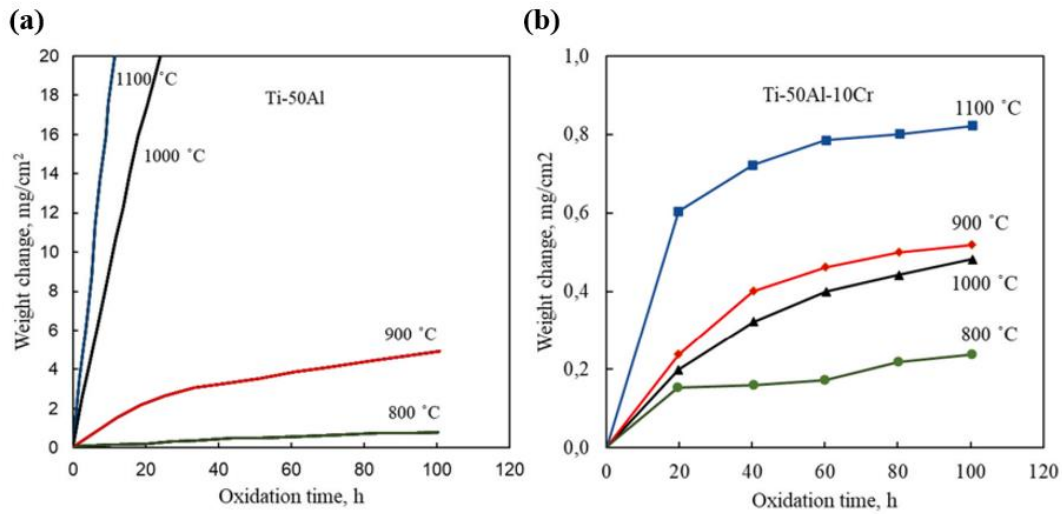


Figure 2.14: Isothermal oxidation kinetics of; (a) Ti-50Al and (b) Ti-50Al-10Cr alloys [98].

In the γ phase, the maximum solid solution of Cr is observed just before the formation of the B2 phase. Figure 2.15 (a) illustrates the variation of yield strengths with increasing Cr content, indicating a similar trend in both 25 °C and 900 °C tension tests. Peak strengths are observed at 1.5 and 2.0 at.% Cr for these respective temperatures, followed by a continuous decrease [99]. The increase in strength is mostly attributable to solid solution strengthening in the γ phase due to the presence of Cr although the formation of the B2 phase reduces ductility, creep resistance and room temperature strengths. Figure 2.15 (b) displays the creep behavior of Ti-48Al-xCr at 800 °C under a stress level of 240 MPa, demonstrating that Cr content has a considerable effect on creep-rupture life. Ti-48Al-1Cr has a creep rupture life of 129.5 hours when the Cr content is 1.0 at.%. This emphasises that the composition of solid solution strengthening components and the formation of the B2 phase influence creep resistance of TiAl alloys [99].

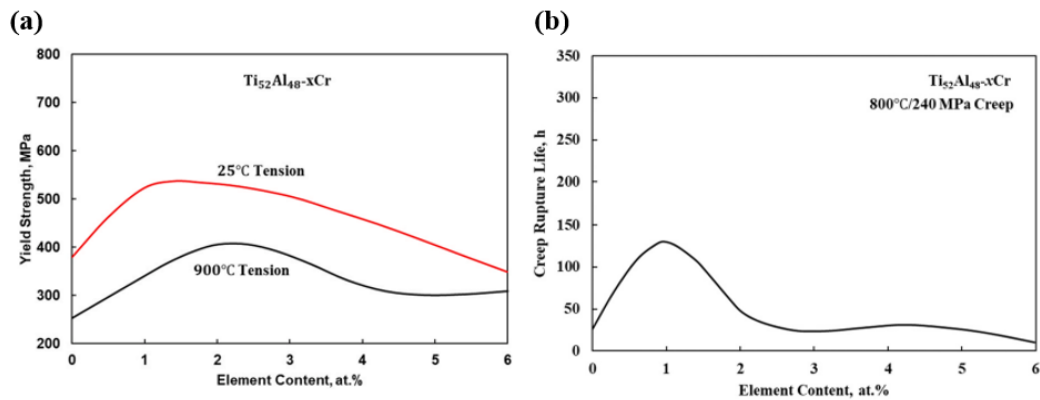


Figure 2.15: (a) Yield strengths in Ti-48Al-xCr alloy at room temperature and 900 °C as a function of Cr percentage. (b) The creep rupture life response to Cr concentration at 800 °C under 240 MPa stress [99].

2.2.2.3 Effect of Niobium

Niobium (Nb) is a crucial element utilized in alloying γ -TiAl. It is well-established that the strength and oxidation resistance of γ -TiAl can be significantly enhanced with the addition of Nb up to 11 at.% [102]. Additionally, Nb is known to high-temperature strength and creep resistance [103]. When in solid solution with TiO₂, the presence of Nb can enhance resistance to oxidation by impeding mass transfer. However, it can lead to the formation of phases like TiNb₂O₇ or AlNbO₄, subsequently diminishing the oxidation resistance when the amount of Nb exceeds a certain threshold [104].

Niobium is an important beta-stabilizing element that influences the microstructure of cast γ -TiAl alloys [105]. Its presence results in a shift from nearly lamellar to fully-lamellar microstructures. This beneficial effect of Nb is due to its doping effect, which increases aluminium activity and diffusivity [106]. Nb's doping effect reduces the concentration of oxygen vacancies in the TiO₂ lattice due to its higher valency than Ti, hence limiting oxygen diffusion. The increased aluminium activity and diffusion rate are required for the creation of a protective Al₂O₃ layer.

Furthermore, Nb limits internal oxidation by lowering the alloy's oxygen solubility and promoting the production of TiN, which inhibits the diffusion of titanium and oxygen ions [107].

Yang et al. investigated the influence of Nb on the oxidation behavior of TiAl alloys at high temperatures using four distinct alloys with variable degrees of Nb addition (0-8 at.%) [108]. Figure 2.16 (a) compares the isothermal oxidation curves at 900 °C. The outermost layer of the scale in all alloys is formed by TiO₂ crystallites, and their thickness decreases as the Nb percentage increases. The best oxidation resistance is demonstrated by Ti47Al5Nb and Ti44.2Al8Nb alloys. While a high Nb content improves gammaTiAl's oxidation resistance, it degrades the material's thermal fatigue properties. As seen in Figure 2.16 (b), the resistance to cracking decreases dramatically as the atomic percentage of Nb in the alloy increases [108].

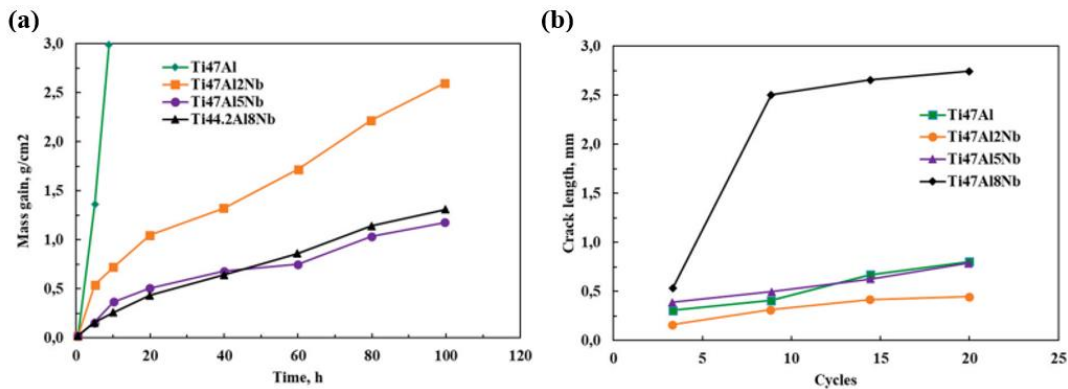


Figure 2.16: (a) Isothermal oxidation at 900 °C and (b) crack length vs. thermal fatigue cycle for Ti-47Al-xNb alloys [108].

2.2.2.4 Effect of Manganese and Vanadium

Manganese (Mn) and vanadium (V) have a comparable impact on lowering the α -transus temperature as Cr [94]. Figure 2.17 demonstrates that the additions of 2Cr, 3V, and 2Mn reduce the alpha-transus temperature. As illustrated in Figure 2.11 (b) these elemental additions have a "ductilizing" impact particularly on duplex alloys [94]. The specific causes for these components' influence on ductility in two-phase alloys remain unknown. Determining the exact mechanisms is difficult because each addition impacts a variety of parameters, particularly planar fault energies [109].

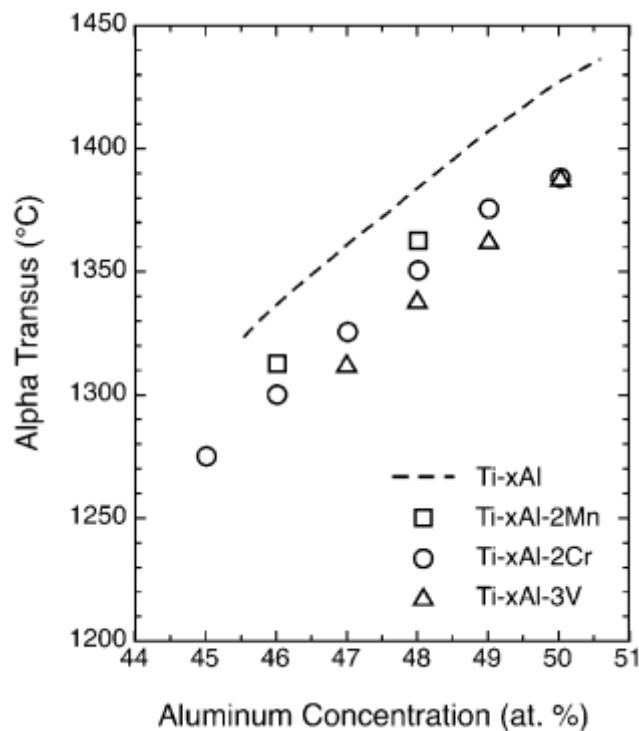


Figure 2.17: The α transus temperature is affected by the additions of 2Cr, 3V, and 2Mn [94].

2.2.2.5 Effect of Tungsten, Molybdenum and Tantalum

Refractory elements like tungsten (W), niobium (Nb), molybdenum (Mo) and tantalum (Ta) have been incorporated into TiAl alloys for a considerable period. Despite the fact that these elements tend to segregate in cast material and cause to increase density, their potential benefits on characteristics, especially at high temperatures, have prompted their greater use [95]. W, Nb, Mo, and Ta additions all contribute to improve oxidation resistance [94]. The β/β_2 phase form with displacing the boundaries of other phases when refractory element additions are large or the aluminium content is low. The β phase softens and ductiles at high temperatures, allowing for hot-working activities. On the other hand, state that β/β_2 can result in decreased high-temperature strength, creep resistance and room-temperature ductility [99]. Hodge et al. find that tiny W additions improve creep properties in near-lamellar microstructures, whereas high additions induce β formation, which reduces creep properties [110]. Ta additions have been used in a unique approach capable of producing fine microstructures via massive gamma transformation [95].

2.2.2.6 Effect of Boron

Boron serves as a grain refiner, enhancing castability, and is typically added in quantities ranging from about 0.1 to 1 at% in TiAl alloys. This addition process enables the production of microstructures with highly refined grain sizes [95]. In cases where TiAl alloys are cast with coarse microstructures, achieving fine-grained microstructures can be challenging, and boron plays a crucial role in addressing this issue [95]. Figure 2.18 illustrates the graph depicting the alteration in grain size resulting from the introduction of TiB_2 to the casting $\text{Ti}_{47}\text{Al}_{53}\text{Mn}_X$ alloy [111]. The curve shows a significant phase of the grain refinement process taking place when the boron concentration attains a specific threshold. Subsequent

additions made after surpassing the critical concentration level of boron in the alloy demonstrate minimal impact on further grain refinement [111].

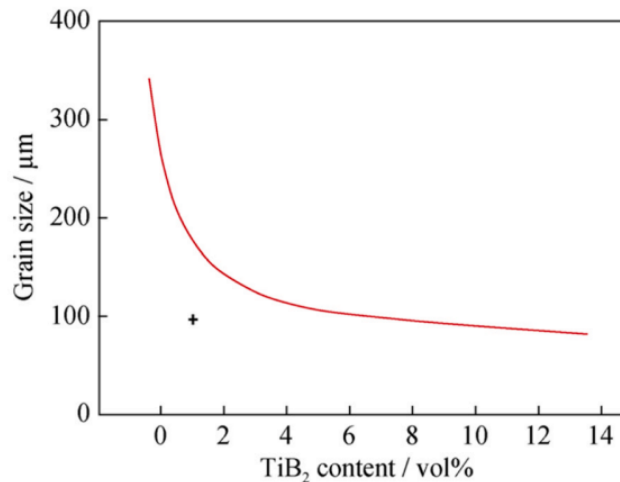


Figure 2.18: The correlation between boron concentration and grain size in cast Ti47Al2MnX. The data point represented by a plus sign (+) corresponds to the alloy Ti47Al2Mn2Nb1B [111].

The introduction of elemental boron results in the formation of four types of titanium borides in casting: TiB₂, Ti₃B₄, TiB (B27), and TiB (Bf). The matrix exhibits a Young's modulus ranging only between 150–180 GPa, whereas the borides possess a higher modulus in the range of 450–550 GPa. This substantial difference in Young's modulus implies that plastic deformations, such as shear and twinning, take place within the matrix but cease at the interface between the boride and the matrix. Consequently, this phenomenon results in the substantial pile up of dislocations [111]. In the casting process, titanium monoborides have a tendency to grow to considerable sizes, adversely affecting ductility. Thus, it becomes imperative to regulate boride dimensions during casting to preserve ductility. Furthermore, beyond size control, it has been observed that flake-type boride precipitates can diminish ductility in comparison to granular precipitates. Any means of reducing the size of boride precipitates tends to enhance ductility [112].

Bryant et al. [113], while working on in-situ composites, discovered the refining effect of Boron when added in the form of TiB_2 to cast TiAl alloys. In alloys with low aluminum content that solidify through the β phase field, even low levels of Boron, ranging from 0.1 to 0.2 at%, can be highly effective, resulting in cast colony sizes of about 30 μm . In this context, the addition of β -stabilizing elements like Nb, W, and Ta can be beneficial, although they may also form monoborides, potentially reducing the available Boron for grain refinement. When the cooling rates during solidification are slow, especially in thick cross sections, long refractory metal borides can form, potentially leading to premature failure during loading [113].

2.2.2.7 Effect of Carbon

The solid solution hardening and the precipitation of fine carbides can lead to a substantial strength enhancement in TiAl-based alloys when carbon is introduced [114]. Recent investigations indicate that finely distributed carbide precipitates not only contribute to resistance to plastic deformation [115] but also enhance creep resistance [116]. Several studies have demonstrated that TiAl alloys incorporating carbon additions exhibit superior mechanical properties at both room and elevated temperatures [1], [114], [117].

Carbon introduced into TiAl alloys can undergo precipitation as either the Ti_3AlC phase (P phase) or the Ti_2AlC phase (H phase), contingent on the carbon concentration [114]. These precipitates serve as formidable barriers, impeding the movement of dislocations, which remain unable to surmount these barriers even with thermal activation. As a result, creep resistance is heightened due to the decreased mobility of dislocations. Furthermore, it has been observed that the coarser Ti_2AlC precipitate is less effective in strengthening TiAl alloys compared to the Ti_3AlC phase [1].

The inclusion of carbon can facilitate the phase transformation from β to α , leading to a reduction in the residual high-temperature β phase, and a substantial expansion

of the unit cell in the α_2 phase. However, it is important to note that the carbon solubility limit in the γ phase is significantly lower than that in the α_2 phase, resulting in almost unchanged unit cell volumes for the γ phase. This phenomenon is illustrated in Figure 2.19 for the TNC, TNC-0.2C and TNC-0.5C alloys [114]. In TiAl alloys with carbon doping, the volume fraction of the B2 phase is notably diminished, and particularly in TNC alloys, the B2 phase almost disappears as the carbon content around 0.5 at%. The volume fraction of the B2 phase decreases as carbon introduces [114].

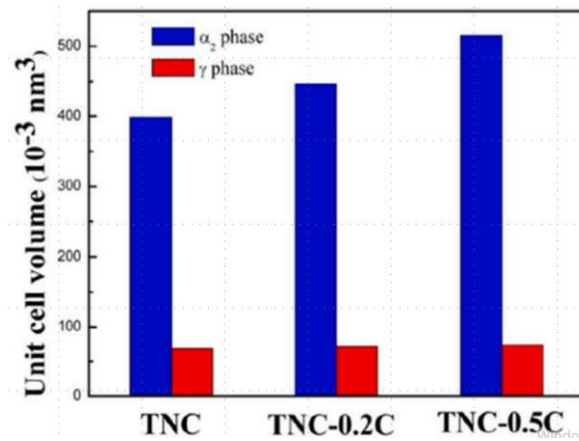


Figure 2.19: α_2 and γ phase unit cell volumes depending on the carbon content [114].

2.2.2.8 Effect of Silicon

The incorporation of silicon into TiAl alloys serves the purpose of enhancing creep strength and elevating oxidation resistance [118], [119]. Figure 2.20 (a) illustrates the enhancement in creep properties in a cast alloy with a nominal composition of Ti-47.5Al-1.5Cr through the incorporation of 0.26 and 0.65 at.% silicon [120]. The development of Ti_5Si_3 precipitates, which have been reported in both aged and creep-deformed materials, is important to the strengthening mechanism. The

addition of silicon up to 0.65 at.% is reported not to adversely affect the tensile properties [120]. However, it has been observed that additions exceeding 1 at.% can diminish creep resistance due to heightened microstructural instability and increased dynamic recrystallization [119].

The addition of silicon induces alterations in the microstructure of the oxidation scale [121]. Silicon augments the thermodynamic activity of aluminum, thereby enhancing oxidation resistance by reinforcing the propensity to form a protective Al_2O_3 layer. Consequently, the thickness of the oxidation scale decreases with an increase in the percentage of silicon, leading to finer oxides formed on the alloys as illustrated in Figure 2.20 (b) [122]. When the silicon content exceeds 3 at%, the Ti_5Si_3 phase is formed. Upon oxidation, coars crystalline TiO_2 is generated on the Ti_5Si_3 phase. However, an increase in the formation of the Ti_5Si_3 phase raises the silicon concentration, initiating a detrimental effect on oxidation resistance. The reason for this adverse impact is that the TiO_2 phase experiences much faster growth than Al_2O_3 . Furthermore, the brittle Ti_5Si_3 phase has the potential to initiate the spallation of oxides, resulting in the development of cracks in the oxidation layers [122].

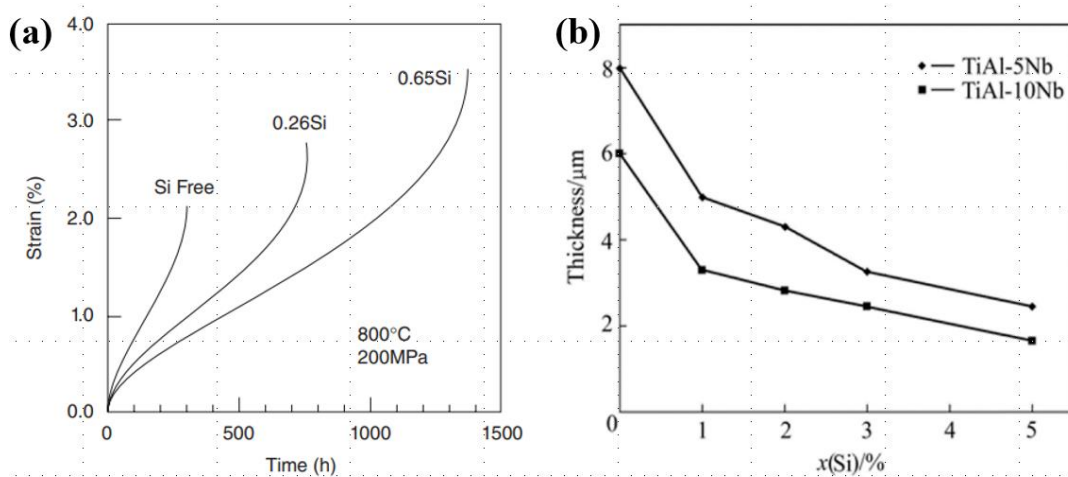


Figure 2.20: (a) The impact of silicon additions on the creep behavior [120] and (b) variation in oxidation scale thickness with Nb and Si contents [122].

2.2.3 Specific γ -TiAl Alloy Systems

A range of γ -TiAl alloys with low aluminum content has been the subject of investigation. Table 1 provides information on various generations of γ -TiAl alloys, including processing processes and developers [66].

Table 2.4: Several specific γ -TiAl alloys with various properties [66].

Stage	Alloys	Processing techniques	Microstructure	YS (MPa)	EL (%)	Developers	Ref.
1st generation	Ti-48Al-1 V-wt%0.1 C	VAR+Forging+HT	DP	392	1.4	Pratt & Whitney Group	[123]
2nd generation	4822(Ti-48Al-2 Nb-2Cr)	VAR+HIP+HT	DP	331	2.3	General Electric Company	[124]
	45XD (Ti-45Al-2Mn-2 Nb-0.8 vol%TiB ₂)	VAR+HIP +HT	FL	550-590	1.5	Howmet and Rolls-Royce Company	[124]
	47WSi (Ti-47Al-2 W-0.5Si)	VAR+HT	DP	425	1	ABB Company	[124]
3rd generation	K5 (Ti-46Al-3 Nb-2Cr-0.2 W-xB-yC/Si)	VAR+Forging+HT	DP/RFL	462/473	2.8/1,2	Y. W. Kim	[124]
	TNB-V5(Ti-45Al-5 Nb-0.2B-0.2 C)	VAR+HIP+extrude+HT	NG	897	0.6	F. Appel	[126]
	TNM(Ti-43Al-4 Nb-1Mo-0.1B)	VAR+Forging+HT	DP	970	1	Research institutions in Australia and Germany	[127]
	Ti-44Al-4 Nb-4Hf-0.1Si-0.1B	PAM+VIM+HIP+HT	NL	602	0,4	D. Hu	[128]
	Ti-44Al-6 Nb-1Mo-0.2Y-0.1B	VAR+PREP+SPS+HT	FL	665	1,25	H.Z. Niu	[129]

In a general classification, various alloys can be grouped into four distinct groups [95]:

- (i) conventional alloys,
- (ii) alloys with high niobium content,
- (iii) β -solidifying alloys,
- (iv) massively transformed alloys.

2.2.3.1 Conventional Alloys

Several alloys within this class are characterized by specific compositions. For example, the Ti48Al2Cr2Nb alloy, developed and patented by General Electric [130], the Ti-48Al-2Cr alloy utilized in various studies on deformability [131], [132]. The Ti-46Al-1Cr-0.2Si alloy developed by Frommeyer et al. [133]. Within this category, notable alloys include the GKSS-developed γ -TAB (Ti-47Al-4(Nb, Cr, Mn, Si, B)) and the Plansee γ -MET (Ti-46.5Al-4(Nb, Cr, Ta, B)). These alloys are characterized by specific compositions, incorporating elements such as niobium, chromium, manganese, silicon, tantalum, and boron. During the period when these alloys were developed, a notable feature was their elevated aluminum content in comparison to more contemporary alloy formulations. It was determined that this increased aluminium content was necessary to achieve favourable room-temperature ductility [54].

The primary phases in these alloys are typically γ and α_2 , despite the presence of B2/ γ has been noted in a low interstitial Ti48Al2Cr2Nb alloy [134]. In the early 1990s, most ductility research concentrated on cast materials, with maximal ductility thought to be focused around 48 at.% Al concentrations. Notably, cast Ti48Al2Cr2Nb elongations of roughly 2.5 to 3.1% was published [135]. However, the determined strength values were relatively low, with yield strengths ranging from 300 to 330 MPa and tensile strengths ranging from 445 to 477 MPa [135].

In an effort to improve strength and creep resistance in later-generation conventional alloys, aluminium content was reduced slightly, and additives such as B, C, and Si were incorporated. However, these alloys lack the features of nickel-based superalloys and lack the oxidation resistance to increase the application temperature beyond 700 °C. Due to this constraint, the significant niobium additions have been introduced to γ -TiAl alloys [54].

2.2.3.1.1 Ti48Al2Cr2Nb Alloy

The Ti48Al2Nb2Cr alloy, classified as a second-generation γ -TiAl alloy developed by GE, belongs to a group characterized by additions of elements with less than 5 at.% [39]. The emphasis during its development was on maximising ductility, which resulted in a high percentage of aluminum with 48 at.% and a duplex $\alpha_2 + \gamma$ microstructure [3]. Ti48Al2Nb2Cr has special features due to its intermetallic nature, which is originated by the alloying of two or more metallic elements, along with non-metallic elements [135]. Intermetallic alloys share characteristics with ceramics and metals due to the covalent or partially ionic nature of their bonds. The resulting solid phases have different crystal structures and physical/mechanical properties than the constituent elements. Intermetallics have exact structure within a sub-lattice, and the long-range ordering is stable up to a certain temperature. This long-range ordering restrains deformation modes, often increasing strength while decreasing ductility and fracture toughness at room temperature [135] – [136]. Table 2.5 represents the typical chemical composition of Ti48Al2Nb2Cr [20]. Its melting point is reported around 1570 °C [136].

Table 2.5: Chemical composition of the Ti48Al2Nb2Cr alloy in wt.% [20].

Elements	Al	Cr	Nb	Fe	O	N	C	Ti
Wt.%	34.1	2.4	4.8	0.03	0.06	0.004	0.005	Bal.

Each element in the composition exerts a distinct influence on the material's overall properties [20]. Aluminium has a significant effect on the transformation in phases during solidification. It has an impact on microstructural properties including the volume fraction of α_2 , and it also effects mechanical properties like strength and ductility. Alloys with an aluminum content below 43 at.% exhibit no plastic elongation at room temperature [95]. The strength of γ -TiAl increases with decreasing aluminum content and/or increasing niobium content. The significance

of aluminum content lies in its influence on lamellar spacing. A decrease in aluminum amount results in an increased α_2 volume fraction, leading to a linear reduction in lamellar spacing and, consequently, a strength increase [95]. Chromium, known for lowering the α transus temperature and improving the ductility, along with niobium, which enhances creep and corrosion resistance at elevated temperatures, are recognized as additional crucial elements in the Ti48Al2Nb2Cr alloy [95].

Various grain structures can arise based on thermal and/or thermomechanical processing. The mechanical properties of Ti48Al2Nb2Cr are highly depend on the morphology of the γ and α_2 phases. In Ti48Al2Nb2Cr, four distinct microstructures are observed as shown in Figure 2.21 [20], [26]:

1. **Fully equiaxed grain structure:** This configuration consists of a single γ phase with a high modulus of elasticity (E) and better high-temperature properties while maintaining a low density. Despite exhibiting isotropic behavior with constant properties along multiple axes, it suffers at room temperature by insufficient fracture toughness and ductility, making it unsuitable for structural applications because to its brittleness.
2. **Fully lamellar grain structure:** This structure, defined by alternating plates of γ and α_2 , has outstanding creep resistance and toughness at elevated temperatures but limited ductility at room temperature. Enhancing microstructural properties, such as decreasing lamellar grain size and spacing, improves elongation and strength at high temperatures. The brittleness of α_2 and the difficult dislocation movement between γ and α_2 limit material's ductility. At elevated temperatures, grain boundaries in fully lamellar structures resist crack propagation more efficiently than those in duplex grain structures, increasing fracture toughness. Despite better creep resistance, interlocking grain boundaries reduce ductility and machinability at room temperature. This grain structure's high anisotropic material characteristics provide challenges for specialised applications such as turbine blade airfoils.

3. **Duplex grain structure:** The duplex grain structure comprises equiaxed and lamellar grain structures, incorporating γ and α_2 phases with the finest and most homogeneous microstructural properties, including γ and lamellar grain sizes and spacing. This structure is highly desirable for its exceptional combination of ductility, strength, and fatigue life.
4. **Near fully lamellar grain structure:** This structure is fully lamellar, with lamellar colonies dominating and equiaxed grains evolving as a minority inside lamellar colonies.

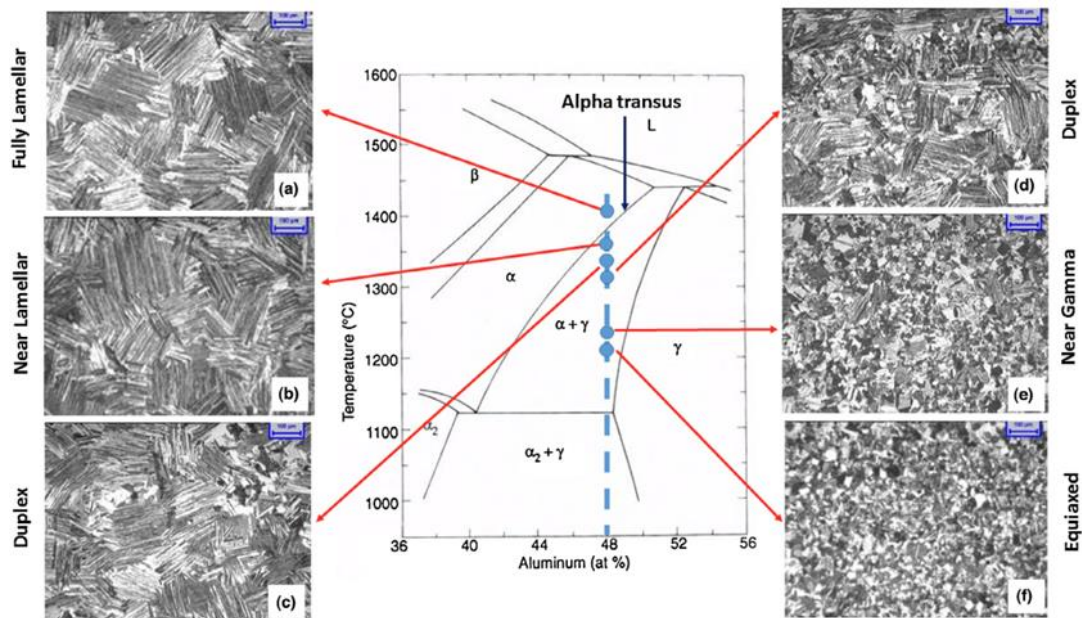


Figure 2.21: Various microstructures obtained after several heat treatment temperatures corresponding to distinct regions in the binary phase diagram for a 48 at.% Al alloy [20].

2.2.3.2 High Niobium Containing Alloys

Cotton et al. [94] were among the first to demonstrate the high strength and oxidation resistance of γ -TiAl alloyed with niobium. Subsequently, Paul et al. [96]

investigated cast materials to uncover the mechanisms behind the heightened strength. They found that the enhanced strength resulted from athermal dislocation obstacles linked to reduced aluminum content, rather than the high niobium content. Lower aluminum levels raised the α_2 content and refined the structure, both of which contributed to higher athermal stress during deformation [96].

The activation parameters for high-temperature deformation in binary and equivalent Al-containing high-Nb ternary alloys were investigated. The activation enthalpy for deformation was slightly greater in high-Nb alloys, which is consistent with previous research on Nb diffusion in TiAl [137]. This suggests that diffusion-assisted deformation processes in such alloys are more difficult, potentially improving creep resistance and high-temperature strength while inhibiting dynamic recrystallization [138]. Deformed high-Nb alloys exhibited significant twinning activity, which could be attributed to lower stacking-fault energy and hence increased ductility [138].

GKSS developed high-Nb alloys, known as TNB, with a composition of Ti-45Al-(5–10)Nb-(0–0.5)B, C [95]. Extruded Ti-45Al-5Nb-0.2B-0.2C TNB achieved room-temperature strength up to 1 GPa with approximately 2 to 2.5% plastic strain. TNB competes favourably with superalloys, unlike conventional TiAl alloys, due to its remarkable strength qualities, extending its high-temperature capacity. Plansee obtained a TNB licence and collaborated on TNB alloy research studies with NASA and Pratt & Whitney. GKSS also worked on projects using TNB alloys with companies such as DaimlerChrysler and Rolls Royce [95].

2.2.3.3 β - Solidifying Alloys

The discovery and benefits of β -solidifying alloys for casting were likely first acknowledged by in elsewhere [5]. These alloys stabilize the β phase, which becomes the initial phase to precipitate during solidification and remains the sole phase afterward. In contrast, the high-temperature α phase is present to a certain

amount in peritectic alloys after solidification. One disadvantage of peritectic alloys is that when the β phase converts into α during additional cooling or further heat treatment, the orientation of the transformed α is governed by the pre-existing α phase. Since the γ phase shares only one orientation relationship with the high-temperature hexagonal α , all lamellae originating from a single α grain will exhibit the same orientation, as outlined in the Blackburn orientation relationship provided in 2.2.1.2 Phase transformation from α to α_2 Section [139].

In alloys solidifying entirely through β and subsequently precipitating α on additional cooling, the α phase forms from the β can have up to 12 different orientation variants [139]. As a result, a substantial grain refinement of the casting and a significant reduction in texture can occur when a large β grain is partitioned by lamellar colonies with up to 12 different orientations. This phenomenon, known as "crystal partitioning" [5], [139]. The most effective additives for promoting β solidification are Fe, Re, and W as well as Cr, Mo, Ta, and Nb with slightly decreasing in strength [5].

Concerns have been raised about β -solidifying alloys, such as decreases in mechanical properties like as high-temperature strength, creep resistance and room-temperature due to the existence of the β /B2 phases [99]. The hard and brittle nature of the aluminum rich B2 phase at room temperature transforms into a soft and ductile β phase at elevated temperatures. Moreover, β /B2 can decompose into omega (ω) phases, potentially contributing to material embrittlement after long-term exposure [5], [140].

The soft character of the high-temperature β phase allows for the employment of forging techniques in alloys such as Ti-42Al-5Mn and Ti-42Al-10V. These alloys have β (B2) and γ as thermodynamically stable phases at room temperature, in contrast to conventional alloys, which have α_2 and γ [141]. Compared to other TiAl alloys, Ti-42Al-5Mn is relatively easy to machine when hot-worked. Although the room-temperature plastic elongation to failure for Ti-42Al-10V is somewhat low

for a hot-worked material, the specific creep strength for Ti-42Al-10V and Ti-42Al-5Mn is stated to be acceptable [141].

To produce acceptable high-temperature characteristics, certain heat treatments capable of eliminating the β /B2 phase are necessary following processing [142]. These "beta-gamma" alloys have the following composition: Ti-(42-45)Al-(2-8)Nb-(1-9)(Cr, Mn, V, Mo)-(0-0.5)(B, C) [142]. Studies conducted by Clemens et al. [127] aimed to ascertain the phase relationships in Ti-43Al-4Nb-1Mo-0.1B. Parts were produced using hot-working procedures. The creep properties at 800 °C and 300 MPa exhibited variations based on the applied heat treatment. Additionally, room-temperature tensile strengths ranged from 800 to 950 MPa, with total elongations reaching up to 2%, contingent on the specific heat treatment employed [127].

2.2.3.4 Massively Transformed Alloys

As highlighted by Wu and Hu [143], the recognition of massive gamma (γ_m) formation in alloys containing 46 to 48 Al dates back several years. This type of γ develops through a displacive transformation without long-range diffusion and is distinguished by a highly faulted γ phase. It is formed under relatively fast cooling rates from the high-temperature α phase, but not so fast to produce metastable α (α_2). Subsequent heat treatment within the ($\alpha + \gamma$) phase field results in the precipitation of α on all four $\{111\}$ planes of the γ_m , yielding a refined microstructure composed of fine alpha α_2 plates within a γ matrix [144]. Such microstructure observed in a 20-mm diameter bar of Ti-46Al-8Nb which underwent oil quenching from 1360 °C, followed by a 2-hour aging process at 1320 °C is provided Figure 2.22 [143].

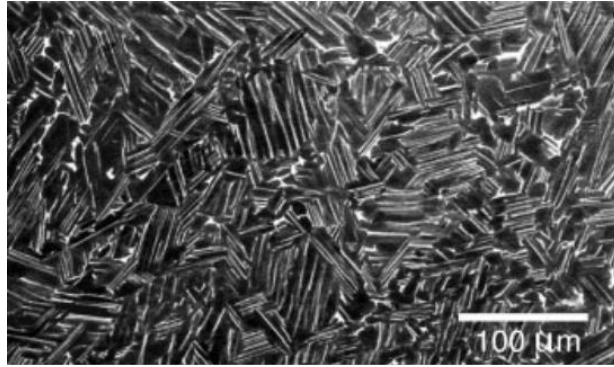


Figure 2.22: Refined "convoluted microstructure" of previously γ_m contained Ti-46Al-8Nb alloy followed by heat treatment within the $\alpha + \gamma$ region [143].

The IRC studied the necessary cooling rate range for γ_m formation and optimized compositions to induce such a microstructure at slower cooling rates which is more representative of those experienced by real components [145]. The study includes measuring the presence of various microstructures along the length of a Jominy. It was shown that the alpha grain size and oxygen levels in Ti-46Al-8Nb alloy both played a role in γ_m transformation. The range of cooling rates required to achieve a fully γ_m microstructure was found to be lower in fine-grained material than in coarse-grained material [145]. Therefore, boron additions were identified as having a detrimental impact on γ_m formation. This microstructural refining process is especially well-suited for cast alloys with large grain sizes. The significant transition was also suppressed by high oxygen levels in the alloy [146].

According to Hu et al. [147], elements that act as weak β stabilisers, exhibit unequal partitioning between the α and γ phases, and are slow diffusers are required for the construction of TiAl alloys that favour massive gamma production. It's recommended to avoid strong β stabilizers, as they can diminish the single-phase α field crucial for the material to undergo the massive transformation during cooling. Elements demonstrating preferential partitioning for α or γ are essential to necessitate significant diffusion for γ phase formation. The use of slow-diffusing

species enhances γ_m formation. Considering these factors, Hu et al. suggest that tantalum is more effective than niobium in promoting γ_m [147].

2.3 Conventional Manufacturing of Titanium Aluminides

Conventional manufacturing methods for producing TiAl parts can be categorized into three subgroups: casting, wroughting, and powder metallurgy (PM) [3]. There are actually four types of manufacturing technologies for TiAl components including additive manufacturing [40]. Chen et al. offer distinct processing routes for each of these manufacturing methods in Figure 2.23 [40]. However, it's important to note that this chapter does not cover additive manufacturing, as it is discussed in detail in Chapter 2.4.

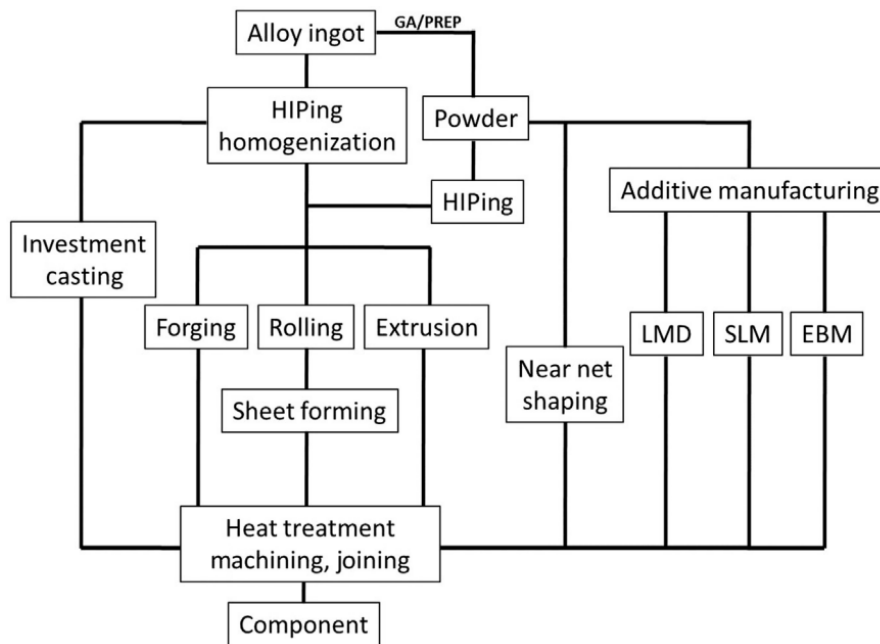


Figure 2.23: Processing routes suggested by Chen et al. [40].

2.3.1 Casting

Casting is the most economically viable way for producing TiAl components. This is mainly due to the widely recognised infrastructure for traditional Ti alloy investment casting [148]. Figure 2.24 showcases an LPT blade manufactured through investment casting [149]. An X-ray image (Figure 2.24 (b)) revealed that the casted blade exhibited an absence of porosities and ceramic inclusions [149].



Figure 2.24: (a) An investing casted LPT blade and (b) its corresponding X-ray picture [149].

The centrifugal casting technique is capable of creating complex objects while minimising casting defects such as misrun, shrinkage and gas porosity. In terms of mass production, the Ti48Al2Cr2Nb LPT blades in the GENx engine and the 45XD LPT blades in Rolls Royce's Trent-XWB engine are currently manufactured via centrifugal casting [41]. Figure 2.25 shows an image of a centrifugally cast GENx net-LPT blade with the gating still connected [41].



Figure 2.25: Centrifugally casted GEnx LPT blade [41].

Solidification following the casting frequently results in micro segregation of alloying components and the development of columnar grains. Columnar formation of grains leads to structural non-uniformities in castings [150], [151]. These characteristics are challenging to improve with additional heat treatments. The morphological texture is significantly more challenging for developing complex components such as turbine blades because of the anisotropy in mechanical characteristics [152], [153]. It is possible to obtain high-quality castings with fine tolerances for small components [150]. However, for component castings constructed of high strength alloys, ductility may need to be compromised to some amount. Large and thick section components are often more challenging to manufacture because they contain coarser microstructures that affect their qualities. In such instances, alloy design is very critical [150].

2.3.2 Wroughting

Forging or extrusion methods produce a more uniform and more refined microstructure, minimising uneven structures and promoting a desired texture with respect to casting [154]. The wrought processing has been demonstrated, with the advantage of increasing microstructural flexibility by thermal-mechanical processing [40]. This produces finer duplex or equiaxed microstructures, which improves ductility. Hot-working of TiAl alloys is typically done above the brittle-to-ductile transition temperature. The ingots are refined during the first hot working stage into a fine-grained, homogeneous microstructure. This is achieved by the use of relatively low deformation rates at temperatures ranging between the γ solvus

and eutectoid. This method promotes dynamic recrystallization while reducing strain-induced porosity [40].

Wrought processing techniques are especially useful to produce jet engine components that must endure strong loading conditions [3]. As shown in Figure 2.26, Thyssen has successfully produced tiny Ti-45Al-8Nb-0.5(B,C) compressor blades employing an ingot extrusion and multistep isothermal forging technique [3]. Ingot extrusion at 1250 °C and isothermal forging were used to manufacture Ti-47Al-3.7(Nb, Cr, Mn, Si)-0.5B high-pressure compressor blades [155]. Pratt & Whitney installed forged LPT blades in the last stage of their GTF engine. Isothermal forging was used, followed by annealing [155].

The wrought processing requires operations at high temperatures, generally above 1100 °C and low deformation rates carried out in many steps because of TiAl's inherent brittleness. Furthermore, hot working necessitates the use of an inert gas environment. Even though the mechanical qualities of wrought TiAl outperform those of casted parts, the amount of wrought processing is limited due to productivity and tool longevity concerns. These factors significantly contribute to elevated processing costs [3], [40], [156].



Figure 2.26: Compressor blades of Ti45Al8Nb0.5(B,C) produced using extrusion and forging process; (a) set of blades and (b) an individual blade [3].

2.3.3 Powder Metallurgy

Powder metallurgy (PM) is a widely employed method for producing net-shaped parts from various metals and alloys [33]. The press and sinter has always been the most common approach for PM production [33]. The ability to produce near net-shaped parts with refined and segregation-free microstructures is a key advantage of PM. PM usually outperform casting because of problems arising in casting such as melted metal – cast mold interactions, macrosegregation, hot cracking, casting texture and high internal stresses. Furthermore, PM allows for the production of composite materials or porous materials [157].

Prealloyed atomized powder must be used to fabricate TiAl components utilising this method. Several atomization processes are described in the literature, such as gas atomization, rotating-disc atomization, the rotating-electrode process (REP) and the plasma rotating-electrode process (PREP) [157]. The powder's quality is critical and is controlled by characteristics such as particle size distribution, particle shape and the degree of interstitial pick-up upon atomization. TiAl powder, unlike common metallic powders, is often too hard for cold compaction. As a result, it is frequently processed with hot isostatic pressing (HIP) after some type of hot-working treatment [157]. Alternative processes including spray forming, metal injection moulding (MIM), microwave sintering, combustion synthesis and spark plasma sintering have been investigated in the literature [158].

The PM process has the advantage of producing high-quality, near-net-shape and uniform parts with significantly less machining and waste. The near-net-shape PM approach is capable of producing a variety of TiAl components with complicated forms [158]. Powder processing holds significant potential, particularly for larger products where segregation can limit the homogeneity of the final products [3]. HIP is primarily used to design and build high-precision aeroengine components. HIP produced compressor rotor for an aeroengine and a machining preform are seen in Figure 2.27 (a) and (b), respectively [159].

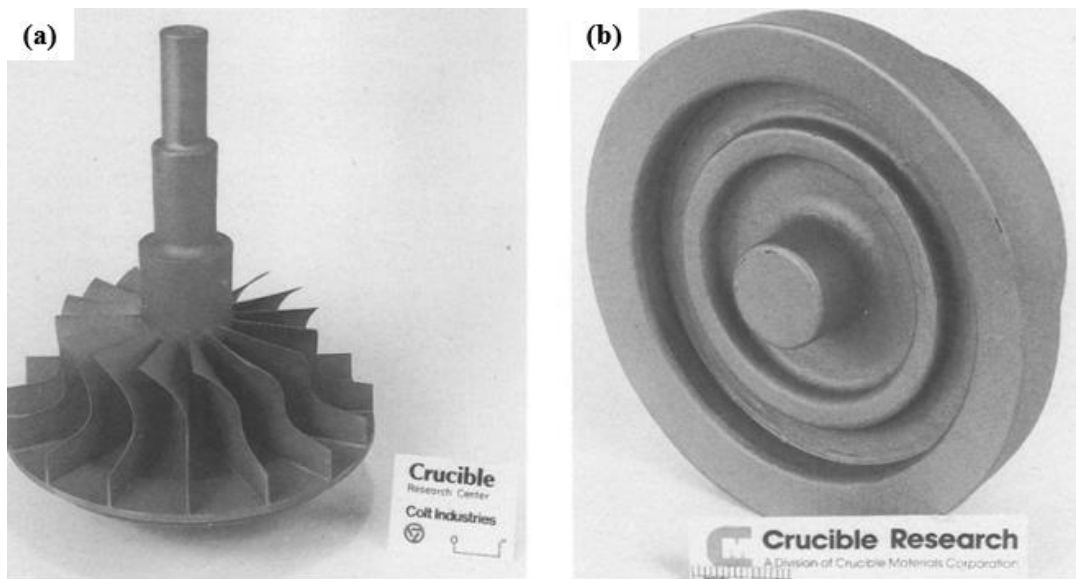


Figure 2.27: HIP produced; (a) turbine engine compressor rotor and (b) machining preform [159].

2.4 Additive Manufacturing of Titanium Aluminides

The integration of computers, heat sources and controllers into everyday life gave rise to the concept of Additive Manufacturing (AM). The primary premise of AM technology has been to generate a model using Computer-Aided Design (CAD) without the requirement for extensive process design, including tools and supplementary fixtures, as required by traditional production techniques. In traditional systems, each extra processing step requires more labour and increases manufacturing time. In contrast, AM requires only a basic understanding of the materials and machinery used. The essence of AM is sequentially layering building materials in a cross-section obtained from a CAD model. Each layer has its own thickness, which eventually shapes the final material [160].

Over the years, various metals and alloys have been extensively studied using AM. Among them, Titanium alloys have received the most attention across a range of AM methods. Figure 2.28 (a) provides an overview of publishing patterns and the

different AM techniques that have been under investigation for TiAl alloys since 2010 [161]. Most of the researches have been conducted utilising powder bed fusion (PBF) methods with either a laser or an electron beam, although there is growing interest in laser based directed energy deposition (DED-LB) for producing TiAl. In 2022, 40% of papers were predominantly dedicated to PBF process (Figure 2.28 (b)) [161]. As an AM method for manufacturing TiAl, electron beam powder bed fusion (PBF-EB) has showed potential. Laser beam powder bed fusion (PBF-LB) approach, on the other hand, currently fall short of fulfilling the needed criteria for two reasons [161]:

- PBF-LB does not heat the environment within the building chamber to high temperatures in order to mitigate severe thermal gradients. Significant heat strains and stresses result eventually leading to cracks development.
- PBF-LB uses an inert gas as the chamber atmosphere, whereas PBF-EB utilises a high-vacuum environment. This high-vacuum atmosphere can reduce impurity pick-up.

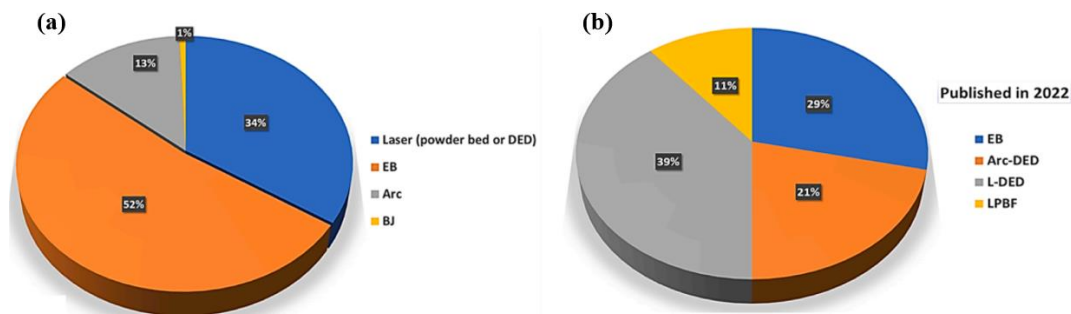


Figure 2.28: (a) The breakdown of various AM techniques employed for fabricating TiAl parts and (b) the primary techniques highlighted in publications of 2022 for printing TiAl [161].

2.4.1 Directed Energy Deposition

In the manufacturing of γ -TiAl, less utilised additive manufacturing methods involves directed energy deposition (DED) method. This technique allows for the utilization of both powder and wire as feedstock materials. In the DED process, feedstock material is directed to the building surface using a nozzle. The power source, whether it be a laser or electron beam, provides the energy to melt the powder in the designated region, enabling the layer-by-layer construction of the part [164]. Another less common deposition-based method for TiAl production is Wire-Arc Additive Manufacturing (WAAM), which is a wire-fed additive manufacturing technique. In wire-fed methods, a continuous wire supplied from the wire feeder undergoes melting by the power source (arc) and solidifies on a building plate [166].

2.4.1.1 Laser Beam Directed Energy Deposition

There has been relatively limited study into laser beam directed energy deposition (DED-LB) TiAl additive manufacturing, with early efforts dating back to 1999 [168], [169]. The powder or wire feedstock material is directly injected into the focused laser beam in this approach, with the laser delivery column and powder nozzle moving as one unit as schematically shown in Figure 2.29 [40]. This method of multilayer deposition involves partially melting or heating preceding layers during subsequent deposition. Processing parameters like as laser power and scanning speed determine the size of the heat-affected zone in each successive deposition. As a result, the cooling rate and microstructure evolution are greatly influenced [40]. Several PBF-LB process parameters to manufacture γ -TiAl parts are given in Table 2.6 [162].

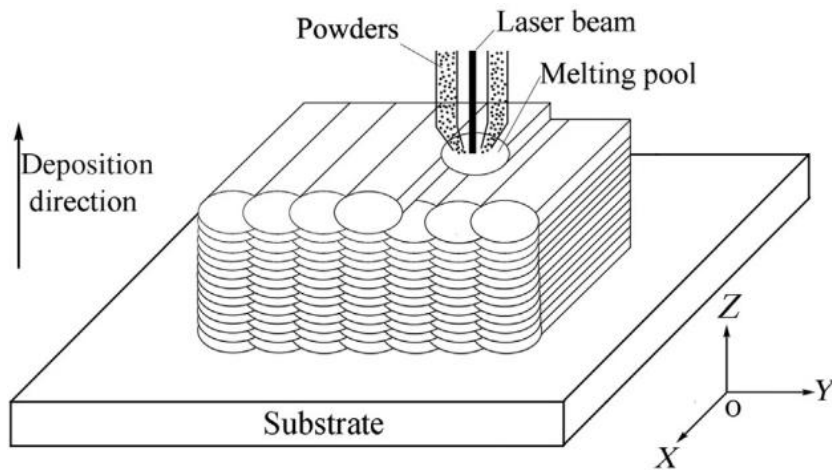


Figure 2.29: Schematic illustration of DED-LB process [40].

Table 2.6: DED-LB process parameters in the literature to manufacture γ -TiAl [162].

Laser Power (W)	Scanning speed (mm/s)	Layer thickness (μm)	Volumetric Energy density (J/mm^3)	Powder rate (g/min)	Reference
4000 - 6000	13.3 - 20	1000 - 1500	33 - 112	10 - 16.6	[167]
1200 - 1800	8.3 - 33.3	830 - 1260	20 - 82	8.8 - 14.5	[202]
150 - 400	10 - 15		20 - 80	2.3	[203]
380	11	254	-	4	[204]
200 - 700	60 - 4000	50 - 1500	0.08 - 19.4	0.5 - 2.2	[171]

The fundamental difficulty with producing bulk TiAl is its cracking susceptibility, especially during the rapid heating-cooling cycles inherent in the DED-LB technique. A comprehensive study on Ti-47Al-2Cr-2Nb indicates that the occurrence of cracks can be mitigated by ensuring continuous deposition [169]. While there were occasional pores inside the material, the composition of the builds nearly followed that of the powder, indicating minimal aluminium loss or capture of oxygen. The microstructure of the as-built material exhibited

irregularities, manifesting as a layered structure with individual deposition layers comprising columnar and equiaxed grains of diverse sizes due to fluctuations in the solidification rate. Furthermore, heat treatment attempts to achieve microstructure homogenization above the α -transus did not result in enhanced tensile properties when compared to the as-built condition [169].

The effect of DED-LB processing parameters on the Ti-48Al-2Mn-2Nb alloy was investigated by Srivastava et al. [170]. The observed heterogeneous microstructure was attributed to remelting and thermal cycles after subsequent layer depositions. Following that, extensive research found major processing parameters influencing build quality, with laser energy input and powder feed rate playing critical roles in determining processability and, thus, build quality. The investigation, however, did not provide crack-free samples or a sufficient surface finish [170].

Alterations in laser power had a profound impact on microstructure uniformity, resulting in diverse grain shapes such as equiaxed, columnar, and dendritic structures [170]. Due to the rapid cooling process associated with laser melting, Ti-48Al-2Mn-2Nb samples produced through DED-LB have a finer microstructure than cast material. A slow laser scan or high laser power generated a huge heat input and a superheated molten pool, extending solidification and raising the temperature of the base material. This resulted in a coarser dendritic microstructure. Samples processed with low heat input, on the other hand, showed less superheating, a wider temperature gradient at the interface, faster cooling rates, and, as a result, a finer microstructure. Achieving satisfactory compositional uniformity without excessive microstructure coarsening following post-processing heat treatments posed a challenge in the as-deposited material [170]. Recent studies show that optimum processing conditions efficiently minimise residual stress cracking. A secondary laser source was introduced beside the nozzle in a study by Thomas et al. to produce a heating region around the laser's focal spot [171]. Because of its low energy density, this new heating source delayed the cooling rate and lessened the thermal gradient. Controlled process parameters, as

shown in Table 2.7, generated Ti-47Al-2Cr-2Nb beads, thin walls, and large blocks [171].

Table 2.7: DED-LB process parameters to produce Ti-47Al-2Cr-2Nb alloy [171].

DED-LB parameters	Min - Max values
Powder size, μm	80 – 125
Laser power, W	200 – 700
Powder feed rate, g/min	0.5 – 2.2
Deposition rate, mm/min	60 – 4000
Z-Increment, mm	0.05 – 1.5
Number of layers	20 – 50

Zhang et al. investigated the as-deposited Ti48Al2Cr2Nb to reveal its metastable and heterogeneous microstructure [172]. Each deposited layer had a metastable structure with a dominating γ phase at the top and the high-temperature α -phase, which transformed into α_2 upon cooling, at the bottom. This was related to a substantially faster cooling rate at the bottom of the layer as a result of rapid heat extraction from the substrate, with thermal gradients favouring textural effects throughout the build direction. The epitaxial development of the γ phase perpendicular to the build direction was produced by sequential laser remelting, resulting in a columnar grain structure along the build axis [173]. Likewise, DED-LB of Ti-47Al-2.5V-1Cr resulted in a directionally solidified columnar grain structure, which was followed by solid-state phase transformation, resulting in a fully lamellar microstructure consisting of α_2 and γ lamellae with lamellar spacing of 0.3-0.5 μm and colony sizes of 50-100 μm [174].

Wang et al. employed the DED-LB method to produce a Ti48Al2Cr2Nb alloy and analysed its microstructure, as shown in Figure 2.30. The top of the sample had an equiaxed microstructure, while the rest had a columnar grain structure. A

combination of duplex and lamellar microstructures was detected in the middle of the plate [167].

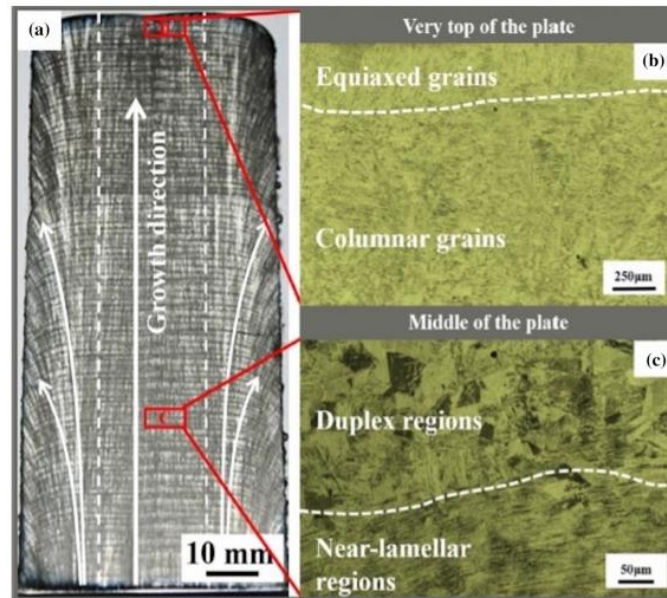


Figure 2.30: Macrostructure and microstructures of Ti48Al2Cr2Nb alloy manufactured by DED-LB [167].

The as-deposited Ti-47Al-2.5V-1Cr and Ti-40Al-2Cr alloys displayed limited tensile ductility, despite having ultimate tensile strength (UTS) comparable to forgings. This reduced ductility persisted even after heat treatment as given in Table 2.8 [174], [175]. In the particular instance of the Ti-47Al-2.5V-1Cr alloy, ductility in both the XY- and Z-directions was less than 0.6% in as-deposited samples. This was linked to the presence of columnar grains inside a fully lamellar microstructure [42]. Recent advances in optimised processing settings and heat treatments for DED-LB processing of Ti-47Al-2Cr-2Nb have presented a well-balanced combination of strength and ductility at room temperature [171]. Notably, tensile ductility variability was minimised, reaching a minimum of 1%. Tensile testing on heat-treated samples revealed a UTS of 519 ± 23 MPa with $1.2 \pm 0.2\%$

elongation in the Z-direction and a UTS of 539 ± 15 MPa with $1.7 \pm 0.2\%$ elongation in the XY-direction. Moll et al. studied a room-temperature tensile strength of about 500 MPa with 1-2% tensile elongation [169].

Table 2.8: Room temperature tensile properties of DED-LB processed Ti-47Al-2.5V-1Cr and Ti-40Al-2Cr [174], [175].

Materials	Condition	UTS, MPa	Elongation, %
Ti-47Al-2.5V-1Cr	As-deposited	550	0.3
	1100C/30 min/AC	620	0.4
	1100C/30 min/WQ	630	0.4
	1125C/30 min/WQ	650	0.6
Ti-40Al-2Cr	As-deposited	560	0.2
	1100C/30 min/AC	560	0.3
	1100C/30 min/WQ	580	0.4
	1125C/30 min/WQ	600	0.6

2.4.1.2 Wire Arc Additive Manufacturing

Wire Arc Additive Manufacturing (WAAM) distinguishes out for its ability to rapidly create or repair complicated metallic components while attaining full density [162]. As a result of the greater deposition rate and lower material waste, processing time and costs are reduced. WAAM's distinguishing characteristics include reduced spatter output and the formation of a quiescent melt pool, which allows for the uniform deposition of material with the required chemical composition [176], [177]. In WAAM, raw materials take the form of wires, and the energy source is typically an electric arc. As energy sources, several arc welding processes such as gas metal arc welding (GMAW), tungsten inert gas (TIG) (schematically seen in Figure 2.31 [166]), gas tungsten arc welding (GTAW), and

plasma arc welding (PAW) can be employed [166]. Utilising a plasma arc as the energy source has advantages such as increased energy density and penetration, resulting in a finer microstructure and more effective alloying element blending, hence improving overall performance in TiAl alloys [178]. Several WAAM process parameters to manufacture γ -TiAl parts are given in Table 2.9 [162].

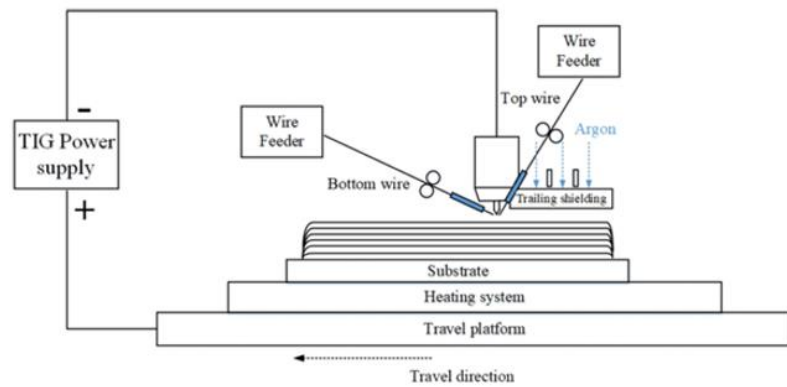


Figure 2.31: Schematic diagram of WAAM setup [166].

Table 2.9: WAAM process parameters found in the literature to manufacture γ -TiAl [162].

Current (A)	Travel speed (mm/min)	Wire speed of Ti (mm/min)	Wire speed of Al (mm/min)	Reference
120	100	800	788	[205]
90	120	1070	930	[206]
90	120	1070	824	[178]
120	100	750	870	[207]
120	95	700	860	[177]

Cai et al. used TIG welding to evaluate the microstructure of the γ -TiAl alloy, employing pure Al and Ti wires in three separate regions [166]. The lower region,

located near the substrate and composed of α_2 grains. In the central region, the dominant characteristics were lamellar colonies, whereas the upper region displayed mainly fine dendrites of γ phases as shown in Figure 2.32 [166].

Wang et al. discovered differences in microhardness findings between the bottom, middle, and top sections, ranging from 369.4 HV to 281.3 HV, respectively [178]. These differences appear to be mostly due to different microstructures in the various regions. The bottom region has the highest microhardness value. Furthermore, the top section had the highest UTS, whereas the bottom portion had the lowest [178]. The tensile strength of TiAl alloy manufactured by WAAM is lower than that of PBF technologies. This decrease is attributed to anisotropy caused by the layer-like buildings [178], [179].

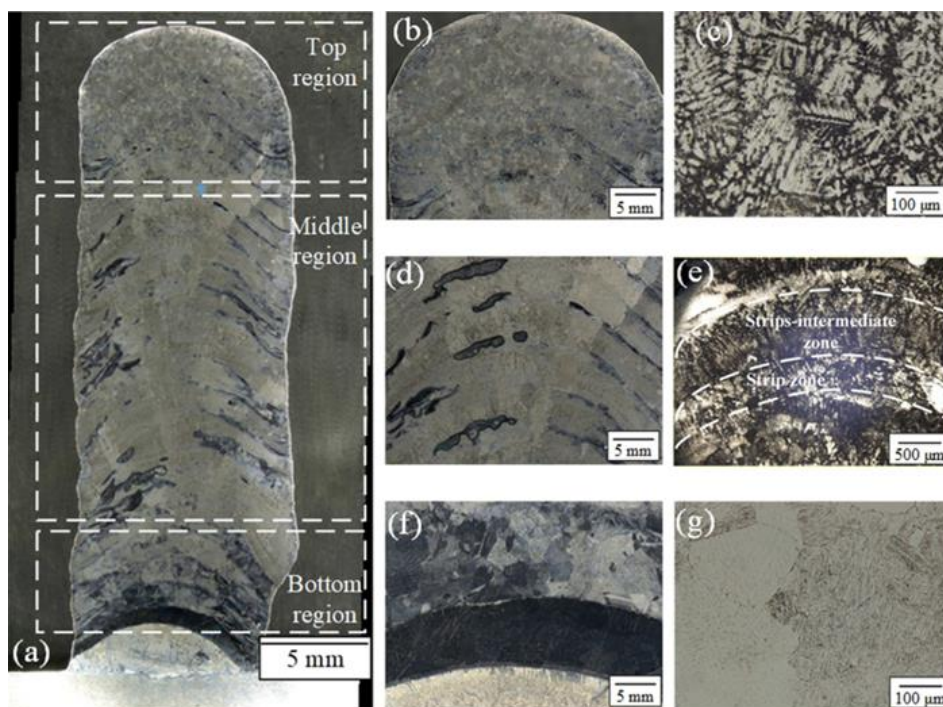


Figure 2.32: Macro and microstructures of γ -TiAl alloy fabricated by TIG method representing; (a) cross-section (x-z plane) morphology; (b) macro- and (c) micro-structure in the top region; (d) macro- and (e) micro-structure in the middle region; (f) macro- and (g) micro-structure in the bottom region. [166].

Wang et al. evaluated the mechanical characteristics of heat-treated materials at four various temperatures [177]. A dominating lamellar structure was obtained after 6 hours of heat treatment 1 (HT1) at 1100 °C. The duplex structure developed during heat treatment 2 (HT2) at 1200 °C. Heat treatments 3 (HT3) and 4 (HT4), which were carried out at temperatures above 1270 °C, resulted in the formation of a coarse-grained lamellar structure. In the HT1 and HT2 samples, the observed microstructures showed a drop in strength but an increase in ductility. The HT3 and HT4 samples, on the other hand, showed decreased strength while preserving a brittle structure. These findings indicate that heat treatment operations in the WAAM process can transform highly brittle structures into ductile ones for γ -TiAl components [177].

2.4.2 Powder Bed Fusion

There are two main types of powder bed fusion (PBF) methods; laser beam powder bed fusion (PBF-LB) and electron beam powder bed fusion (PBF-EB). The operating principle of the PBF-EB method closely resembles that of PBF-LB. Nevertheless, there are notable distinctions. A key difference is the utilization of an electron beam as the power source in PBF-EB, as opposed to a laser. Additionally, PBF-EB operates within a vacuum environment instead of inert gas, and it includes a preheating step before producing the each layer [164].

2.4.2.1 Laser Beam Powder Fusion

Laser beam powder bed fusion (PBF-LB) is a popular additive manufacturing process that is commonly used by researchers in industries such as automotive, aviation, and medicine [162]. Notably, GE Aviation's commitment to make 100,000 fuel nozzles for LEAP engines by 2020 was a key milestone, establishing PBF-LB as the first additive manufacturing technique used to manufacture crucial jet engine components. Despite its broad application, PBF-LB has yet to be

demonstrated as a suitable method for γ -TiAl alloys [40]. Several PBF-LB process parameters to manufacture γ -TiAl parts are given in Table 2.10 [162].

Table 2.10: PBF-LB process parameters found in the literature to manufacture γ -TiAl [162].

Laser Power (W)	Scanning speed (mm/s)	Layer thickness (μm)	Volumetric Energy density (J/mm^3)	Reference
100 - 175	317 - 1590	100	10 - 21	[11]
250 - 350	500	100	250 - 350	[13]
50 - 150	5 - 1500	60	7 - 6250	[199]
100 - 400	10 - 90	100	110 - 816	[182]
120 - 280	600 - 1200	30	42 - 194	[200]
250	700	50	-	[201]

The initial effort to manufacture a Ti48Al2Cr2Nb alloy using PBF-LB in 2011 was unsuccessful due to the inability to get samples free of cracks [180]. Löber et al. performed a parametric research on a TNM alloy with a particle size range of 45-63 μm and a layer thickness of 75 μm in 2014 [181]. To stabilise the process and obtain appropriate shape for individual beads, the laser power and scanning speed were modified. To produce a processing map for the TNM alloy, a complete investigation was undertaken by altering scanning speed laser power (50-250 W) and (50-100, 350-2100 mm/s). At low laser power and scanning speed, there was noticeable cracking, which was attributed to the rapid cooling rate during solidification [181]. The optimized parameters for laser power and scanning speed include 100 W and 50 mm/s for the infill, and 175 W and 1000 mm/s for the outer contour. A hatch distance of 0.3 mm and a layer thickness of 75 μm were also utilized in the stripe hatching scanning strategy [181]. These optimised parameter sets were utilised to generate tiny cylinders and dodecahedron cells with a relative

density of 99% and a fine-grained nearly lamellar microstructure, as shown in Figure 2.33 (a) and (b), respectively. Due to nonuniform cooling rates, the as-built material has an inhomogeneous microstructure (Figure 2.33 (b)). Implementing a two-step heat treatment at 1230 °C followed by 950 °C led to the formation of a uniform duplex microstructure, comprising β and α_2 grains, with some lamellae present in α_2/γ colonies. (Figure 2.33(c)). Compression testing on the Selective Laser Melted (PBF-LBed) TNM alloy revealed strength levels comparable to cast samples [181].

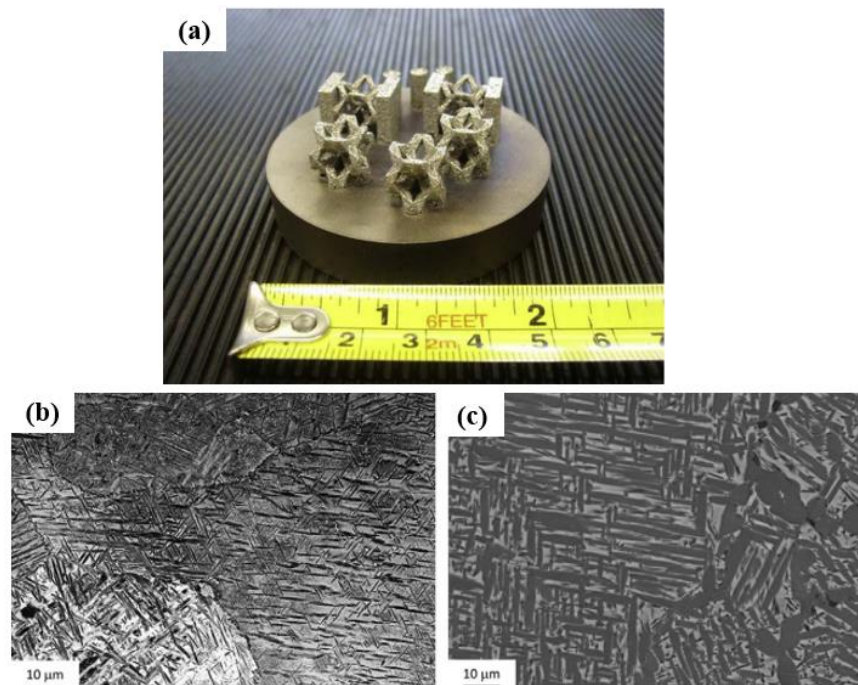


Figure 2.33: TNM alloy produced by PBF-LB method that shows; (a) 3D-dodecahedron structures, (b) SEM image of as-built and (c) SEM image of two step heat treated sample [181].

Shi et al. manufactured Ti-47Al-2Cr-2Nb specimens using a laser power of 250 W and a scanning speed of 40 mm/s [182]. Despite having a relative density of 98.95%, the specimens fractured severely. The principal cause of failure was

cracking caused by the brittle nature of the γ -TiAl alloy. This alloy indicated unable to withstand the high residual stress caused by the PBF-LB process's extremely fast heating and cooling cycles [182].

Gussone et al. examined the microstructure and tensile properties of Ti-44.8Al-6Nb-1.0Mo-0.1B [12]. When the laser energy input exceeded 55 J/mm³, it was possible to obtain samples with 99% density. Aluminium loss was proportional to laser energy input, with higher losses at higher energy densities indicating considerable overheating. As seen in the left column of Figure 2.34, samples fabricated with the highest energy input of 300 J/mm³ showed α_2 platelets within the β /B2. Similar needles/platelets were observed at a medium energy input of 110 J/mm³, but with a lamellar α_2/γ substructure (Figure 2.34, top row, middle column). As shown in Figure 2.34, middle row, right column, a globular-shaped ultrafine α_2/γ lamellar colonies was observed along with β /B2 and γ grains at colony boundaries at low energy densities of 60 J/mm³. Furthermore, samples produced at a preheating temperature of 1000 °C had a coarser microstructure than those produced at 800 °C. However it was observed a microcrack in the sample produced with 300 J/mm³ energy input as well as 800 °C preheating temperature as shown in Figure 2.34, middle row, left column [12].

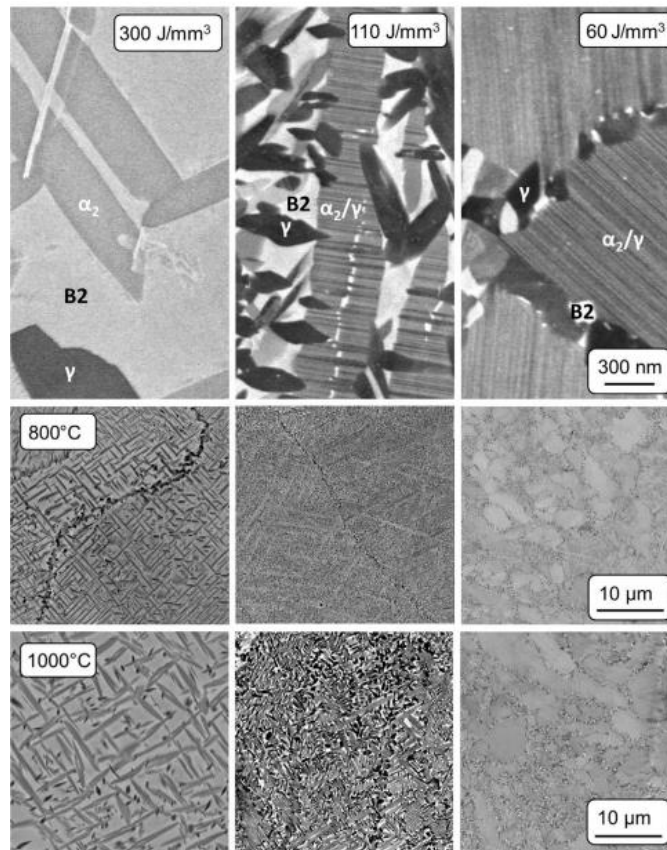


Figure 2.34: SEM images of the samples produced at 800 °C (top row and middle row) and 1000 °C (bottom row) preheating temperatures [12].

Li et al. examined the microstructure, phase transition, and nano-hardness of Ti-45Al-2Cr-5Nb alloy produced at 500-800 mm/s laser scanning speed. A faster scanning speed produced finer grains and a higher volume fraction of α_2 and B2 phases [183]. Post-HIPing at 1200 °C under 200 MPa pressure for 4 h increased the tensile strength of Ti-44.8Al-6Nb-1.0Mo-0.1B to up to 900 MPa and, in some cases, decreased below 400 MPa. The low ductility in the samples was due to significant oxygen pickup during the PBF-LB process as well as defects that remained after HIPing [12].

Löber et al. conducted a comparison between the PBF-LB and PBF-EB methods [180]. The microstructures of Ti48Al2Cr2Nb alloy produced using PBF-EB and

PBF-LB methods are given in Figure 2.35 where the production direction is indicated by an arrow. The production direction is indicated by arrows in the figure. The microstructures of these samples, which were generated using laser power ranging from 100 to 175 W, a layer thickness of 100 μm , and an energy density of 10-21 J/mm^3 in the PBF-LB process, revealed that a substantial number of cracks developed in comparison to the PBF-EB sample [180].

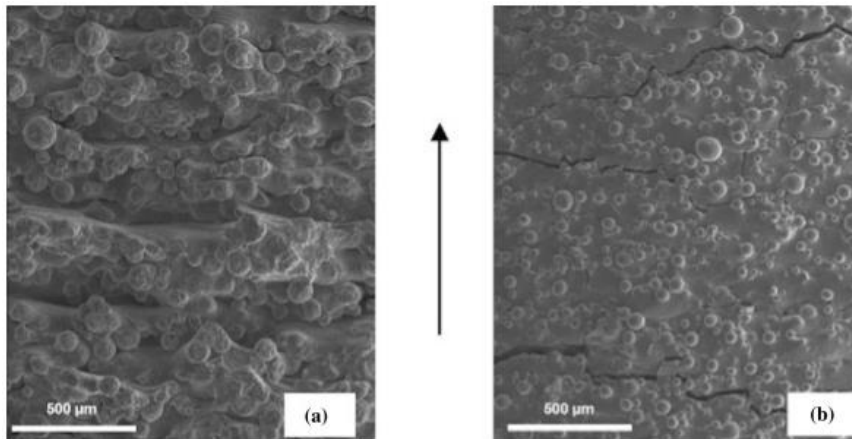


Figure 2.35: SEM images of the surfaces of Ti48Al2Cr2Nb samples produced by the (a) PBF-EB and (b) PBF-LB methods [180].

2.4.2.2 Electron Beam Powder Bed Fusion

Electron Beam Powder Bed Fusion (PBF-EB) is the most common method for producing γ -TiAl alloy components [162]. As γ -TiAl alloy is naturally brittle at room temperature, substantial preheating throughout production and preheating before each layer contributes in preventing damage caused by thermal or residual stresses. As a result, PBF-EB is an excellent method for processing γ -TiAl alloys. Several EB-PBF process parameters to manufacture γ -TiAl parts are given in Table 2.11 [162]. PBF-EB is being used in the aviation and automotive industries to

manufacture components such as Low-Pressure Turbine (LPT) blades, seen in Figure 2.36, and turbocharger wheels [40], [184].

Table 2.11: EB-PBF process parameters found in the literature to manufacture γ -TiAl [162].

Beam Current (mA)	Scanning speed (mm/s)	Layer thickness (μm)	Line energy (J/mm)	Building temperature ($^{\circ}\text{C}$)	Reference
10	5000	90	0.12	1050	[24]
15 - 25	2000	100	0.45 - 0.75	900	[186]
25	1200	-	1.25	1100	[187]
3.5 - 15	300 - 6000	70 - 100	0.15 - 1.1	930 -950	[15]
10	600	90	1	1050	[196]
-	-	100	0.1275	1000	[197]
18	2200	90	0.5	1100	[184]
25	1200	-	1.25	1100	[198]
-	2000 - 8000	50	0.125 - 0.150	1000	[26]
-	-	70	500	1050	[2]
10	10000	50	0.06	-	[12]



Figure 2.36: PBF-EB manufactured as-built (left) and subsequently machined (right) Ti48Al2Cr2Nb LPT blade [40].

When analysing the microstructure of parts manufactured using the parameters indicated in Table 2.11, Seifi et al. [24] reported a grain size of around 25 μm . In comparison, the typical grain size of γ -TiAl alloy manufactured by casting is approximately 1000 μm , while it ranges from 100 to 300 μm when produced by wrought process. This considerable difference suggests that the grains in parts manufactured using the PBF-EB process are fine, which is predicted to improve characteristics such as hardness and strength [23], [24], [185].

The ability to generate full-density parts is a critical criterion when evaluating process parameters. Two forms of porosity are commonly encountered in the PBF-EB method of producing γ -TiAl. One type is caused by process variables and

frequently manifests as insufficient interlayer bonding. The other form of porosity originates from the gas atomized powder utilized in the process [15], [20]. Excessive energy input can cause large melt pools to occur, resulting in irregular top surfaces with waves. Surface defects induce significant changes in the thickness of the powder layer deposited in following layers, resulting in inadequate interlayer bonding. Such porosities have a negative impact on the density of the component [15].

Biamino et al. explored the feasibility of achieving fully dense PBF-EB manufactured Ti48Al2Cr2Nb alloy [20]. While process optimisation successfully removed defects caused by a lack of fusion between successive layers, random spherical pores with diameters less than 20 μm remained. These pores were generated by the entrapment of argon gas within the particles during the atomization [20]. Mohammad et al. investigated defect distribution in PBF-EB manufactured Ti48Al2Cr2Nb using micro-CT [187]. Increasing the energy input (0.97, 2.71, and 4.07 J/mm^2) resulted in a reduction in the total number and volume fraction of defects. Notably, samples with low energy density had a higher prevalence of larger defects, indicating inadequate layer fusing. Lower energy, on the other hand, resulted in an equiaxed microstructure, whilst higher energies led to in a totally lamellar. Only with the proper amount of areal energy was found to generate a duplex microstructure [187].

Cormier et al. introduced the use PBF-EB to produce a Ti-47Al-2Cr-2Nb sample [186]. When comparing the as-built sample to the initial powder, a 7.4 at.% loss of Al was detected, which was attributable to Al evaporation throughout the PBF-EB process in a vacuum. Decreased beam currents and reduced melt pool overheating were discovered as key factors in decreasing Al evaporation in a comprehensive parametric research on PBF-EB fabricated Ti48Al2Cr2Nb alloy by Schwerdtfeger et al. [15]. Through parameter adjustments, Al loss was minimized to 0.5 at.%. However, uneven distribution of Al was seen in the samples displayed in Figure 2.37, which could affect the solidification process and, as a result, the microstructure [15]. Biamino et al. reported a 1 at.% Al loss but did not provide

specifics on the process parameters utilized [20]. Ge et al. further highlighted the importance of energy input on Al evaporation in Ti-47Al-2Cr-2Nb powders [18].

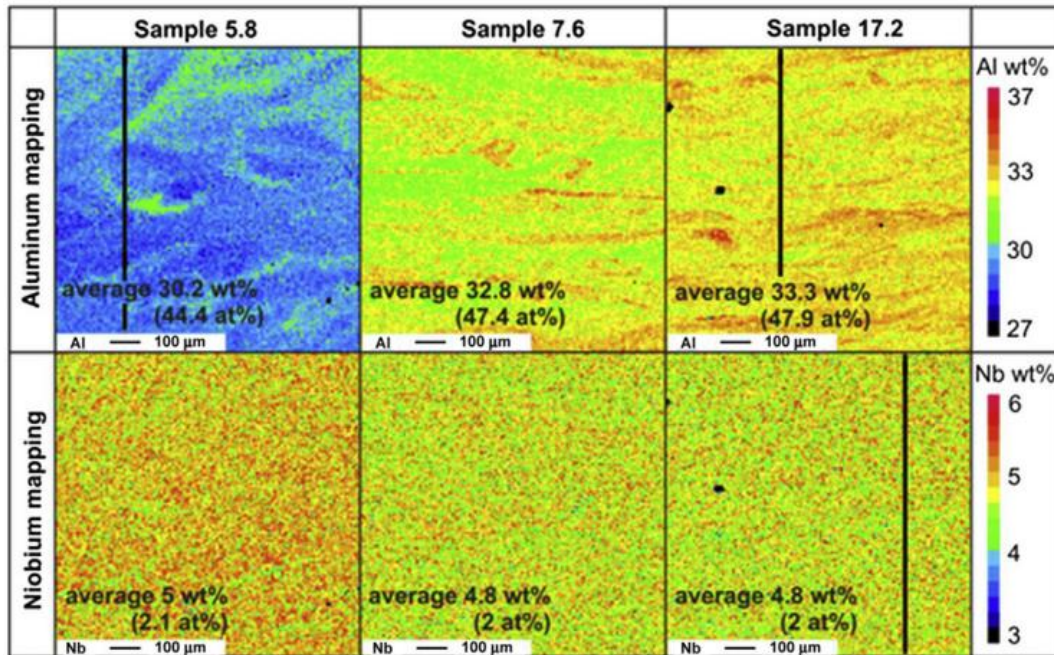


Figure 2.37: Microprobe measurements, reflected in the element mappings, reveal an uneven distribution of Al attributed to the evaporation process occurring in the upper region of the melt pool [15].

The thermal history of the Ti48Al2Cr2Nb during PBF-EB was divided into two stages as schematically illustrated in Figure 2.38 (a) [188]. When the beam scans the highest layers in the first stage, the microstructure melts and cools. This stage has a variable temperature and a short duration. After melting and cooling, the microstructure advances to the second stage, known as annealing or in-situ heat treatment. In this step, the time and temperature are determined by the distance from the building platform. The building duration is approximately 3 h from a height of 5-20 mm, reflecting the duration of in-situ heat treatment at a height of 5 mm. Determining the annealing temperature at different heights is challenging due to the thermocouple connection at the bottom of the build platform. The analysis

suggests an approximate temperature decrease of 80 °C for every 10 mm along the part's height (Figure 2.38) [188]. As per the binary Ti-Al phase diagram, annealing temperatures between 1020–1150 °C result in the degradation of lamellar colonies into equiaxed α_2 , γ , and B2 phases, accompanied by coarsening of colony boundaries [188].

Investigating the heat stability of Ti48Al2Nb2Cr at elevated temperatures, particularly in the 1050 to 1250 °C range during the PBF-EB process, is crucial due to the material's preheating requirement of 1050–1100 °C [189]. The observed trend indicates that an escalation in annealing temperature from 1050 to 1250 °C induces the breakdown of lamellar colonies and the decomposition of α_2 lamellae [189]. This degradation is attributed to the cyclic heating and cooling experienced by previously deposited layers during PBF-EB. During the scanning of successive and upper layers, the microstructure undergoes fast heating and cooling cycles, resulting in the breakdown of lamellar colonies and α_2 laths. At an annealing temperature of 1050 °C, ellipsoidal B2 precipitates formed along the α_2 lamellae, uniformly propagated throughout lamellar colonies. The microstructure converted into (γ /B2) laths after additional annealing at 1250 °C [189].

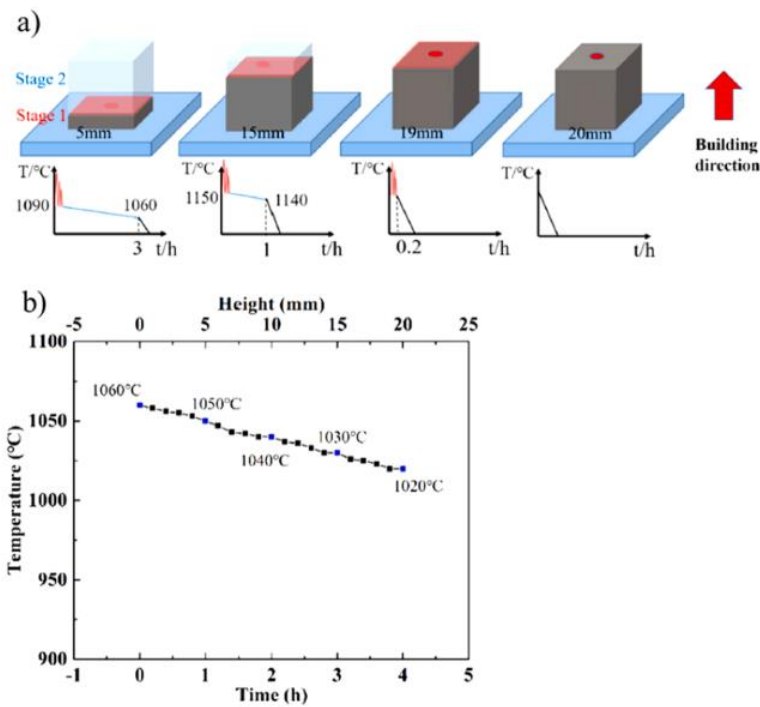


Figure 2.38: a) The schematic representation of the temperature history at different heights of the as-built specimen during PBF-EB, b) changes in the build plate temperature over time and building height [188].

The microstructures of as-built specimens exhibit gradual changes concerning the distance to the upper surface. Figure 2.39 displays fully-lamellar, near-lamellar, duplex, and equiaxed γ structures depending on the built height [23]. On the fully lamellar and near-lamellar sections near the top surface, in-situ heat treatment cycles are effective. With the number of powder fusion cycles, the distance between these regions and the top surface increases. As a result, the zones annealed at roughly 1250 °C undergo discontinuous coarsening transition into a duplex-like region [23].

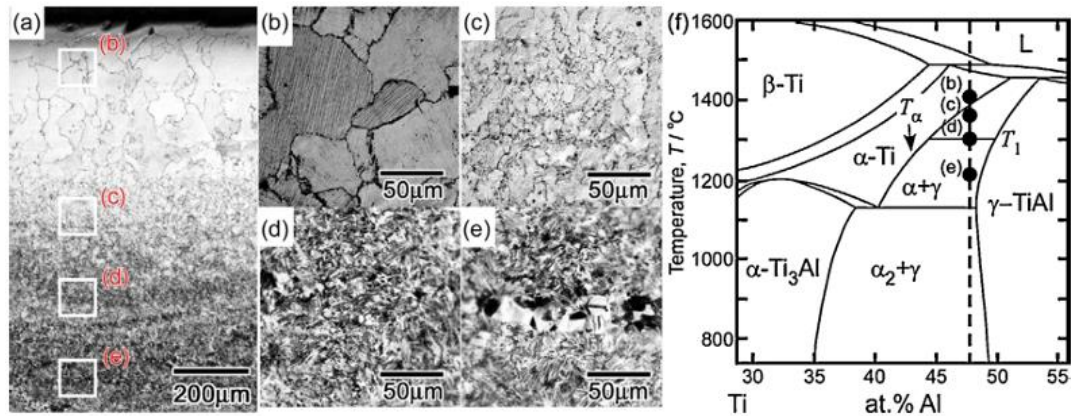


Figure 2.39: Microstructure of as-built Ti48Al2Cr2Nb that shows; (a) upper and lower regions, (b) fully-lamellar, (c) near-lamellar, (d) duplex, (e) equiaxed γ microstructures and (f) central portion of the Ti–Al binary phase diagram [23].

According to Baudana et al., the existence of larger γ grains in the PBF-EB process is caused by local overheating, heat diffusion processes during the melting of the successive powder layer, and simultaneous remelting of a section of the previously melted layer [26]. Todai et al. found that, the cumulative thickness of one duplex and one γ band is roughly 90 μm , matching the thickness of each powder layer [23]. The heat-treatment effects of the electron beam due to rapid solidification result in all of these distinct microstructures. The electron beam melts the powder layer and a portion of the layer below it, causing the material beneath the melting pool to be warmed to various temperatures depending on the distance in Z axis. Right below the top surface, fully and nearly lamellar zones occur. The annealing temperature for these areas gradually decreases with each build cycle, resulting in the formation of a duplex microstructure. As a result, annealing just above the eutectoid temperature changes a portion of the duplex region into γ bands, contributing to the periodic development of γ bands, as this phenomena illustrated in Figure 2.40 [23].

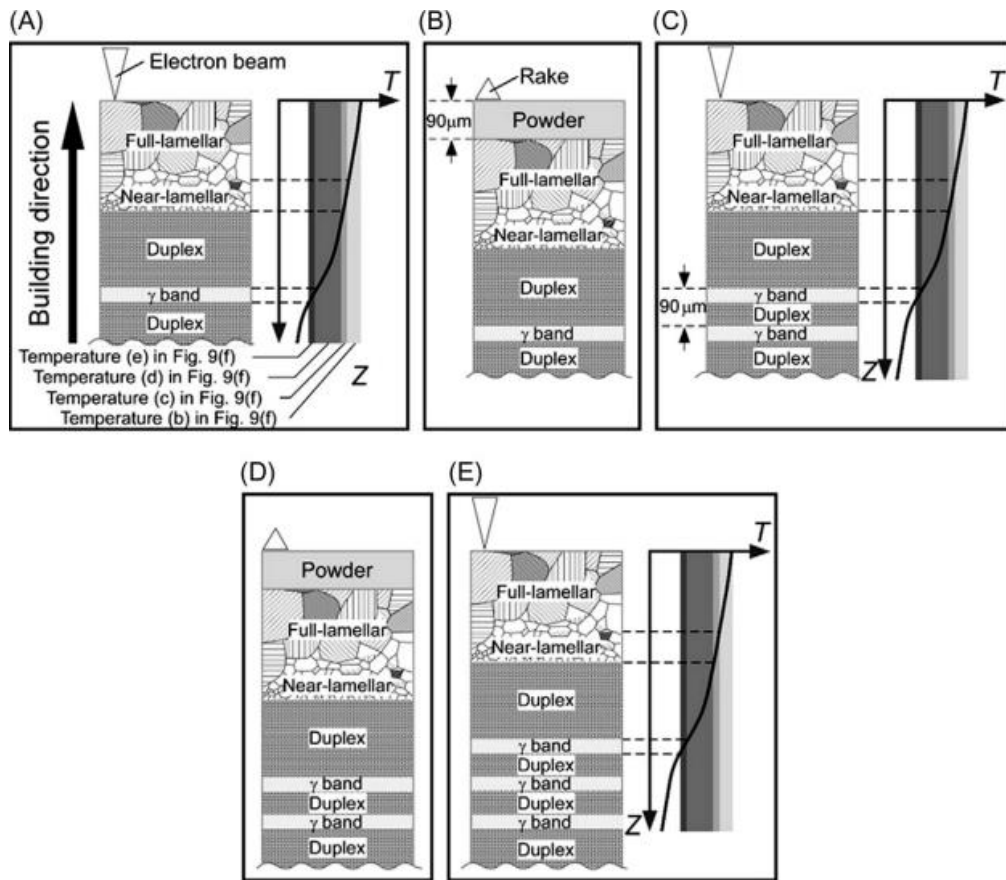


Figure 2.40: Schematic illustrations that show the evolution of microstructure and the distinctive formation of layered microstructures during the PBF-EB process. (a) Snapshot during the PBF-EB process, (b) powder layer feed, (c) fusion of several layers, (d) next layer feed, and (e) fusion of several layers again [23].

The continuous cooling transformation (CCT) diagram for Ti48Al2Nb2Cr is depicted in Figure 2.41 [190]. The diagram illustrates that various microstructural features can be produced depending on the cooling rate through solid-state phase changes. Increasing the cooling rate allows the generation of a near γ microstructure. With increasing cooling rate, the diffusion-related phase transformation transforms to a diffusion-free phase transition. It is assumed that an PBF-EB material undergoing a cooling rate of 10^3 – 10^5 K/s would exhibit a structure close to γ , as indicated by the the CCT diagram in Figure 2.41.

Additionally, the as-built specimen was found to contain a few micro-sized α_2 grains at certain grain boundaries [190].

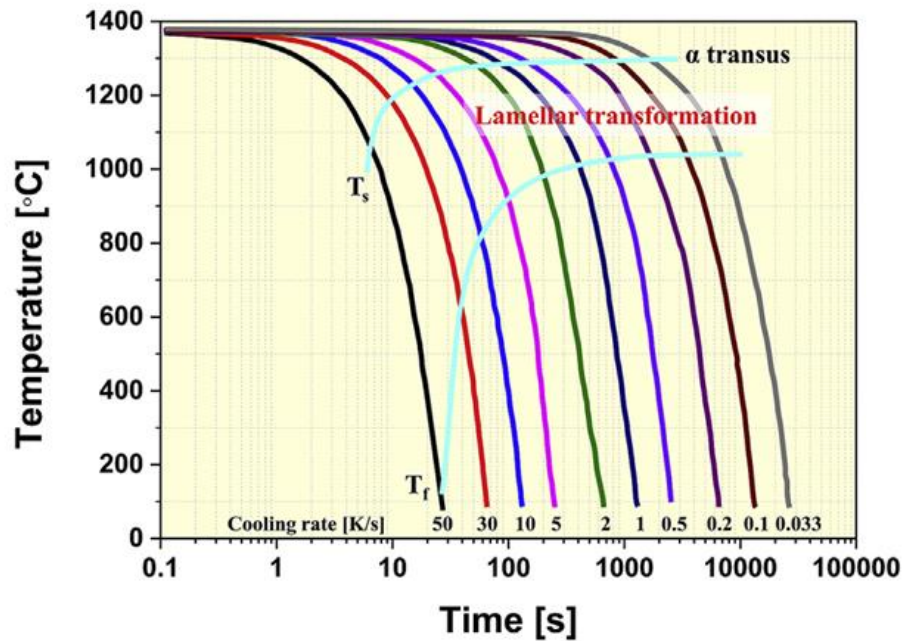


Figure 2.41: The CCT diagram for the Ti48Al2Cr2Nb [190].

The PBF-EB processing parameters significantly influence the cooling conditions, leading to variations in the as-built microstructural characteristics [188]. For instance, parts produced with higher line energy (1.1 J/mm) exhibited a lamellar microstructure with colony sizes in the range of 10–30 μm [15]. In contrast, parts manufactured with lower line energy (0.15 J/mm) showed only a minimal number of lamellar regions. This implies that high cooling rates at high scanning speeds (low line energy) are adequate to induce a γ phase transformation. Lowering the line energy resulted in a considerably finer microstructure [15]. In addition to scanning speed, the beam current was identified as a significant process parameter affecting the type of microstructure [18]. At low beam current values (low line energy), the γ phase was the major phase, while at higher beam current values, the

α_2 phase became dominant. The microstructure was reported to be lamellar in the upper region with a thickness of α_2 laths of 1 μm and coarsened in the lower region with a thickness of α_2 laths of 5 μm [18]. The size of the grain structure was also influenced by the melt pool [190]. Figure 2.42 (a) illustrates the formation of a near γ microstructure, consisting of both coarse and fine grain regions. The fine grains were attributed to the relatively low thermal dependence and faster cooling rate at the melt pool boundary. The EBSD mapping in Figure 2.42 (b) indicated the random orientation of the γ phase, which was attributed to the transformation from α to γ with no alteration in composition. The lack of an orientation relationship resulted in a random crystallographic orientation, and the α_2 phase was detected at the grain boundary [190].

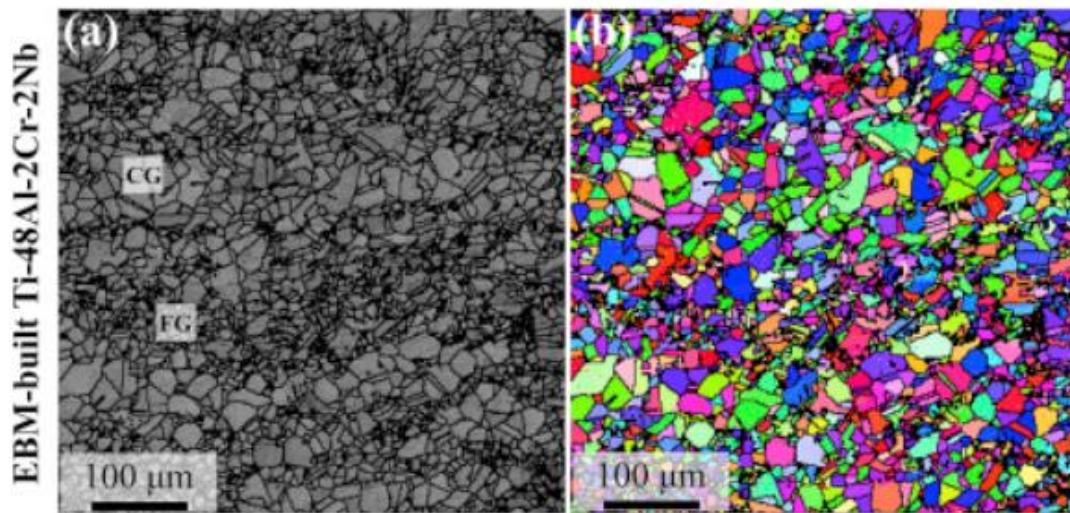


Figure 2.42: EBSD analysis results:; (a) band-contrast maps, (b) grain-orientation maps [190].

To avoid contamination during heat treatment (HT), it is recommended to use a furnace with a W/Mo chamber in a shielded or high-vacuum environment. The oxidation behavior of γ -TiAl at temperatures above 700 $^{\circ}\text{C}$ is critical to examine

since it results in the development of Ti oxides, which is especially important when these materials are intended for usage at high temperatures [26].

Biamino et al. investigated the influence of HT on microstructural characteristics in a PBF-EB turbocharger wheel prototype. The component had an equiaxed grain structure when it was first manufactured, but heat treatment caused it to change into a fully lamellar structure [16].

Yue et al. investigated the impact of annealing on the microstructure of two distinct parts fabricated with different volumetric energy density values (24.07 and 35 J/mm³) [191]. The annealing conditions are outlined in Table 2.12 [191]. At a PBF-EB energy density of 24.07 J/mm³, annealing at 1310 °C for 3 hours resulted in an elongated lamellar structure composed of (α_2/γ) lamellar colonies oriented along the build direction as illustrated in Figure 2.43 (a). Conversely, the same sample showed minimal elongated grains after annealing at 1370 °C for 2 hours, as depicted in Figure 2.43 (b). The rationale behind this phenomenon is that the annealing temperature of 1370 °C falls within the $\alpha+\beta$ phase region, where the β phase has 12 potential orientations during its transformation into the α phase during furnace cooling. As a consequence, the orientation of lamellae within a lamellar colony underwent changes, leading to a decrease in the aspect ratio along the building direction. However, there was an increase in grain size. Furthermore, in the sample produced at a high energy density of 35 J/mm³, the elongated grain morphology after 2 hours of annealing at 1370 °C was persistent (Figure 2.43 (c)). Yue et al. attributed the observed difference between various volumetric energy densities to the elongated grains spanning multiple layers and lamellar colonies exhibiting a preferred orientation. Consequently, altering the morphology of the grains completely becomes challenging, as the grains inherit the previous lamellar orientation of columnar grains during the grain growth process [191].

Table 2.12: Heat treatments according to Yue et al. [191].

Sample	Annealing Temperature (°C)	Holding time	Cooling
24.07 J/mm ³ (S1)	1310	3 h	Furnace cooling
	1370	2 h	Furnace cooling
	1310	20 min	Water quenched
35 J/mm ³ (S2)	1370	2 h	Furnace cooling

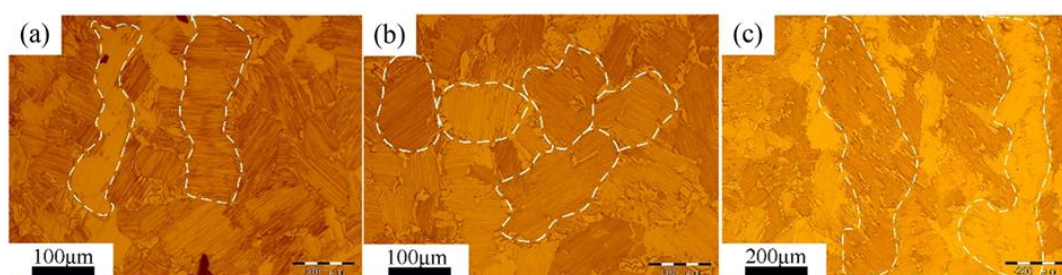


Figure 2.43: Micrographs of sample S1 after annealing at; (a) 1310 °C for 3 h and (b) 1370 °C for 2 h and sample S2 after annealing at; (c) 1370 °C for 2 h, followed by furnace cooling (vertical cross section) [191].

Hot isostatic pressing (HIP) serves as a post-treatment method to enhance the density of the as-built material. While some sources advocate a single-step HIP, others propose a combination of HIP followed by subsequent heat treatment [161]. In a study by Mohammad et al., a one-step HIP was employed at 1200 °C for 4 hours in an argon environment at 100 MPa pressure [192]. The microstructure of the alloy, in both the as-built and HIPed conditions, was lamellar as shown in Figure 2.44 (a) and (b), respectively. Figure 2.44 depicts in the HIPed samples that the lamella width and grain size were notably larger. The relative density increased from 99% in the as-built condition to around 99.7% after HIPing. The texture of both HIPed and non-HIPed samples was largely randomised, with no apparent variations. The proportion of high-angle grain boundaries (HAGBs) increased

significantly from 0.55 in the as-built condition to 0.86 following HIPing [192]. As a result, during HIPing, HAGBs resulted in a rapid increase in HAGBs. This mechanism causes dislocation annihilation, resulting in a larger proportion of dislocation-free zones in the HIPed samples [192].

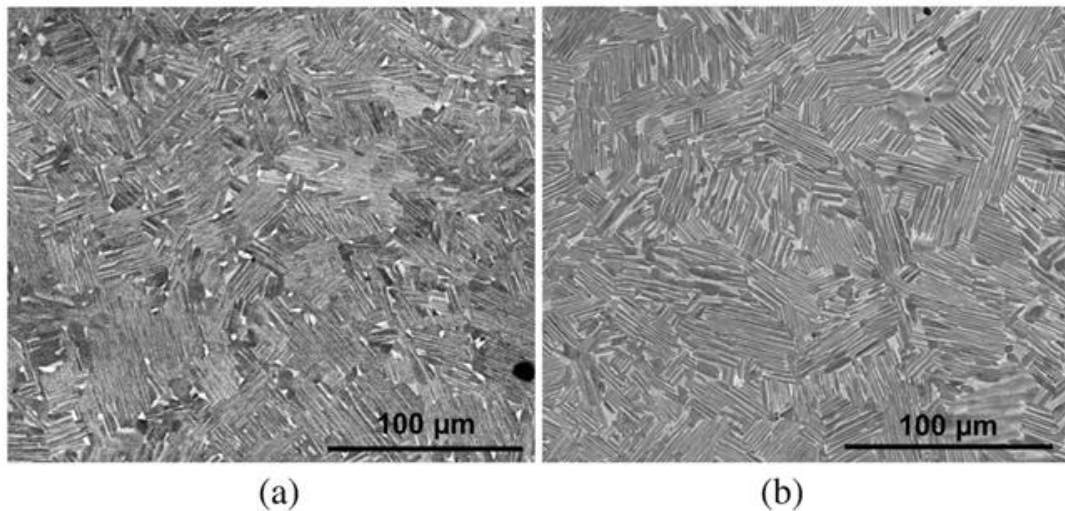


Figure 2.44: (a) PBF-EB as-built and (b) HIPed Ti8Al2Cr2Nb SEM-BSE images [192].

Cakmak et al. applied HIP without subsequent heat treatment, resulting in a substantial reduction of the initial porosity content [193]. The as-built equiaxed duplex microstructures consisting of γ and α_2 phase, were preserved after HIPing, potentially accompanied by some grain growth. The study attributes the development of an equiaxed fine microstructure to a solidification path involving sequential stages of liquid (L) $\rightarrow L + \alpha \rightarrow L + \alpha + \gamma \rightarrow \alpha + \gamma \rightarrow \gamma \rightarrow \gamma + \alpha_2$. This process effectively disrupts epitaxial growth and induces phase transformations during multiple melt-solidification cycles [193]. The EBSD phase map suggested by Cakmak et al. is shown in Figure 2.45. As a result, the duplex microstructure, featuring $\gamma + \alpha_2$ lamellar colonies and a coarse γ banded structure, remained after

the HIP process. However, there was a notable increase in the α_2 phase fraction, particularly at the γ grain boundaries, following the HIP process [193].

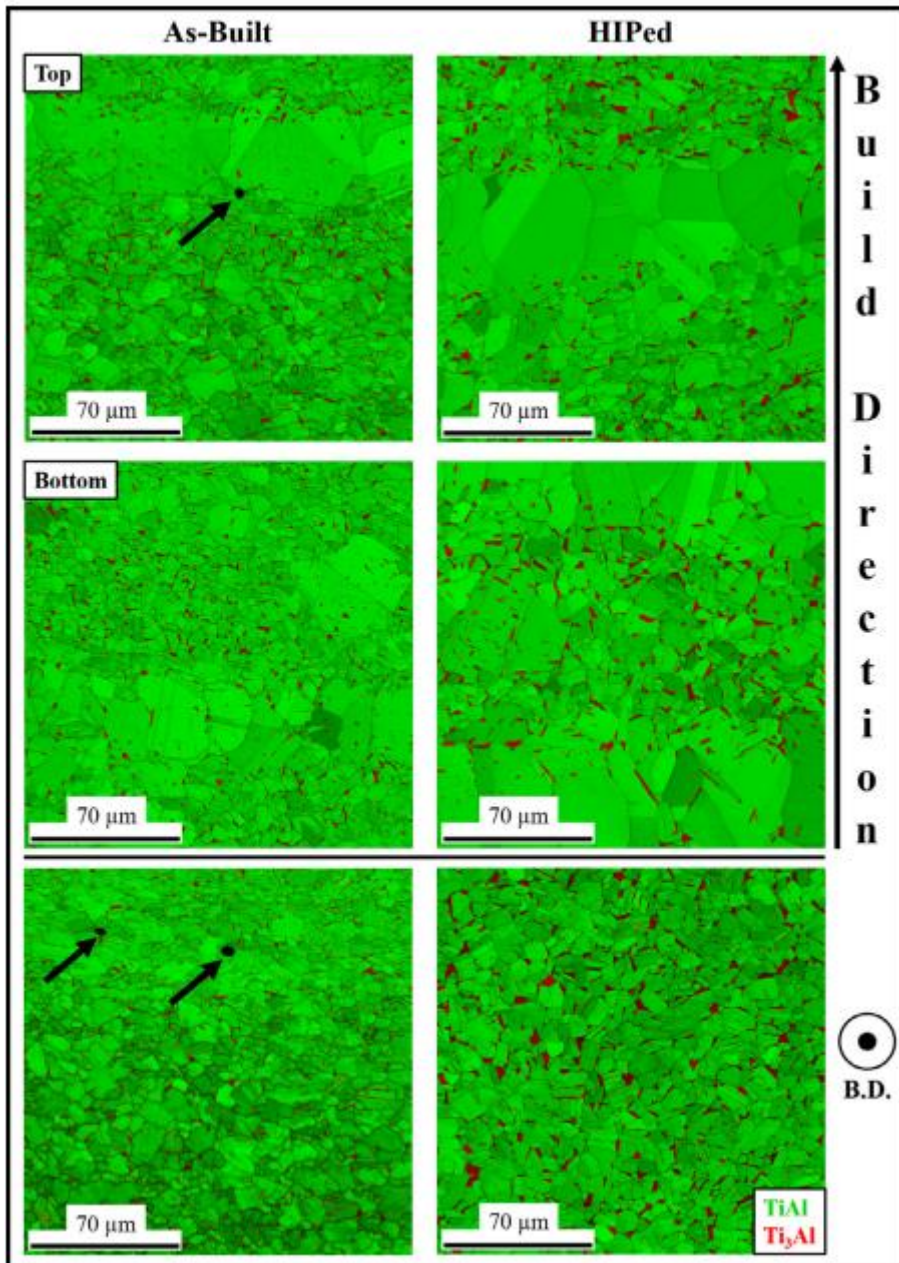


Figure 2.45: EBSD phase maps of the as-built and HIPed Ti₄₈Al₂Cr₂Nb [193].

In a study involving as-built samples, both HIP and HT cycles were applied [20]. The HIP applied for 4 hours at 1260 °C and 170 MPa, aiming to achieve the duplex microstructure. Subsequently, a 2-hour heat treatment at 1300 °C was done after HIP. The HIPed microstructure, as shown in Figure 2.46 (c), exhibited complete recrystallization, resulting in a nearly equiaxed microstructure with grain expansion around 20 μm . A duplex microstructure was obtained after the heat treatment as illustrated in Figure 2.46 (d). The microstructure was dominated by the lamellar phase, which had an average colony size of around 100 μm and was accompanied by fine equiaxed grains (around 15 μm). This shows that there was little grain formation during the heat treatment [20].

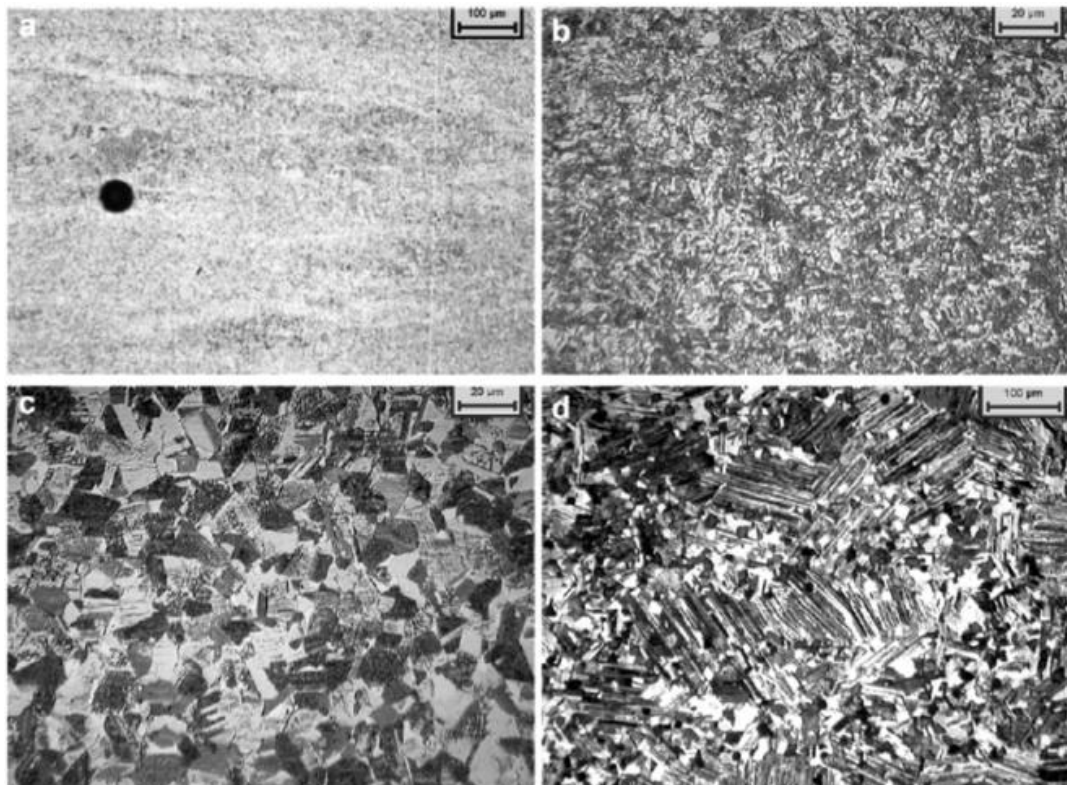


Figure 2.46: (a) A pore in PBF-EB Ti48Al2Nb2Cr sample. Microstructures of; (b) as-built, (c) HIPed and (d) HTed samples [20].

Manufacturing TiAl parts with PBF-EB presents unique problems due to the material's intrinsic brittleness, resulting in higher complexity when compared to typical Ti alloys like Ti-6Al-4V. In order to mitigate cracking, the chamber temperature must be maintained around 1050 °C. The as-built PBF-EB processed Ti48Al2Cr2Nb exhibited a room temperature tensile strength of 503 ± 18 MPa [192]. However, ductility was essentially nonexistent, attributed to defects like small pores and occasional lack-of-fusion [194]. Defects on the fracture surface included unmelted powder and spherical pores [192]. Todai et al. reported high strength for the as-built Ti48Al2Cr2Nb, with a room temperature tensile strength along the build direction of approximately 640 MPa and a tensile elongation of around 0.5% [23]. Tensile strength at 45 and 90 degrees from the building direction was similar, and average tensile elongations were both greater than 2% [23]. The room temperature tensile properties of the PBF-EB manufactured Ti48Al2Cr2Nb alloy along the build (z) direction are summarized in Table 2.13.

Table 2.13: The room temperature tensile properties of the PBF-EB manufactured Ti48Al2Cr2Nb alloy along the build (Z) direction.

Material condition	Microstructure	YS (MPa)	UTS (MPa)	El. (%)
As-built [40]	Equiaxed	-	503 ± 18	0
As-built [23]	Equiaxed	605	640	0.5
1200 °C HIP [40]	Equiaxed	467 ± 15	501 ± 25	1.3 ± 0.7
1260 °C HIP [20].	Equiaxed	375	430	1.2
HIP + 1260 °C/2 h [40]	Duplex	382 ± 11	474 ± 23	1.3 ± 0.3
HIP + 1300 °C/2 h [40]	Near lamellar	377 ± 10	441 ± 9	1.0 ± 0.2
HIP + 1360 °C/2 h [40]	Fully lamellar	373 ± 13	429 ± 26	0.8 ± 0.2

Microcracks were identified in the as-built Ti48Al2Cr2Nb material, necessitating the implementation of HIP to eliminate defects [40]. Figure 2.47 depicts the average tensile properties at various temperatures of HIPed Ti48Al2Cr2Nb, treated

for equiaxed (HIP at 1200 °C), duplex (HIP at 1260 °C for 2 hours), nearly lamellar (HIP at 1300 °C for 2 hours), and fully lamellar (HIP at 1360 °C for 2 hours) microstructures. The tensile strength was relatively temperature-independent up to 800 °C. The HIPed material's room temperature tensile strength equals that of the as-built material, with an increase in ductility from 0% to 1.3% due to the closure of pores and microcracks inside the material [40].

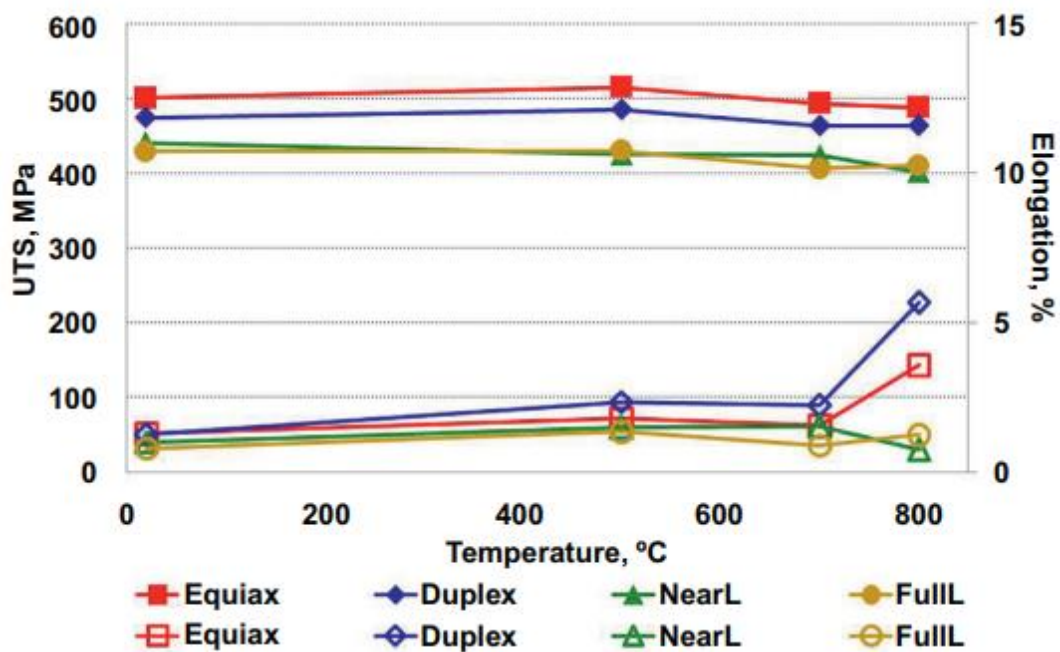


Figure 2.47: UTS versus temperature relationship of PBF-EB processed Ti48Al2Cr2Nb alloy in various microstructures [40].

The strength of the duplex microstructure decreased whereas ductility increased slightly [20]. Tensile strength and ductility both decreased when the volume fraction of the lamellas increased. Tensile characteristics of fully lamellar material were found to be quite similar to those of Ti48Al2Cr2Nb castings with comparable grain size. Tensile experiments on samples heat treated for 10 hours at 650 °C

demonstrated a significant drop in room temperature ductility, which decreased as temperature increased [20].

The Ti-48Al-2Nb-0.7Cr-0.3Si alloy, subjected to heat treatment at 1360 °C for 2 hours to achieve a nearly lamellar microstructure [26]. At room temperature, UTS and elongation were measured as 336 ± 26 MPa and $0.27 \pm 0.1\%$, respectively. At 800 °C, these values change to 426 ± 22 MPa and $1.96 \pm 0.5\%$, respectively. Additionally, the creep properties for this alloy were also given in Table 2.14 [26].

Table 2.14: Creep properties of PBF-EB manufactured Ti-48Al-2Nb-0.7Cr-0.3Si alloy [26].

Creep stress (MPa)	Final creep strain (%)	Rupture time (h)	Larson-Miller parameter
200	5.72	372	24.22
300	8.32	23.7	22.93

The available fatigue data for PBF-EB manufactured TiAl is limited. A Haigh diagram indicates superior performance of PBF-EB manufactured Ti48Al2Cr2Nb compared to its casting counterpart across various temperature and stress conditions [195]. The measured fatigue crack growth threshold is 6.13–6.7 MPa $m^{1/2}$, higher than the value in GE's reference data by more than 30%. The room-temperature fatigue limit of the HIPed at 1200 °C material with an equiaxed microstructure was 450 MPa [40]. However, there is considerable variability in life at higher stress levels. Fatigue cracks were found to initiate from ceramic particles, likely oxides of Al and Si, potentially mixed during the gas atomization process. Given the low ductility of TiAl, defects play a pivotal role in determining mechanical properties, highlighting the significance of defect tolerance and management for parts produced by PBF-EB [40].

The tensile properties and stress-strain curves examined by Lin et al. are presented in Figure 2.48 [196]. The room-temperature yield strength of the HIPed sample was approximately 460 MPa. Both duplex (DP) and fully lamellar (FL) samples exhibited a yield strength of around 360-380 MPa. The heightened strength of HIPed samples was attributed to the smaller grain size and potentially the strengthening effect of a high dislocation density in the as-built material, which had not been completely eliminated by HIP [196]. In the Z-direction, the average yield strength was 15 MPa and 30 MPa higher than XY-direction samples for HIP and DP microstructures, respectively. The difference in FL microstructure between XY and Z samples was insignificant. At 850 °C, the yield strength disparity between HIP and DP/FL dropped to around 50 MPa, since lamellar microstructures preserved greater strength at higher temperatures [196]. The anisotropy in the yield strengths of HIP and DP samples decreased as well, owing to more uniform deformation caused by the activation of new slip systems at high temperatures [196]. The samples' room temperature ductility was classified into three levels based on elongation. HIP-XY and DP-XY samples had the maximum ductility, with elongation more than 2%. Elongations in the FL-XY, HIP-Z, and DP-Z samples ranged from 1 to 1.5%. The FL-Z samples had the lowest ductility, with less than 1% elongation and negligible plastic deformation [196].

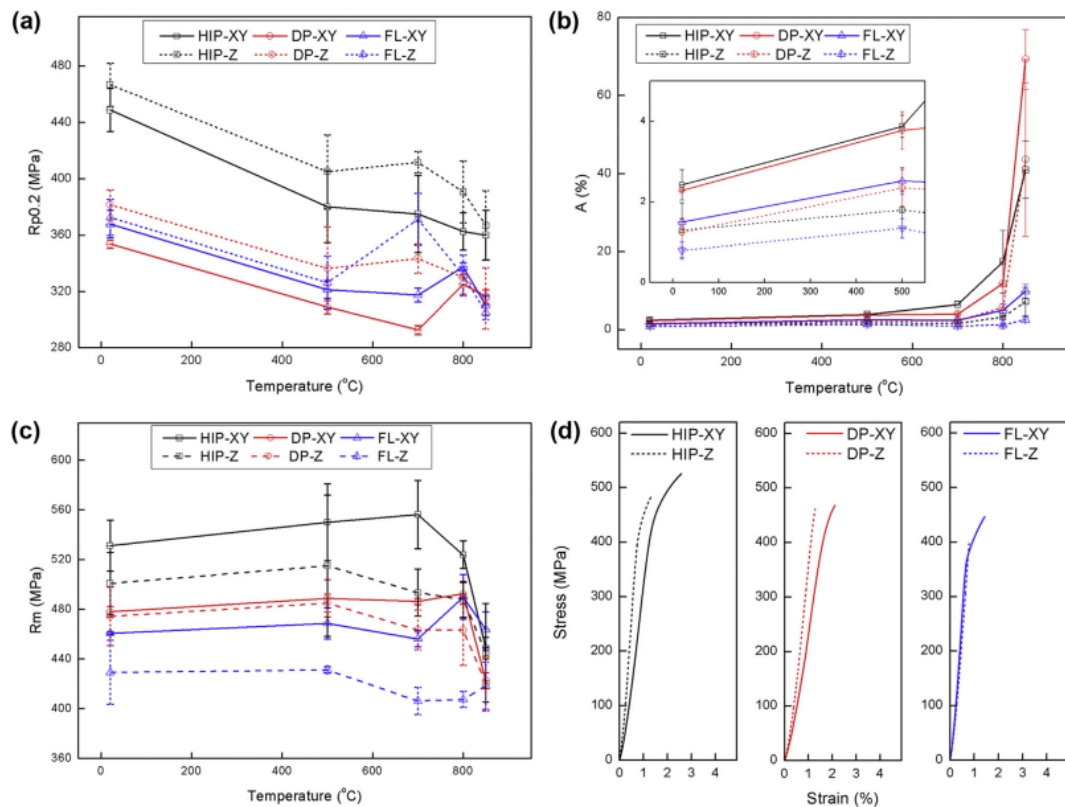


Figure 2.48: Tensile test results of PBF-EB manufactured Ti48Al2Cr2Nb alloy subjected to HIP and heat treatment; (a) yield strength, (b) elongation, (c) UTS and (d) stress-strain curves [196].

2.5 Insights into Electron Beam Powder Bed Fusion Method

2.5.1 History of the Technology

Additive manufacturing (AM) technologies, which have been in use since the early 1990s, were initially used to create models emphasising visual aesthetics and prototypes to visually check the fit and operation of parts. Previously used to assure visual coherence in tool/mold production and prototype manufacturing, these technologies have now turned their attention to direct part manufacturing across a variety of industries [163].

Direct part production within AM has undergone significant changes since the 2000s, constituting approximately 60% of the total layered manufacturing as of today [163]. Since the 2000s, direct part production within additive manufacturing has seen considerable changes, accounting for around 60% of overall layered manufacturing today [163]. The rising interest in this technology domain by the aviation industry has contributed to the quicker uptake of AM technologies in an industrial environment. GE's acquisition of Morris Technologies and Rapid Quality Manufacturing in 2012 was critical in accelerating AM initiatives [163].

Notable breakthroughs demonstrating the importance of layered manufacturing in the field of aircraft engines include the utilisation of Laser Beam Powder Bed Fusion (PBF-LB) for fuel nozzles and Electron Beam Powder Bed Fusion (PBF-EB) for the series manufacture of low-pressure turbine blades in the LEAP engine. These developments demonstrate the expanding significance of additive manufacturing in aviation engines [208]. In addition to these developments, GE demonstrated its commitment to additive manufacturing in 2018 by acquiring Concept Laser, a manufacturer of PBF-LB equipment, and Arcam AB, a previous sole producer of PBF-EB systems [209].

Electron Beam Powder Bed Fusion (PBF-EB) is a successful method among the fusion techniques in powder beds [210]. PBF-EB utilizes a high-energy electron beam to fuse metal powders. This method was developed at Chalmers University of Technology in Sweden, leading to the establishment of ARCAM AB in 1997 [210]. ARCAM AB released its first commercial machine to the market in 2002 and has been listed on the NASDAQ OMX Stockholm since 2012. Acquired starting in 2016 and subsequently integrated into GE Additive in 2018, ARCAM AB, currently dominating the industry, relocated to the Excellence Center in Gothenburg, Sweden, covering an area of 15,000m² in 2019 [211].

Despite ARCAM AB's success with PBF-EB technology, it currently resides in the shadow of the PBF-LB method. As of the end of 2019, Ampower, a metal additive manufacturing consultant, reported a total of 9,111 machines worldwide using the

powder bed melting method [211]. According to the Wohlers Report's examinations between 2018 and 2020, only 6% of systems utilizing powder bed melting (approximately 510 machines) belong to the PBF-EB technology. In other words, for each PBF-EB machine, 16 PBF-LB machines are introduced to the market [212].

While electron beams have been employed in the scientific community for over 120 years, laser technology dates back only 60 years [213]. Arcam AB initiated PBF-EB production in the late 1990s, while the first commercial PBF-LB machine emerged in 1994. Despite a relatively short time gap between the two technologies, the number of companies utilizing electron beams for production remains limited. This circumstance has led to a recent increase in the number of PBF-EB manufacturing companies, indicating their intention to bring the potential of PBF-EB technology to the market through diverse marketing strategies [209].

2.5.2 Application Areas in Aviation Industry

Parts with simple geometry produced through the PBF-EB process may be more expensive for mass production compared to conventional methods; however, it is a competitive manufacturing method for low-volume production [163]. Particularly for customized parts tailored to customer expectations, the PBF-EB process proves to be an effective solution. Additionally, PBF-EB can eliminate the need for assembly for many parts with the ability of geometric consolidation. Regardless of the quantity of parts, they can be produced without the need for molds through PBF-EB. The PBF-EB method is used in a variety of industries, primarily in the aerospace and medical sectors [163].

The cost of components used in aviation is significantly high due to the substantial amount of material that needs to be removed between the final geometry and the pre-processing geometry [214]. It is common in the industry to encounter situations where 90% of the initially used material is machined and removed as chips from

the part. Static components in aviation engines are generally made from cast or forged parts. However, as these parts are not produced close to the final geometry, the buy-to-fly (BTF) ratios are quite high. BTF ratios of 10 and above are considered normal in the aviation engine sector [214]. AM methods play a crucial role in reducing the BTF ratio in the aviation sector, offering significant potential for lower costs and shorter processing times. Using the PBF-EB process, components with BTF ratios approaching 1 can be produced [214].

Many aviation companies use PBF-EB in aircraft engines. Honeywell was the first company to produce aviation components using PBF-EB. They designed and manufactured a novel tube for the Honeywell HTF7000 jet engine from Inconel 718 material Figure 2.49 [215].



Figure 2.49: A tube component redesigned through PBF-EB for the HTF7000 Turbofan engine [215].

Rolls-Royce manufactures front bearing housing from Ti6Al4V material using the PBF-EB method Figure 2.50 [216].



Figure 2.50: A front bearing housing produced by Rolls Royce [216].

CalRAM Inc. utilizes the PBF-EB method to produce various parts for rocket engines, early warning systems, and landing gear from Titanium alloys Figure 2.51 [217].

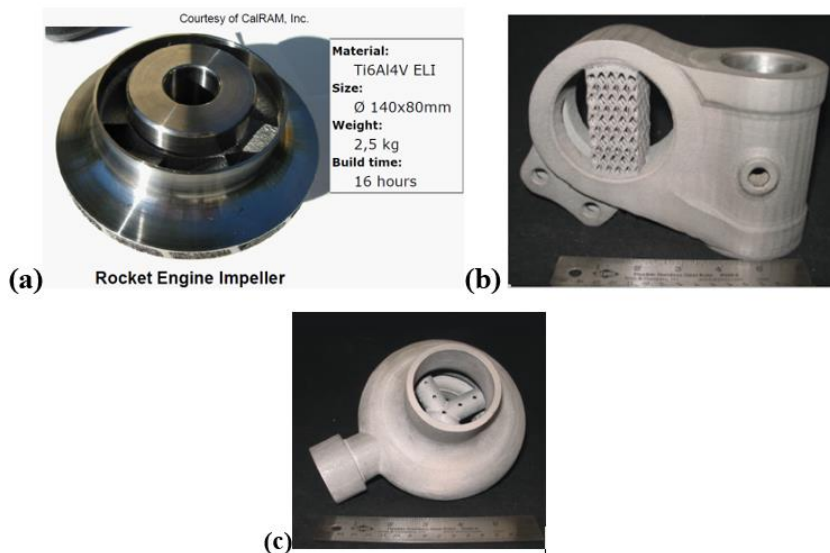


Figure 2.51: (a) A rocket engine impeller, (b) a landing gear hinge, (c) an early warning system mixing part produced by CalRAM Inc. [217].

GE Aviation's subsidiary in Italy, Avio Aero, utilizes this technology to produce low-pressure turbine blades for the GE9X engine using γ -TiAl material Figure 2.52. The company is known to have over 60 machines in its inventory [218].



Figure 2.52: γ -TiAl turbine blades produced by Avio Aero [218].

EADS has produced the motor attachment hinge for the Airbus A320 platform using the Arcam A2X machine and Ti6Al4V material. The company not only replaced the traditional steel material with Ti6Al4V but also applied topology optimization, achieving a weight advantage of over 50% (Figure 2.53) [219].



Figure 2.53: Airbus A320 engine attachment hinge; in the background: geometry produced with traditional methods, in the foreground: geometry produced with PBF-EB and topology optimization [219].

NASA used PBF-EB to develop an Environmental Control and Life Support System (ECLSS) test chamber for CO₂ removal in space stations (Figure 2.54) [220].



Figure 2.54: ELCSS test chamber [220].

The spread of PBF-EB machines has expanded the number of service providers for part production and process development [209]. The FIT Additive Manufacturing

Group, located in Germany, provides services for the production of Titanium alloy parts and secondary processes using Arcam S12, Q10, and Q20 machines. Beamit produces Ti6Al4V parts with the Arcam Q10 machine. At the Fraunhofer Institute for Manufacturing Technology and Advanced Materials IFAM, production is currently carried out with the Arcam A2X machine using Ti6Al4V and CoCr materials. Process development studies are also conducted on aluminum alloys, steel, superalloys, and heat-resistant metals. EWI works on process development and part production with the Arcam A2X machine. Several universities also provide services in part production and process development. The Henry Royce Institute, affiliated with the University of Sheffield, offers services on Titanium alloys using Arcam Q10Plus and Q20Plus machines. The Center for Additive Manufacturing and Logistics at NC State University uses Arcam S12, A2, and Q10 machines for the prototype production of Ti6Al4V parts [209].

2.5.3 Powder Characteristics

In AM, the laser diffraction method is commonly used to measure the particle size distribution of metal powders [221]. In a study conducted by Liu et al., the laser diffraction method is employed to illustrate the particle size distribution of two different metal powders, as shown in Figure 2.55 [221]. Although the powders in this study were used for PBF-LB, the PBF-EB technology, like PBF-LB, is a powder bed layered manufacturing method, so the impact of particle size distribution on fluidity is expected to be similar [221]. The graph in Figure 2.55 indicates that the powder from LPW Technology exhibits a more homogeneous particle size distribution. On the other hand, the Osprey company's powder has relatively smaller powder particles compared to LPW powder. The average particle size of Osprey powder is stated to be 27.5 μm , while the average particle size of LPW powder is 29.3 μm . In AM, different-sized powder particles are desired in the powders used to achieve as high a density as possible in the powder bed for high-density part production. Even a high distribution of small-sized particles allows for

a high-density powder bed, but it leads to increased friction between particles, causing agglomeration and reducing flowability [221]. The Hausner ratio of the Osprey company's powder with smaller particles is higher than that of LPW company's powder, indicating that the flowability of the Osprey powder is worse [221].

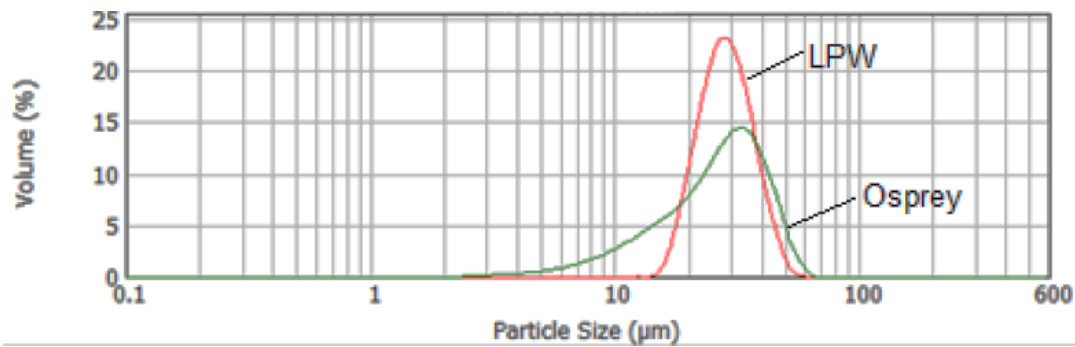


Figure 2.55: The particle size distribution of metal powder for PBF-LB [221].

Stanford et al. investigated the effects of particle size on the flow characteristics of 304 steel plasma spray produced powders [222]. They attempted to determine the powder flowability by measuring the Hall flowmeter and calculating the Hausner ratio. The researchers noted that reducing the particle sizes within led to the formation of more surface area. This increase in surface area reduces powder flowability by increasing interparticle cohesive forces and frictional forces. It was suggested that the ratio of the total surface area of a powder particle to the powder volume in a powder particle could be used to determine flowability. A higher value of this ratio also indicates poor powder flowability [222].

To evaluate the shapes of metal powder particles used in AM, microstructure images are captured using optical microscopy and scanning electron microscopy. Upon examining these images, it can be determined whether the metal powders have spherical, irregular/angular, satellite, and porous morphologies [223]. In the literature review conducted by Yang et al., it was generally understood that

spherical particles flow more than non-spherical ones, and larger-sized particles exhibit easier flowability compared to smaller-sized ones [223]. The study also mentioned that electrostatic forces between particles, as well as temperature and humidity, affect flowability. Humidity influences the charging of powder particles [223]. Schueren et al. noted that the flowability of the powder changes depending on the friction between powder particles. Therefore, it is understood that spherical particles, due to their smaller contact areas, create less friction and, consequently, have higher flowability [224].

Galati and Iuliano reported that four conditions arise as a result of the interaction between electron beams and powders: splashing of powder particles, sintering of powders, melting of powders, and partial melting of some alloying elements [226]. Figure 2.56 shows the splashing of powders at different deposition times in the PBF-EB process [227]. The splashing of powders is caused by the evaporation of moisture in the powders, momentum transfer from electrons to powders, and the negative charging of powders, causing them to repel each other [227], [228]. Moisture in the powders is minimized through gas atomization powder production and preheating in PBF-EB, while preventing momentum transfer can only be achieved by using large-sized powders [253]. Additionally, during sintering, the heating of powders and the wetting of powders by the molten metal can reduce splashing [226].

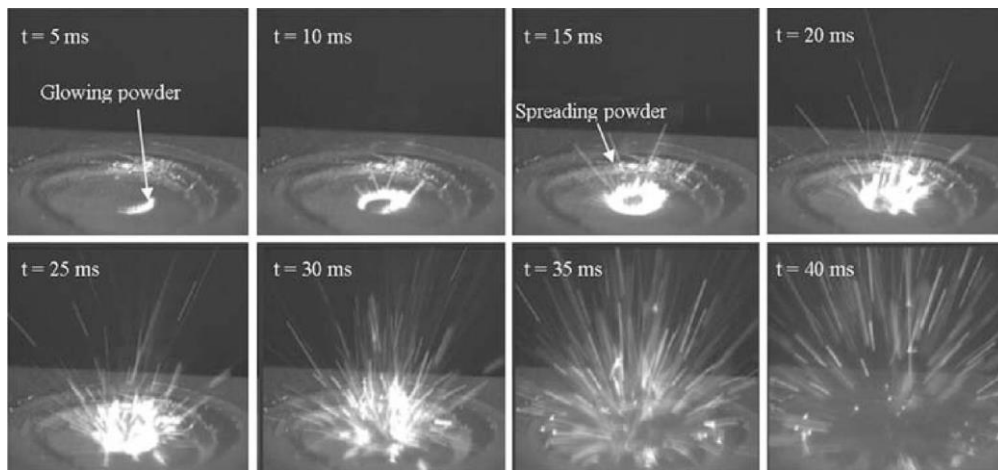


Figure 2.56: The time-dependent powder spattering behaviors [227].

Rafi et al. conducted a study comparing the differences between Ti6Al4V parts produced using PBF-LB and PBF-EB Technologies [230]. In this study, EOS powders were used for PBF-LB, and Arcam powders were used for PBF-EB. The average size of the PBF-LB powders, as seen in Figure 2.57, is $36\ \mu\text{m}$, while the PBF-EB powders are $60\ \mu\text{m}$. Additionally, in Figure 2.57 (c) and (d), it can be observed that PBF-LB powders have a broader size distribution, and some agglomeration is present in these powders. The publication does not provide information about the production technology of the powders used in this study [230].

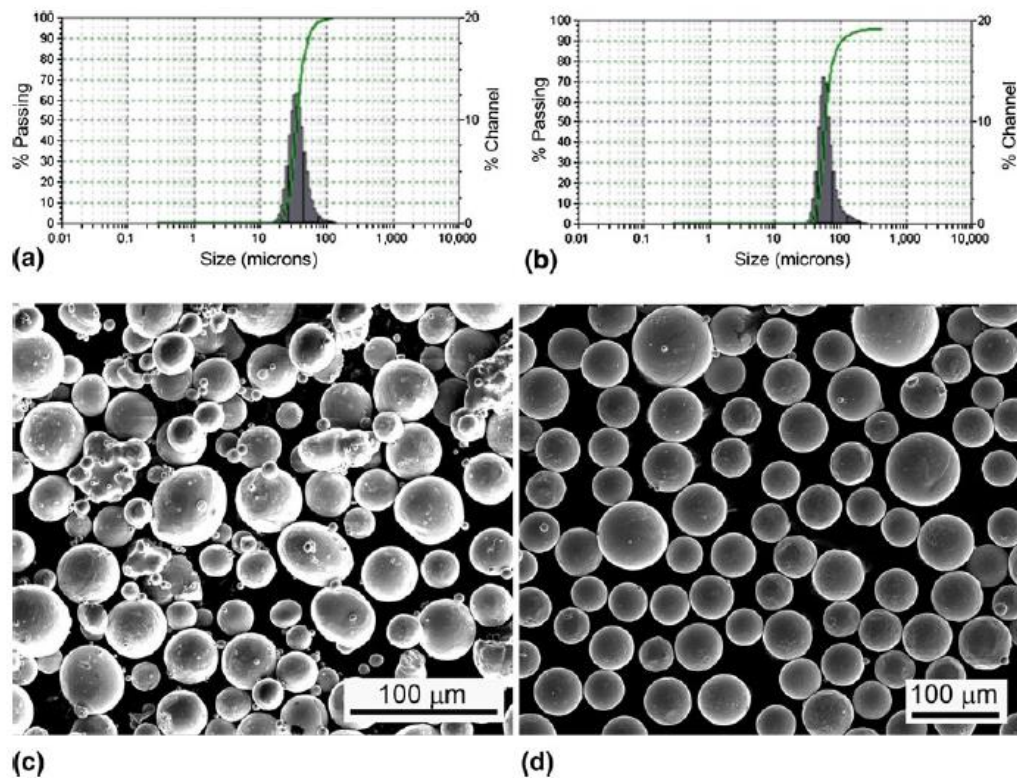


Figure 2.57: (a) Particle size distribution of EOS Ti6Al4V powder, (b) particle size distribution of Arcam Ti6Al4V powder, (c) SEM images of EOS Ti6Al4V powder, (d) SEM images of Arcam Ti6Al4V powder [230].

Körner reported that PBF-EB technology typically uses powders produced through gas atomization. Recommended powder sizes were indicated to range between 40 and 105 μm . Deviating from these sizes adversely affects the spreadability [253]. Gong et al. emphasized in their study that Ti6Al4V powders used for PBF-EB are generally produced through gas atomization, with powder particle diameters ranging from 45 to 100 μm [220]. According to Körner, as the powder size decreases, friction between particles will increase, and consequently, flow properties will be adversely affected [253]. The study also noted that powders produced using the plasma rotating electrode process (PREP) are more spherical with less agglomeration, indicating better flow properties. Figure 2.58 (a) shows the particle size distribution of CMSX-4 powders produced by gas atomization, and

Figure 2.58 (b) displays Ti6Al4V powders, where high agglomeration is noted for the powders in Figure 2.58 (b) [253].

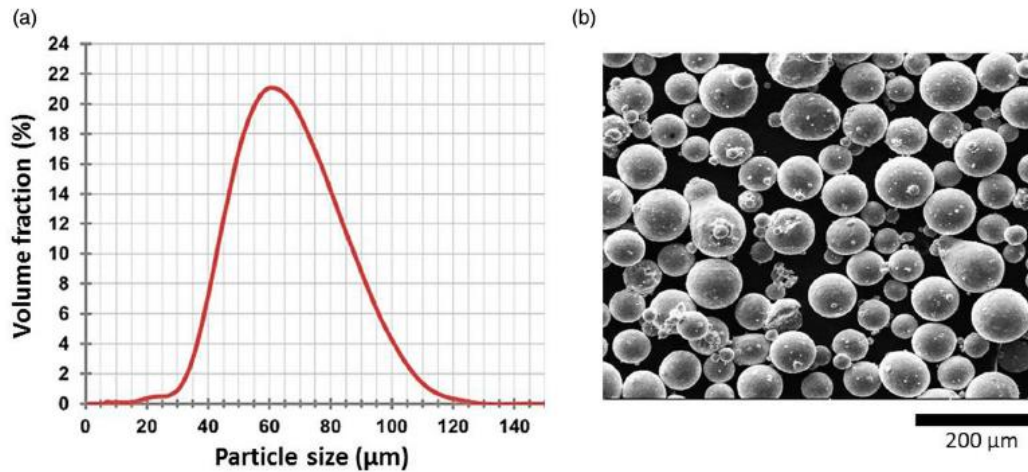


Figure 2.58: (a) Particle size distribution of CMSX-4 powder produced by gas atomization, (b) SEM image of Ti6Al4V powder produced by gas atomization [253].

Strondl et al. conducted a study comparing the particle size, shape, and flow characteristics of gas-atomized powders for PBF-LB and PBF-EB [231]. In this study, Inconel 718 powder was used for PBF-LB, and Ti6Al4V powder was used for PBF-EB. Figure 2.59 illustrates the sizes of PBF-LB and PBF-EB powder particles. The average sizes of PBF-LB and PBF-EB powders were calculated to be approximately 30 μm and 60 μm, respectively [231].

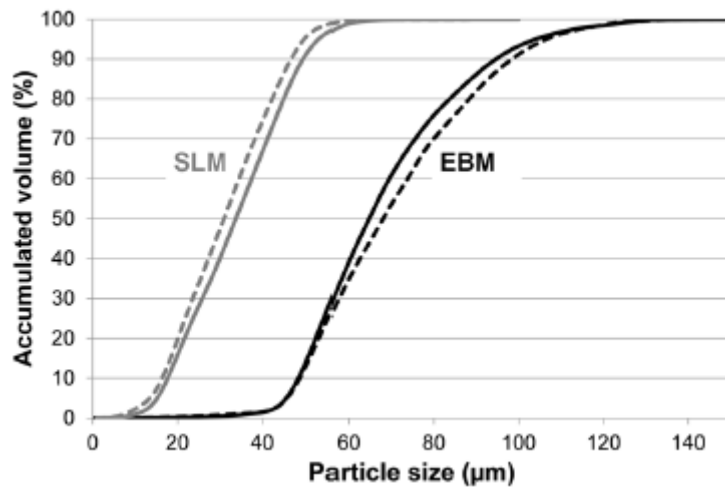


Figure 2.59: Particle size distributions. Dashed lines = new powder, solid line = recycled powder [231].

In another study comparing Inconel 718 powders, it was reported that the flowability of powders produced by PREP was significantly superior to those produced by gas atomization [232]. As illustrated in Figure 2.60, the reasons given for the worse flowability of powders generated by gas atomization were intra-particle porosity and poorer spherical shape. Furthermore, when PREP particles were employed, it was discovered that the melt pool in the powder bed was wider, resulting in slower cooling. This lowers the material's internal stresses, resulting in a more stable microstructure [232].

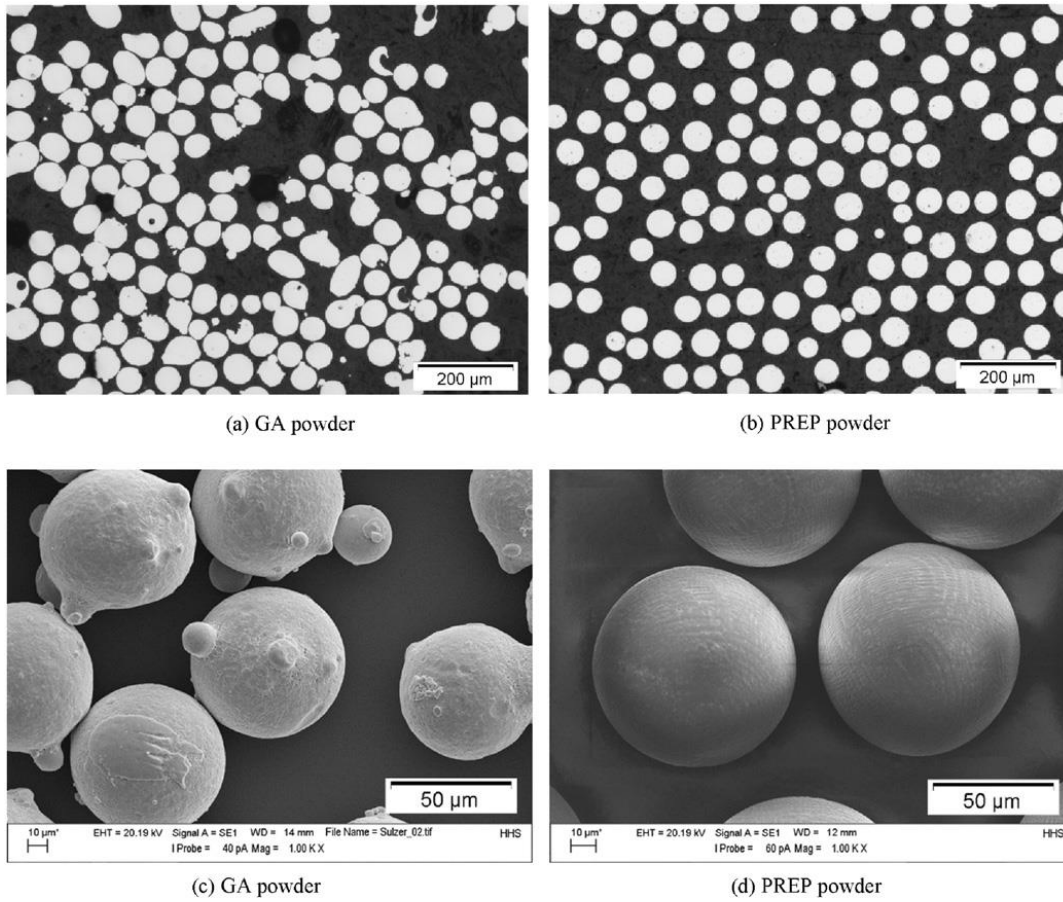


Figure 2.60: SEM images of Inconel 718 produced by; (a), (c) gas atomization and (b), (d) PREP [232].

The SEM images and particle size of the TiAl powders used by Biamino et al. is shown in Figure 2.61. The TiAl powders exhibit a larger size distribution (45 to 150 μm) compared to Inconel 718 and Ti6Al4V powders [232].

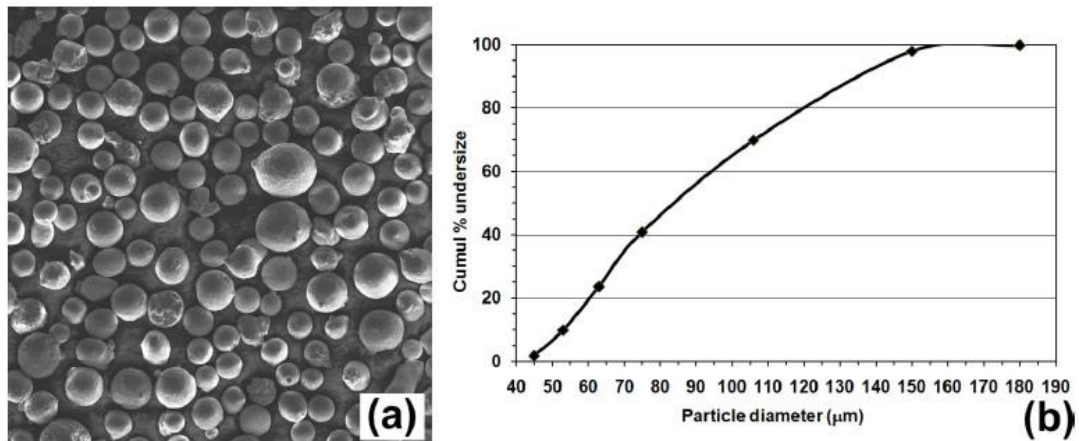


Figure 2.61: TiAl powders used in PBF-EB; (a) SEM image, (b) particle sizes [232].

In this section, criteria for the powders used in the PBF-EB method, is examined. The nature of the powders used in the PBF-EB method is crucial as it affects various properties, ranging from the density of the parts to be produced to their mechanical characteristics. Powders that can fill the powder bed and exhibit good flowability are preferred in PBF-EB technology. Accordingly, powders that are spherical, free from agglomeration, without pores, and with a specific particle size distribution should be used. In particular, the flowability of spherical powders is better than that of non-spherical powders. Moreover, the particle size distribution of metal powders should have a Gaussian curve. Among the various atomization methods, those involving gas and plasma particle production are more effective in obtaining spherical powders compared to water atomization. Additionally, these methods are generally more cost-effective than newer production methods such as PREP. However, according to many studies in the literature, it is possible to obtain spherical powders without agglomeration and pores using PREP, making it a prominent production method for PBF-EB technology. While various results exist regarding powder particle size, the literature generally suggests an optimal powder particle size in the range of 60-80 μm for PBF-EB, considering an average layer thickness varies between 50-150 μm.

2.5.4 Fundamentals of the Process

In the PBF-EB method, a focused electron beam scans over a pre-deposited thin layer of metal powder, inducing localized melting and subsequent solidification [163]. In PBF-EB technology, when a high voltage is applied to a material used as the cathode (filament, crystal, etc.), electron beams scatter toward the anode. Following the anode, electron beams pass through ion trap and drift tube apparatuses, forming a beam through electromagnetic coils. These are respectively named astigmatism lens, focusing lens, and deflection lens. A PBF-EB system is schematically shown in Figure 2.62 [233]. Due to the rapid response of electromagnetic coils to machine parameters, the electron beam can scan rapidly or slowly. Due to its inherent nature, an electron beam can be moved swiftly from one point to another without the need to scan the intervening space, allowing for rapid movement [163].

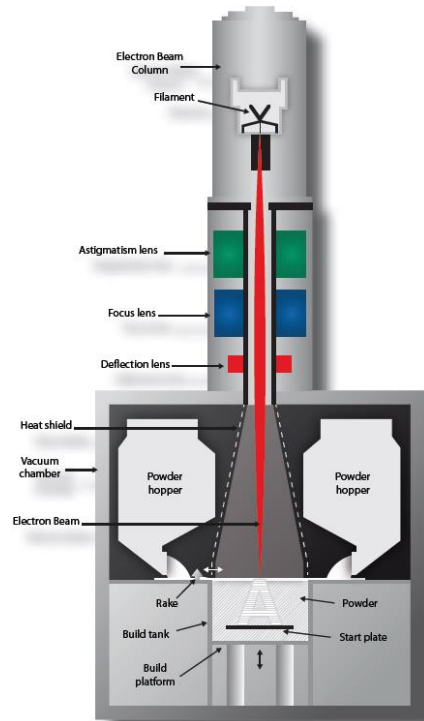


Figure 2.62: Schematic of a PBF-EB system [233].

The electron beam reflects as it passes through a gas, hence this procedure must be carried out under low pressure in a vacuum atmosphere [234]. It is possible to produce extremely reactive compounds like titanium without oxidation by using this vacuum-operated technique. The heating and melting of powder particles are achievable through the transfer of kinetic energy from electrons [235]. However, when powder particles interact with electrons, their negative charges increase. If the electrical conduction in the powder bed is poor, negatively charged powder particles repel each other, leading to the formation of a powder cloud (smoking). Additionally, the increased negative charge repels incoming electrons in the opposite direction, resulting in a more dispersed, broadened focal point [235]. To mitigate such process-related difficulties, the powders are preheated in two steps. Heated powders are sintered, allowing them to come into contact with one another [236], [237]. As a result, improved electrical conduction aids the dispersion of electron beams onto the powders, preventing negatively charged particles from being repelled. The powder bed in the PBF-EB technique must be conductive, limiting its use to materials that conduct electricity [236], [237].

In the PBF-EB method, the build platform and powder particles are rapidly heated by focusing electron beams [238]. The electron beam rapidly scans the entire surface of the powder bed, heating it quickly and uniformly to the desired temperature. Therefore, during the preheating process, the temperature of the powder bed is increased without the use of any resistance-based heaters. The elevated temperature of the powder bed allows for the production of materials with a risk of micro-crack formation [252]. Additionally, the loose structures of the heated powders are disrupted and sintered. As a result, a sintered layer is formed on the production platform [238]. The amount of support material required during production is minimal due to the high temperature and sintered nature of the powders. Maintaining the powder bed at a high temperature results in significantly reduced residual stress in parts produced by PBF-EB systems. Consequently, there is no need for a stress-relief heat treatment for components manufactured using PBF-EB [252].

Due to the process characteristics mentioned above, productions using PBF-EB technology exhibit some differences compared to those using laser systems. In laser methods, scanning is achieved by adjusting the direction of mirrors, while in PBF-EB, the instantaneous positioning of the beam over the entire production platform is facilitated through electromagnetic coils [239]. This allows PBF-EB to create multiple melt pools simultaneously, enabling much faster production compared to laser systems [239]. Although PBF-EB machines may appear disadvantageous for the production of large parts due to their smaller size compared to laser systems, the vacuum requirements of PBF-EB machines, along with the natural support provided by sintered powders, allow for filling the entire build volume with parts stacked on top of each other. Consequently, the unit cost per part for PBF-EB can be significantly lower [240].

The high energies of electron beams heat the surrounding powder particles more than laser beams do [240]. Therefore, compared to the PBF method with a laser, a deeper and wider melt pool is obtained, as seen in Figure 2.63 [209]. While this situation entails some advantages such as high energy density and production efficiency, the minimum geometric feature size, resolution, and surface quality achievable with PBF-EB are limited compared to laser systems [241]. Although it is possible to reduce the melt pool size with scanning strategies, the PBF-EB method lags behind laser methods in this regard [242]. Additionally, while it is possible to enhance the quality of parts produced using small-diameter powders and low layer thickness, as the diameter of the powders decreases, negatively charged powder particles are more likely to resist gravity and frictional forces and fly away due to electron beams. Despite efforts to reduce the diameters of PBF-EB powders and improve surface quality, larger-diameter powders are currently preferred in practice [240].

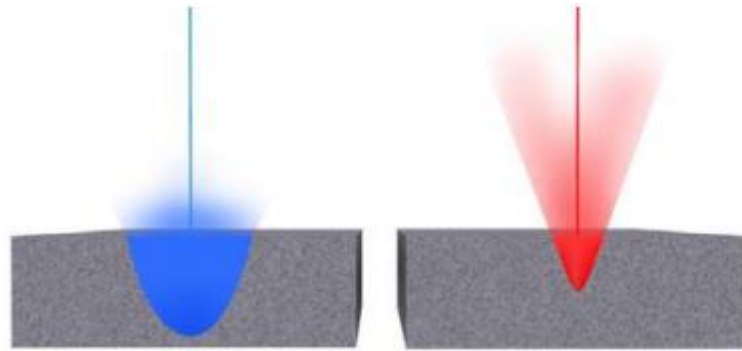


Figure 2.63: Melt pool width and shape in; (left) PBF-EB, (right) PBF-EB [209].

The line energy E_L according to Equation (1.2) is frequently used to quantify the process energy input in the PBF-EB process:

$$E_L = \frac{U \cdot I_{\text{beam}}}{V_{\text{scan}}} = \frac{P}{V_{\text{scan}}} = \frac{J}{\text{mm}} \quad (1.2)$$

The acceleration voltage is represented by U , while the beam current is represented by I_{beam} , the beam power is represented by P , and the scan velocity is represented by V_{scan} . In the Arcam A2X machine, the U value is 60 kV [197], [243].

The area energy E_A is mainly used to define the energy input per scanned area as given in Equation (1.3):

$$E_A = \frac{U \cdot I_{\text{beam}}}{V_{\text{scan}} \cdot l_{\text{offset}}} = \frac{E_L}{l_{\text{offset}}} = \frac{J}{\text{mm}^2} \quad (1.3)$$

The line offset (l_{offset}) is defined as the distance between adjacent hatch lines [244].

An alternative commonly employed measure for describing process energy input is the volumetric energy density E_V as given in Equation (1.4):

$$E_V = \frac{U \cdot I_{\text{beam}}}{V_{\text{scan}} \cdot l_{\text{offset}} \cdot t} = \frac{E_A}{t} = \frac{J}{\text{mm}^3} \quad (1.4)$$

The layer thickness (t) is the measure of the distance for each layer from the previously scanned layer [244].

Higher E_V was observed to correlate with decreased part porosity [245], [246]. Insufficient energy density typically leads to small melt pool dimensions and low temperatures [247], [248], causing unmelted powder particles [249] and lack-of-fusion defects [197] between layers. Conversely, excessive energy input is known to induce melt pool instabilities and swelling [247], [248].

The beam return time (t_R) is the time required for the electron beam to return to the same position in the adjacent line, as determined by Equation (1.5) [250]:

$$t_R = \frac{L}{V_{scan}} \quad (1.5)$$

Furthermore, scan velocity and line offset determines the lateral velocity (V_{lat}), which is defined as the velocity of the melt pool perpendicular to the scan direction, as calculated in Equation (1.6) [251].

$$V_{lat} = \frac{V_{scan} * l_{offset}}{L} = \frac{l_{offset}}{t_R} \quad (1.6)$$

As a result, these data strongly suggest that E_L or E_V individually cannot be used to predict or control process conditions and microstructure evolution in PBF-EB [252].

2.5.5 Effects of the Process Variables on Part Quality

Figure 2.64 provides a schematic representation of the PBF-EB process [253]. The system generally obtains information for the process from the CAD data of the product, which is typically separated into layers with a constant layer thickness [253]. The process is conducted at a pressure of approximately 10^{-3} mbar. Helium gas is employed to regulate the vacuum. Additionally, helium is used to prevent electrostatic charging and powder dispersion. In the Arcam A2X device, electrons emitted from the tungsten cathode are accelerated to 60 keV and directed by electromagnetic lenses. The beam current ranges from 1 to 50 mA, and the beam power can reach a maximum of 3 kW. The process cycle for each layer consists of

four steps, as illustrated in Figure 2.65 [253]. To expedite the cooling at the end of production, helium is passed through the build chamber [253].

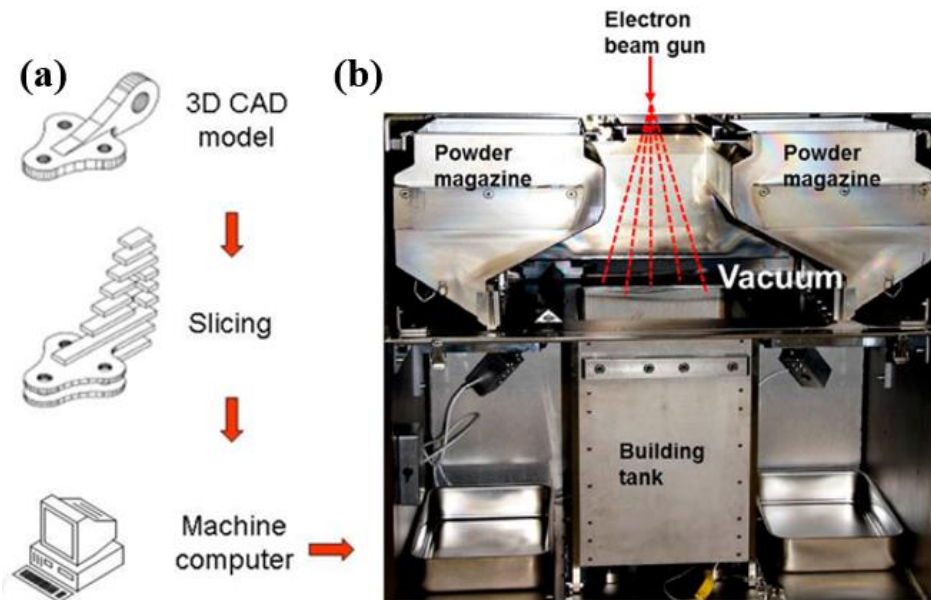


Figure 2.64: (a) Part production cycle and (b) Arcam A2X process chamber [253].

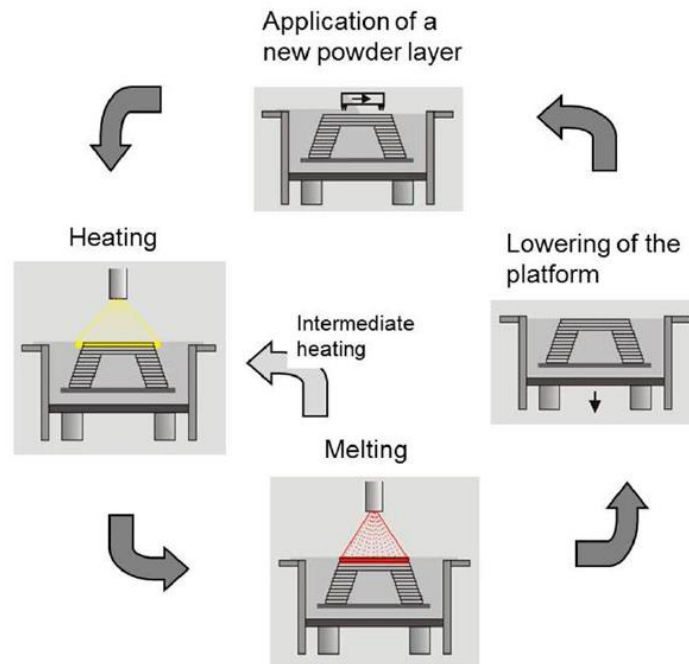


Figure 2.65: Steps involved in producing a layer in PBF-EB [253].

2.5.5.1 Powder Bed Pre-Heating

A layer of powder with a thickness between 50-150 μm is spread onto the preheated platform as a first step of the process cycle. During the preheating stage, the defocused electron beam scans the powder at high scanning speeds for several times [254]. Preheating prevents the powder from flying in a vacuum environment and, to some extent, leads to sintering. This approach reduces residual stresses and promotes better mechanical properties by minimizing temperature differences during production times [254]. Additionally, the melting of smaller-sized particles contributes to an additional bonding mechanism. The preheating temperature, speed, and strategy may vary depending on the powder material properties [220], [255].

2.5.5.2 Powder Flowability

The ratio of apparent density to tap density defines the flowability of the powder. This ratio is known as the Hausner ratio, and it is expected to be as close to "1". Powders produced by the gas atomization process are typically predicted to have diameters ranging from 40 to 105 μm [253].

In a study investigating the repeated use of Ti6Al4V powder after the process, the oxygen weight ratio within the powder increased from 0.08% to 0.19% after 21 uses, leading to increased tensile strength [27]. There was just a minor decrease in aluminum and vanadium contents. It was noticed that the powder lost its spherical shape, a few satellite particles formed after the 11th use, and most particles experienced collisions after the 16th use. The flowability of the powder increased with the number of uses due to the reduction in satellite particles, loss of moisture in particles exposed to vacuum and high temperatures. Smoke formation during production was also eliminated. The reuse of the powder did not result in any undesirable effects on the parts such as surface deviation, distortion, etc [27].

2.5.5.3 Layer Thickness

Layer thickness effects the dimensional accuracy of the part [27]. Increasing the layer thickness results in an increased stair-step effect and, consequently, surface roughness. Additionally, when the layer thickness is increased, the capacity to melt the previous layer decreases, leading to bonding issues between the layers as shown in Figure 2.66 [27].

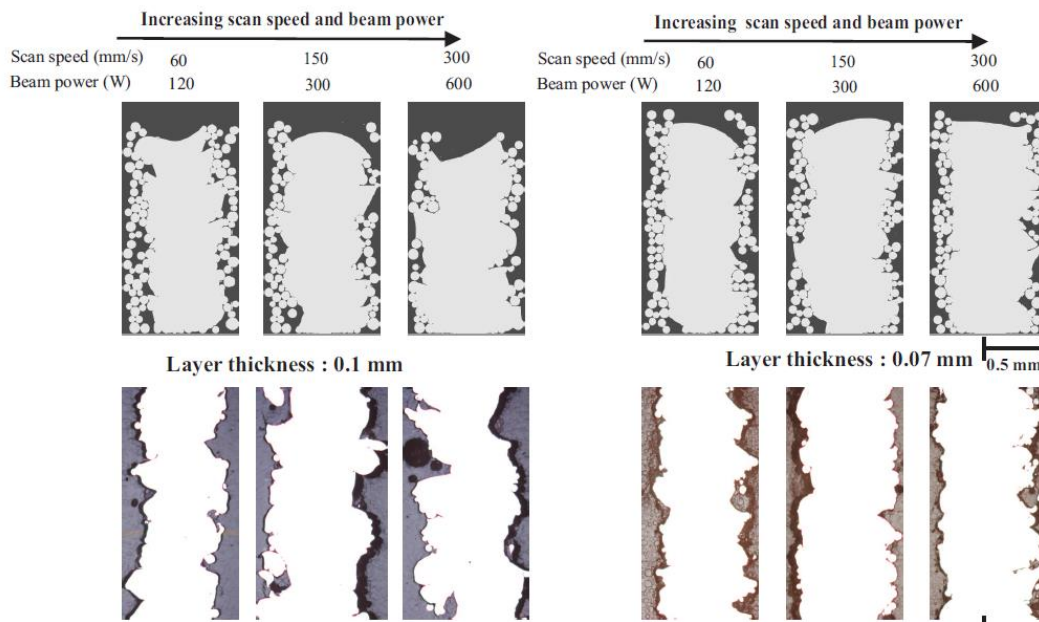


Figure 2.66: The effect of increasing scanning speed and beam power on the production of Ti6Al4V material with different layer thicknesses [27].

In a study conducted by Karlsson on Ti6Al4V, the effects of different powder particle sizes and layer thicknesses on the parts were investigated [27]. In this context, productions with two different powder sizes and two different layer thicknesses were carried out. The results of the study showed that the surface roughness was higher when using smaller powder particles. This was attributed to a higher number of sintered particles adhering to the surface in samples produced with smaller powder. On the other hand, as shown in Figure 2.67, the melted surface beneath the powder particles appeared less undulated and smoother [27]. Variation in layer thickness were found to have a low impact on surface roughness. This was attributed to the energy input being sufficient to melt the material and the layers beneath within the chosen layer thickness range, thus eliminating the need for re-melting the layers. Furthermore, within the selected parameter range, there was no statistically significant difference in the elastic moduli and hardness values of the produced samples [27].

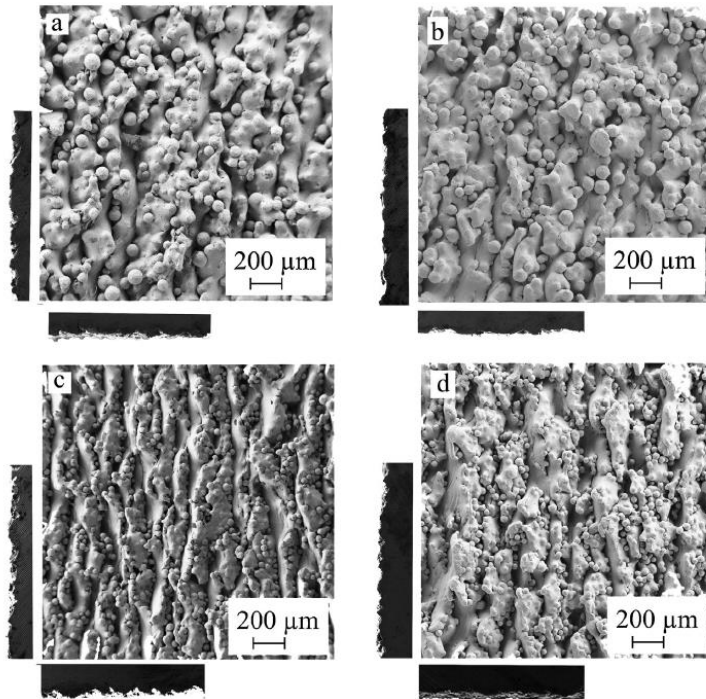


Figure 2.67: SEM surface images of samples produced with different powder sizes and layer thicknesses; a) 45 - 100 μm powder size distribution and 70 μm layer thickness, b) 45 - 100 μm powder size distribution and 50 μm layer thickness, c) 25 - 45 μm powder size distribution and 70 μm layer thickness, d) 25 - 45 μm powder size distribution and 50 μm layer thickness [27].

2.5.5.4 Hatch and Contour Scanning Strategy

In the Arcam A2X machine, after preheating, the electron beam scans the powder at speeds up to 8000 m/s, melting the powder particles. As shown in Figure 2.68, the melting stage is divided into hatch and contour scanning. In the hatch scanning, the beam direction changes 90° in each scanning line and layer. The system enables melting up to 100 points simultaneously by passing the electron beam [253].

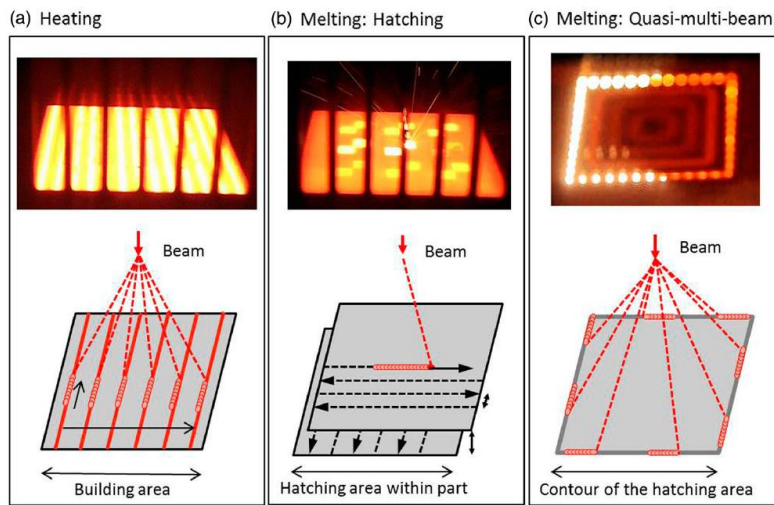


Figure 2.68: PBF-EB heating and melting stages of; (a) preheating (b) melting: Hatch scanning, (c) melting: Contour scanning with multiple beams [253].

In the PBF-EB contouring stage, there are two strategies: single-beam (Non-multispot) and multi-beam (Multispot-Multibeam) [27]. With the single-beam strategy, contouring creates a continuous melting pool that progresses around the frame of the part. The scanning speed of the beam is calculated with a speed function algorithm, considering the beam current, defocus, and speed function effects. When using multiple beams, several melting pools are active simultaneously, making it faster due to the absence of movement during the progression [27].

In multi-beam contouring, in Figure 2.69 (b), since there is less movement of the beam, it is faster than single-beam contouring [27]. Multi-beam contouring creates layer contours by dividing them into shorter segments, focusing on the outer edges of the part. After each focus, it sequentially focuses on the next section almost simultaneously. Various parameters in this method include the number of focuses, focusing time, overlap of focuses (in mm), contouring beam current (in mA), and defocus of the beam (in mA) [27].

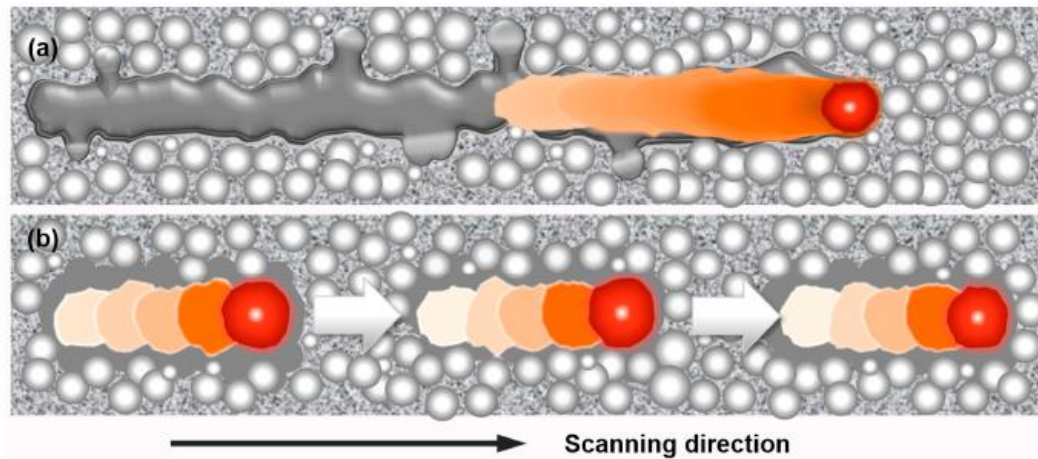


Figure 2.69: (a) Single-beam and (b) multi-beam illustration. Arrows indicate the scanning direction [27].

Williams discovered that when the scanning speed and scanning distance were both reduced on the Arcam S12 using Ti6Al4V material, the pore size decreased [27]. Additionally, in Figure 2.70, it is evident that changes in machine scanning settings affect pore ratio and distribution [27]. The Arcam standard scanning method is performed with two fundamental parameters. The defined two-dimensional boundaries of the geometry are first traced using the contour scanning parameter. Subsequently, the region between contours is filled in a zigzag pattern through the part's internal scanning method. Irregular pores are observed towards the parts where contour scanning has been done, and this irregularity may be attributed to the Arcam Multibeam feature, causing an imbalance due to the simultaneous activation of numerous melt pools [27].

In the same study, the effects of energy density on porosity were also investigated [27]. Increasing energy density leads to the formation of larger and deeper melt pools, allowing trapped gas bubbles to escape through repeated melting in the interpass areas and reducing pore formation. Energy density can be increased by increasing the beam power, reducing the line offset, or decreasing the scanning speed. The individual effects of these parameters may vary; for example, reducing

the scanning speed is more effective on porosity compared to reducing the line offset [27].

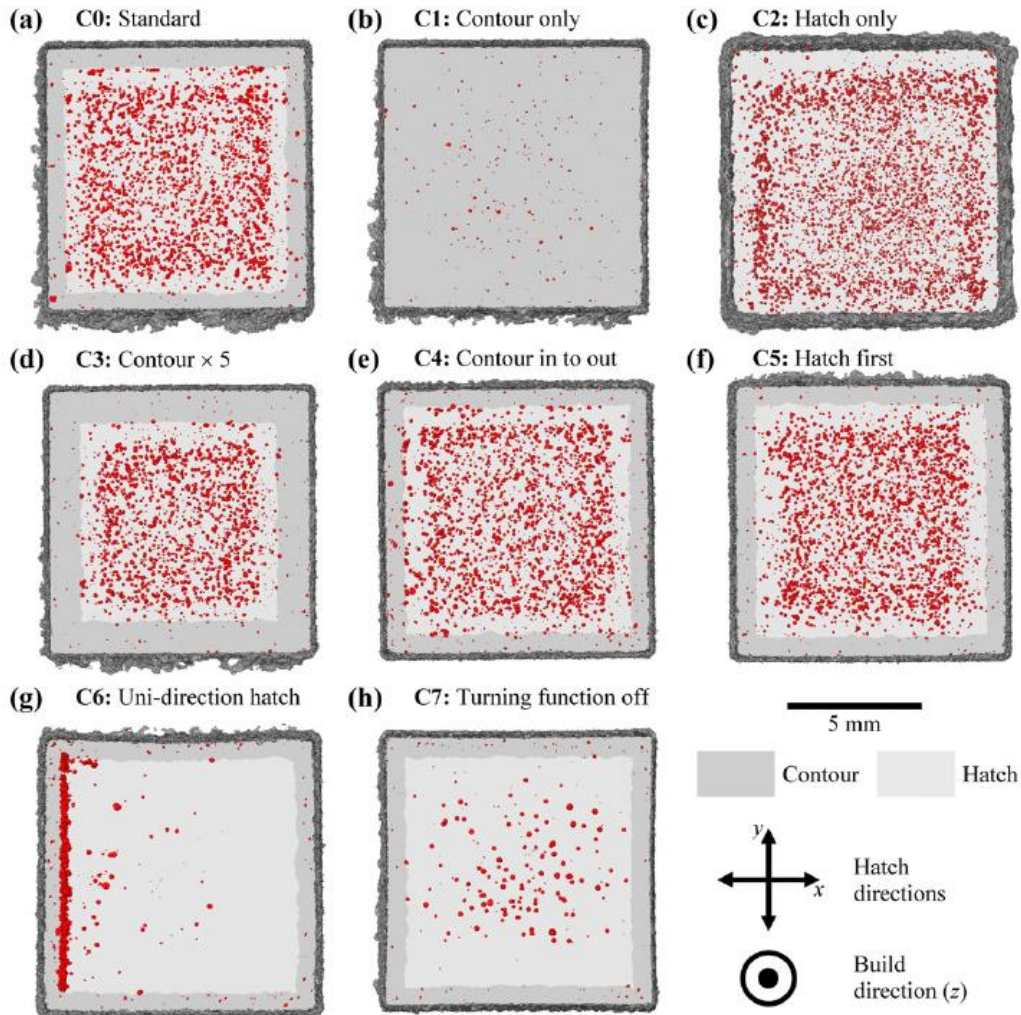


Figure 2.70: Pore densities and distributions obtained through 3D XCT scanning in different process modes (coded as C0-C7) [27].

The production of support structures at different angles and diameters was examined under different parameters [27]. As presented in Figure 2.71, when contour scanning is not performed, the production capability of geometric elements in the part is lower [27]. Additionally, as shown in Figure 2.72, when the build

angle is high and contour scanning is not performed, and the energy density is reduced, dimensional error rates decrease due to the thermal insulating properties of the powder [27]. It has been observed that in structures with a larger diameter (diameter 10 mm, compared to 2 mm), the error rate is lower. For negative angled structures, although reducing energy density yields better dimensional results, it leads to an increase in the number and sizes of pores. These pores can be eliminated through the HIP process [27].

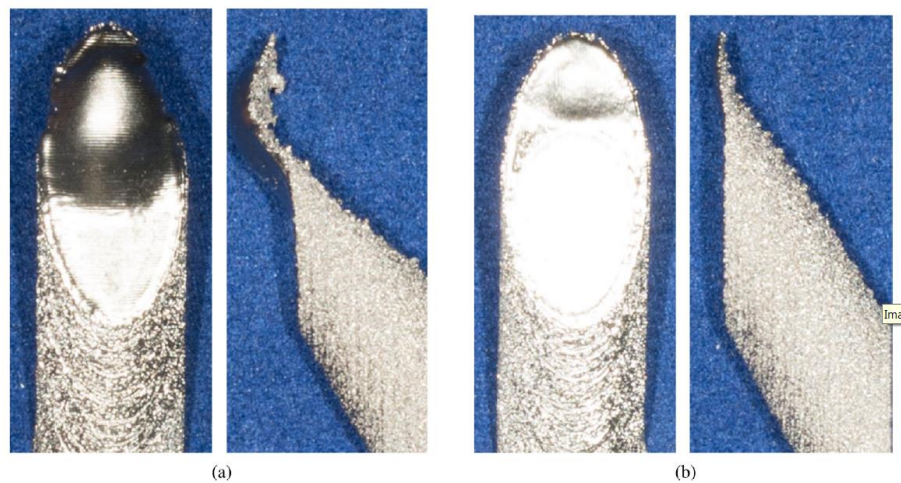


Figure 2.71: Support structures; a) without contour scanning and b) when contour scanning is enabled [27].

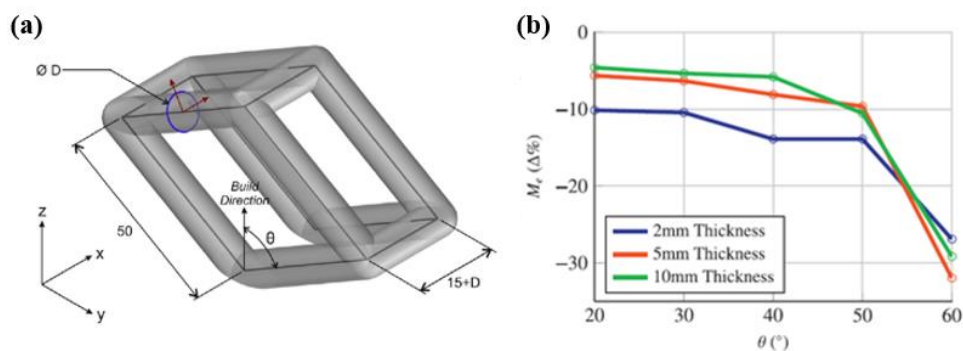


Figure 2.72: a) Support structure example and (b) error rate between the model and the produced part according to the part thickness [27].

Scanning strategy also affects surface roughness. In Figure 2.73, three-dimensional surface examples taken for single-beam and multi-beam strategies are shown [259]. The color variation indicates the peaks and valleys on the surface. A worse surface is obtained with multi-beam at the same process parameters. However, while the multi-beam strategy causes high surface roughness, it simultaneously improves geometric accuracy. Surface roughness can be reduced by increasing the number of active and overlapping spots. In the single-beam strategy, the anisotropic surface structure is formed due to the large melt pool. Surface roughness is 30% higher in the direction perpendicular to the production than in the horizontal direction [259].

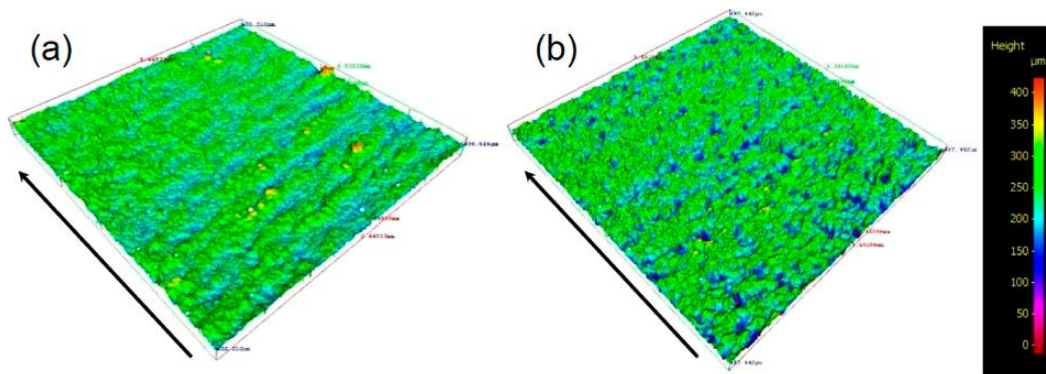


Figure 2.73: Three-dimensional surface measurement of parts produced with; (a) single beam and (b) multi-beam strategies under the same parameters. The arrow direction indicates the production direction [259].

Process parameters can cause significant variations in the microstructure and mechanical properties of a part [27], [253]. The grain structure, texture and size of the same material can be altered with different parameters. As shown in Figure 2.74, increasing the scanning speed for Ti6Al4V leads to an increase in the cooling and solidification rate, resulting in a reduction in the thickness of acicular α plates [27].

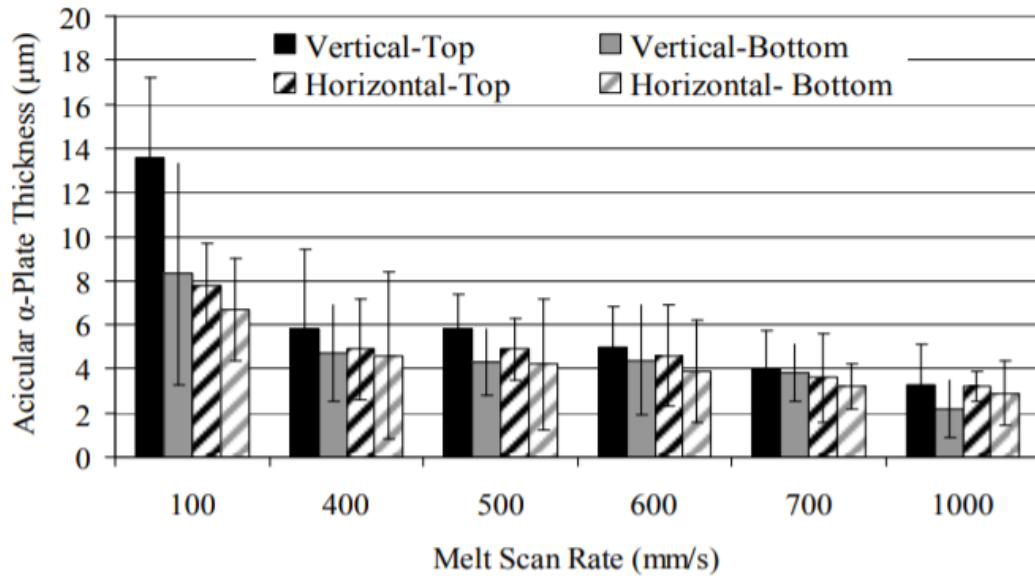


Figure 2.74: The change in the thickness of acicular α plates with scan rate [27].

The thickness of α lamellae increased with the increase in energy density in Ti6Al4V. This resulted in an increase in tensile and yield strength (Figure 2.75) [253]. In another study, an increase in scanning speed led to a faster cooling rate, resulting in a decrease in columnar structure and the presence of fine α phase particles [27].

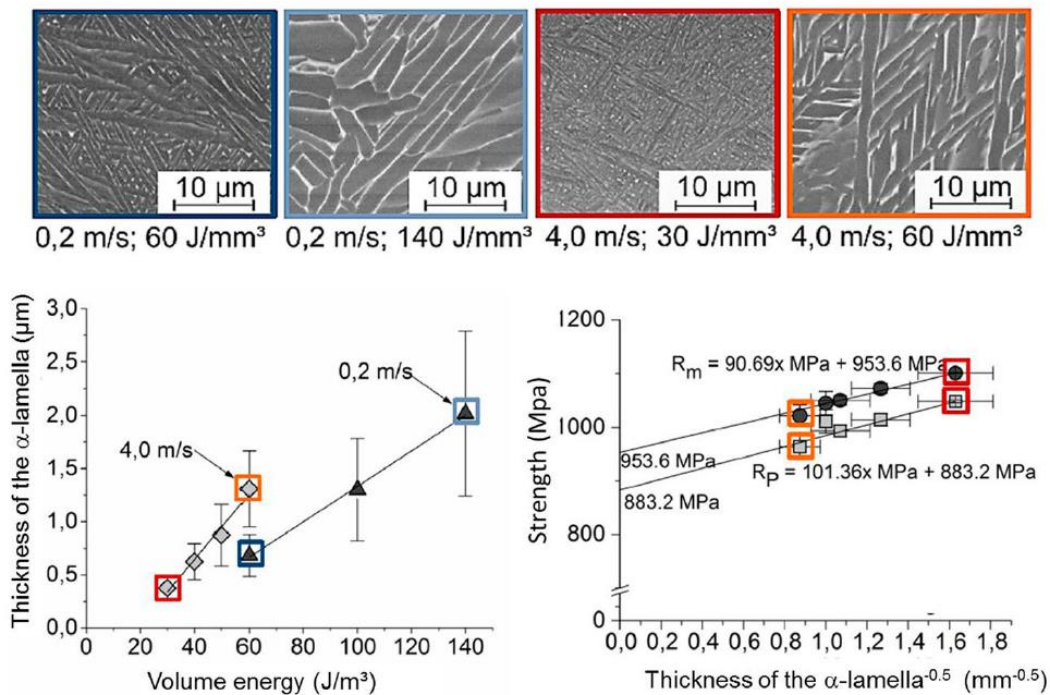


Figure 2.75: The variation in α -lamella thickness with energy input for Ti6Al4V material [253].

Decreasing scan speed increases the heat input per unit area [262]. This leads to the enlargement of the melting pool and deformation. However, excessively increasing the scan speed may result in the inability to melt the powder and the formation of unmelted powder pools within the part [262]. In a study conducted with Ti6Al4V-ELI, it was observed that as the scan speed increased, production closer to part tolerances was achieved [27]. For the PBF-EB process, a 60 kV acceleration voltage, 5 mA current, 100 μm scan distance, and 50 μm layer thickness were used. Scan speeds of 0.1, 0.5, 1, 1.5, 2, and 3000 mm/s were tested. Figure 2.76 shows images of the produced samples from different observation directions. In these images, the deformation caused by the increased heat input due to the reduced scan speed is clearly visible on the first sample [27].

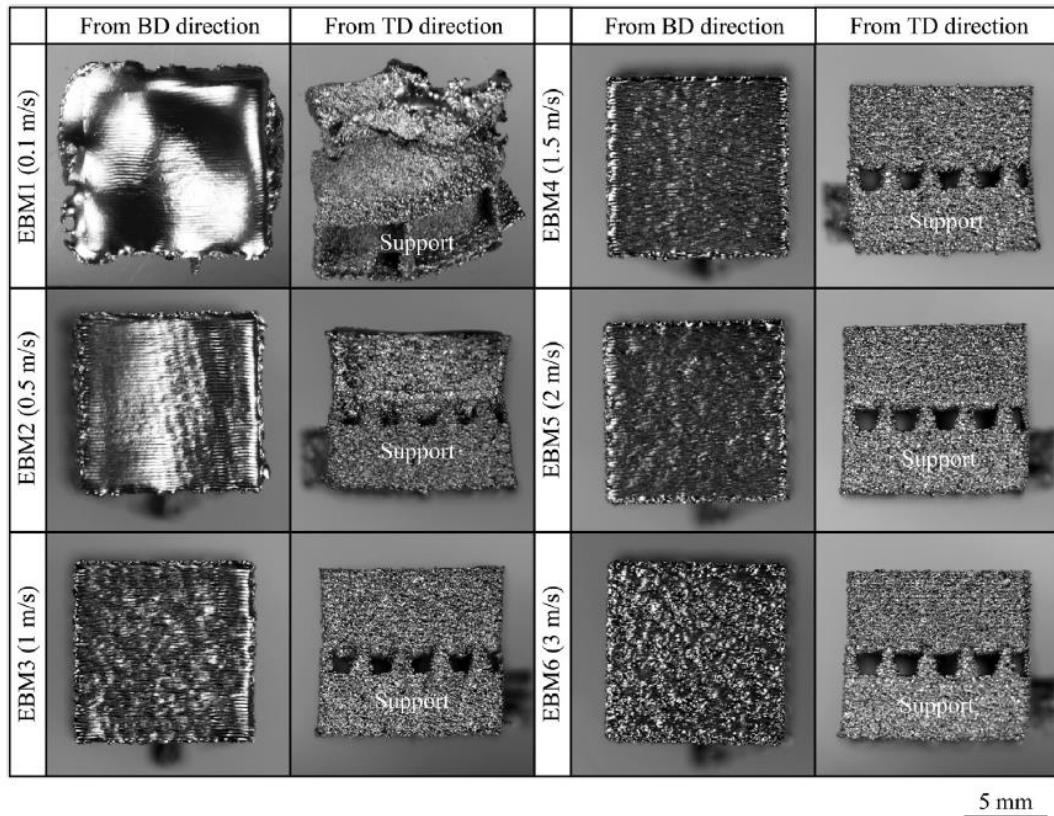


Figure 2.76: Perpendicular and parallel to the build direction views of samples produced at different scanning speeds [27].

DeRoy et al. conducted a comprehensive literature review, examining different AM methods, materials, types of errors that can occur in different methods, and the effects of different parameters on part quality [249]. The study also investigated the manufacturability of different materials using AM. As a result of the research, a process map was established. Figure 2.77 graphically shows the variation in part quality based on beam current and scanning speed for the PBF-EB process with Ti6Al4V material [249]. According to Figure 2.77, samples with volumetric porosity greater than 1% were observed in productions with low linear heat input. Additionally, metallographic examinations of samples with high linear heat input showed decreases in aluminum content. On the upper surfaces of samples where linear heat input exceeded 300 J/mm, swelling was observed. According to these

results, the suitable operating range for beam current and scanning speed is in the region where linear energy is between 100 and 200 J/mm [265]. When it is desired to increase the production speed by increasing the scanning speed, the pore structure below 1% can be improved with the HIP process [266].

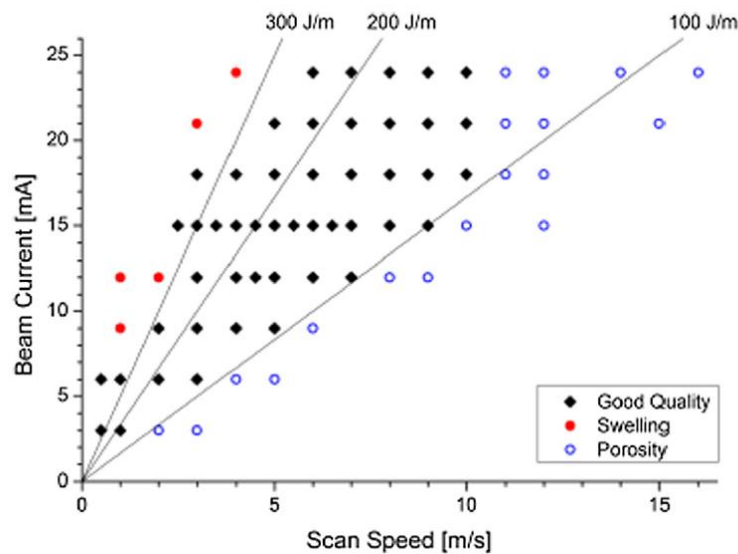


Figure 2.77: Process map for Ti6Al4V [249].

In a study investigating the effects of process parameters on surface roughness, eight samples were produced from Ti6Al4V material using two different scanning speeds, two different beam currents, and two different focus offsets, as shown in Table 2.15 [267]. According to the results, the parameter with the greatest impact on surface roughness is the focus offset value. Increasing the offset value increases roughness and also leads to a decrease in part density. Additionally, it was observed that increasing beam current and decreasing scanning speed also result in an increase in surface roughness [267].

Table 2.15: The process parameters used in experimental design [267].

Sample number	Number of replicates	Beam current	Beam speed	Offset focus	Beam current (mA)	Beam speed (mm/s)	Offset focus (mA)
		Coded values			Experimental values		
1	3	-1	-1	-1	5	3000	0
2	3	+1	-1	-1	10	3000	0
3	3	-1	+1	-1	5	6000	0
4	3	+1	+1	-1	10	6000	0
5	3	-1	-1	+1	5	3000	25
6	3	+1	-1	+1	10	3000	25
7	3	-1	+1	+1	5	6000	25
8	3	+1	+1	+1	10	6000	25

The effects of electron beam at different focus distances on the material have been investigated [27]. When the beam focus is away from the production surface, the electron beam diameter increases, reaching its minimum level when the focus point is on the production surface. As the diameter of the electron beam decreases, the energy density increases [27]. This increases the amount of evaporated material and the size of the melt pool. Additionally, due to the focused beam, if a sufficient cooling rate cannot be achieved, it deviates from directed cooling, leading to the formation of dendrite arms around the particles. This results in the formation of smaller particles, as shown in Figure 2.78 [27]. When the focus diameter is smaller, the higher energy density leads to an increase in the amount of evaporated material, causing an increase in the vapor pressure in the melt pool. As a result, the melt pool becomes irregular, leading to surface fluctuations and an increase in trapped gas beneath the surface, reducing the process window. In Figure 2.79, process maps created based on speed and power can be seen for Inconel 718 at two different focus diameters [27].

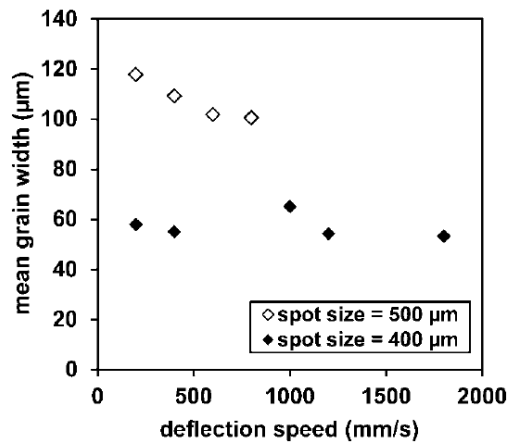


Figure 2.78: The particle width variation at two different beam diameters (400 and 500 μm) [27].

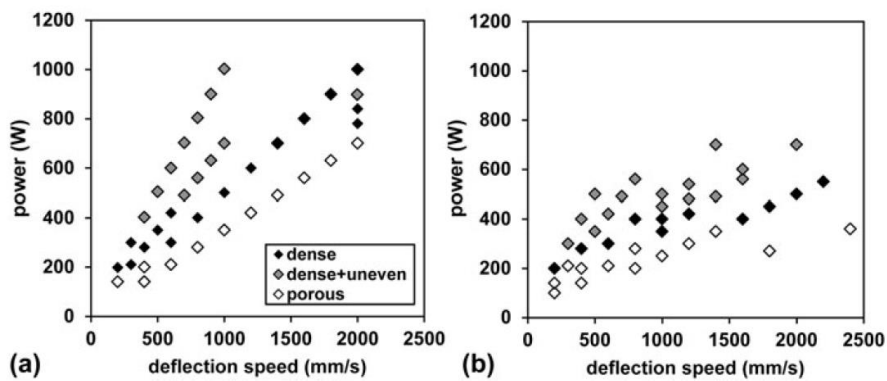


Figure 2.79: Process maps obtained from studies conducted at different scan (deflection) speeds for Inconel 718; (a) defocused electron beam (beam diameter of 500 μm), (b) focused electron beam (beam diameter of 400 μm) [27].

2.5.5.5 Part Location and Orientation

The location and orientation of the part within the build area also affect the microstructure [27]. The temperature is higher in the center of the build area, resulting in slower cooling. Parts placed on the outer side are expected to have a

finer-grained microstructure and higher mechanical properties compared to parts on the center [27].

To investigate the impact of part placement in the build area on the mechanical properties of Ti6Al4V, parts were positioned in various regions of the build area in both horizontal and vertical orientations, as shown in Figure 2.80 [27]. The study assumed that the temperature is higher near the center of the build area and decreases towards the outer regions. Consequently, it was anticipated that parts on the outer side would have a finer-grained microstructure and better mechanical properties. However, the analysis of the obtained data revealed that, contrary to expectations, the mechanical properties of parts in the inner region were better. Nevertheless, the differences in mechanical properties between the parts were relatively low, suggesting that they might be attributed to measurement uncertainties [27].

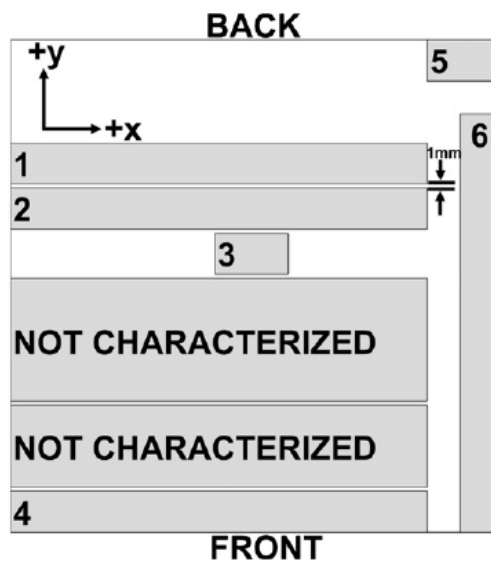


Figure 2.80: The schematic representation of samples produced in a study examining part orientation and position [27].

The size of the part can influence the cooling rate and, consequently, the microstructure [27]. It was observed that the variation in mechanical properties for Ti6Al4V parts of different sizes produced with the same parameters was small, with a 1% change for UTS and a 2% change for yield strength. No significant variation were observed in the elongation at break and the amount/size of α and β lamellae thickness [27].

CHAPTER 3

EXPERIMENTAL PROCEDURE

This chapter presents experimental procedures and techniques utilized during secondary treatments and characterization of PBF-EB fabricated Ti48Al2Cr2Nb alloys

3.1 Starting Materials

The pre-alloyed gas atomized Ti48Al2Cr2Nb powders were supplied from Praxair S.T. Technology, Inc., USA. Chemical composition of the powders given in Table 3.1 has been reported by Praxair S.T. Technology, Inc. Elemental percentages of Al, Cr, Nb, Fe and Ti had been measured by inductively coupled plasma mass spectrometry (ICP-MS) while inert gas fusion and combustion methods had been used to analyze O, N, H and C, respectively.

Table 3.1: The chemical composition of Ti48Al2Cr2Nb powders supplied by Praxair S.T. Technology, Inc.

Al	Cr	Nb	Fe	C	O	N	H	Ti
33.500	2.800	4.800	0.080	0.009	0.010	0.010	0.002	Balance

The powder size distribution (PSD) is given in Figure 3.1 and D10, D50, and D90 values are provided in Table 3.2. Microtrac Flowsync Particle Size and Shape Analyzer Device was used to analyse powder size and its distribution. This analysis employed the laser diffraction method following the guidelines outlined in ASTM B822 [270].

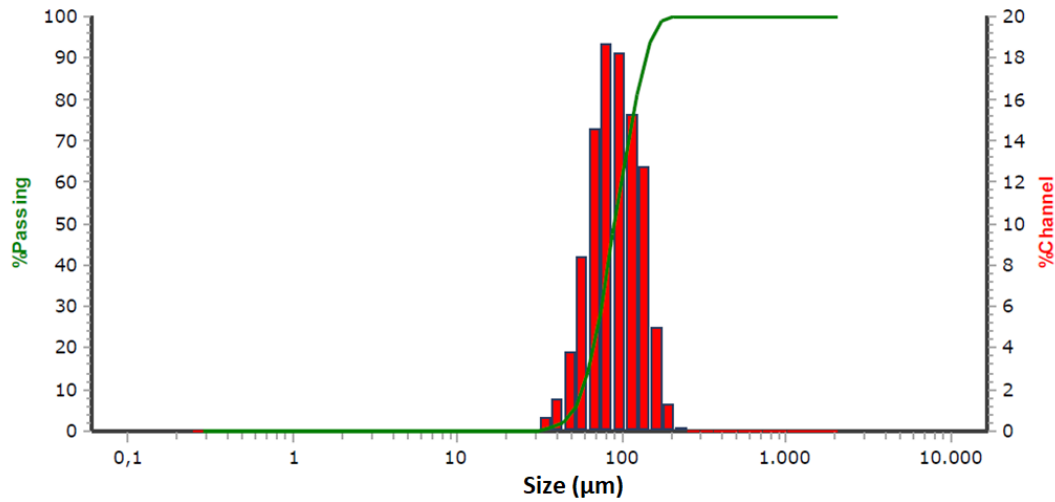


Figure 3.1: PSD analyze of Ti48Al2Cr2Nb powders.

Table 3.2: D10, D50 and D90 values of Ti48Al2Cr2Nb powders.

D10	D50	D90
57.77µm	90.07 µm	139.70 µm

Various techniques utilized for measuring metal powder density in additive manufacturing are outlined in ASTM F3049 [271]. One such method involves the use of a Hall flowmeter, a density characterization technique specified in ASTM B212 [272]. This method calculates the apparent density of powders based on the mass of free-flowing powders in a container with a specific volume [272].

Tapped density, another crucial density parameter, was determined according to ASTM B527 by mechanically tapping a powder container at a rate of 100 to 300 taps per minute [273]. The ratio of tapped density to apparent density yields the Hausner Ratio, a key indicator of powder flowability. A Hausner ratio exceeding 1.25 indicates poor flowability, while ratios surpassing 1.40 imply non-flowing powders [274], [275].

The Hall Flowmeter, in accordance with ASTM B213, was also employed to assess powder flowability by measuring the time required for 50 grams of powder to flow through the Hall Funnel [276]. Table 3.3 provides the values for apparent density, tapped density, Hausner Ratio, and Hall Flow Rate for gas-atomized Ti48Al2Cr2Nb powders.

Table 3.3: Powder flow characterization of Ti48Al2Cr2Nb powders.

Apparent Density g/cm ³	2.11
Tapped Density g/cm ³	2.50
Hausner Ratio	1.18
Hall Flow Rate (s/50g)	43.44

Figure 3.2 (a) displays a scanning electron microscopy (SEM) image of the powders utilized in the PBF-EB productions, captured at lower magnification. The powders exhibited high sphericity which is a characteristic attributed to the gas atomization powder production method. In Figure 3.2 (b), a closer examination reveals irregular-shaped particles in specific regions, deviating from the expected spherical shape. Additionally, small satellite particles were observed, attached to the main powder particles.

In Figure 3.2 (c), the X-ray diffraction (XRD) pattern of the Ti48Al2Cr2Nb virgin powder is presented. The XRD analysis confirmed the presence of two constituent phases: TiAl (γ) and Ti₃Al (α_2).

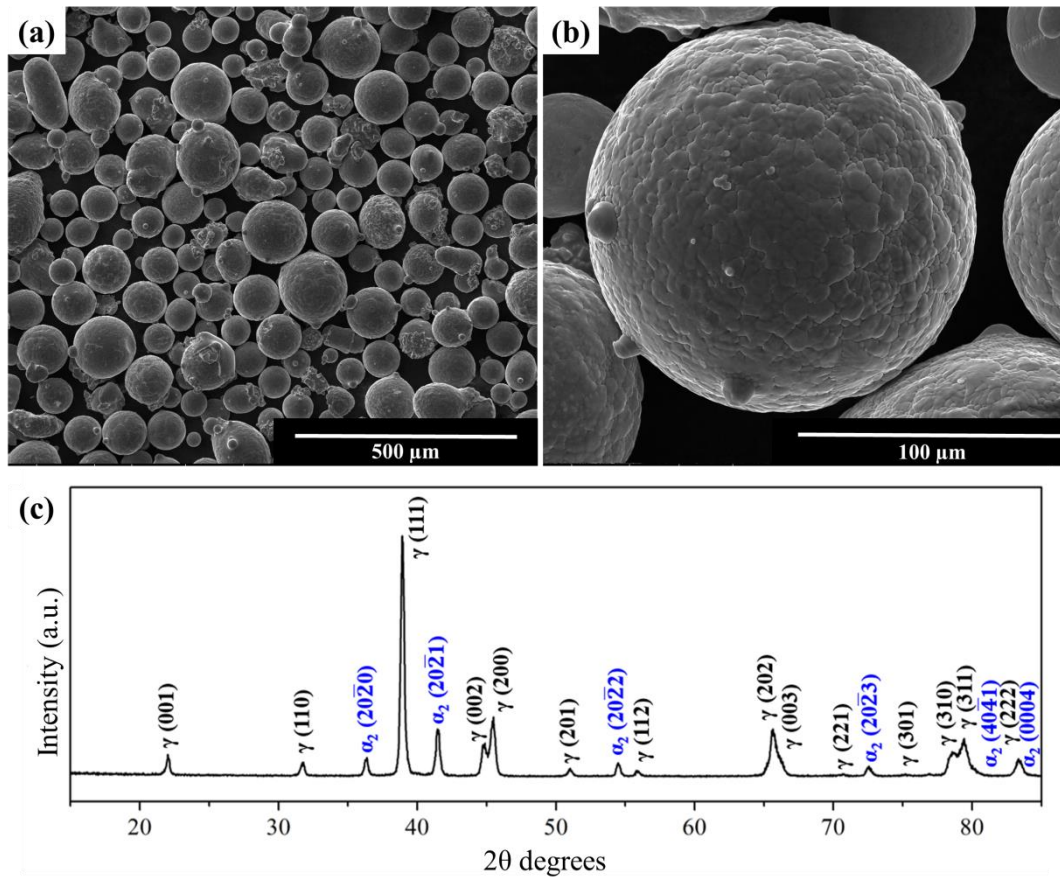


Figure 3.2: SEM images illustrating: (a) the overall appearance of powders at lower magnification, (b) irregularly shaped powders and satellites, and (c) the XRD pattern of Ti48Al2Cr2Nb powder.

3.2 Electron Beam Powder Bed Fusion Fabrication

Ti48Al2Cr2Nb alloy specimens were manufactured using the Arcam A2X Electron Beam Melting (PBF-EB) machine located at TUSAS Engine Industries Inc. in Eskişehir, Turkey. This machine operates in a vacuum and uses electrons with a 60 kV accelerating potential as energy source. Its capacity to reach temperatures up to 1100 °C makes it well-suited for material development and research activities [277].

The machine, which has a tungsten filament cathode, allows for adjustable beam currents ranging from 1 to 50 mA. The maximum beam scan speed is 8000 m/s. During the build process, the chamber pressure is maintained at a minimum of 5×10^{-4} mbar, with a typical build pressure of 2×10^{-3} mbar [277]. Table 3.4 provides the technical data for the A2X machine, and Figure 3.3 shows the A2X.

Table 3.4: Arcam A2X machine technical data [278].

Maximum build size	200 mm x 200 mm x 380 mm
Maximum beam power	3 kW
Cathode type	Tungsten filament
Beam current	1 – 50 mA
Maximum beam scan speed	8000 m/s
Minimum chamber pressure	5×10^{-4} mbar
Typical build pressure	2×10^{-3} mbar
Process temperature range	600 – 1100 °C



Figure 3.3: Picture of the Arcam A2X machine [278].

In this study, a layer thickness of 90 μm was chosen for each layer in the PBF-EB process, while maintaining a process temperature of approximately 1060 $^{\circ}\text{C}$. The selection of a 90 μm layer thickness was based on its proportionality to the grain size of the powders, which had a D50 value of 90.86 μm . To effectively sustain the high process temperature throughout the build, a smaller build platform with dimensions of 150 mm x 150 mm in the 2D plane was utilized. It is noteworthy that only a 135 mm x 135 mm area was scanned by electron beams, intentionally leaving 15 mm safety margins from the edges. This safety margin is essential to prevent loose powders from negatively charging when situated right next to the build platform.

The initial step in the PBF-EB fabrication process is preheating, aimed at establishing a uniform heat environment and ensuring mechanical anchoring of parts through sintered powders. Sintering in PBF-EB serves not only to prevent part swelling but also to enhance both thermal and electrical conductivity throughout the powder bed. This mechanism is crucial for efficiently averting powder explosions caused by repulsive negative forces generated from the electron beam. In the case of Ti48Al2Cr2Nb manufacturing, the process temperature was set at 1060 $^{\circ}\text{C}$. To optimize conductivity and achieve the desired temperature, a maximum beam current of 45 mA, variable scan speeds ranging from 150,000 to 350,000 mm/s, focus offsets of 40 and 50 mA, and average currents of 20 and 30 mA were used during preheating stage. These parameters were applied with 5-time repetitions for each layer before the bulk melt scanning process started.

In PBF-EB technology, an advantageous approach involves employing a variable function resulting from the scan line size, especially for materials with well-established process parameters. Typically, the beam current is directly proportional to the scan line size (hatch), increasing with larger scan line sizes up to a certain maximum beam current value. This relationship defines the scan speed with varying beam current, ensuring equal scanning time for different hatches. This function, known as the speed function, proves valuable in optimizing productivity after standard parameter determination. However, it is noteworthy that in this

study, constant beam current and scan speed were utilized to produce of Ti48Al2Cr2Nb samples.

The production of Ti48Al2Cr2Nb alloy has not been standardized yet in the Arcam A2X system by the company. Consequently, various process variables were explored to produce Ti48Al2Cr2Nb, aiming to investigate their effects on bulk density. Following parameter trials on 20 mm x 20 mm x 20 mm cubes, the PBF-EB "melt theme process variables" that yielded the highest density, were identified. These process parameters are summarized in Table 3.5, were employed to produce the samples in this study.

Table 3.5: PBF-EB melt theme process variables used in this study.

Parameter	Value
Beam Current (mA)	12
Scan Speed (mm/s)	1600
Line Offset (mm)	0.200
Line Energy (J/mm)	0.450
Area Energy (J/mm ²)	2.25

In Figure 3.4 shows the machine temperature log extracted from the Arcam A2X build file of mechanical test specimens, each with a length of 100 mm.. A thermocouple, positioned beneath the build platform, continuously measures and monitors the temperature. The temperature values depicted in Figure 3.4 are the temperature values of the layers adjacent to the build platform, representing the temperatures of initially produced layers. Consequently, the powder bed temperature for the upper layers was approximately 1000 - 1100 °C during the local melting of the samples. In other words, the melted Ti48Al2Nb2Cr material rapidly cools down to 1000 - 1100 °C. Throughout the 22-hour production time,

the initially produced layers, bottom sections of built alloys, gradually cool down to 880 °C.

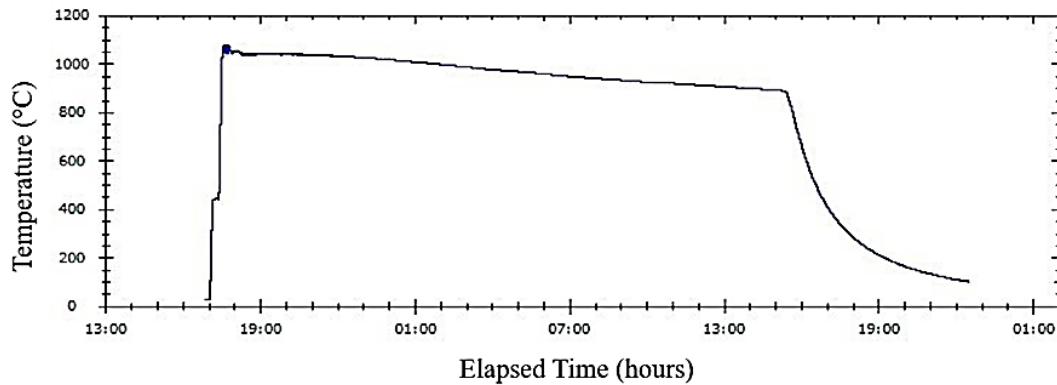


Figure 3.4: Arcam A2X temperature log for the mechanical test samples.

To investigate the tensile behavior of specimens fabricated parallel to the build direction (referred to as Z-direction samples), cylindrical test samples with a diameter of 16 mm and a height of 110 mm were produced, as depicted in Figure 3.5. These samples were vertically oriented to align with the build direction. Additionally, blocks measuring 16 x 110 x 110 mm in XYZ dimensions were manufactured using PBF-EB. Subsequently, these blocks were cut perpendicular to the build direction by utilizing wire EDM. As a result, rectangular prism test samples with dimensions of 16 x 110 x 15 mm in XYZ were obtained, facilitating the examination of the tensile behavior in specimens fabricated perpendicular to the build direction (referred to as XY-direction samples). Figure 3.5 (b) illustrates the configuration of these XY-direction samples.

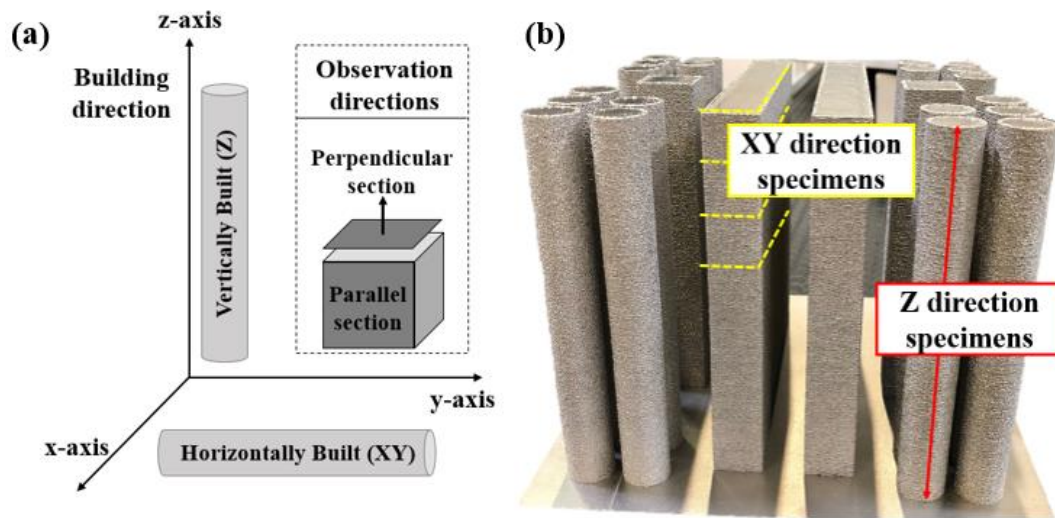


Figure 3.5: (a) Schematics illustrating horizontally and vertically built tensile test samples along with the observation directions for microstructural examinations, and (b) as-built samples on the building plate, with emphasis on the XY-direction samples to indicate the cutting direction.

3.3 Post Processing: Hot Isostatic Pressing

Hot isostatic pressing (HIP) is a widely employed technique to enhance the density of PBF-EB as-built parts. It is important to note that HIP not only serves as a densification method but also plays a crucial role in stabilizing the mechanical properties of the parts. A challenge associated with additive manufacturing is the relatively inferior fatigue properties compared to those produced through conventional methods, primarily due to the layered microstructure. HIP has been extensively utilized to improve fatigue properties, especially for critical components in dynamic aero-engine applications, such as turbine blades [21], [293] – [295].

In this study, Ti48Al2Cr2Nb as-built specimens were subjected to HIP using American Isostatic Pressing AIP6-30H equipment. In the HIP process, heating and cooling rates were set at 10 °C/min, and the utilized HIP parameters are given in

Table 3.6. In the subsequent sections, specimens treated with HIP are referred to as "HIPed".

Table 3.6: HIP parameters of Ti48Al2Cr2Nb alloy produced by PBF-EB.

Temperature	1200 °C
Time	2 h
Pressure	100 MPa
Atmosphere	Argon

3.4 Post Processing: Conventional Annealing Heat Treatment

The conventional annealing heat treatment of the samples was performed using the Nabertherm VHT 40/22-GR H2 furnace at temperatures of 1200 °C and 1400 °C. Specifically, two different process temperatures were applied to achieve a duplex or duplex-like microstructure at 1200 °C and a fully lamellar microstructure at 1400 °C. In accordance with the Ti-Al binary phase diagram (given in Figure 2.7), 1200 °C corresponds to the $\gamma + \alpha$ phase region, while 1400 °C corresponds to the α phase regions for the composition of the alloy given in Table 3.1. To prevent oxidation of samples, both types of conventional annealing heat treatments were conducted under high vacuum (10^{-5} mbar), and the samples were cooled under vacuum in the furnace down to room temperature. The conditions of both conventional annealing heat treatments are summarized in Table 3.7. In the subsequent sections, the heat treatments conducted at 1200 °C and 1400 °C were labelled as HT1 and HT2, respectively.

Table 3.7: Conventional annealing heat treatment conditions.

	Heat Treatment 1 (HT1)	Heat Treatment 2 (HT2)
Temperature	1200 °C	1400 °C
Time	2 h	2 h
Atmosphere	Vacuum	Vacuum
Heating Speed	10 °C/min	10 °C/min

3.5 Structural and Chemical Analysis

Various characterization techniques were employed on both the as-built and post-processed specimens. This section will provide comprehensive details about all the experimental methods used for structural and chemical characterization of the samples.

3.5.1 Density Measurement

Density and porosity measurements of the PBF-EB fabricated as-built and post processed specimens were conducted following Archimedes' principle in accordance with ASTM B311 [287]. To enhance the accuracy of bulk density evaluation, a 2 mm thick layer was removed from surface sections of 20 mm x 20 mm x 20 mm cubic samples (as shown in Figure 3.5 (a)) using wire electrical discharge machining (EDM). This process aimed to eliminate surface defects potentially caused by sintered powders and contour roughness.

Bulk densities of the as-built samples were then measured on surface layer cut samples of 16 mm x 16 mm x 16 mm dimensions after cleaning all EDM-cut surfaces using sandblasting. Each cube underwent three measurements, and the arithmetic averages were taken to determine the final density.

3.5.2 Computed Tomography Scans

A micro-focus RX Solutions Easytom 230 X-ray computed tomography (XCT) device was used to perform computed tomography measurements. The XCT scans were conducted at 230 kV accelerating voltage, a 120 mA tip current, and 1440 images per scan conditions. During the scanning process, a 2 mm physical copper filter was used. The scan resolution varied between 15 and 30 μm . The resulting 2D images were reconstructed to provide 3D volumes, which allowed for the examination of defect volume and distribution within the samples. The reconstructed 3D volumes were analysed using the VG Studio MAX 3.2 software. The algorithm of the software was used for porosity distribution analysis, allowing the detection of any porosity or inclusions in the samples [297]. XCT analysis was performed on both XY- and Z-direction of as-built, HIPed, HT1 and HT2 processed samples to evaluate the impact of building direction and secondary processes on porosity and the presence of internal defects.

3.5.3 Thermal Expansion Measurements

The Linseis L75 Platinum Horizontal H1600 Dilatometer was utilized to assess the thermal expansion behavior of PBF-EB fabricated Ti48Al2Cr2Nb samples. Cylindrical samples, measuring 25 mm in height and 5 mm in diameter, underwent cyclic heating and cooling up to 1000 °C and 27 °C, respectively. Three heating and cooling cycles were executed with 10 °C intervals under a helium atmosphere for each sample. A heating rate of 0.5 °C/min was applied until reaching 200 °C, and then it was maintained at 3 °C/min between 200 and 1000 °C. The cooling rate was fixed at 3 °C/min for the temperature range of 1000 – 27 °C. The pushrod tip was held at a 0.5 mN contact force throughout the experiment.

3.5.4 X-ray fluorescence Analysis

X-ray fluorescence (XRF) analysis, according to ASTM E539 [298], was conducted using Zetium PANalytical having 2.4 kW to evaluate the chemical composition of a 120 mm long and 30 mm diameter as-built sample, as illustrated in Figure 3.6. Five cross-sections were taken perpendicular to the build direction and at least three XRF measurements were carried out in each section.

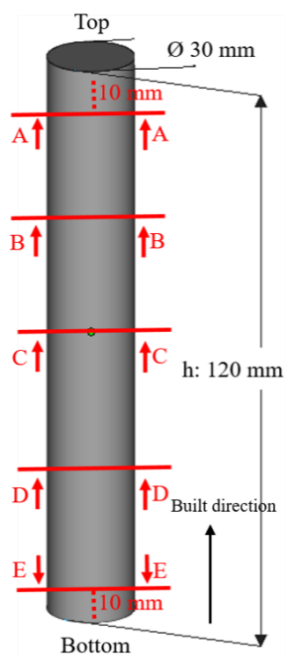


Figure 3.6: A sketch of XRF measurement sample that shows sectioning planes.

3.5.5 X-Ray Diffraction Analysis

X-ray diffraction (XRD) was conducted to investigate the phase constituents of as-built, HIPed, HT1, and HT2 samples. Prior to the XRD analysis, all specimens underwent grinding using SiC papers. The Bruker D8 Advance Eco device was

employed to acquire XRD patterns, utilizing Cu-K α radiation ($\lambda = 1.5406 \text{ \AA}$). The analysis involved continuous scanning at 40 kV over the 2θ range of 15° to 90° , with a fixed scan speed set of $0.1^\circ/\text{min}$.

3.5.6 Metallographic Examinations

For microstructural assessments, the specimens underwent an initial mechanical grinding process using SiC papers up to a 2000 grit size to achieve smoother surfaces and eliminate any potential oxide layers. Subsequently, the specimens were polished using diamond pastes containing diamond particles with sizes of $6 \mu\text{m}$, $3 \mu\text{m}$, and $1 \mu\text{m}$. Following the polishing step, the specimens were etched for 10-15 seconds in Kroll's Reagent (refer to Table 3.8 for details). After etching, the specimen surfaces were thoroughly rinsed with diluted water and ethanol. Finally, the specimens were dried using hot air.

Table 3.8: The constituents of Kroll's reagent.

Components	Volume
Hydrogen fluoride (HF)	2 ml
Nitric acid (HNO ₃)	6 ml
Distillated water (H ₂ O)	92 ml

Microstructural observations were conducted using both a digital optical micrograph (Huvitz HDS-5800) and a scanning electron microscope (SEM) (Nova NanoSEM 430, FEI), operated at an accelerating voltage of 20 kV. Topographical and quantitative examinations were performed using the SEM, which was equipped with an energy dispersive X-ray spectroscopy (EDS) analysis system. To obtain average atomic and weight percentages of the elements, a minimum of ten EDS analyses were conducted. Microstructural examinations were carried out on cube shaped samples, as schematically illustrated in Figure 3.5 (a), with dimensions of

20 mm x 20 mm x 20 mm. These cubes were sectioned parallel (Z-axis) and perpendicular (XY-axis) to the build direction, enabling the examination of microstructural variations depending on the build direction.

3.5.7 Electron Back Scatter Diffraction

The Electron backscatter diffraction (EBSD) technique was employed to observe and assess microstructural details, including grain morphology, misorientation, and crystallographic texture of the as-built, HIPed, HT1, and HT2 samples in the parallel to the built direction section (Z-direction). The samples were initially ground using SiC papers up to a 2500 grit size and then polished using oxide polishing suspension (OP-S) from Struers Inc. For EBSD analysis, a Zeiss Merlin field emission gun (FEG) SEM with an accelerating voltage of 15 kV, a beam current of 6.0 nA, and a working distance of 14 mm was utilized. The SEM was equipped with an EDAX/TSL EBSD system and a Hikari EBSD camera. EBSD maps, covering an area of 160 x 160 μm on a hexagonal grid 7 with a step size of 0.5 μm , were obtained. The raw EBSD data were analyzed using TSL-OIM Analysis v7.3.1 software. For texture analysis, the generalized spherical harmonic series expansion method of Bunge [288] was employed. The harmonic series were expanded to a rank (L) of 34, and Gaussian smoothing with a half-width of 5° was applied.

3.5.8 Thermodynamic Modelling Studies

The thermodynamic calculations for the Ti–Al binary and Nb/Cr modified Ti–Al–Cr–Nb quaternary phase systems were performed under equilibrium conditions using the computational thermodynamic method with the TCTI database in Thermo-Calc software. Initially, standard atmospheric pressure was introduced to the software to calculate equilibrium conditions in both binary and quaternary systems. Subsequently, a pressure input value of 100 MPa was added to simulate

the conditions during hot isostatic pressing (HIP). Equilibrium phase fractions were calculated at room temperature, 1200 °C, and 1400 °C. Finally, Scheil simulations were implemented for both the binary and quaternary systems.

3.6 Mechanical Characterization

3.6.1 Microhardness

The Innovatest Falcon 501 V2 microhardness device was employed with a load of 100 g for 10 seconds to determine the Vickers hardness of the specimens. Prior to the microhardness measurements, specimens underwent etching to reveal the microstructure specifically.

3.6.2 Tensile Tests

Room and elevated temperature tensile tests were conducted in accordance with ASTM E8/E8M and E21 standards, respectively [289], [290]. A single type of PBF-EB fabricated, and subsequently machined tensile test specimen was used for both room and elevated temperature tensile tests. The dimensions of the tensile test samples were as follows:

- 36 mm gage length,
- 6 mm diameter,
- 12 mm at both ends to fix the specimen to the holding grips (refer to Figure 3.7 and Figure 3.8).

The 100 kN capacity Zwick/Roell Z100 Testing Machine, equipped with a clip-on extensometer for contact measurement, was employed with a constant crosshead speed of 0.5 mm/min to determine the stress-strain behavior at room and elevated temperature tensile testing. For elevated temperature tensile tests, a furnace was directly mounted around the crossheads of the Zwick/Roell Z100.

Tensile yield strengths were determined using the 0.2% offset method. The elastic modulus of the specimens was calculated from the slopes of the linear regions of the stress-strain diagram.



Figure 3.7: A picture of room and elevated temperature tensile test specimen.

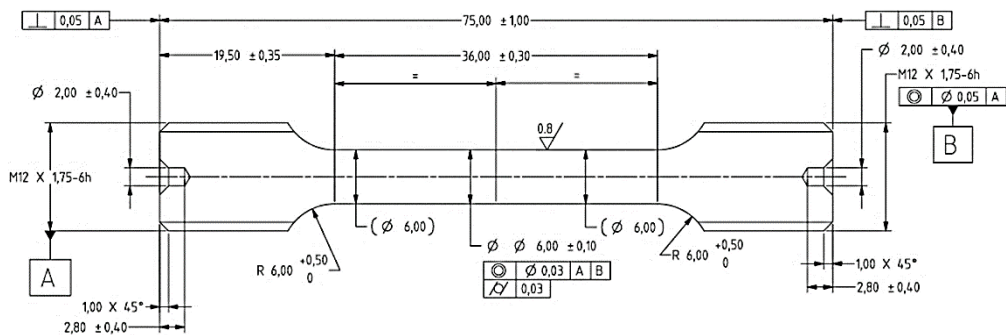


Figure 3.8: A technical drawing of room and elevated temperature tensile test specimen.

CHAPTER 4

RESULTS AND DISCUSSION

In this chapter, experimental findings including structural analyses, microstructural evaluations and mechanical property examinations and discussions are given in detail.

4.1 Porosity and Density Investigations

The average density for both XY- and Z-direction as-built samples was calculated as 3.94 g/cm³ using Archimedes' principle. After HIP, the density increased to 3.96 g/cm³ for both XY- and Z-direction samples, while HT1 and HT2 did not alter the as-built density, remaining at 3.94 g/cm³ for both XY- and Z-direction

A micro-focus RX Solutions Easytom 230 X-ray computed tomography (XCT) device was employed to examine the porosity of both the as-built and post-processed samples. The analysis involved 3D scanning of the gage length of the tensile test specimens, as shown in Figure 4.1. No longitudinal gaps or cavities indicative of joining, melting, and lamination defects were observed in any of the samples. All identified defects took the form of spherical-shaped pores. Consequently, all defects detected by the XCT device were considered as spherical pores.

For the as-built XY sample, the total pore amount was 0.60% (Figure 4.1 (a)), while it was 0.63% in the as-built Z-sample (Figure 4.1 (b)). Furthermore, the largest pore size in the XY-direction was measured as 0.563 mm, and in the Z sample, the largest pore size was determined to be 0.667 mm. The XCT device's resolution allows the measurement of porosity down to 15 and 30 μm. Therefore, pores smaller than 15-30 μm in the samples were not included in the calculations.

The XCT examinations revealed that the errors and pore amounts in both the XY- and Z-directions were similar. Consequently, it was concluded that porosities were randomly distributed throughout the samples, independent of the building direction.

HIPing was found to be effective in decreasing the porosity of both XY and Z-built samples. According to XCT measurements, the initial porosity (0.60%) in XY-direction as-built samples reduced to 0.07% after HIPing. However, the effect of HT1 and HT2 on the porosity of the samples was negligible. The porosity content of the HT1 and HT2 processed XY-direction samples was around 0.62% and 0.59%, respectively, which is close to that of the as-built samples.

In Z-direction built samples, the initial porosity (0.63%) was found to be similar to XY-direction HIPed samples, with a reduced value of 0.07%. However, similar to the XY-direction, the effect of HT1 and HT2 on the porosity of the Z-direction samples was negligible. The porosity content of the HT1 and HT2 processed samples was around 0.61% and 0.62%, respectively.

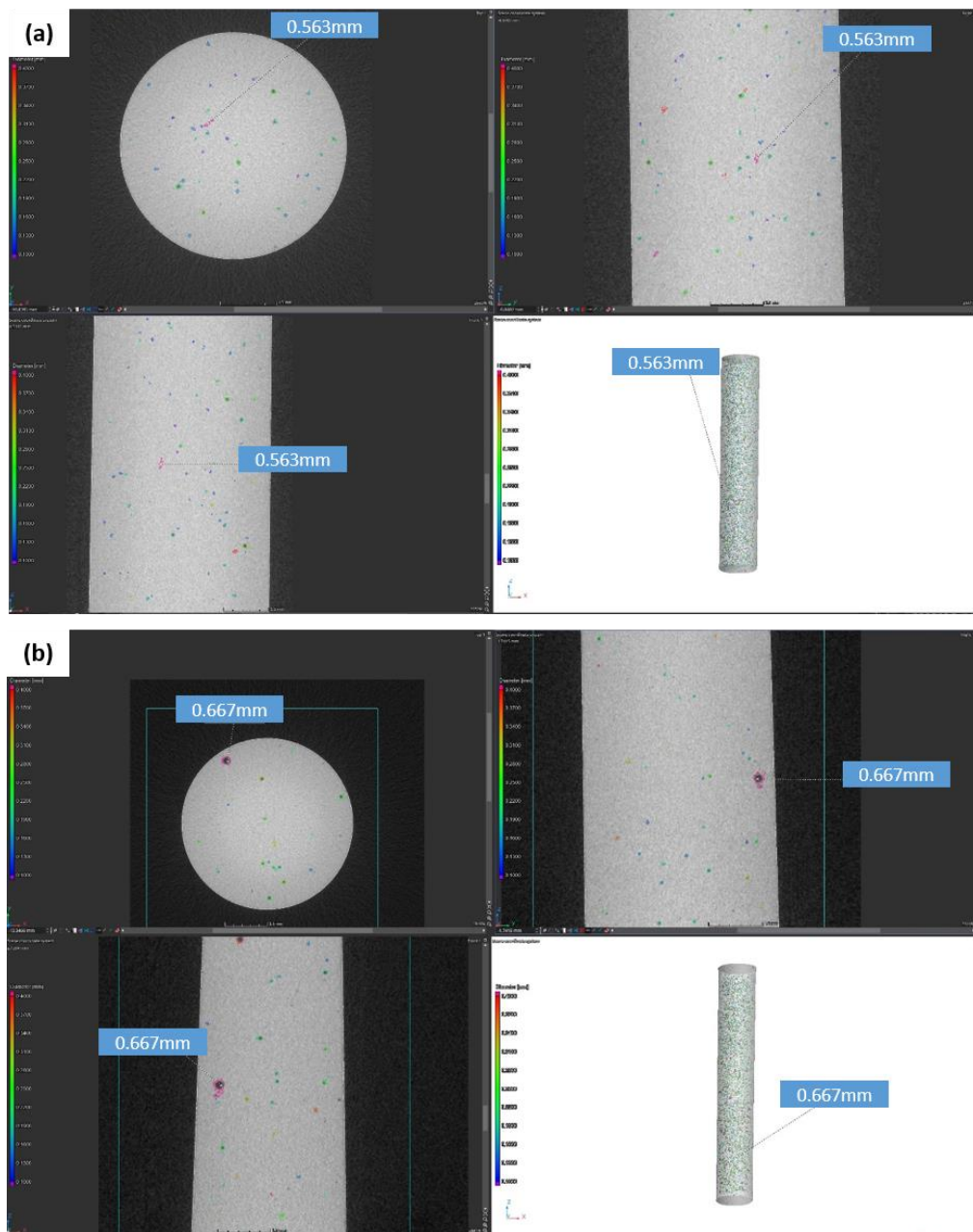


Figure 4.1: XCT reconstructed images that show the spatial distribution of pores in the tensile test samples of; (a) as-built in XY-direction, (b) as-built in Z-direction.

4.2 Thermal Expansion Measurements

The dilatometer measurements conducted on the PBF-EB as-built Ti48Al2Cr2Nb samples in the XY- and Z-directions between 27 °C and 1000 °C are illustrated in Figure 4.2. Notably, no significant difference was observed in the coefficient of thermal expansion (CTE) values between the XY and Z samples. At 30 °C, the CTE value for the XY-direction sample was measured as $9.83 \times 10^{-6}/\text{K}$, while for the Z-direction sample, it was measured as $9.89 \times 10^{-6}/\text{K}$. At the highest temperature of the measurement (1000 °C), the CTE value was $13.06 \times 10^{-6}/\text{K}$ in the XY-direction, and it was $13.05 \times 10^{-6}/\text{K}$ in the Z-direction.

It was observed that the CTE values were not dependent on the manufacturing direction in PBF-EB, as seen in Figure 4.2. The CTE values measured at increments of 10 °C are presented in Table A.5.1 for the samples in both XY- and Z-directions.

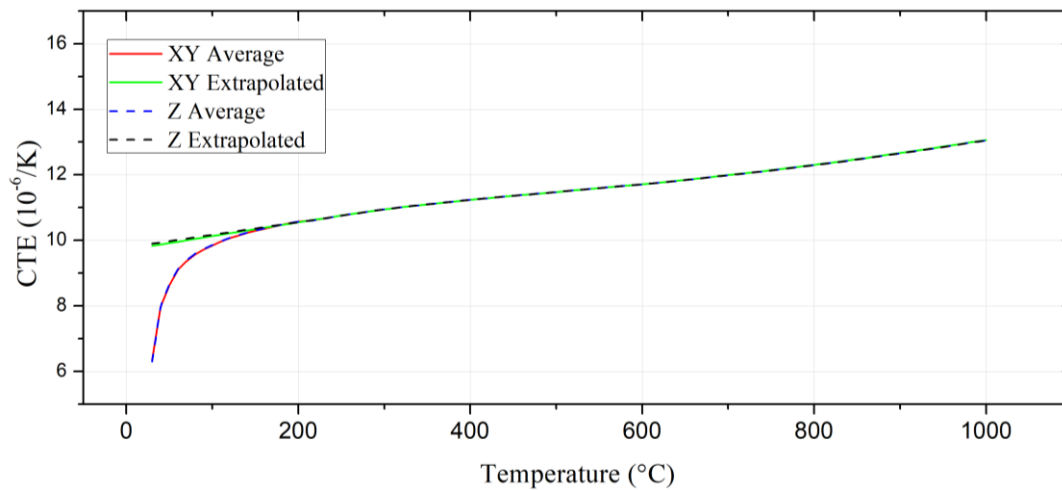


Figure 4.2: CTE values varying at different temperatures for XY- and Z-direction samples.

4.3 Chemical Composition Measurements

The averages of XRF results obtained from five different build heights, as shown in Figure 3.6, are presented in Table 4.1. According to XRF measurements, it is evident that the aluminum content varies, particularly across the build height. For the cylindrical specimen with a height of 120 mm, the average aluminum content in sections A, B, and C, taken from the upper and middle parts of the specimen, were found to be 33.234 ± 0.057 , 33.036 ± 0.121 , and 33.310 ± 0.135 wt.%, respectively. In the lower sections D and E of the specimen, the aluminum content was determined to be 32.831 ± 0.098 and 32.889 ± 0.076 wt.%, respectively. The aluminum content in sections D and E was below the specimen's average of 33.060 ± 0.208 wt.%.

As shown in the temperature log in Figure 3.4, following the melting, the temperature rapidly drops to around 1000 - 1100 °C. During the PBF-EB process of the samples, as the build height increases, the temperature in the lower layers decreases to as low as 880 °C. This indicates that the aluminum loss is more pronounced in the lower regions of the specimen exposed to higher temperatures for a longer duration compared to the upper regions. The phenomenon of approximately 1 wt.% aluminum loss (evaporation) due to electron beam interaction has been investigated by Knörlein et al. [305]. According to Wartbichler et al., an increase in the line energy during the PBF-EB process leads to a higher aluminum evaporation [306].

Table 4.1: XRF measurements (wt.%) of Ti48Al2Cr2Nb as-built sample.

Al	Cr	Nb	Fe	Ti
33.060 ± 0.208	2.616 ± 0.054	4.926 ± 0.055	0.076 ± 0.004	Balance

4.4 X-Ray Diffraction Analysis

The X-Ray Diffraction (XRD) patterns in Figure 4.3 were obtained by conducting room temperature XRD analyses on the perpendicular and parallel sections of the PBF-EB as-built Ti48Al2Cr2Nb samples. It was observed that the as-built samples in perpendicular and parallel sections comprised only γ -TiAl and α_2 -Ti₃Al phases.

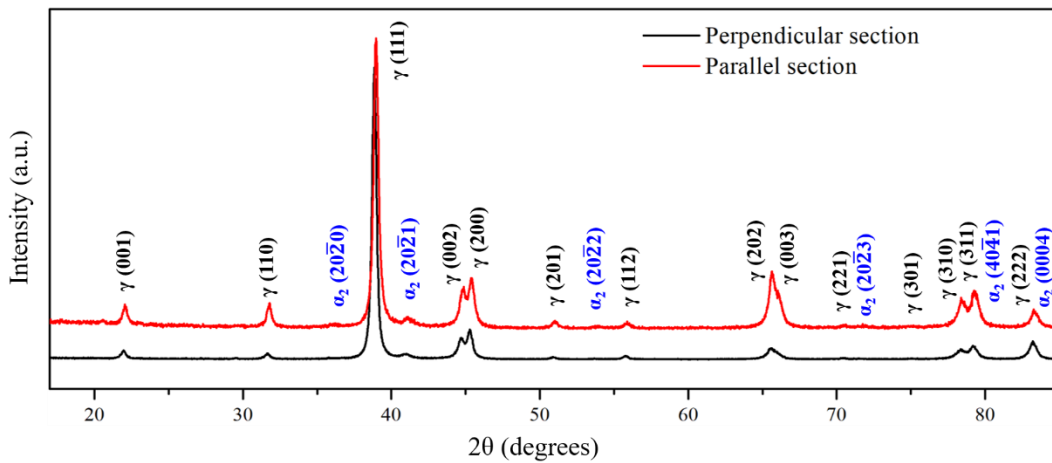


Figure 4.3: XRD patterns obtained from the as-built sample in perpendicular and parallel to build direction sections.

The XRD patterns presented in Figure 4.4 were obtained through room temperature XRD analyses on the PBF-EB as-built, HIPed, HT1, and HT2 processed Ti48Al2Cr2Nb samples. As revealed in Figure 4.3, since the same phases appeared in both sectioning planes, the XRD patterns seen in Figure 4.4 were obtained from sections parallel to the manufacturing direction. It was determined that as-built, HIPed, HT1, and HT2 processed samples consisted γ -TiAl and α_2 -Ti₃Al phases. The preheating temperature around 1060 °C (as indicated in the temperature log shown in Figure 3.4) and a cooling rate of 10³-10⁵ K/s [307], [308] favored the formation of γ and α_2 in the as-built sample. The presence of γ and α_2 phases after PBF-EB production has been previously reported by Youn et al [309]. Further heat

treatments and HIP did not result in the development of any phases other than γ and α_2 .

The γ phase possesses a face-centered tetragonal (fct) L10 ordered structure within the P4/mmm space group, and it remains homogeneous at room temperature for aluminum contents ranging between 48 - 53 at.% in the binary Ti-Al system [1], [2], [291], [292]. On the other hand, the α_2 phase exhibits a hexagonal D019 ordered structure belonging to the P63/mmc space group, and it remains homogeneous at room temperature for aluminum contents between 21 - 35 at.% in the binary Ti-Al system. The α_2 phase maintains its ordered structure up to 1180 °C before transforming into a disordered hcp α phase for 32 at.% aluminum content [1], [2], [291], [292].

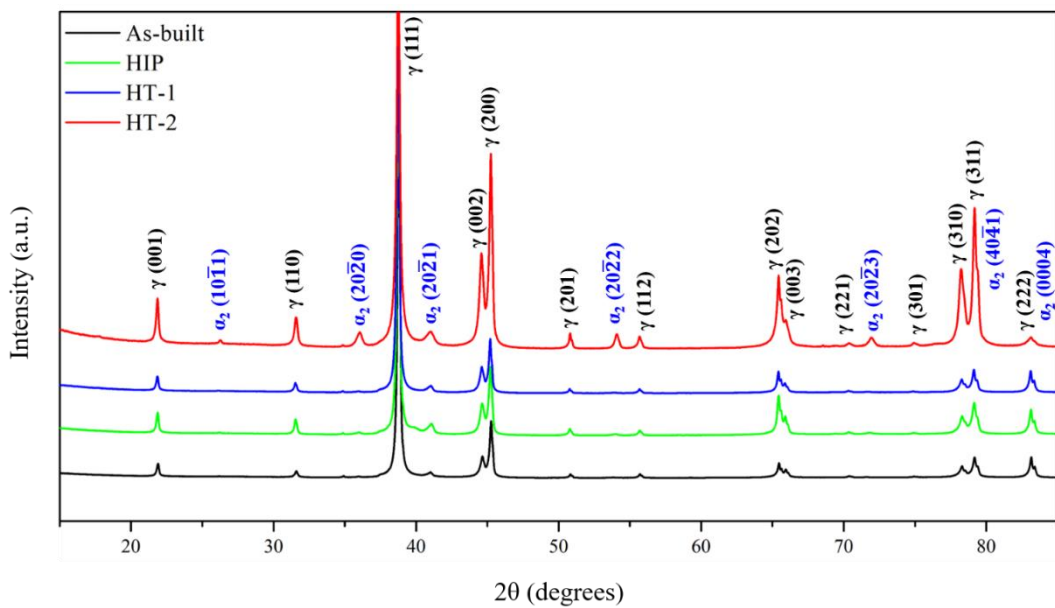


Figure 4.4: XRD patterns obtained from the as-built, HIPed, HT1 and HT2 processed samples in parallel to build direction.

The α_2 -Ti₃Al phase exhibits a hexagonal D019 ordered structure belonging to the P6₃/mmc space group, with lattice parameters a= 0.58 nm and c= 0.48 nm,

resulting in a c/a ratio of 0.8. The α_2 -Ti₃Al phase remains homogeneous at room temperature for aluminum contents between 21-35 at.%. It maintains its ordered structure up to 1180 °C before transforming into a disordered hcp α -phase for 32 at.% aluminum content. Further heating leads to the transformation of hcp α phase into a bcc β Ti phase [1], [291].

The γ -TiAl phase has a face-centered tetragonal (fct) L10 ordered structure belonging to the P4/mmm space group, with lattice parameters $a= 0.40$ nm and $c= 0.41$ nm, resulting in a c/a ratio of 1.02. As aluminum content decreases, the c/a ratio approaches 1, and the structure becomes ordered fcc [2]. The γ -TiAl phase remains homogeneous at room temperature for aluminum contents between 48 – 53 at.% [1], [291], [292].

XRD analysis confirmed that the α_2 phase of the HT2 sample exhibited higher peak intensity at 36, 42, and 54° 2θ angles. Additionally, the α_2 phase peaks at 26 and 71° for the HT2 sample were not distinguishable for the as-built, HIPed, and HT1 processed samples. Phase fractions, determined through Rietveld refinement, are presented in Table 4.2. The α_2 phase fractions for the as-built, HIPed, HT1, and HT2 processed samples were found to be 1.45 wt.%, 3.64 wt.%, 2.27 wt.%, and 4.24 wt.%, respectively, with the balance being the γ phase. The α_2 phase fraction is higher in the HIPed sample (7.1 wt.%) compared to the PBF-EB as-built condition (4.8 wt.%), as noted by Cakmak et al. in their XRD analysis [193]. However, the increase in α_2 content in the HIPed sample, which shares the same process temperature as HT1, has not been reported in previous studies. It was observed that a pressure of 100 MPa at 1200 °C caused the α_2 phase to increase by 1.37% compared to HT1.

Table 4.2: Phase fractions obtained by rietveld refinement.

	As-built	HIP	HT1	HT2
α_2 (wt.%)	1.45	3.64	2.27	4.24
γ (wt.%)	98.55	96.36	97.73	95.76

4.5 Metallographic Examinations

4.5.1 Microstructural Evaluations on of As-Built Samples

The microstructures of the as-built samples were analyzed in cross-sections perpendicular and parallel to the building direction. Sections were obtained from three different heights, and their microstructures were examined in both perpendicular and parallel observation planes to the build direction. As discussed in Chapter 3.2, the samples were manufactured at a preheat temperature of 1060 °C during PBF-EB production. As the production height increases in PBF-EB, the first produced layers are consistently exposed to high temperatures due to the subsequent melting layers, as well as longer preheating exposure times.

Grain growth was observed in the lower and middle layers, which were exposed to high temperatures for a long duration, while a finer microstructure was observed in the upper layers, which were exposed to high temperatures for a short duration and thus cooled rapidly. As depicted in the microstructures presented in Figure 4.5 (a) and (b), it was determined that the microstructures in both perpendicular and parallel directions to the build direction, taken from the upper parts of the Ti48Al2Cr2Nb as-built sample, were finer than those taken from the middle (Figure 4.5 (c) and (d)) and lower (Figure 4.5 (e) and (f)) sections. However, it was observed that the grain sizes did not consistently increase from the uppermost section to the bottom. The largest grains were observed in the region between the

middle and lower sections. The microstructure was relatively finer in the lower section due to the faster heat transfer in this section, which was solidly attached to the production platform.

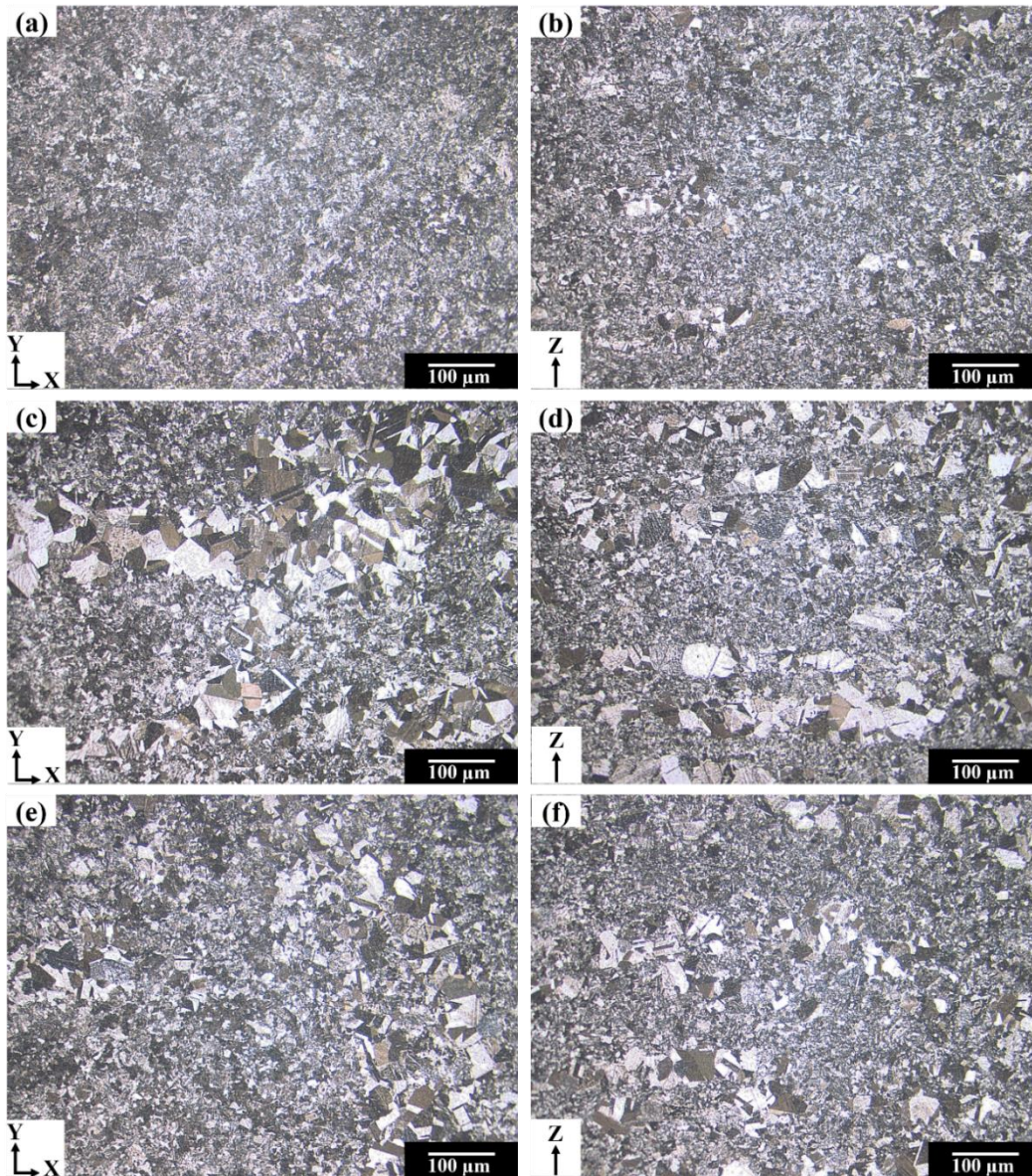


Figure 4.5: Optical micrographs of as-built Ti48Al2Cr2Nb samples produced via PBF-EB. The images captured in various sections: (a) Upper section in the perpendicular direction, (b) upper section in the parallel direction, (c) middle section in the perpendicular direction, (d) middle section in the parallel direction, (e) lower section in the perpendicular direction, and (f) lower section in the parallel direction, all at a magnification of 500x.

The microstructures of the middle section of as-built samples were also examined in cross-sections perpendicular and parallel to the building direction in detail, and the corresponding microstructures are illustrated in Figure 4.6. Two distinct microstructures were observed upon changing the observation direction, as depicted in Figure 4.6. In cross-sections perpendicular to the building direction (Figure 4.6 (a) and (c)), layer traces were not clearly discernible. However, when observing cross-sections parallel to the building direction (Figure 4.6 (b) and (d)), layer trace formation at a 90° angle to the building direction was evident.

In both observation directions, spherical pores were detected, consistent with observations from XCT examinations (Figure 4.1). The average diameter of the pores measured in perpendicular and parallel cross-sections was similar, with values of $48 \pm 37 \mu\text{m}$ and $50 \pm 29 \mu\text{m}$, respectively. The spherical shape of the pores suggests that gases trapped within the powders during gas atomization were likely released during the PBF-EB manufacturing process, as also indicated in [20].

Higher magnification backscattered electron SEM images in cross-sections perpendicular and parallel to the building directions are shown in Figure 4.6 (e) and (f), respectively. The as-built microstructure in both observation directions revealed a bimodal structure with fine and coarse grains.

Figure 4.3 displays XRD patterns in two directions, revealing identified peaks only for the α_2 and γ phases. The microstructure in both orientations exhibits a duplex-like structure consisting of γ/α_2 lamellae and equiaxed γ grains. Grain growth appears to have occurred in regions with lower amounts of α_2 , as the lower layers underwent annealing at high temperatures during PBF-EB. However, in regions with a higher amount of α_2 , grain growth was hindered, possibly due to their pinning effect on γ grains (highlighted areas in Figure 4.6 (e) and (f)).

In areas with a lower α_2 content, γ grains undergo coarsening as grain boundaries were not pinned during prolonged intrinsic annealing, leading to abnormal grain growth, also known as discontinuous grain growth or secondary recrystallization [310]. Furthermore, in cross-sections parallel to the building direction, it was

observed that fine regions formed sandwiched (or banded) structures between the coarse grains. These coarse regions are commonly referred to as γ bands, given the limited presence of the α_2 phase within the coarse grain area, as mentioned in [20] - [23]. On the other hand, in perpendicular cross-sections, the coarsened grains did not form a banded structure in any particular direction.

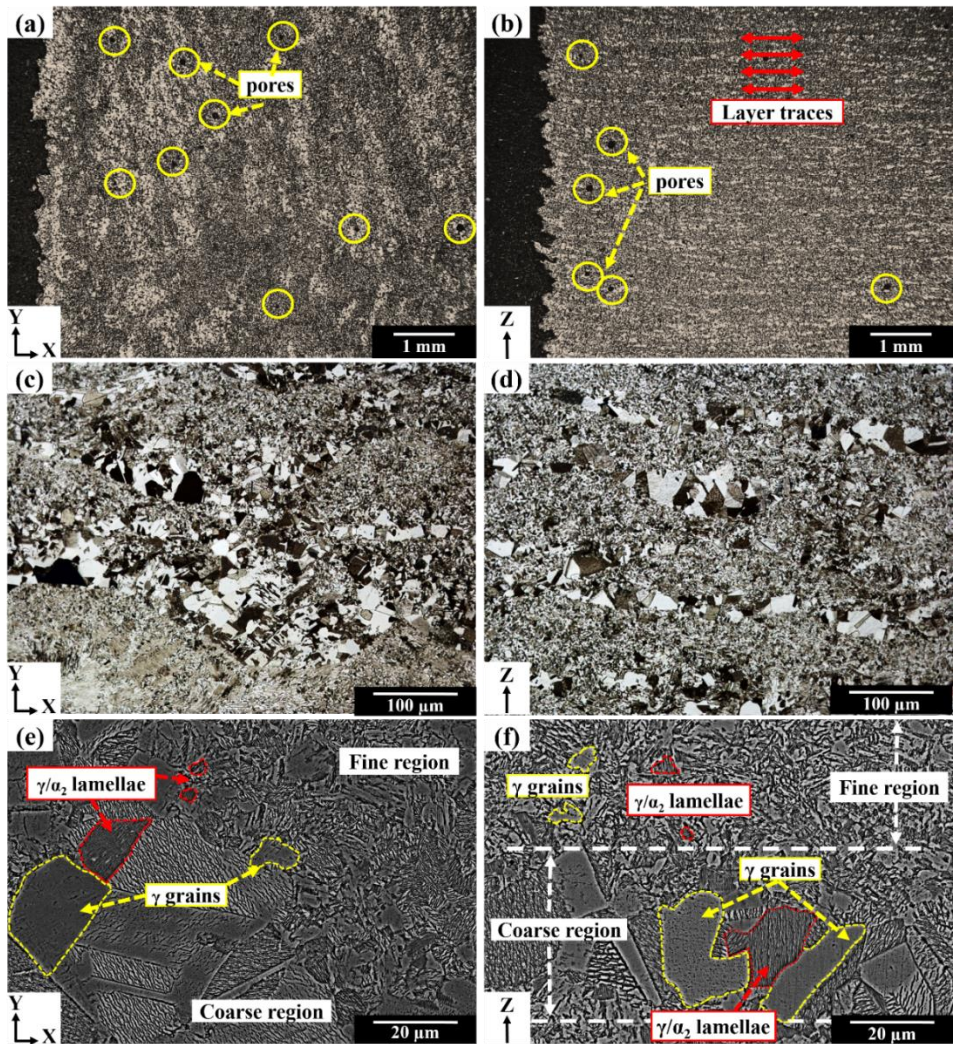


Figure 4.6: Optical micrographs of two different observation directions; in cross-sections at 50x; (a) perpendicular and (b) parallel to building direction, at 200x; (c) perpendicular and (d) parallel to building direction. Backscattered electron SEM images at 2500x in cross-sections; (e) perpendicular and (f) parallel to building direction.

The γ bands observed in the microstructures shown in Figure 4.5 (b), (d), and (f) were further analyzed in the SEM images presented in Figure 4.7, focusing on the Z-direction as-built sample. EDS measurements were conducted at the points marked in yellow in Figure 4.7 (a) to identify any variations in chemical composition between the coarse bands and the fine region. Measurements were performed at points A, B, C, G, H, and I for coarse colonies, while points D, E, and F were analyzed for fine lamellae.

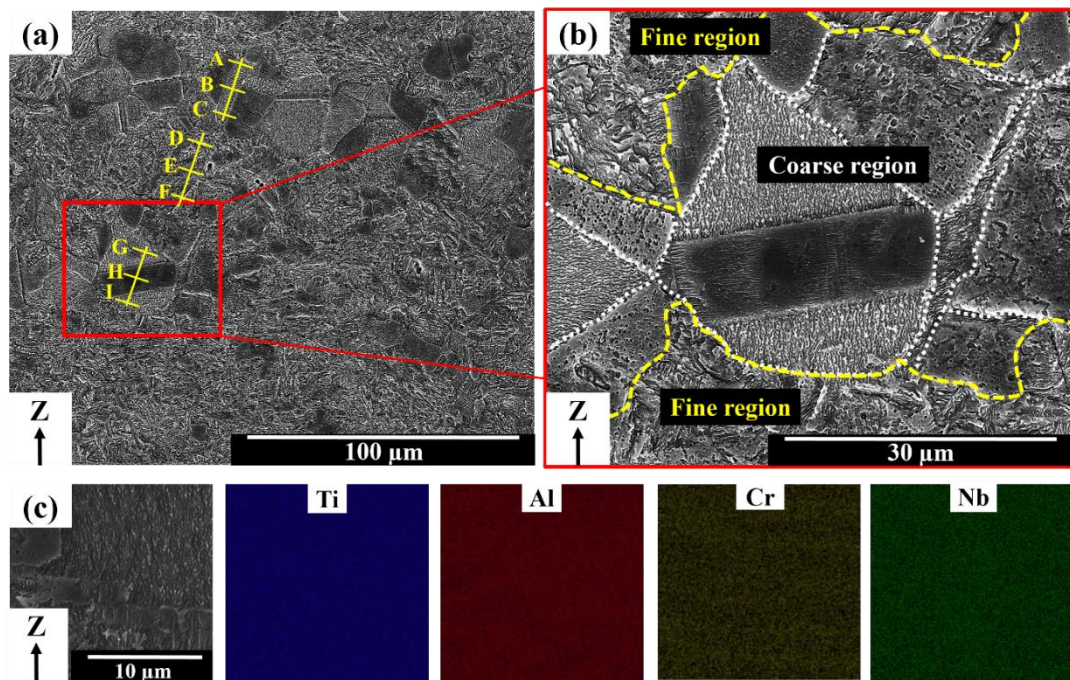


Figure 4.7: Secondary electron SEM images taken from parallel observation direction in as-built sample that shows; (a) duplex microstructure at 1500x, (b) fine lamellae + equiaxed grains separated by coarse colonies at 5000x, (c) EDS elemental maps obtained from the coarse and lamellar regions.

EDS analyses were conducted at nine different yellow points in Figure 4.7, and the results are provided in Table 4.3. In measurements A, B, C, located in the coarse-banded region shown in Figure 4.7 (a), the average aluminum content was found to be 32.41 wt.%. Similarly, in measurements G, H, I, performed in another coarse-

banded region illustrated in Figure 4.7 (a), the average aluminum content was determined to be 32.37 wt.%. Notably, measurements D, E, F, taken from a different region, exhibited an average aluminum content almost 1 wt.% lower than that of both the A, B, C and G, H, I regions, with values of 31.28 wt.% on average.

The titanium content was observed to be approximately 1 wt.% higher in the D, E, F region. This discrepancy in chemical composition between the coarse and banded grains (A, B, C, and G, H, I regions) and the fine-grained regions (D, E, F regions) was evident. Additionally, noteworthy findings from the EDS analyses indicated that the aluminum content of the powder material, as stated in Table 3.1, was 1.1% higher than that of the coarse region and 2.2% higher than that of the lamellar region, respectively. This suggests that the amount of aluminum, characterized by its low melting and evaporation temperature, decreases upon interaction with the electron beams in PBF-EB technology.

Figure 4.7 (b) highlights the coarse and fine regions separated by dashed yellow lines. It was found that the coarse γ colonies along the cross section in the parallel observation direction sample were oriented perpendicular to the production direction in the form of bands at regular intervals. EDS mapping in Figure 4.7 (c) reveals the absence of elemental segregation at the interface of the coarse bands and the fine grains. The banded nature in parallel section microstructures can be attributed to process related uneven aluminum distribution because of aluminum loss during PBF-EB production, as indicated by EDS measurements in both coarse and fine regions shown in Figure 4.7 (a). This aluminum loss is associated with the formation of a banded microstructure. Wartbichler et al. revealed that the increase in aluminum evaporation is correlated with a rise in the α_2 phase content, depending on PBF-EB parameters [306]. This phenomenon, along with the elevated aluminum concentration of the γ phase in thermodynamic equilibrium at the PBF-EB operating temperature, leads to abnormal grain growth in regions with a lower concentration of α_2 , where the impact of second-phase particles on grain boundary movement is diminished [306].

Table 4.3: EDS analysis of as-built sample in parallel to build direction at nine different points showed in Figure 4.7 (a).

	Weight%				Atomic%			
	Al	Cr	Nb	Ti	Al	Cr	Nb	Ti
A	32.27	2.62	4.94	60.17	46.79	1.97	2.08	49.15
B	32.32	2.66	5.20	59.81	46.90	2.01	2.19	48.90
C	32.63	2.88	5.22	59.27	47.28	2.17	2.19	48.37
Average	32.41	2.72	5.12	59.75	46.99	2.05	2.15	48.81
D	31.32	2.81	5.01	60.86	45.72	2.13	2.12	50.03
E	31.11	2.72	5.22	60.95	45.50	2.06	2.22	50.22
F	31.40	2.81	5.37	60.42	45.87	2.13	2.28	49.72
Average	31.28	2.78	5.20	60.74	45.70	2.11	2.21	49.99
G	31.87	2.63	4.73	60.76	46.30	1.98	2.00	49.72
H	32.42	2.60	5.02	59.96	47.11	1.90	2.11	48.88
I	32.81	2.68	5.22	59.29	47.39	2.10	2.16	48.35
Average	32.37	2.64	4.99	60.00	46.93	1.99	2.09	48.98

4.5.2 Microstructural Evaluations on Post Processed Samples

The parameters given in Table 3.6 and Table 3.7 were employed in processing the samples with both HIP and conventional annealing processes, respectively. The objective of the procedure conducted at 1200 °C (HT1) was to subject the samples to annealing in the $\gamma + \alpha$ region, whereas the purpose of the treatment at 1400 °C was to anneal the samples in the single α region, thereby ensuring the development of diverse microstructures. Additionally, to observe the effect of a 100 MPa pressure on the microstructure, HIP was applied at 1200 °C.

In Figure 4.8, optical microscope images taken at 200x magnification depict samples in the parallel and perpendicular observation directions. The yellow-circled regions in Figure 4.8 indicate the presence of pores in the samples. As demonstrated in Figure 4.8 (a) and (b), the as-built specimens initially contained

spherical-shaped pores. Following HIP treatment at 1200 °C, 100 MPa, and 2 hours, it was observed that the pores in the as-built microstructure were eliminated (Figure 4.8 (c) and (d)). However, after HT1 and HT2 treatments, it became evident that the pores were not adequately removed, as clearly seen in Figure 4.8 (e), (f) and Figure 4.8 (g), (h) respectively.

It was determined that specimens subjected to HIP, HT1, and HT2 exhibited a duplex microstructure consisting of equiaxed γ and γ/α_2 lamellae, similar to the as-built condition. In the perpendicular observation direction, illustrated in Figure 4.8 (a), (c), and (e) for as-built, HIPed, HT1 and HT2 processed samples respectively, coarse colonies were observed randomly dispersed within the fine region. However, this pattern differed in the parallel observation direction, as illustrated in Figure 4.8 (b), (d), and (f) for as-built, HIPed, HT1 and HT2 processed samples, respectively. Particularly, it was noted that the banding in the HT1 processed sample in Figure 4.8 (e) resembled that in the as-built sample Figure 4.8 (b). In the parallel observation direction of the HIPed sample (Figure 4.8 (c)), banding was nearly dispersed, with coarse colonies occasionally aligning perpendicular to the production direction. HT2 annealing resulted in a fully lamellar microstructure consisting of γ/α_2 lamellae in both perpendicular (Figure 4.8 (g)) and parallel (Figure 4.8 (h)) observation directions. Another notable observation in the HT2 sample was the complete disappearance of banding in both examination directions.

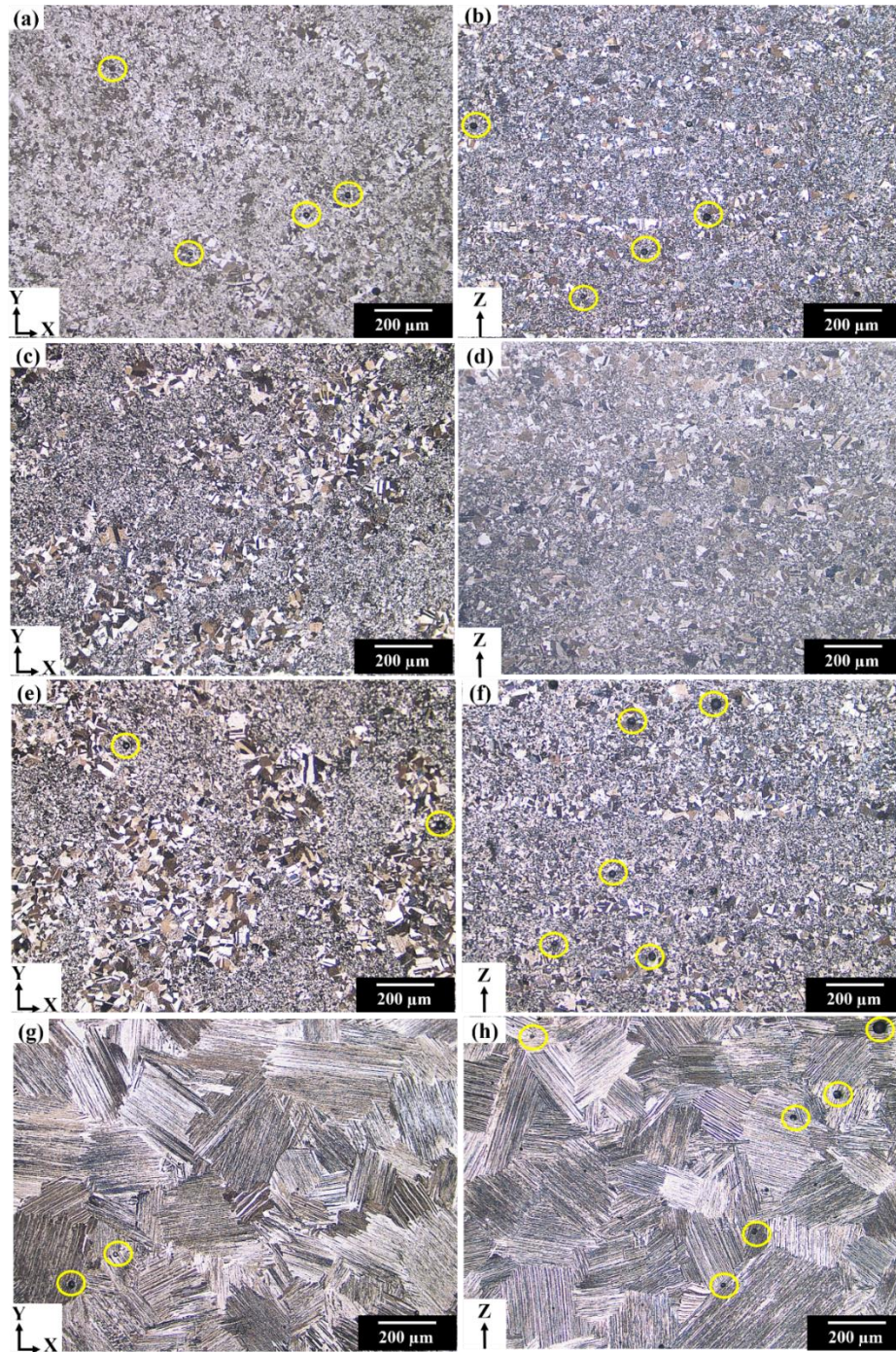


Figure 4.8: PBF-EB fabricated Ti48Al2Cr2Nb alloy optical micrographs at 200x magnification. As-built sample in the observation direction of; (a) perpendicular and (b) parallel. HIPed sample in the observation direction of; (c) perpendicular and (d) parallel. HT1 processed sample in the observation direction of; (e) perpendicular and (f) parallel. HT2 processed sample in the observation direction of; (g) perpendicular and (h) parallel.

In Figure 4.9, secondary electron SEM images are presented for as-built, HIPed, HT1 and HT2 processed samples, illustrating their sections in the perpendicular and parallel observation directions. The larger images in Figure 4.9 were captured at a magnification of 500x using secondary electron imaging, while the small squares located on the left side of each image have a magnification of 2500x to provide a more detailed visual representation. It was observed that the duplex-like microstructure, consisting of γ and α_2 phases, in the as-built sample (Figure 4.9 (a) and (b)) was retained after HIPed (Figure 4.9 (c) and (d)) and HT1 (Figure 4.9 (e) and (f)) samples. However, after HT2 treatment, a fully lamellar microstructure formed as shown in Figure 4.9 (g) and (h). This occurred when the Ti48Al2Cr2Nb material slowly cooled from the single-phase α region after heating up to 1400 °C, leading to the subsequent growth of lamellae consisting of γ and α_2 phases within the prior α phase regions.

It was observed from the SEM images in Figure 4.9 (c) for the HIPed and Figure 4.9 (e) for the HT1 processed perpendicular sectioned samples, as well as in Figure 4.9 (d) for the HIPed and Figure 4.9 (f) for the HT1 processed parallel sectioned samples that the temperature of 1200 °C used for both processes was not sufficient to alter the γ colonies and γ/α_2 lamellae, thereby maintaining the duplex microstructure. However, Figure 4.9 (d) revealed a distinct microstructural characteristic in the HIPed sample, wherein banded γ grains were observed to be separated. This separation was in contrast to the microstructure of the HT1 sample, as shown in Figure 4.9 (f). Coarse γ colonies were observed in both perpendicular and parallel sections of all samples except for the HT2 sample. The both build directions exhibited a duplex-like microstructure consisting of coarse γ colonies and fine lamellae in the as-built, HIPed, and HT1 samples. Minor grain growth was observed in the γ colonies of the HIPed and HT1 samples compared to the as-built sample, as will be further discussed in the section presenting the EBSD results.

A fully lamellar microstructure was not observed until the heat treatment temperature was raised to 1400 °C. A subsequent cooling rate of 5 °C/min was applied after holding the sample at 1400 °C for 2 hours. During slow cooling from

the single α phase region, γ and α_2 lamellae developed within the prior α boundaries for both perpendicular and parallel observation directions, as shown in Figure 4.9 (g) and Figure 4.9 (h), respectively. The lamellar colony size was measured $186.7 \mu\text{m} \pm 41.6 \mu\text{m}$ and $192.0 \mu\text{m} \pm 45.5 \mu\text{m}$ for perpendicular and parallel observation direction samples, respectively. Platelets of the γ and α_2 phases formed during the $\alpha \rightarrow \alpha + \gamma \rightarrow \alpha_2 + \gamma$ phase formation sequence for the both building directions. The formation of γ lamellae initiated in the $\alpha + \gamma$ two-phase region. At the eutectoid temperature, the $\alpha \rightarrow \alpha_2$ ordering reaction initiated, leading to an increase in the volume fraction of the γ phase. The development of a lamellar microstructure is desirable when the Ti48Al2Cr2Nb alloy is subjected to stress at elevated temperatures. Therefore, in order to increase the creep strength after PBF-EB production, a heat treatment above the α transition temperature should be employed to achieve the microstructure shown in Figure 4.9 (g) and Figure 4.9 (h) [190], [296].

Spherical pores were observed in both the XY- and Z-directions of the as-built, HT1, and HT2 samples in Figure 4.9. Despite the low pore ratio in the PBF-EB as-built samples, complete elimination of spherical pores could not be achieved. It was noted that the pores were effectively eliminated through the HIP process. However, after heat treatments at 1200 °C (HT1) and 1400 °C (HT2) without applying pressure, the pores were not completely eliminated.

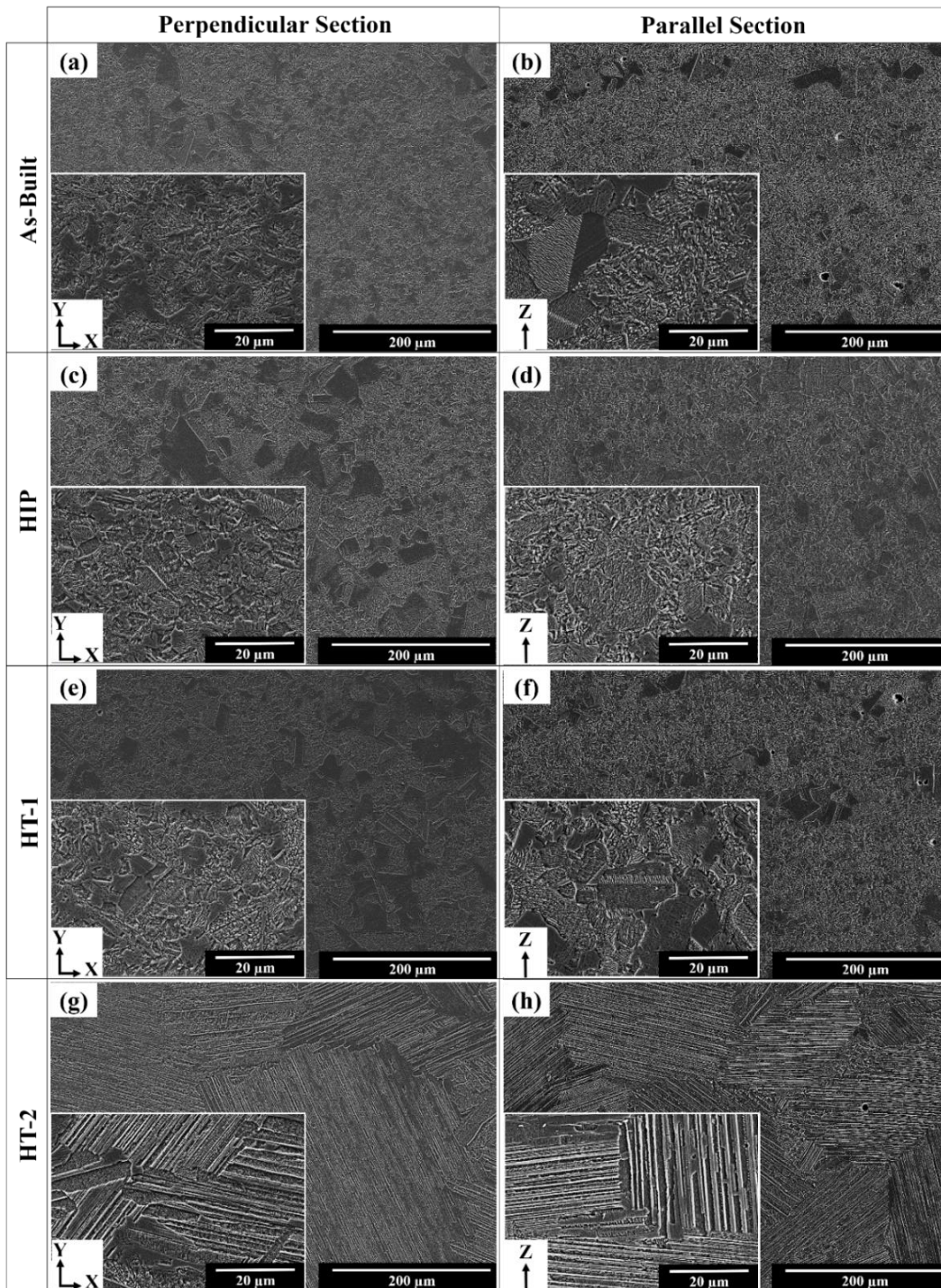


Figure 4.9: PBF-EB fabricated Ti48Al2Cr2Nb alloy secondary electron SEM images. As-built sample in; (a) perpendicular and (b) parallel observation direction. HIPed sample in; (c) perpendicular and (d) parallel observation direction. HT1 processed sample in; (e) perpendicular and (f) parallel observation direction. HT2 processed sample in; (g) perpendicular and (h) parallel observation direction.

To gain a clearer understanding of the banded structure in parallel observation directions, a more in-depth examination was conducted on samples exhibiting a duplex-like microstructure, including as-built, HIPed, and HT1 processed specimens. Figure 4.9 presents optical micrographs and SEM images of as-built, HIPed, and HT1 processed samples observed in parallel section. All samples exhibited a duplex-like microstructure consisting of γ colonies and γ/α_2 lamellae, suggesting that this structure persisted after both HIPing and HT1 processing. Notably, Figure 4.9 (b) and (e) revealed a unique microstructural feature in the HIPed sample, where the banded structure in γ grains began to diminish, distinguishing it from HTed samples (Figure 4.9 (c) and (f)). In HT1 processed samples, coarse γ colonies aligned perpendicular to the building direction, forming a banded structure similar to that of the as-built sample. The impact of the building direction on the microstructure was less evident in the HIPed samples, with coarse colonies showing no distinct banded structure. Minor grain growth was observed in the coarse colonies of the HIPed and HTed samples compared to the as-built sample, as discussed further in section 4.6 on Electron Backscattered Diffraction Evaluation.

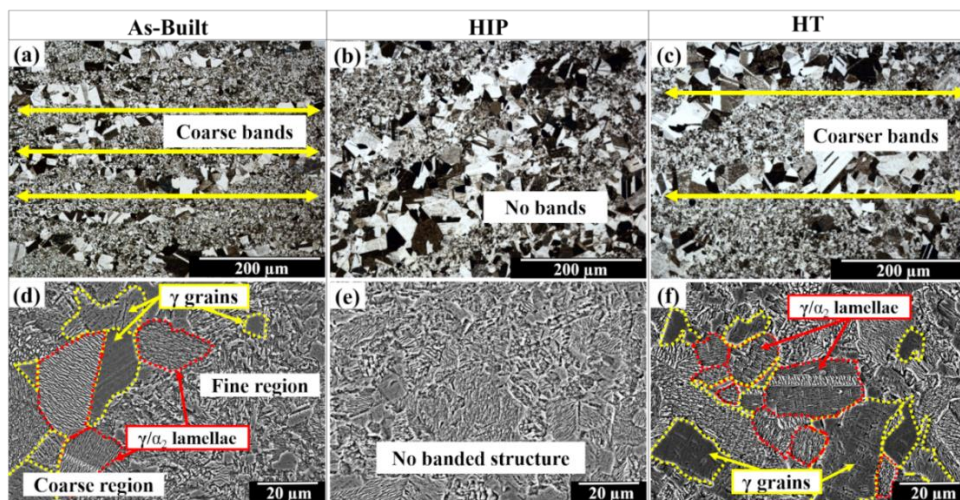


Figure 4.10: Optical microscope images taken from cross-sections parallel to building directions in; (a) as-built, (b) HIPed, and (c) HT1 processed conditions. Secondary electron SEM images taken from identical sections in; (d) as-built, (e) HIPed, and (f) HT1 processed conditions.

The influence of the production direction on the microstructure was eliminated in the HT2 processed samples. In both perpendicular and parallel observation direction samples, there were no visible coarse γ colonies, and the microstructure consisted of α_2 and γ lamellae as seen in Figure 4.9 (g) and (h). The microstructure of the HT2 processed sample in the perpendicular observation direction was examined in detail in Figure 4.11 to elaborate the effect of the HT2 process. Figure 4.11 (a) presents bright particles distributed throughout the dark structure on the less etched surface. Figure 4.11 (b) shows the bright particles located between γ and α_2 lamellae. In Figure 4.11 (c), EDS analyses were conducted on the bright particle labeled as "1" and its neighboring dark region which was labeled as "2". The elemental distribution of particle "1" was found to be an average of 61.89 wt.% (51.72 at.%) Ti, 29.51 wt.% (43.78 at.%) Al, 6.23 wt.% (2.69 at.%) Nb, and 2.36 wt.% (1.82 at.%) Cr. The dark region labeled as "2" exhibited an average elemental distribution of 61.85 wt.% (51.35 at.%) Ti, 30.01 wt.% (44.24 at.%) Al, 5.39 wt.% (2.31 at.%) Nb, and 2.75 wt.% (2.10 at.%) Cr. Accordingly, it was found that the bright particle contained 0.84 wt.% more Nb compared to the neighboring dark region. In Figure 4.11 (d), the EDS map presented the elemental distribution of the region shown in Figure 4.11 (c). It was observed that the amount of aluminum was lower in the α_2 lamellae dispersed between the γ phase. Additionally, it was determined that the bright particle exhibited Nb microsegregation. The previous study has identified the formation of particles with Nb microsegregation within the fully lamellar microstructure of Ti48Al2Cr2Nb alloy produced by plasma melting [309]. Furthermore, it is known that Nb microsegregation occurs in titanium aluminides with high Nb content [311]. In our study, the as-built duplex-like microstructure resulting from PBF-EB production was transformed into a fully lamellar structure through the HT2 process. It was found that the HT2 process caused Nb microsegregation.

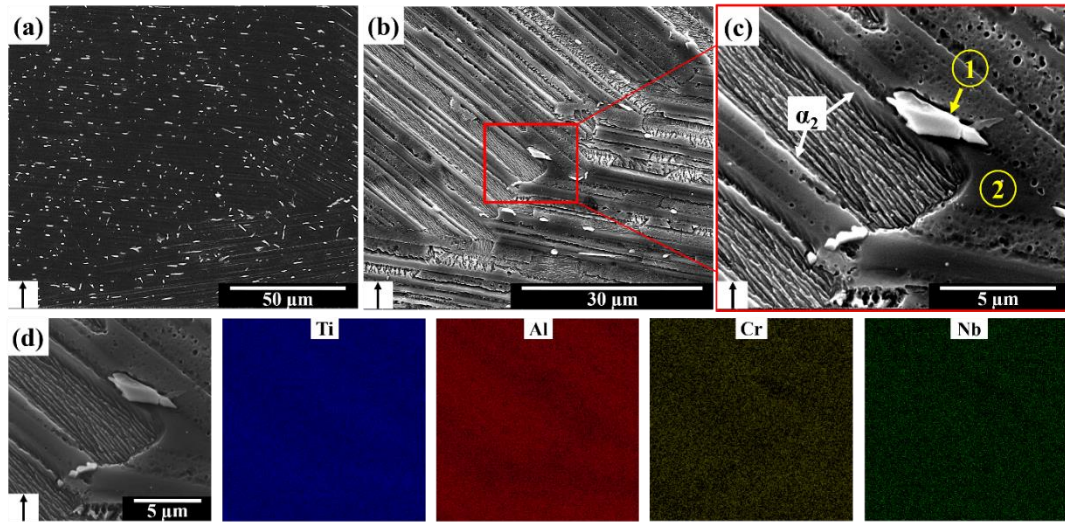


Figure 4.11: Secondary electron SEM images of parallel observation direction of HT2 processed sample. (a) Less etched surface to represent bright particles, (b) the bright particles located between the γ/α_2 lamellae, (c) EDS point analyses regions, (d) EDS mapping obtained from the lamellar region.

4.6 Electron Backscattered Diffraction Evaluation

The phase maps of the as-built, HIPed, HT1, and HT2 samples are depicted in Figure 4.12 to assess the distribution of γ and α_2 phases in the parallel to build direction section. In the phase maps, red areas represent the α_2 phase, while the remaining regions consist of the γ phase. The as-built sample, illustrated in Figure 4.12 (a), exhibited a composition of 1.7% α_2 phase and 98.3% γ phase. The rapid cooling rate in the PBF-EB process resulted in a γ grain size of approximately $4.27 \pm 2.82 \mu\text{m}$, while the average grain size for the α_2 phase was approximately $1.32 \pm 0.28 \mu\text{m}$ in the as-built sample.

The α_2 phase content increased to 3.1% after the samples underwent HIPing, aligning with the Rietveld analysis results indicating an increase in α_2 phase content due to HIPing. In the as-built sample, the α_2 phase primarily formed in finer-grained regions and was rarely observed in the banded coarse areas. However, in the HIPed sample, the banded microstructure almost disappeared, resulting in a

more uniform distribution of the α_2 phase compared to the as-built sample. Fine α_2 grains with an average grain size of $2.23 \pm 0.91 \mu\text{m}$ formed at the relatively coarse γ grain boundaries, as shown in Figure 4.12 (b). HIPing led not only to an increase in the α_2 phase content but also in the average grain size of γ grains to $17.90 \pm 12.71 \mu\text{m}$. The γ grain size increased almost four times, while the size of the α_2 phase increased 1.5 times for HIPed samples compared to the PBF-EB as-built condition.

It was found that the amount of α_2 phase remained the same, at 1.7%, as in the as-built sample when HT1 was applied, as indicated in the phase map shown in Figure 4.12 (c). The α_2 phase was identified in the finer γ -phase regions, and its presence hindered additional grain growth during HT1, exerting a pinning effect. However, in the as-built sample, the banded γ grain regions experienced further coarsening during HT1, as the α_2 phase was nearly absent in this region. Consequently, a more pronounced banded structure emerged in the microstructure of the HT1 processed samples, exhibiting two distinct regions comprising coarse and fine grains. HT1 caused a slight increase in γ grain size to $5.42 \pm 3.48 \mu\text{m}$, while the average size for α_2 phase was $1.23 \pm 0.29 \mu\text{m}$.

HT2 was conducted well above the α transition temperature, resulting in a fully lamellar microstructure upon slow cooling. The lamellar microstructure illustrated in Figure 4.12 (d) occurred after HT2 performed above the α single-phase region transition temperature. HT2 led to an enormous increase in the content of α_2 phase. The HT2 processed sample contained 9.0% α_2 and 90.8% γ phases. It was found that both γ and α_2 grain sizes coarsened following HT2. The average grain size increased to $72.7 \pm 35.43 \mu\text{m}$ for γ and to $4.4 \pm 1.98 \mu\text{m}$ for α_2 grains due to slow cooling done in the furnace.

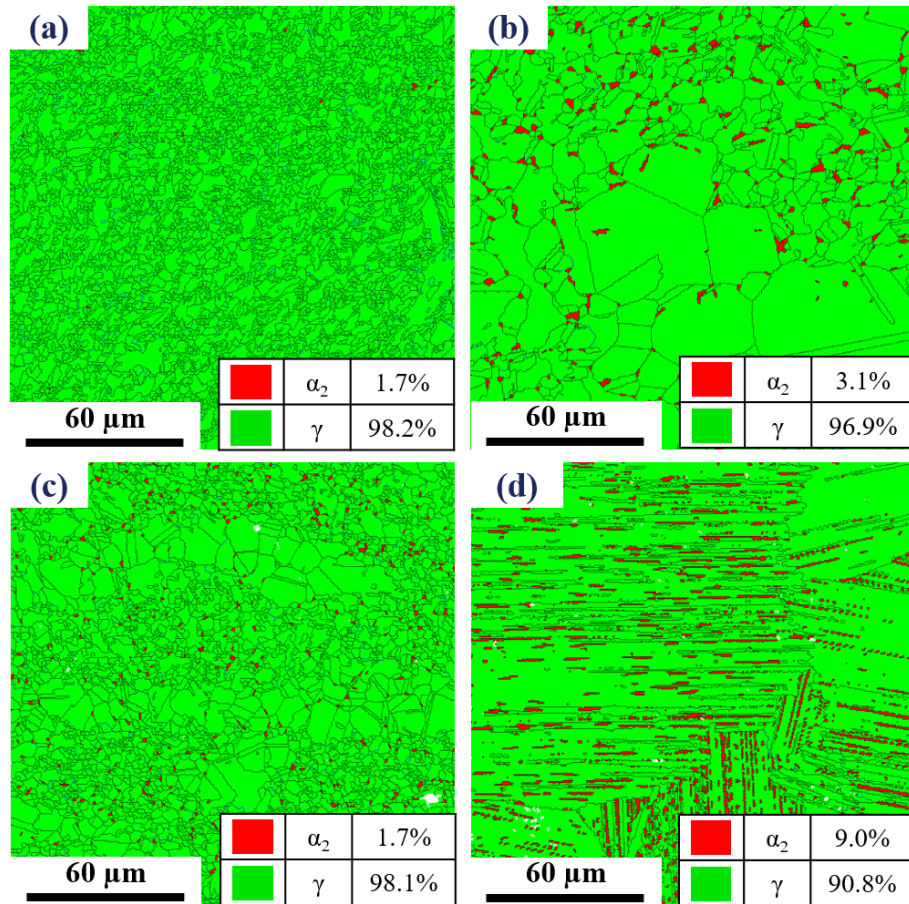


Figure 4.12: Phase maps of; (a) as-built, (b) HIPed, (c) HT1 and (d) HT2 processed samples in parallel observation direction.

The image quality and grain boundaries (IQ-GBs) maps are shown in Figure 4.13 along with the misorientation angle fractions of the as-built, HIPed, HT1, and HT2 processed samples. In Figure 4.13, low angle grain boundaries (LAGBs) are characterized by blue lines for $5 - 15^\circ$, while high angle grain boundaries (HAGBs) are represented by black lines for $15 - 90^\circ$. On the other hand, red lines correspond to γ phase twin boundaries with a 60° misorientation angle. The misorientation distribution of the as-built sample mainly consisted of HAGBs with a rate of 77.1%. The fraction of HAGBs increased to 80.8%, 95.3%, and 98.2% for the HIPed, HT1, and HT2 samples, as shown in Figure 4.13 (b), (c), and (d), respectively. As thermal treatment was applied, LAGBs conversely tended to

decrease due to the reduction in the dislocation density. LAGBs generally consist of more sub-structures formed by the rearrangement of dislocations [302], hence it is normal to expect a lesser amount of LAGBs in the HIPed, HT1, and HT2 samples when compared to the as-built condition. Twin boundaries, illustrated by the red lines in IQ-GB maps in Figure 4.13, were observed for all of the samples. Twin boundaries favor the material strength and the resistance to intergranular degradation [303]. Twin boundary fractions on (111) for the as-built sample, HIPed, HT1, and HT2 samples were 0.123, 0.177, 0.157, and 0.372, respectively. It can be summed up that the twin boundary fraction increased with the increment of heat treatment temperature. On the other hand, the twin boundary fraction of the HIPed sample increased more even if the treatment temperature was similar to HT1. The twin boundary fractions of the HT2 sample were more than 3 times higher when compared to the as-built sample. It is clear that the amount of α_2 phase, which was formed along with γ lamellae, increased as a result of slow cooling after the heat treatment at 1400 °C. Therefore, the twin boundary fraction on (111) for the HT2 sample showed a tendency to increase with increasing α_2 content at the grain edges next to non-recrystallized regions.

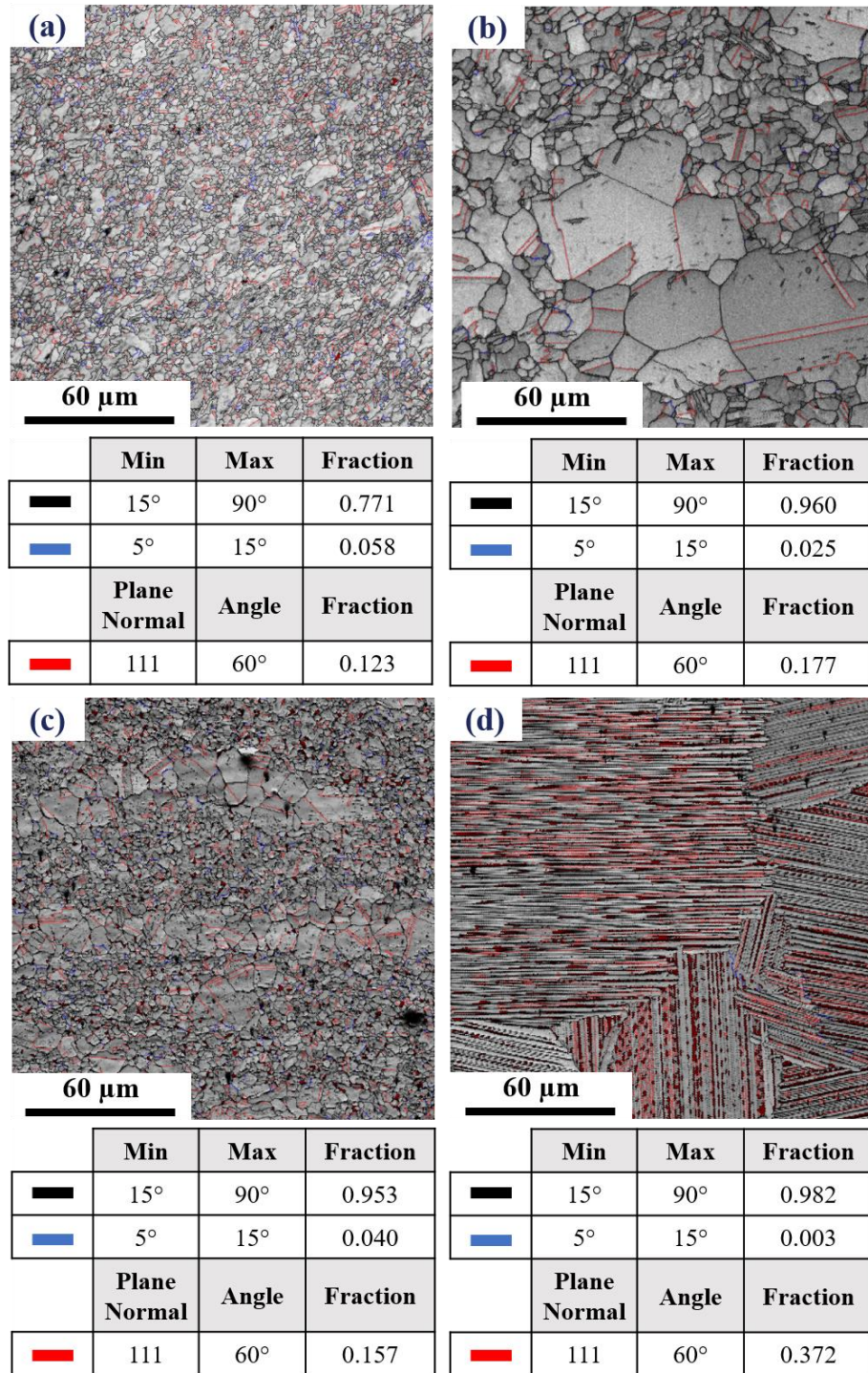


Figure 4.13: IQ-GBs maps of; (a) as-built, (b) HIPed, (c) HT1, and (d) HT2 processed samples in parallel observation direction.

The crystallographic texture of the parallel to build direction sections of the as-built, HIPed, HT1, and HT2 samples is revealed in the inverse pole figure (IPF) maps shown in Figure 4.14 (a), (b), (c), and (d), respectively. The as-built, HIPed, and HT1 samples exhibited a duplex-like microstructure, characterized by the presence of coarse, equiaxed grains and fine lamellae consisting predominantly of γ phases. In addition to the lamellar region, fine α_2 grains were also observed along the grain boundaries of the γ phase, mainly in the HIPed samples. These α_2 grains formed at the interfaces between the coarse, equiaxed γ grains, contributing to the duplex microstructure. The presence of fine α_2 grains along the grain boundaries indicates a localized precipitation of the α_2 phase in these regions. In contrast to the as-built, HIPed, and HT1 samples, the HT2 sample exhibited a distinct microstructure where α_2 and γ grains grew within the prior α grains, forming thin lamellae. The parallel to build direction sections of the as-built, HIPed, and HT1 samples contain mainly fine lamellae alternating with coarse γ grains, while the HT2 sample only exhibits a lamellar microstructure.

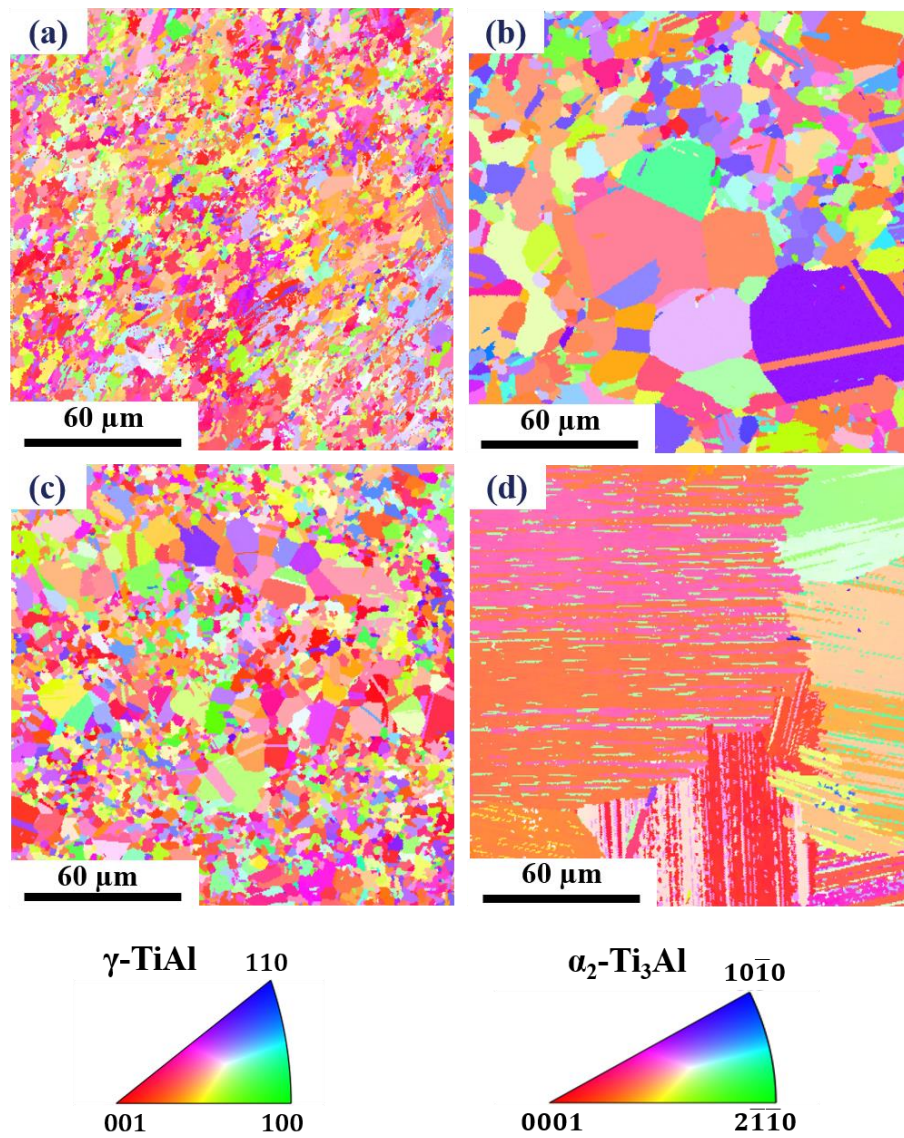


Figure 4.14: IPF maps of; (a) as-built, (b) HIPed, (c) HT1, and (d) HT2 processed samples in parallel observation direction.

The crystallographic orientations of the samples produced in their as-built state, after HIP, following the first heat treatment (HT1), and after the second heat treatment (HT2) are depicted in the inverse pole figures (IPFs) in Figure 4.15 (a), (b), (c), and (d) respectively. The prevalent texture in all samples is the $\langle 001 \rangle // \text{BD}$ (BD: Building Direction). The IPFs reveal a distinct cube texture in the as-built

sample, where $\langle 001 \rangle$ aligns parallel to the building direction, corresponding to the heat flux direction in the PBF-EB process. HT1 significantly enhanced the $\langle 001 \rangle$ texture, increasing its intensity by 65.2% compared to the as-built sample. However, HIP seems to have introduced some degree of randomization in the crystallographic texture. Thus, while HT1 promotes the cube texture, HIP tends to diversify it. Conversely, HT2 annealing resulted in a substantial increase of both the $\langle 001 \rangle // \text{BD}$ texture and its intensity. The intensity of the $\langle 001 \rangle // \text{BD}$ texture became more than four times higher than that of the as-built sample. It is evident that elevating the annealing temperature contributes to an increased PBF-EB texture. HIP was identified as the sole effective method for diminishing the textured structure arising from the heat flux direction in PBF-EB.

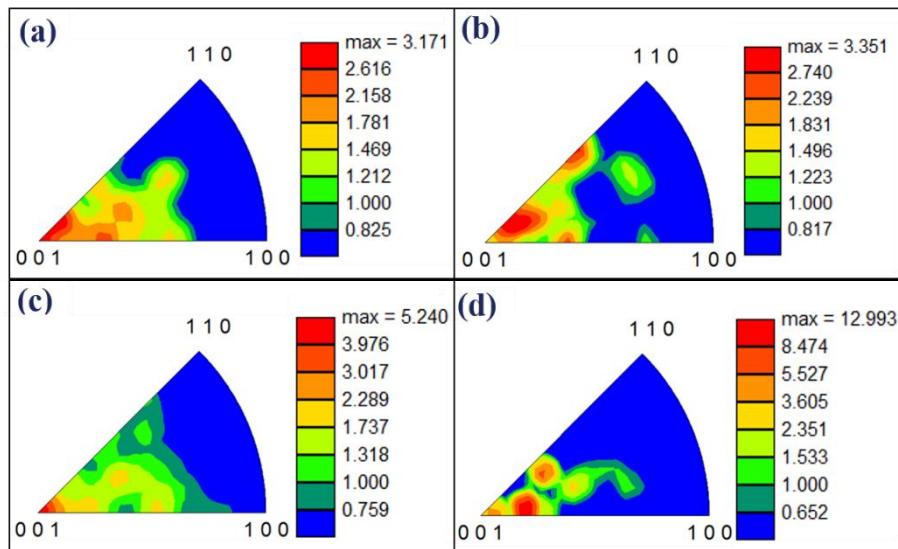


Figure 4.15: IPFs of; (a) as-built, (b) HIPed, (c) HT1 and (d) HT2 processed samples in parallel observation direction.

The kernel average misorientation (KAM) maps for the sections parallel to the build direction of the as-built, HIPed, HT1, and HT2 processed samples are illustrated in Figure 4.16 (a), (b), (c), and (d), respectively. KAM is a technique

used to quantify the local grain misorientation within a microstructure, providing insights into the distribution of deformation and plastic strain within a material. Higher KAM values indicate regions of elevated plastic strain and increased dislocation density [304]. The KAM maps utilize a rainbow scale, where blue and red represent the minimum and maximum misorientation ($0 - 5^\circ$), respectively.

In Figure 4.16 (a), the PBF-EB as-built sample displays higher KAM values compared to the heat-treated and HIPed samples. The KAM maps of the HIPed and HT1 samples (Figure 4.16 (b) and (c), respectively) reveal blue regions indicative of recrystallized grains. Notably, despite both being treated at 1200°C , the KAM value of the HIPed sample is higher than that of the HT1 sample, suggesting that the pressure applied during HIP hindered the recrystallization process, leading to the formation of α_2 precipitates at the γ grain boundaries.

Moreover, in Figure 4.16 (d), the KAM map for the HT2 sample indicates a more pronounced dislocation density along the α_2 lamellae. These maps highlight that the precipitation of the α_2 phase significantly contributes to reducing the amount of recrystallized grains during the thermal treatment.

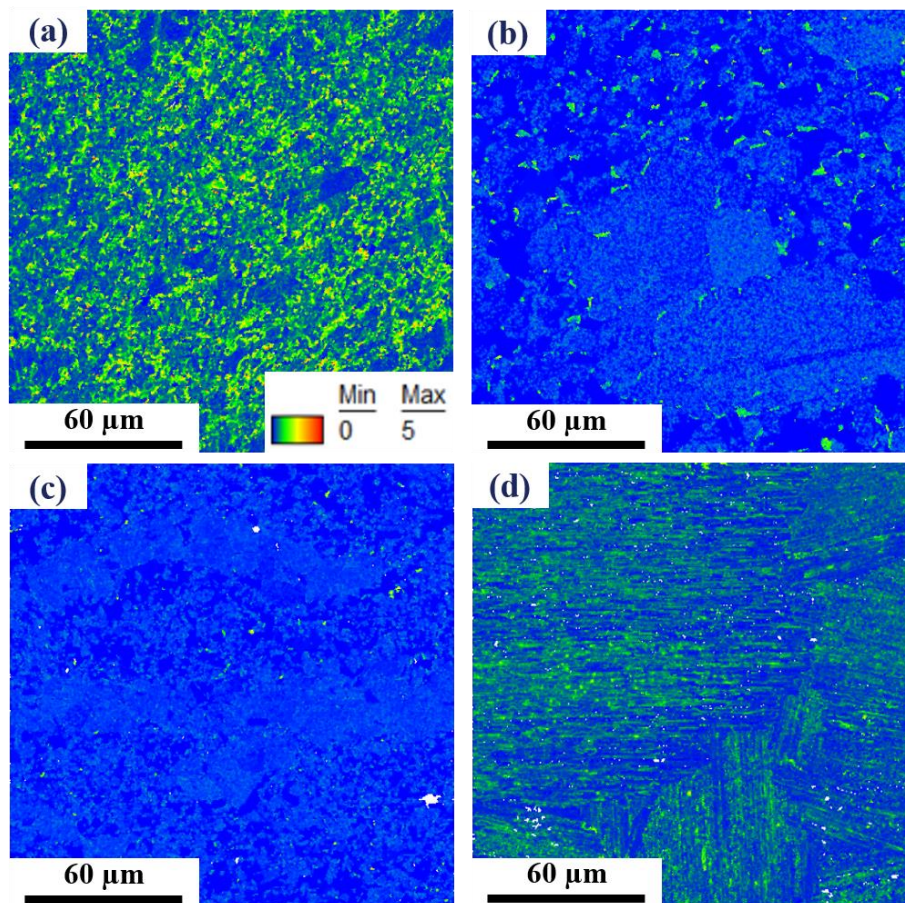


Figure 4.16: KAM maps of; (a) as-built, (b) HIPed, (c) HT1 and (d) HT2 processed samples in parallel observation direction.

The rapid cooling rate experienced during the solidification process in PBF-EB leads to local strain inhomogeneity, resulting in a high dislocation density. Grain orientation spread (GOS) measures the average misorientation angles with respect to the mean orientation of the grains [304]. The GOS maps, labeled with a rainbow scale where blue and red colors represent minimum and maximum GOS angles, display a similar trend to the KAM for the as-built, HIPed, HT1, and HT2 processed samples in Figure 4.17 (a), (b), (c), and (d), respectively.

In Figure 4.17 (a), the PBF-EB manufacturing process resulted in a higher GOS value for the as-built condition compared to the subsequent HIP, HT1, and HT2

processes. The higher GOS value observed in the as-built sample was attributed to the rapid solidification rate and the associated high temperature gradient encountered during PBF-EB production, leading to a heterogeneous microstructure with a higher degree of misorientation among neighboring grains.

Similar to KAM maps, more α_2 precipitates distributed at the γ boundaries caused fewer blue regions, indicating higher GOS angles after the HIP (Figure 4.17 (b)) compared to HT1 (Figure 4.17 (c)). The HT1 sample exhibited more blue regions in the GOS map compared to the as-built condition, despite having the same α_2 fraction (1.7%). This suggests that the dislocation density in the as-built condition was significantly higher, independent of the α_2 ratio. The fully lamellar HT2 sample had a higher GOS value mainly due to the higher α_2 fraction, as illustrated in Figure 4.17 (d).

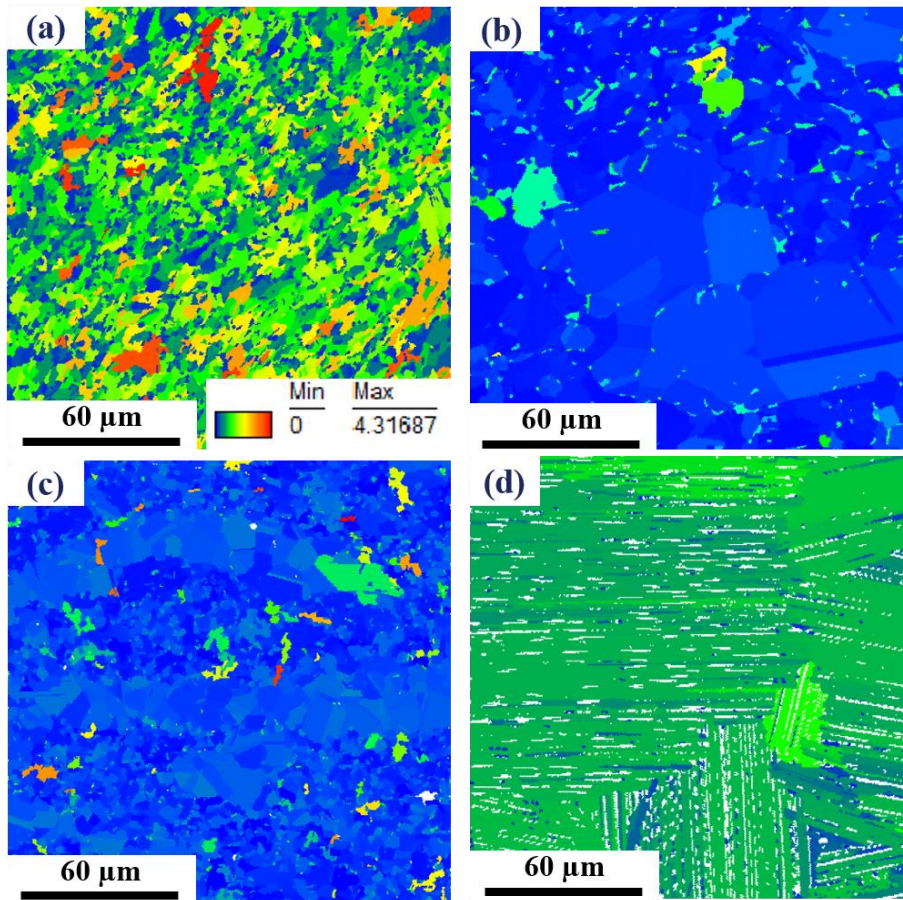


Figure 4.17: GOS maps of; (a) as-built, (b) HIPed, (c) HT1 and (d) HT2 processed samples in parallel observation direction.

The recrystallization fraction of the as-built sample was 74.5%. This proportion grew to 80.5%, 99.4% and 99.9% after HIP, HT1 and HT2 processes, respectively. The KAM and GOS maps show that the HT1 treated sample achieved full recrystallization. In contrast, the HIPed sample had a greater misorientation angle, which was most likely caused by isostatic pressing, resulting in dynamic recrystallization. The HIPed sample's grain coarsening resulted in a decreased recrystallization fraction, with coarser grains leading to a higher misorientation angle.

4.7 Mechanical Evaluations

4.7.1 Microhardness Measurements

To assess the mechanical response of both the coarse equiaxed and fine lamellar regions, microhardness measurements were carried out on the etched surface of the parallel observation direction of the as-built sample. The indentation marks in the microstructure are illustrated in Figure 4.18. Specifically, four measurements in Figure 4.18 (a) – (d) were taken from regions with coarse grains along the build direction, while another four measurements in Figure 4.18 (e) – (h) were taken from the fine region. The microhardness values for the PBF-EB as-built sample are given in Table 4.4. The hardness of the coarse grains in the as-built sample was observed to be lower (272.38 ± 20.92 HV0.1) compared to the fine regions (370.83 ± 24.52 HV0.1). As shown in the Figure 4.6 (b) and (d), fine region are separated by coarse γ bands that are aligned perpendicular to the building direction in the parallel observation direction. The γ phase fraction was determined to be 98.55% using the Rietveld refinement method (Table 4.2) and 98.2% in the EBSD phase map (Figure 4.12 (a)) in the as-built sample. Therefore, it was determined that both coarse grains and fine grains primarily contained the γ phase, while the α_2 phase was present in the form of fine lamellae. It is known that the yield strength of the α_2 phase is higher than that of the γ phase [1]. However, the 98 HV0.1 hardness difference between coarse and fine grains cannot be solely attributed to the amount of α_2 in the lamellar region. The abundance of high-angle grain boundaries (HAGBs) within the lamellar region consisting of fine grains also contributes to the increase in hardness. The discrepancy in hardness between coarse γ grains and γ/α_2 lamellae led to a variation in mechanical properties, serving as a point of crack initiation during uniaxial tensile tests, as further discussed in Chapter 4.7.2.

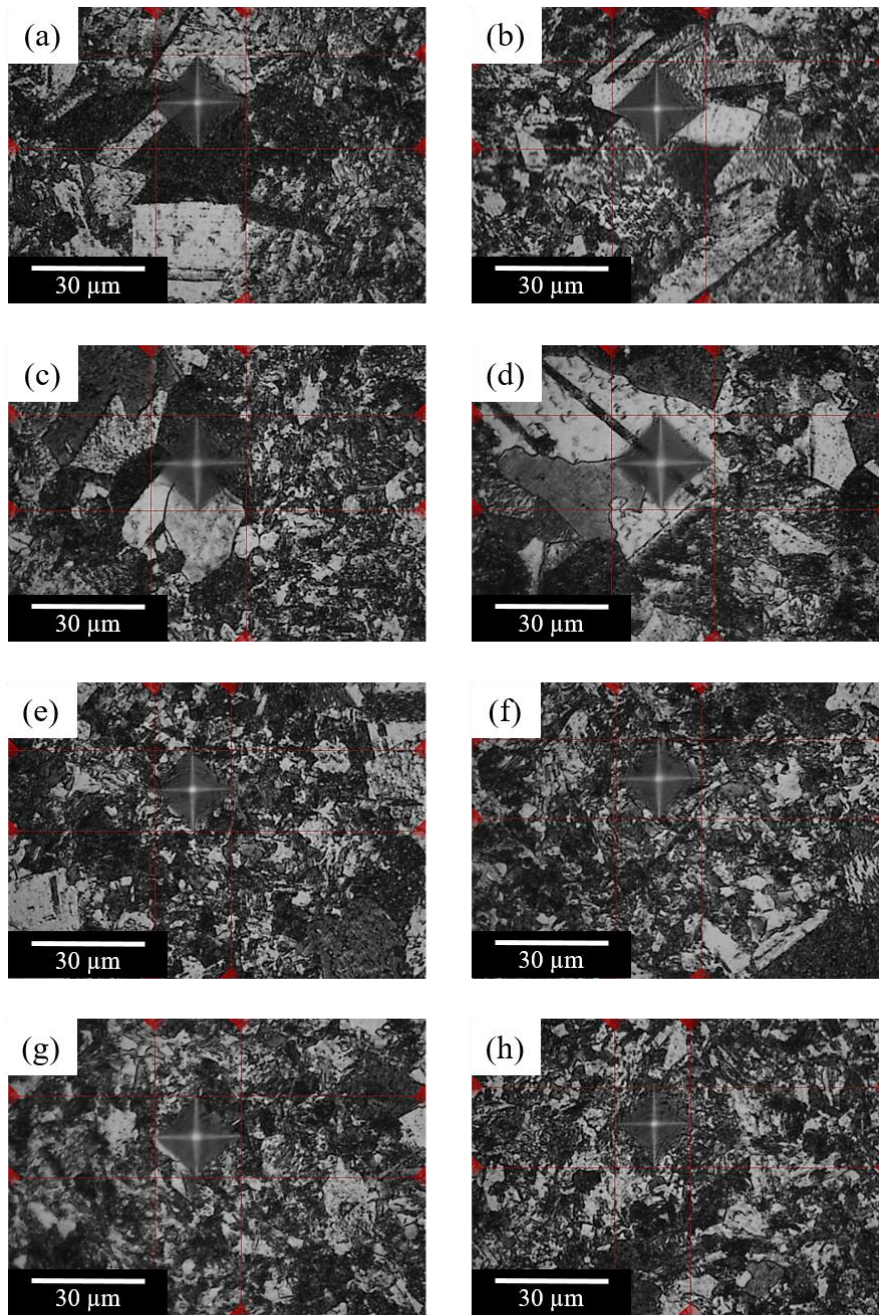


Figure 4.18: Microhardness indentation marks; in γ grains from the; (a) measurement 1, (b) measurement 2, (c) measurement 3, (d) measurement 4 and in $\alpha_2 + \gamma$ lamellae from the; (e) measurement 5, (f) measurement 6, (g) measurement 7, (h) measurement 8.

Table 4.4: Microhardness values of PBF-EB as-built sample.

Region	Measurement No	Hardness (HV-0.1)	Average (HV-0.1)
Coarse γ	1	284.06	272.38 \pm 20.92
	2	294.00	
	3	264.53	
	4	246.94	
Lamellar $\alpha_2+\gamma$	5	390.02	370.83 \pm 24.52
	6	356.09	
	7	344.01	
	8	393.18	

4.7.2 Tensile Tests

Tensile tests were performed at room temperature (RT) and elevated temperatures (600, 700, 800 and 850 °C) on Ti48Al2Cr2Nb as-built samples produced by PBF-EB. HIPed and heat treated samples were tested at RT, 700 and 800 °C.

4.7.2.1 Tensile Tests of As-Built Samples

4.7.2.1.1 Tensile Test Results of As-Built Samples

Table 4.5 and Figure 4.19 present the results of tensile tests conducted on as-built samples produced in the XY-direction. The average yield strength (YS) and ultimate tensile strength (UTS) of Ti48Al2Cr2Nb as-built sample were 560.63 \pm 33.85 and 636.87 \pm 42.43 MPa, respectively, with an elongation (El.%) value of 1.67 \pm 0.53% at room temperature (RT). At 700 °C, YS and UTS values were 476.02 \pm 12.34 and 571.58 \pm 7.14 MPa, respectively, while the El.% was 2.50 \pm 0.00. The XY-direction sample retained its brittle character up to 800 °C. In the

800 °C tensile tests, the average YS and UTS of XY samples were 437.61 ± 1.58 and 568.64 ± 3.68 MPa, respectively, with an El.% of $54.17 \pm 4.39\%$. The elongation value increased approximately 22 times from 700 to 800 °C, while the yield strength decreased by 8% and the tensile strength by 0.5%. The results suggest that the PBF-EB as-built Ti48Al2Cr2Nb sample in the XY-direction undergoes a ductile transition between 700-800 °C.

In the tensile tests conducted on as-built samples at RT and 700 °C, it was observed that the Z-direction samples underwent premature failure, exhibiting an average UTS of 501.50 ± 122.75 and 563.17 ± 64.20 MPa at RT and 700 °C, respectively, with minimal elongation. These samples failed before reaching the yield point, displaying an extremely brittle behavior. At 800 °C, the Z-direction sample demonstrated $10 \pm 8.36\%$ elongation before fracture, with a UTS of 559.00 ± 48.17 MPa and YS of 423.52 ± 8.80 MPa. The notably different mechanical response at 800 °C was attributed to the ductile transition of the Ti48Al2Cr2Nb sample in the Z-direction in the 700–800 °C range.

Table 4.5: Tensile test average results of as-built Ti48Al2Cr2Nb samples.

	Test Temperature (°C)	UTS (MPa)	0.2% YS (MPa)	Elongation (%)
XY-direction	RT	636.87 ± 42.43	560.63 ± 33.85	1.67 ± 0.53
	700	571.58 ± 7.14	476.02 ± 12.34	2.50 ± 0.00
	800	568.64 ± 3.68	437.61 ± 1.58	54.17 ± 4.39
Z-direction	RT	501.50 ± 122.75	-	-
	700	563.17 ± 64.20	-	1.50 ± 0.92
	800	559.00 ± 48.17	423.52 ± 8.80	10.00 ± 8.36

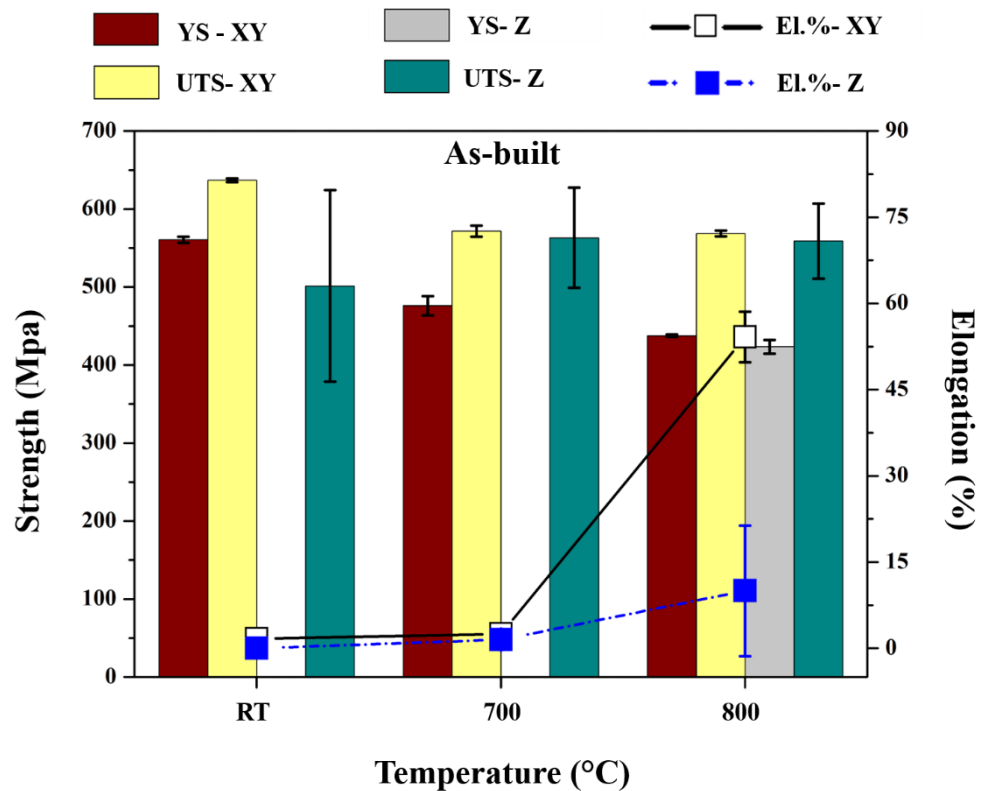


Figure 4.19: Temperature dependent yield strength, tensile strength and elongation values of as-built samples.

4.7.2.1.2 Tensile Test Fracture Surfaces of the As-Built Samples

Figure 4.20 depicts SEM images of the fracture surfaces of the PBF-EB as-built XY- and Z-direction samples. The fracture surfaces resulting from the tensile tests at room temperature and 700 °C were notably flat and brittle, featuring transgranular cracks and interlamellar separation in both building directions. However, on the fracture surfaces of XY and Z samples tested at 800 °C, increased ductility was evident, illustrated by the cup-and-cone formation. Notably, the presence of pores on the fractured surfaces of all samples was observed.

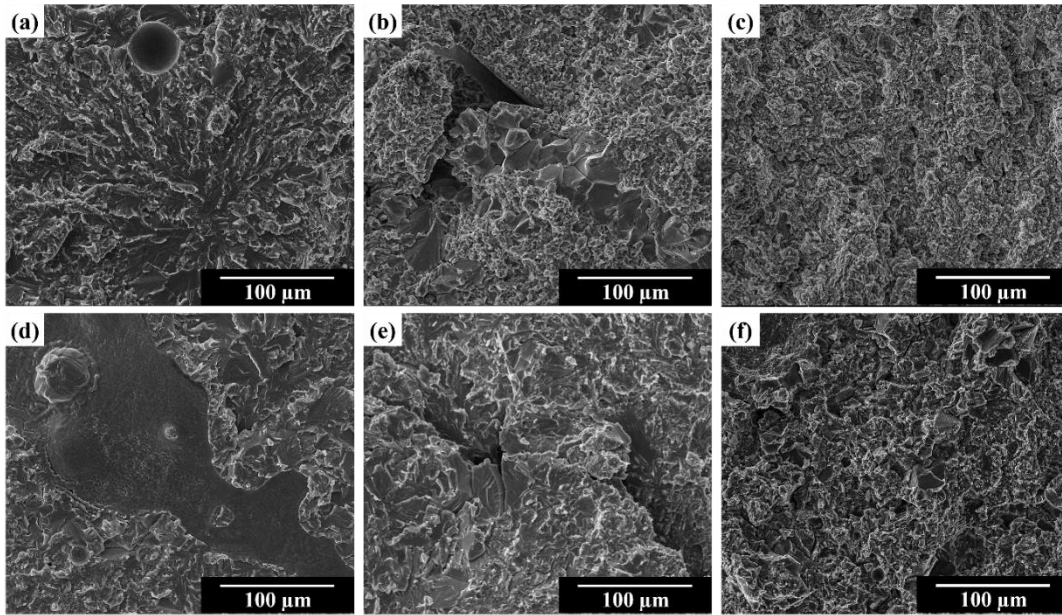


Figure 4.20: SEM images of fracture surfaces of as-built PBF-EB fabricated in XY-direction; (a) room temperature, (b) 700 °C, (c) 800 °C and in Z-direction; (d) room temperature, (e) 700 °C, (f) 800 °C tensile test specimens.

The fracture surface of the as-built XY-direction specimen tested at room temperature is illustrated in Figure 4.21. In Figure 4.21 (a), the region where the fracture initiated and propagated rapidly is depicted. This region exhibits transgranular cracks and flat surfaces, characteristic of brittle fracture. Figure 4.21 (b) zooms in on one of the cracks present on the surface. EDS measurements conducted on both the left (marked as 1 in Figure 4.21 (c)) and right (marked as 2 in Figure 4.21 (d)) sides of the crack revealed a 2.53 wt.% higher aluminum content on the right side and a 3.83 wt.% higher titanium content on the left side of the crack.

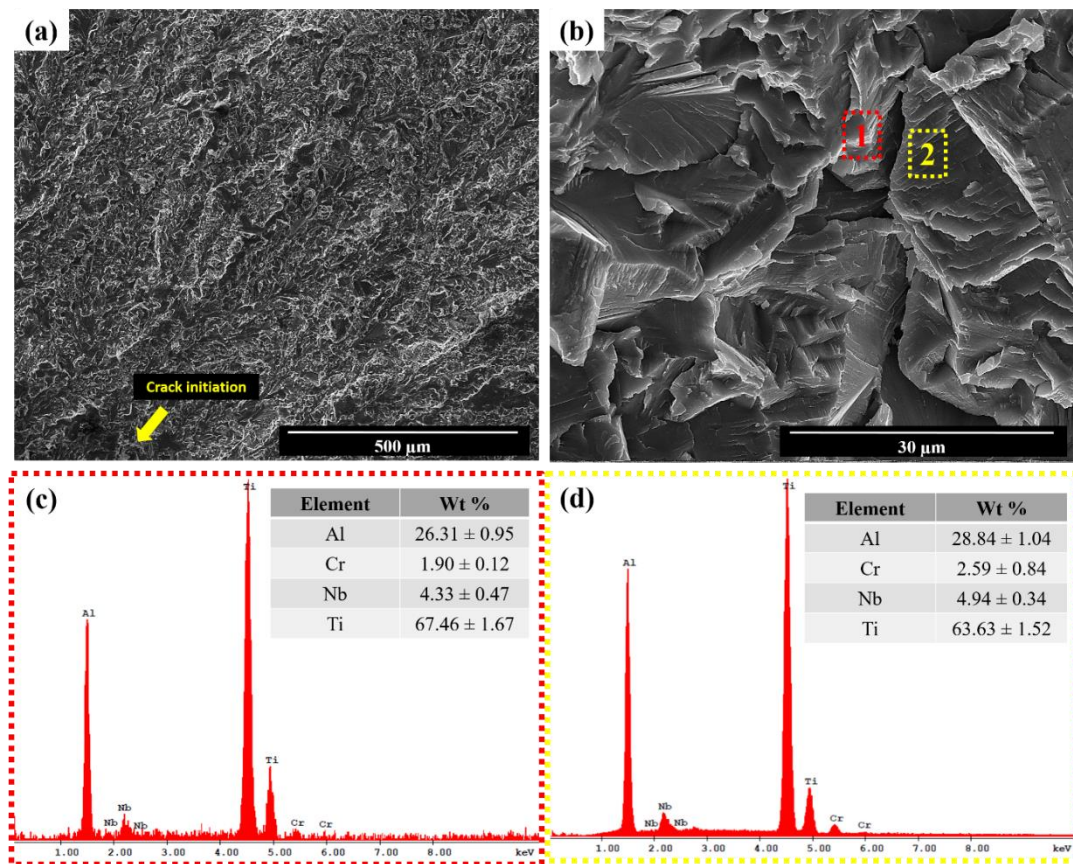


Figure 4.21: SEM images of the fracture surface from room temperature tensile tests on the as-built XY-direction specimen at; (a) 250x, (b) 5000x magnification, along with EDS analysis for (c) the left side (marked as 1) and (d) the right side (marked as 2) of the crack.

The fracture surface of the Z-direction as-built specimen tested at room temperature is depicted in Figure 4.22. In Figure 4.22 (a), the region where the fracture initiates is shown. Traces extending from the rupture initiation site to the forward region of the surface indicate catastrophic fracture propagation. Pores are also observed on the fracture surface, and the main fracture mechanism involves transgranular cracks and extremely flat surfaces. EDS analysis was conducted for one of the cracks appearing on the surface (Figure 3.21 (b)). The aluminum content was found to be 10.17 wt.% lower on the left side (marked as 1 in Figure 4.22 (c)) than on the right side (marked as 2 in Figure 4.22 (d)) of the crack. Additionally,

the amount of titanium was 11.85 wt.% higher on the left side. It was determined that the cracks on the fracture surface of the Z-direction as-built sample propagated through regions with different chemical compositions, resulting in a brittle fracture.

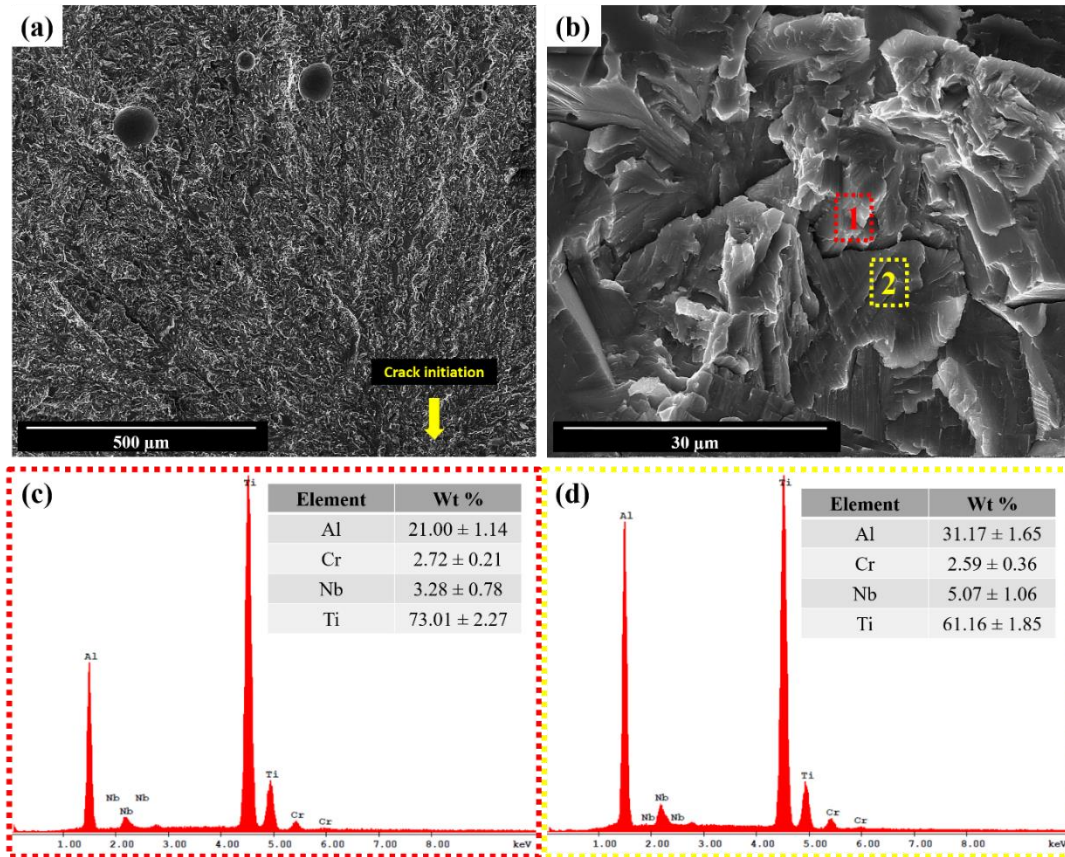


Figure 4.22: SEM images of the fracture surface from room temperature tensile tests on the as-built Z-direction specimen at; (a) 250x, (b) 5000x magnification, along with EDS analysis for (c) the top side (marked as 1) and (d) the bottom side (marked as 2) of the crack.

Figure 4.23 presents optical microscope images of the cross-sections of the room temperature tensile test fracture surfaces for both as-built XY- and Z-direction samples. The specimens were sectioned perpendicular to the fracture planes and then prepared metallographically, as detailed in Chapter 3.5.6, to obtain these optical microscope images. The intersection between the black regions and the

sample surfaces on the left side of the images indicates the fractured regions in Figure 4.23.

Upon closer examination, it was observed that the coarse γ grains were not dispersed at regular intervals in the XY samples, as shown at different magnifications in Figure 4.23 (a) – (d). In contrast, the Z-direction samples, depicted in Figure 4.23 (e) – (h), exhibited γ bands that extended parallel to the fracture surfaces. The optical microscope study also revealed that subsurface cracks in PBF-EB as-built Z-direction samples propagated between coarse γ and fine regions. This investigation highlights that the banding observed in the Z-direction samples during PBF-EB production contributed to premature failure, as elaborated in Chapter 3.7.2.1.

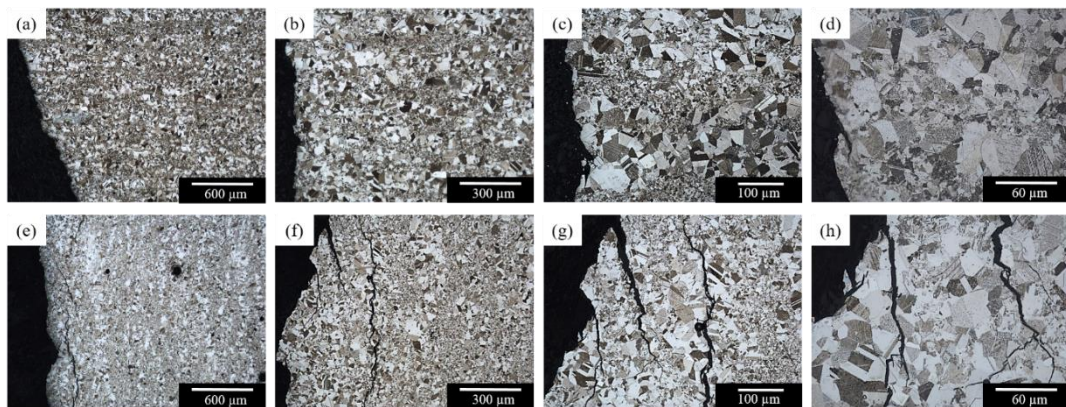


Figure 4.23: Cross section optical micrographs of room temperature tensile test fracture surfaces for PBF-EB fabricated Ti48Al2Cr2Nb as-built samples in XY-direction at; (a) 50x, (b) 100x, (c) 200x, (d) 500x magnifications and in Z-direction at; (a) 50x, (b) 100x, (c) 200x, (d) 500x magnifications.

SEM images of the cross-section of the as-built room temperature tensile testing Z-direction specimen are given in Figure 4.24. In Figure 4.24 (a), it is observed that the γ grains exhibit a banded structure, appearing almost like a line. It's noteworthy that the banded structure observed is perpendicular to both the direction of tensile

testing and the PBF-EB build plane, which is parallel to the fracture surface. Figure 4.24 (b) presents a composite image obtained by superimposing SEM images taken at 1000x magnification with showing the direction of sub-surface crack propagation. The crack was observed to propagate parallel to the fracture surface at the interface where the coarse γ grains are separated from the fine lamellar region. The crack progressed rapidly along the coarse γ grains during the tensile test, leading to premature failure in the as-built samples produced in the Z-direction. Figure 4.24 (c) illustrates the presence of a crack that separates the coarse and fine regions. EDS analyses were performed on the zones labeled as 1 and 2, corresponding to the lamellar and coarse regions, respectively. These analyses enabled the determination of the elemental composition on both sides of the crack. The aluminum content in Zone 1 was found to be 2.22 wt.% lower than in Zone 2, while the titanium content in Zone 2 was 1.71 wt.% lower. This difference in aluminum and titanium content between the coarse γ grains and the fine (lamellar γ/α_2 + equiaxed γ) region contributed to variations in the mechanical properties, as evidenced by the hardness measurements provided in Table 4.4. The premature failure observed in the as-built Z-direction sample can be attributed to the orientation of the coarse γ grains perpendicular to the direction of tensile testing. Furthermore, EBSD analysis revealed that the as-built Z-direction sample exhibited higher KAM (Kernel Average Misorientation) and GOS (Grain Orientation Spread) values compared to the other samples, providing additional evidence for the premature failure in the Z-direction.

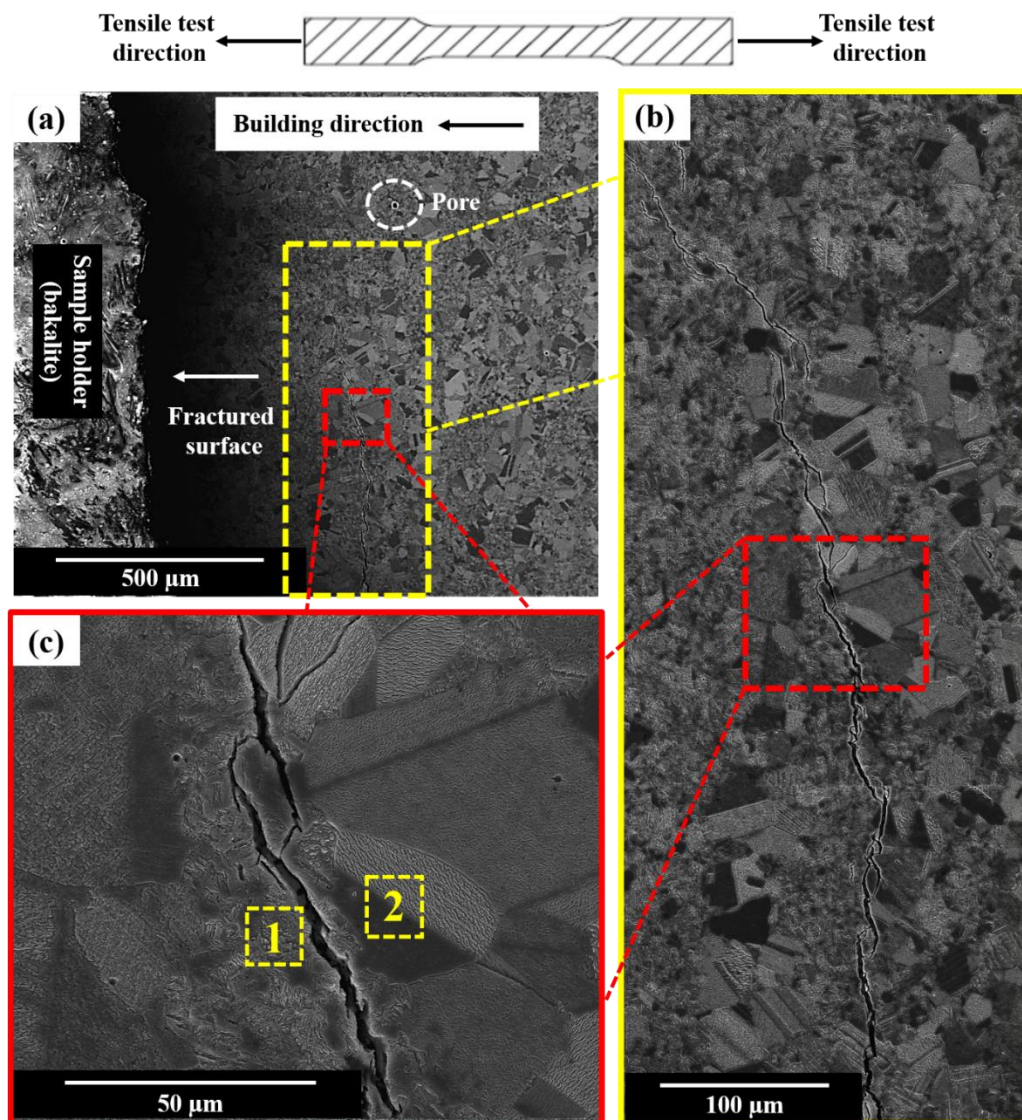


Figure 4.24: Secondary electron SEM images of the cross section of as-built Z-direction room temperature tensile test specimen revealing; (a) sub-surface crack path at a magnification of 1000x, (b) coarse grains aligned parallel to fracture surface at a magnification of 250x, (c) crack zone at a magnification of 2500x.

Figure 4.25 presents optical micrographs of the cross sections for the fracture surfaces of the as-built samples after tensile tests conducted at 700 and 800 °C. The microstructure of the XY-direction samples tested at 700°C (Figure 4.25 (a) and (b)) was found to be similar to the microstructure observed in the room temperature

tests shown in Figure 4.23 (a) and (d). However, at 800 °C (Figure 4.25 (c) and (d)), elongated grains in the tensile direction was observed, indicating a ductile transition. The average elongation at 800 °C was $54.17 \pm 4.39\%$, while at 700 °C, it was $2.50 \pm 0.00\%$ for XY-direction samples. This ductile transition at 800°C is associated with the microstructures illustrated in Figure 4.25 (c) – (d).

In contrast, no elongated grains were observed in the fracture surface microstructure of Z-direction samples at both 700 °C (Figure 4.25 (e) and (f)) and 800 °C (Figure 4.25 (g) and (h)). This lack of elongation suggests premature failure, similar to what occurs at room temperature. However, it must be noted that the subsurface cracks between coarse γ and fine (lamellar γ/α_2 + equiaxed γ) regions observed in the room temperature microstructures (Figure 4.23 (e) - (h)) did not occur at 700 and 800°C, as illustrated in Figure 4.25 (e) and (f).

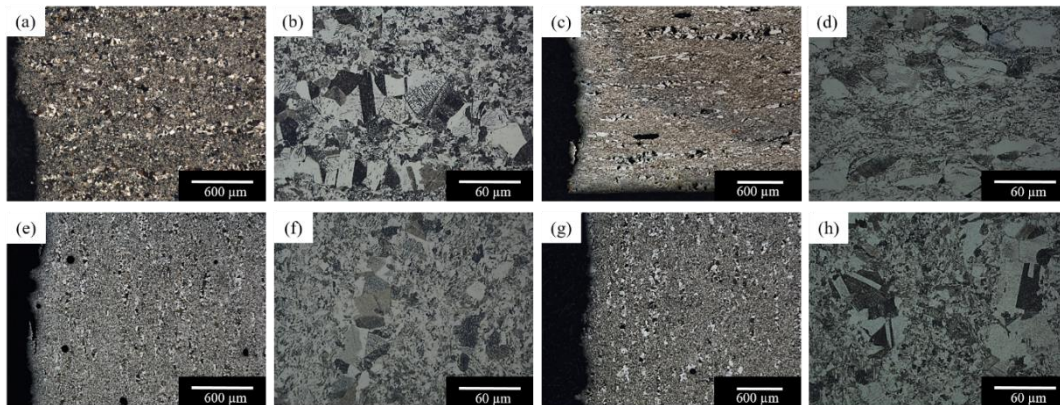


Figure 4.25: Cross-sectional optical micrographs of PBF-EB fabricated Ti48Al2Cr2Nb as-built samples in the XY-direction for; (a) 700 °C tensile test fracture surface at 50x, (b) 700 °C tensile test fracture surface at 500x, (c) 800 °C tensile test fracture surface at 50x, (d) 800 °C tensile test fracture surface at 500x, and in the Z-direction for; (e) 700 °C tensile test fracture surface at 50x, (f) 700 °C tensile test fracture surface at 500x, (g) 800 °C tensile test fracture surface at 50x, (h) 800 °C tensile test fracture surface at 500x.

4.7.2.2 Tensile Tests of HIPed Samples

4.7.2.2.1 Tensile Test Results of HIPed Samples

Table 4.6 and Figure 4.26 present the tensile test results for XY-direction PBF-EB manufactured and subsequently HIPed samples. The average yield strength (YS) of the XY-direction produced HIPed sample was 504.96 ± 17.39 MPa, and ultimate tensile strength (UTS) was 561.03 ± 28.23 MPa, with an elongation (El.%) value of $2.19 \pm 0.45\%$ at room temperature (RT). At 700 °C, YS and UTS values were 453.50 ± 34.65 and 536.47 ± 50.01 MPa, respectively, while the El.% was 3.13 ± 0.88 . This sample maintained its brittle behavior up to 800 °C. In the 800 °C tensile tests, the average YS of XY samples was 418.50 ± 21.92 MPa, UTS was 527.75 ± 9.55 MPa, and the El.% was $34.50 \pm 3.00\%$. Graphs illustrating YS, UTS, and El.% values of XY-direction produced HIPed samples are provided in Figure 4.26. The increase in elongation from 700 to 800 °C indicates a ductile transition temperature between 700-800 °C for XY-direction PBF-EB manufactured and then HIPed Ti48Al2Cr2Nb.

In the tensile tests conducted at RT on HIPed samples, it was observed that the Z-direction samples did not experience premature failure, unlike the as-built test specimens. The average YS of Z-direction produced HIPed sample was 514.49 ± 6.1 MPa, and UTS was 551.81 ± 13.76 MPa, with an El.% value of $2.29 \pm 0.13\%$ at room temperature. At 700 °C, YS and UTS values were 446.50 ± 2.12 and 537.00 ± 41.01 MPa, respectively, while the El.% was 3.75 ± 0.00 . The Z-direction produced HIPed sample maintained its brittle character up to 800 °C with a slightly lower elongation. In the 800 °C tensile tests, the average YS and UTS of Z samples were 390.13 ± 27 and 515.20 ± 17.00 MPa, respectively, while the El.% was $17.50 \pm 7.00\%$. Graphs containing YS, UTS, and El.% values of Z-direction produced HIPed samples are given in Figure 4.26. Raising from 700 to 800 °C, the El.% of the material increased approximately 4.67 times, while the YS decreased by 12.6% and the UTS by 4.1%. According to these values, it was determined that Z-

direction PBF-EB produced and then HIPed Ti48Al2Cr2Nb has a ductile transition temperature between 700-800 °C.

Table 4.6: Tensile test average results of HIPed Ti48Al2Cr2Nb samples.

	Test Temperature (°C)	UTS (MPa)	0.2% YS (MPa)	Elongation (%)
XY-direction	RT	561.03 ± 28.23	504.96 ± 17.39	2.19 ± 0.45
	700	536.47 ± 50.01	453.50 ± 34.65	3.13 ± 0.88
	800	527.75 ± 9.55	418.50 ± 21.92	34.50 ± 3.00
Z-direction	RT	551.81 ± 13.76	514.49 ± 6.1	2.29 ± 0.13
	700	537.00 ± 41.01	446.50 ± 2.12	3.75 ± 0.00
	800	515.20 ± 17.00	390.13 ± 27	17.50 ± 7.00

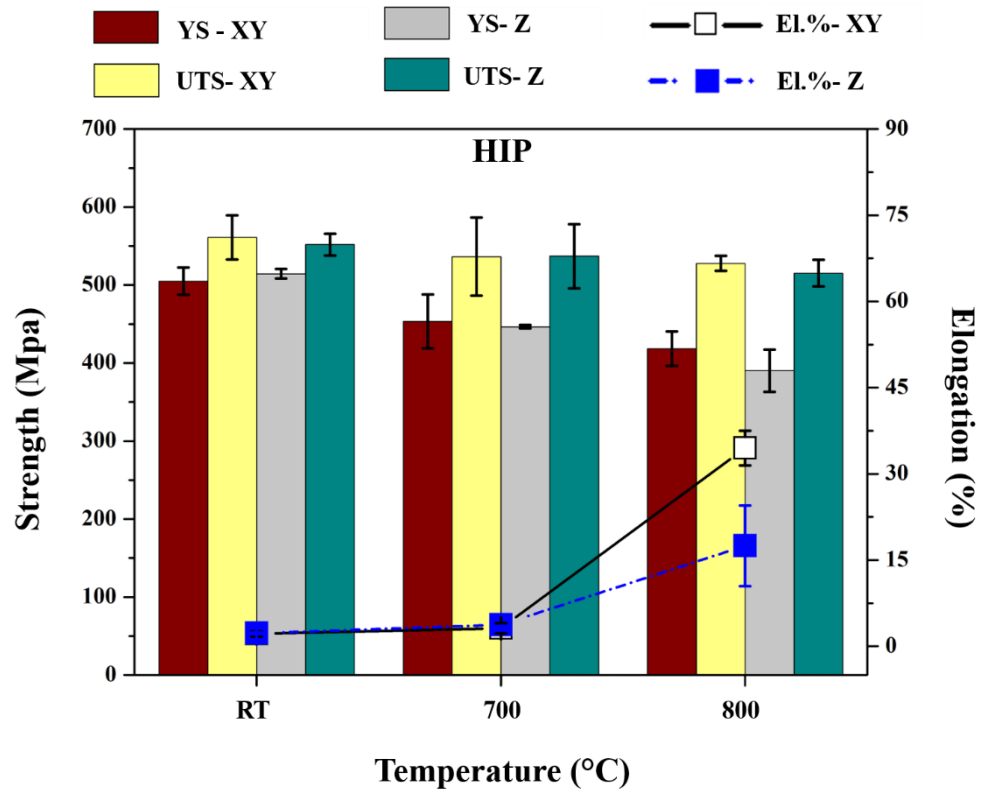


Figure 4.26: Temperature dependent yield strength, tensile strength and elongation values of HIPed XY-direction samples.

4.7.2.2.2 Tensile Test Fracture Surfaces of the HIPed Samples

Figure 4.27 (a) shows that the fracture surface of the XY-direction specimen tested at room temperature was flatter than those tested at 700 (Figure 4.27 (b)) and 800 °C (Figure 4.27 (c)). The dimple formation increased as the tensile test temperature increased for XY-direction samples. This is also confirmed by the tensile elongation values shown in Table 4.6. The tensile elongation of HIPed XY-direction specimens at 700 °C was $3.13 \pm 0.88\%$, while at 800 °C it was quite ductile with $34.50 \pm 3.00\%$. This value was $2.19 \pm 0.45\%$ at room temperature for the HIP applied XY-direction specimen. γ banding was seen on the room temperature (Figure 4.27 (d)) and 700 °C (Figure 4.27 (e)) tensile test fracture

surfaces of the HIP applied Z-direction samples. The fracture surfaces were flatter in the Z-direction compared to the XY-direction samples, implying that the fracture initiated from the γ bands oriented perpendicular to the production direction. As presented in Table 4.6, the tensile elongation of the HIP applied Z-direction specimens was $2.29 \pm 0.13\%$ at room temperature and $3.75 \pm 0.00\%$ at $700\text{ }^{\circ}\text{C}$. As a result of the $800\text{ }^{\circ}\text{C}$ tensile test, the tensile elongation was $17.50 \pm 7.00\%$, which was well below the XY-direction. In addition, as seen in Figure 4.27 (f), the fracture surface was quite flat and dimple-free compared to the XY-direction sample. No pores were found on any of the HIP-applied sample fracture surfaces in either the XY-direction or the Z-direction as seen in Figure 4.27.

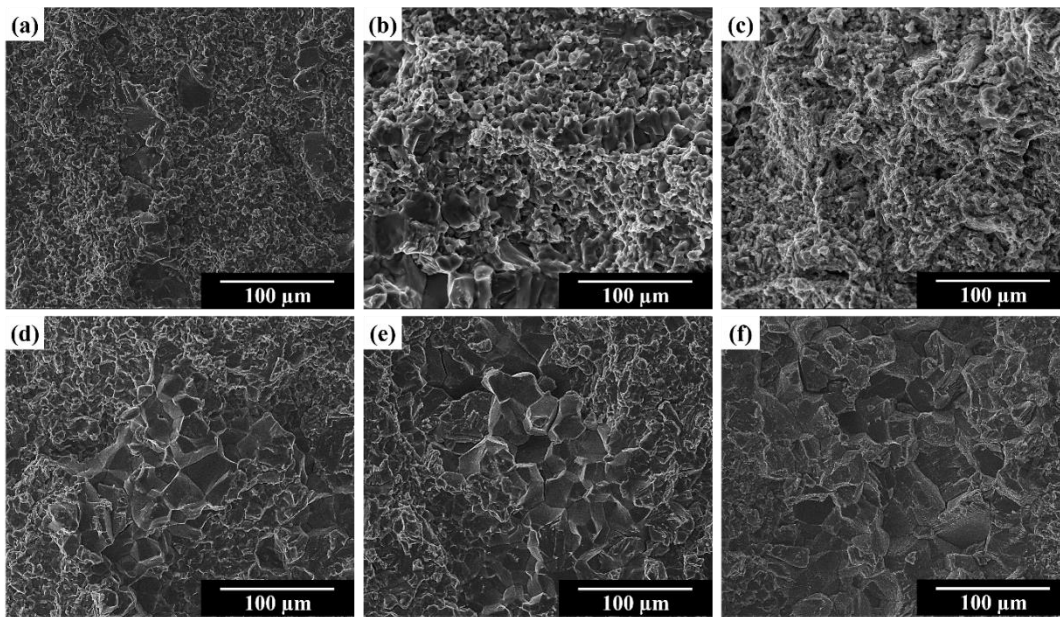


Figure 4.27: SEM images of the fracture surfaces of XY-direction HIPed samples after tensile tests at; (a) room temperature, (b) $700\text{ }^{\circ}\text{C}$, (c) $800\text{ }^{\circ}\text{C}$ and Z-direction HIPed samples after tensile tests at; (d) Room temperature, (e) $700\text{ }^{\circ}\text{C}$, (f) $800\text{ }^{\circ}\text{C}$ tensile test specimens.

The fracture surfaces of the HIPed XY- and Z-direction specimens tested at room temperature are shown in Figure 4.28 and Figure 4.29, respectively. In addition to

transgranular cracks, intergranular cracks were observed in samples from both build directions. The aluminum content difference on either side of the crack in Figure 4.28 (b) for the XY sample was 2.77 wt.%, while in the Z sample in Figure 4.29 (b), it was 9.68 wt.%. This phenomenon was consistently observed in samples that underwent HIP after fabrication in both XY- and Z-directions. Unlike the other samples, no pores were found on the fractured surfaces of the HIPed samples.

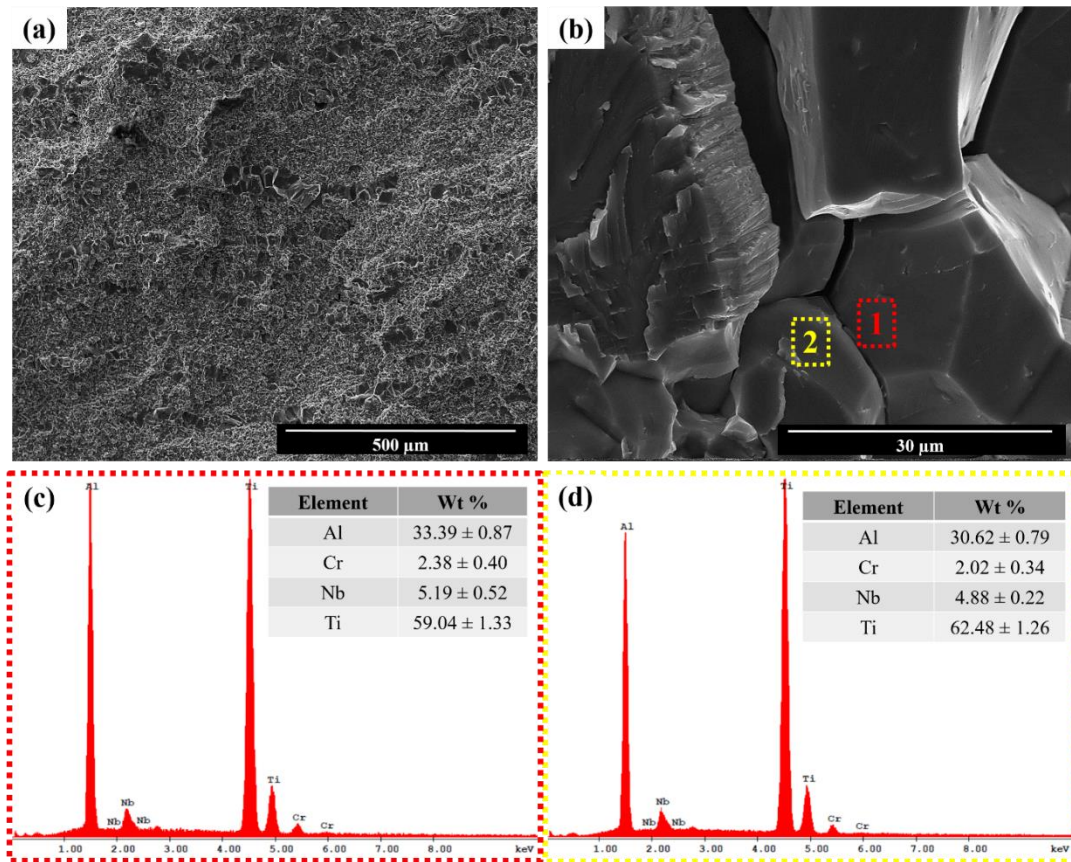


Figure 4.28: SEM images of the fracture surface from room temperature tensile tests on the HIPed XY-direction specimen at; (a) 250x, (b) 5000x magnification, along with EDS analysis for (c) the right side (marked as 1) and (d) the left side (marked as 2) of the crack.

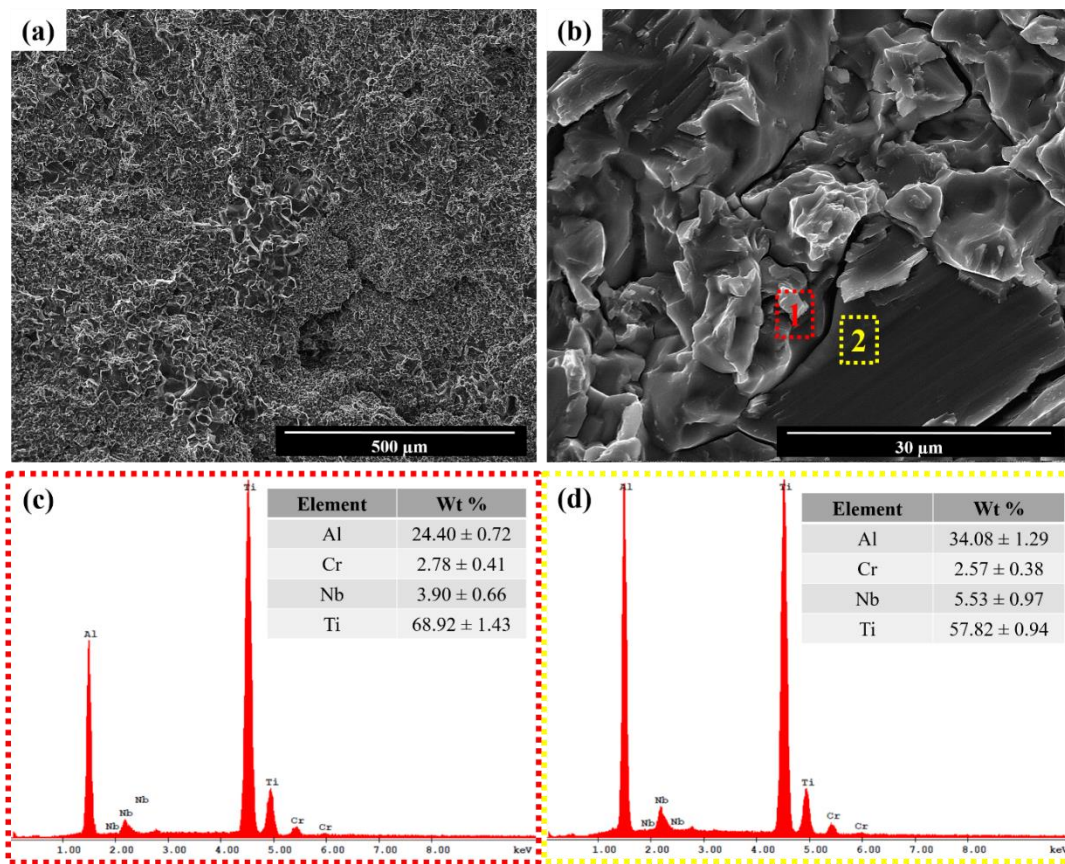


Figure 4.29: SEM images of the fracture surface from room temperature tensile tests on the HIPed Z-direction specimen at; (a) 250x, (b) 5000x magnification, along with EDS analysis for (c) the left side (marked as 1) and (d) the right side (marked as 2) of the crack.

In Figure 4.30, cross-sectional optical microscope images of the room temperature tensile test fracture surfaces for HIPed XY- and Z-direction samples are presented. Both YS and El.% were nearly identical for XY- and Z-direction samples, although anisotropy in the microstructure was not completely eliminated after HIPing. During the room temperature tensile test, a crack (clearly visible in Figure 4.30 (h)) was observed between the coarse γ and fine regions in the subsurface of the Z-direction sample. However, unlike the as-built Z-direction sample, room temperature tensile tests did not result in premature rupture. In Figure 4.30 (a) – (d), it was found that the crack proceeded by cutting through both coarse and fine

grains vertically when the cross section of the fracture surface in the XY-direction was examined. On the other hand, in Z-direction samples, shown in Figure 4.30 (e) – (h), the crack progressed at the coarse γ and fine grain interfaces. Upon examining the fracture surfaces in Figure 4.30, it was observed that there were no pores in either the XY or Z-direction sample. Although the anisotropy in the microstructure was not completely removed by HIP, it was seen that the pores were eliminated.

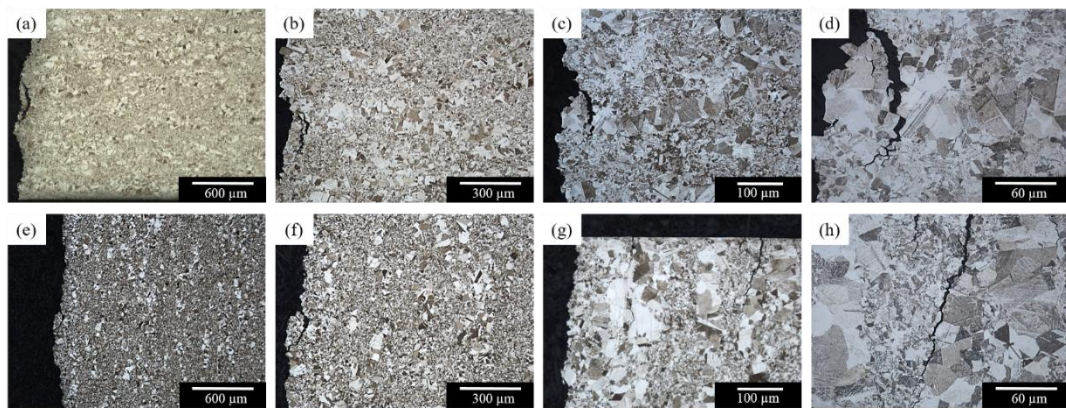


Figure 4.30: Cross section optical micrographs of room temperature tensile test fracture surfaces for PBF-EB fabricated Ti48Al2Cr2Nb HIPed samples in XY-direction at; (a) 50x, (b) 100x, (c) 200x, (d) 500x magnifications and in Z-direction at; (a) 50x, (b) 100x, (c) 200x, (d) 500x magnifications.

Figure 4.31 presents optical micrographs of the cross sections for the HIPed sample fracture surfaces after tensile tests at 700 and 800 °C. The fracture surface microstructure of the XY-direction samples tested at 700°C (Figure 4.31 (a) and (b)) was found to be similar to the room temperature test microstructure shown in Figure 4.30 (a) and (d). However, as shown in Figure 4.31 (c) and (d), it was observed that the grains elongated in the tensile direction as the test temperature increased to 800 °C. The El.% at 800 °C was $34.50 \pm 3.00\%$, while the average elongation at 700 °C was $3.13 \pm 0.88\%$ in the tensile tests for XY-direction samples. The ductile transition occurring at 800 °C was correlated with the

microstructures illustrated in Figure 4.31 (c) – (d). On the other hand, elongated grains were not found in the fracture surface microstructure for Z samples at 700°C (Figure 4.31 (e) and (f)). There was a slight grain deformation observed along the tensile test direction when the tests were done at 800 °C, as illustrated in Figure 4.31 (g) and (h). The elongation value for the Z-direction at 800°C ($17.50 \pm 7.00\%$) was almost half of that for the XY-direction sample at 800°C ($34.50 \pm 3.00\%$).

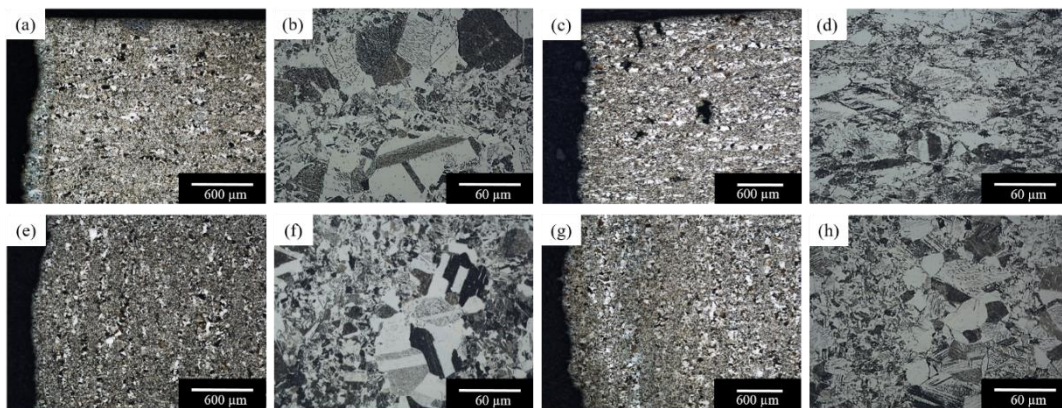


Figure 4.31: Cross-sectional optical micrographs of PBF-EB fabricated Ti48Al2Cr2Nb HIPed samples in XY-direction for; (a) 700 °C tensile test fracture surface at 50x, (b) 700 °C tensile test fracture surface at 500x, (c) 800 °C tensile test fracture surface at 50x, (d) 800 °C tensile test fracture surface at 500x and in Z-direction for; (e) 700 °C tensile test fracture surface at 50x, (f) 700 °C tensile test fracture surface at 500x, (g) 800 °C tensile test fracture surface at 50x, (h) of 800 °C tensile test fracture surface at 500x.

4.7.2.3 Tensile Tests of HT1 Processed Samples

4.7.2.3.1 Tensile Tests of HT1 Processed Samples

Table 4.7 and Figure 4.32 present the tensile test results of 1200 °C for 2 hours heat-treated (HT1) samples following XY-direction PBF-EB manufacturing. The average yield strength (YS) and ultimate tensile strength (UTS) of HT1 XY

material were 540.00 ± 4.24 and 598.18 ± 1.22 MPa, respectively, while the elongation (El.%) was $2.50 \pm 0.00\%$ at room temperature (RT). At $700\text{ }^{\circ}\text{C}$, YS and UTS values were 457.75 ± 3.18 and 546.14 ± 13.87 MPa, respectively, while the El.% was 3.75 ± 0.00 . It was observed that the sample maintained its brittle character up to $800\text{ }^{\circ}\text{C}$. In the $800\text{ }^{\circ}\text{C}$ tensile tests, the average YS of XY-direction samples was 414.00 ± 18.38 MPa, UTS 499.78 ± 55.47 MPa, while the El.% was 26.88 ± 14.23 . Graphs containing YS, UTS, and El.% values of HT1 processed XY-direction samples are given in Figure 4.32. Raising from 700 to $800\text{ }^{\circ}\text{C}$, the YS, UTS, and El.% of the sample increased approximately 7.17 times, while the YS decreased by 15.2% and the UTS by 8.8%. According to these values, it was determined that XY-direction PBF-EB produced and HT1 processed Ti48Al2Cr2Nb has a ductile transition temperature between 700 - $800\text{ }^{\circ}\text{C}$.

In the tensile tests conducted at RT on HT1 processed samples, it was observed that the Z-direction samples did not experience premature failure, unlike the as-built test specimens. The average YS of HT1 processed Z-direction sample was 474.58 ± 21.23 MPa, and the average UTS was 532.25 ± 32.42 MPa, while the El.% was $2.40 \pm 1.32\%$ at room temperature. At $700\text{ }^{\circ}\text{C}$, YS and UTS values were 457.85 ± 17.18 and 516.40 ± 39.03 MPa, respectively, while the El.% was 2.50 ± 0.00 . It was observed that the Z-direction sample maintained its brittle character up to $800\text{ }^{\circ}\text{C}$ with a slightly low elongation. In the $800\text{ }^{\circ}\text{C}$ tensile tests, the average YS and UTS of Z-direction samples were 394.85 ± 18.17 and 515.59 ± 1.77 MPa, respectively, while the El.% was $12.50 \pm 7.07\%$. Graphs containing YS, UTS, and El.% values of HT1 processed Z-direction samples are given in Figure 4.32. Raising from 700 to $800\text{ }^{\circ}\text{C}$, the YS, UTS, and El.% of the material increased approximately 5 times, while the YS decreased by 13.8% and the UTS by 0.16%. According to these values, it was determined that PBF-EB produced and HT1 processed Ti48Al2Cr2Nb in the Z-direction has a ductile transition temperature between 700 - $800\text{ }^{\circ}\text{C}$.

Table 4.7: Tensile test average results of HT1 processed Ti48Al2Cr2Nb samples.

	Test Temperature (°C)	UTS (MPa)	0.2% YS (MPa)	Elongation (%)
XY-direction	RT	598.18 ± 1.22	540.00 ± 4.24	2.50 ± 0.00
	700	546.14 ± 13.87	457.75 ± 3.18	3.75 ± 0.00
	800	499.78 ± 55.47	414.00 ± 18.38	26.88 ± 14.23
Z-direction	RT	532.25 ± 32.42	474.58 ± 21.23	2.40 ± 1.32
	700	516.40 ± 39.03	457.85 ± 17.18	2.50 ± 0.00
	800	515.59 ± 1.77	394.85 ± 18.17	12.50 ± 7.07

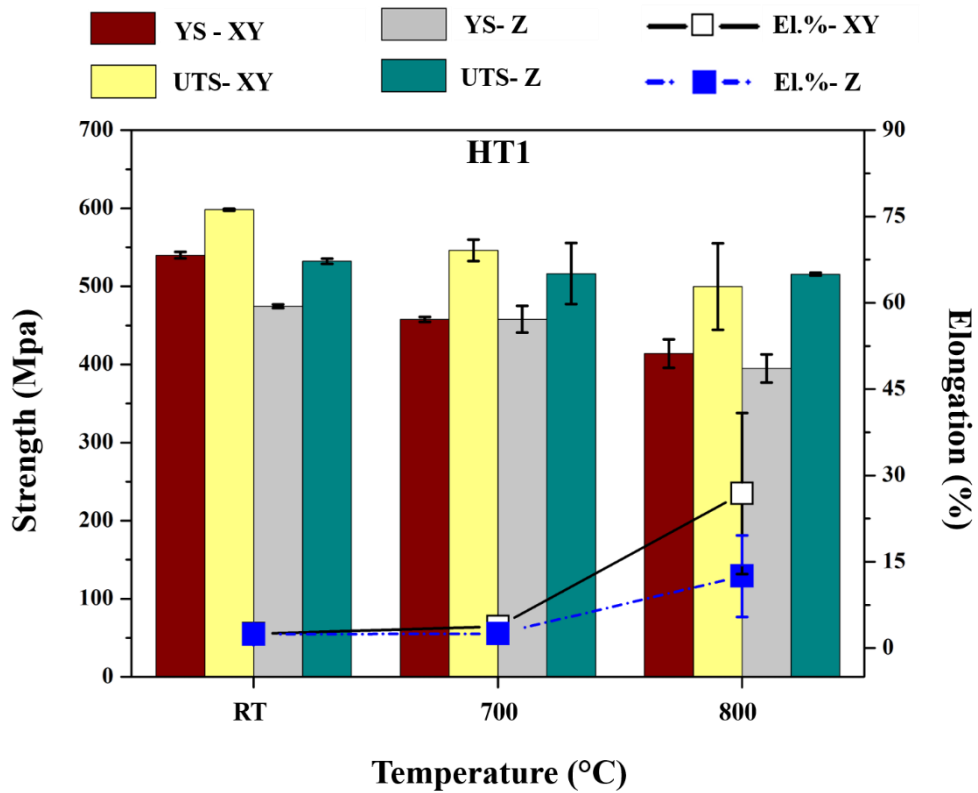


Figure 4.32: Temperature dependent yield strength, tensile strength and elongation values of HT1 processed samples.

4.7.2.3.2 Tensile Test Fracture Surfaces of HT1 Processed Samples

The tensile test fracture surfaces of the HT1 applied XY- and Z-direction specimens, as seen in Figure 4.33 (a) and Figure 4.33 (d), respectively, were quite flat. As a result of the room temperature tensile tests, no dimple was observed in either the XY-direction or the Z-direction. As presented in Table 4.7, the room temperature tensile elongation of the HT1 applied sample was 2.50% in both XY- and 2.40% in the Z-direction. The flat regions on the fracture surface of the Z-direction (Figure 4.33 (e)) specimen, were seen along with a relatively more ductile fracture was observed after the tensile tests of the XY-direction (Figure 4.33 (b)) specimen at 700 °C. In addition, γ bands were also seen on the fracture surface of the Z-direction sample after the 700 °C tests. At 700 °C, the tensile elongation in the XY-direction was $3.75 \pm 0.00\%$, while in the Z-direction it was $2.50 \pm 0.00\%$. Only the fracture surface of the XY sample at 800 °C showed highly ductile fracture where the surface is shown in Figure 4.33 (c). While the tensile elongation of the HT1 applied XY sample was $26.88 \pm 14.23\%$, the tensile elongation of the Z sample (Figure 4.33 (f)) was only $12.50 \pm 7.07\%$ at this temperature. All samples processed with HT1 had pores on their fracture surfaces.

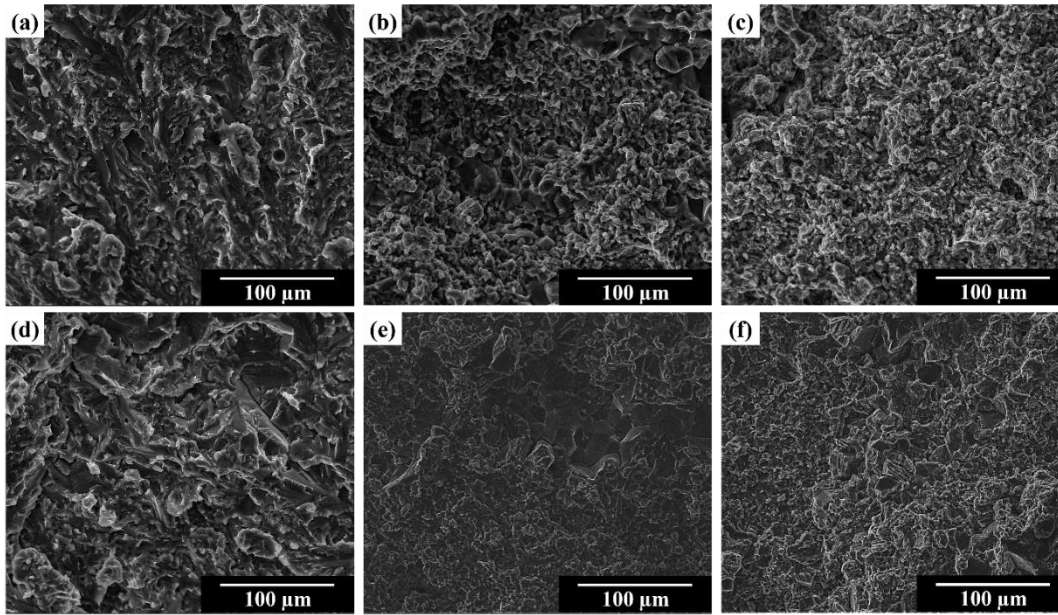


Figure 4.33: SEM images of fracture surfaces of XY-direction HT1 samples after tensile tests at; (a) room temperature, (b) 700 °C, (c) 800 °C and Z-direction HT1 samples after tensile tests at; (d) Room temperature, (e) 700 °C, (f) 800 °C tensile test specimens.

The fracture surfaces of the HT1 processed XY- and Z-direction specimens tested at room temperature are displayed in Figure 4.34 and Figure 4.35, respectively. Clear fracture initiation sites were observed for both HT1 processed samples in Figure 4.34 (a) and Figure 4.35 (a), indicating a catastrophic failure similar to that observed in as-built samples. EDS analyses were conducted on both sides of a crack in the XY- and Z-direction HT1 processed samples, as shown in Figure 4.34 (b) and Figure 4.35 (b), respectively. It was found that the chemical composition on both sides of the crack was almost similar in both HT1 building directions. In Figure 4.34 (c) and (d), the aluminum content was measured at 27.42 ± 0.72 wt.% and 28.16 ± 0.93 wt.%, respectively, in the HT1 processed XY-direction sample. In the EDS analyses presented for the HT1 processed Z-direction sample in Figure 4.35 (c) and (d), the aluminum content was found to be 28.07 ± 0.64 wt.% and 28.47 ± 0.59 wt.%, respectively. After the 1200 °C annealing heat treatment, it was

revealed that chemical homogenization was achieved, thus preventing the rapid propagation of the crack, especially in the as-built Z-direction sample.

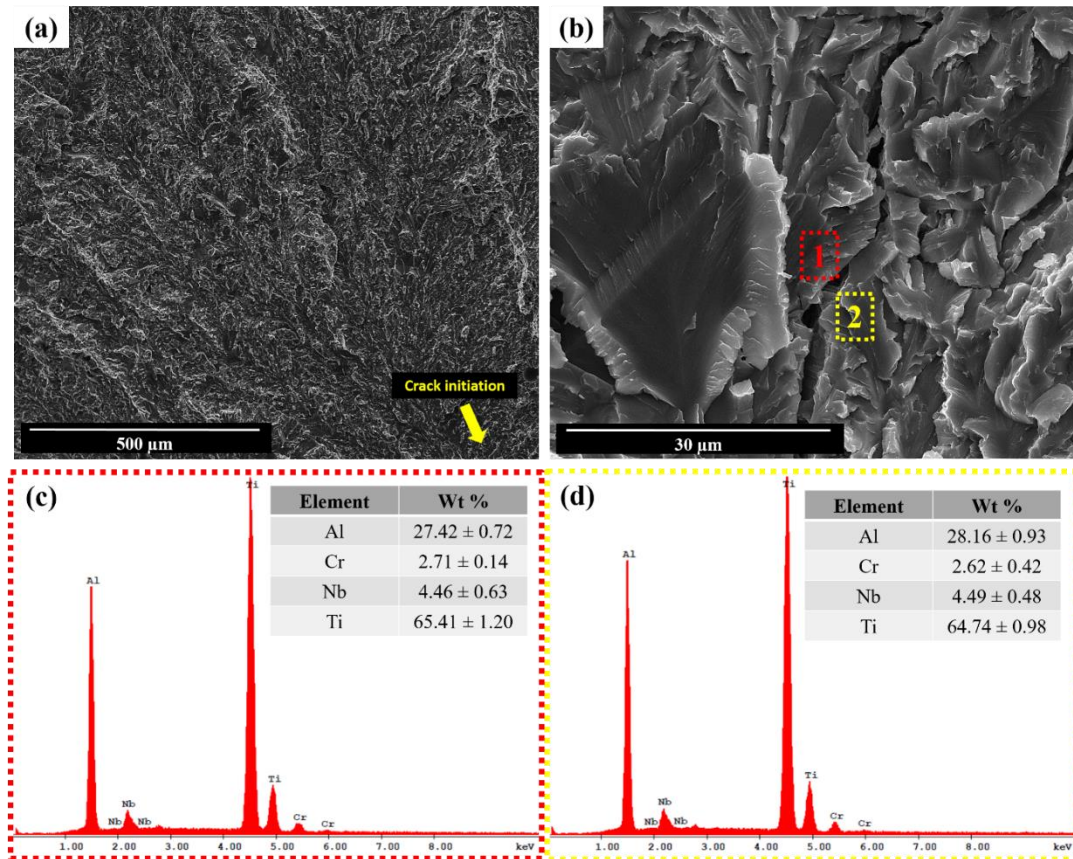


Figure 4.34: SEM images of the fracture surface from room temperature tensile tests on the HT1 processed XY-direction specimen at; (a) 250x, (b) 5000x magnification, along with EDS analysis for (c) the left side (marked as 1) and (d) the right side (marked as 2) of the crack.

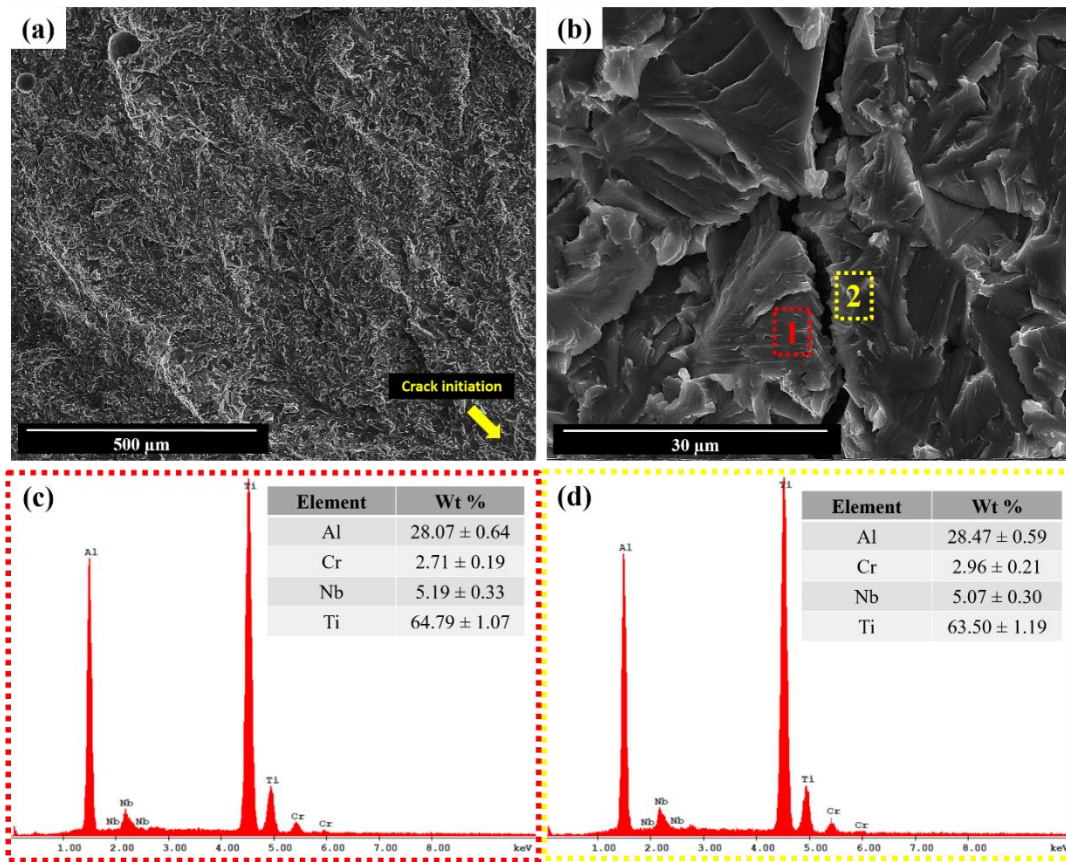


Figure 4.35: SEM images of the fracture surface from room temperature tensile tests on the HT1 processed Z-direction specimen at; (a) 250x, (b) 5000x magnification, along with EDS analysis for (c) the left side (marked as 1) and (d) the right side (marked as 2) of the crack.

In Figure 4.36, optical microscope images of the cross sections for the room temperature tensile test fracture surfaces of HT1 processed XY- and Z-direction samples are displayed. Although the YS was slightly higher for the XY-direction (540.00 ± 4.24 MPa) than the Z-direction (474.58 ± 2.23 MPa), the El.% at break values were similar for both directions ($2.50 \pm 0.00\%$ and $2.40 \pm 1.32\%$ for XY- and Z-directions, respectively) at room temperature. In Figure 4.36 (a) – (d), similar to HIPed samples, it was found that the crack proceeded by cutting the coarse γ and fine grains vertically when examining the cross section of the fracture surface in the XY-direction. On the other hand, in Z-direction samples, shown in

Figure 4.36 (e) - (h), the crack propagated at the coarse γ and fine grain interfaces. Pores were observed in the regions where the crack propagated.

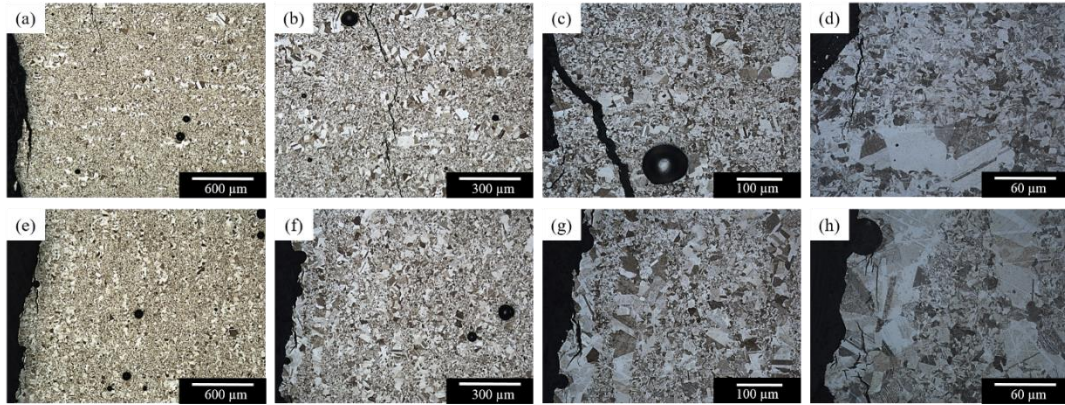


Figure 4.36: Cross section optical micrographs of room temperature tensile test fracture surfaces for PBF-EB fabricated Ti48Al2Cr2Nb HT1 samples in XY-direction at; (a) 50x, (b) 100x, (c) 200x, (d) 500x magnifications and in Z-direction at; (a) 50x, (b) 100x, (c) 200x, (d) 500x magnifications.

Figure 4.37 displays optical micrographs of the cross sections for the fracture surfaces of HT1 processed samples after tensile tests were conducted at 700 and 800 °C. The fracture surface microstructure of the XY-direction samples tested at 700 °C (Figure 4.37 (a) and (b)) did not differ from the room temperature test microstructure shown in Figure 4.36 (a) and (d). However, as presented in Figure 4.37 (c) and (d), it was observed that the grains elongated in the tensile direction as the test temperature increased to 800 °C. While the average elongation at 800 °C was $26.88 \pm 14.23\%$, the average elongation at 700 °C was $3.75 \pm 0.00\%$ in the tensile tests for XY-direction samples. The ductile transition occurring at 800 °C was correlated with the microstructures illustrated in Figure 4.37 (c) – (d). On the other hand, elongated grains were not found in the fracture surface microstructure for Z-direction samples at 700 °C (Figure 4.37 (e) and (f)). There was a slight grain deformation observed along the tensile test direction when the tests were done at 800 °C, as illustrated in Figure 4.37 (g) and (h). The elongation value for Z-

direction at 800 °C ($12.50 \pm 7.07\%$) was less than half of the XY ($26.88 \pm 14.23\%$) direction sample at 800°C.

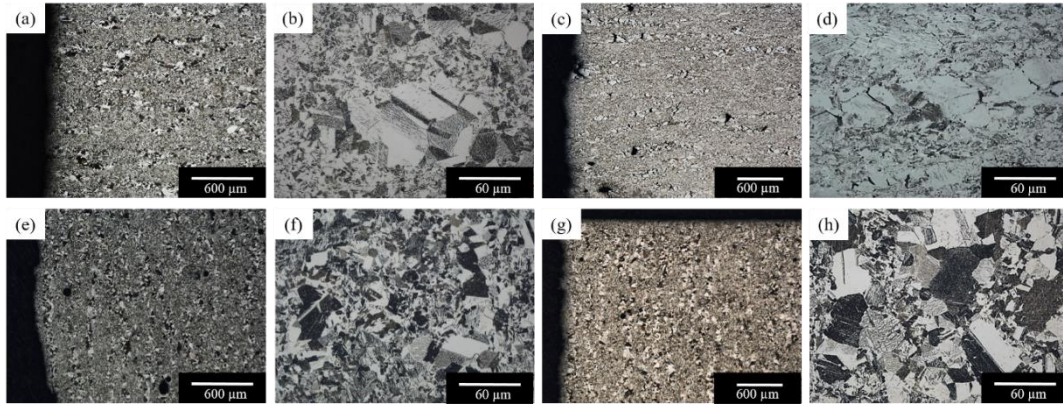


Figure 4.37: Cross-sectional optical micrographs of PBF-EB fabricated Ti48Al2Cr2Nb HT1 processed samples in XY-direction for; (a) 700 °C tensile test fracture surface at 50x, (b) 700 °C tensile test fracture surface at 500x, (c) 800 °C tensile test fracture surface at 50x, (d) 800 °C tensile test fracture surface at 500x and in Z-direction for; (e) 700 °C tensile test fracture surface at 50x, (f) 700 °C tensile test fracture surface at 500x, (g) 800°C tensile test fracture surface at 50x, (h) of 800 °C tensile test fracture surface at 500x.

4.7.2.4 Tensile Tests of HT2 Samples

4.7.2.4.1 Tensile Test Results of HT2 Processed Samples

Table 4.8 and Figure 4.38 present the tensile test results of samples heat-treated at 1400 °C for 2 hours (HT2) following the XY-direction PBF-EB manufacturing. The average yield strength (YS) of HT2 processed XY-direction sample was 372.50 ± 2.12 MPa, and the average ultimate tensile strength (UTS) was 435.75 ± 9.19 MPa, while the elongation (El.%) was $2.09 \pm 0.01\%$ at room temperature. At 700 °C, YS and UTS values were 303.55 ± 11.67 and 389.67 ± 28.76 MPa, respectively, while the El.% was 3.13 ± 0.88 . It was observed that the sample

maintained its brittle character up to 800 °C. In the 800 °C tensile tests, the average YS and UTS of XY-direction samples were 295.25 ± 0.07 and 388.50 ± 56.92 MPa, respectively, while the El.% was $4.38 \pm 0.88\%$. Graphs containing YS, UTS, and El.% values of HT2 processed XY-direction samples are given in Figure 4.38. Raising from 700 to 800 °C, the YS, UTS, and El.% of the sample increased approximately 1.4 times, while the YS decreased by 2.7% and the UTS by 0.3%. According to these values, it was determined that a heat treatment done above the α -transition temperature did not lead to a ductile transition temperature between 700-800 °C, unlike other samples.

In the tensile tests performed at RT on HT2 samples, the Z-direction samples did not prematurely fail, unlike as-built test specimens. The average YS of HT2 processed Z-direction material was 362.00 ± 2.12 MPa, the UTS was 405.70 ± 9.90 MPa, while the El.% was $1.73 \pm 0.10\%$ at room temperature. At 700 °C, YS and UTS values were 303.00 ± 9.55 and 389.85 ± 14.35 MPa, respectively, while the El.% was 3.75 ± 0.00 . It was observed that the sample maintained its brittle character up to 800 °C with a slightly low elongation. In the 800 °C tensile tests, the average YS and UTS of Z samples were 298.25 ± 1.41 and 358.00 ± 3.25 MPa, respectively, while the El.% was $3.75 \pm 0.00\%$. YS, UTS, and El.% values of HT2 processed Z-direction samples are given in Figure 4.38. Raising from 700 to 800 °C, the YS, UTS, and El.% of the sample did not change drastically, while the YS decreased by 1.6% and the tensile strength by 8.2%. According to these values, it was determined that a heat treatment done above the α -transition temperature did not lead to a ductile transition temperature between 700-800 °C, unlike other samples.

Table 4.8: Tensile test average results HT2 processed Ti48Al2Cr2Nb samples.

	Test Temperature (°C)	UTS (MPa)	0.2% YS (MPa)	Elongation (%)
XY-direction	RT	435.75 ± 9.19	372.50 ± 2.12	2.09 ± 0.01
	700	389.67 ± 28.76	303.55 ± 11.67	3.13 ± 0.88
	800	388.50 ± 56.92	295.25 ± 0.07	4.38 ± 0.88
Z-direction	RT	405.70 ± 9.90	362.00 ± 2.12	1.73 ± 0.10
	700	389.85 ± 14.35	303.00 ± 9.55	3.75 ± 0.00
	800	358.00 ± 3.25	298.25 ± 1.41	3.75 ± 0.00

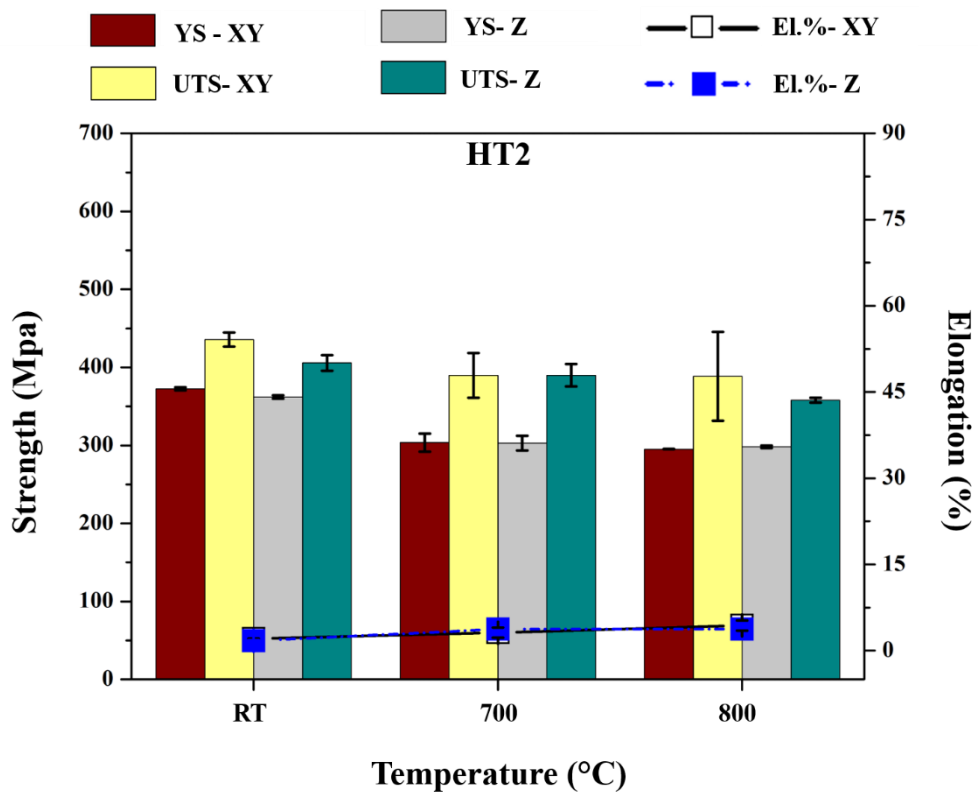


Figure 4.38: Temperature dependent yield strength, tensile strength and elongation values of HT2 processed XY-direction samples.

4.7.2.4.2 Tensile Test Fracture Surfaces of HT2 Processed Samples

Fracture surfaces of HT2 samples represented in Figure 4.39 differed from all other samples with very flat surfaces observed at all tensile test temperatures in both XY- and Z-directions. In addition, the pores on the fracture surfaces were quite high at all temperatures. Another remarkable point is that the traces of the lamellar microstructure that emerged after the HT2 annealing were visible on the fracture surfaces. On the fracture surfaces, translamellar fracture across the lamellae and interface delamination were detected. Translamellar fracture propagation was accompanied by simultaneous interfacial delamination. As a result of the tensile tests of the HT2 specimens at 800 °C, the tensile elongation in the XY-direction was $4.38 \pm 0.88\%$, while this value was $3.75 \pm 0.00\%$ in the Z-direction sample, where the fracture surfaces are given in Figure 4.39 (c) and Figure 4.39 (f), respectively.

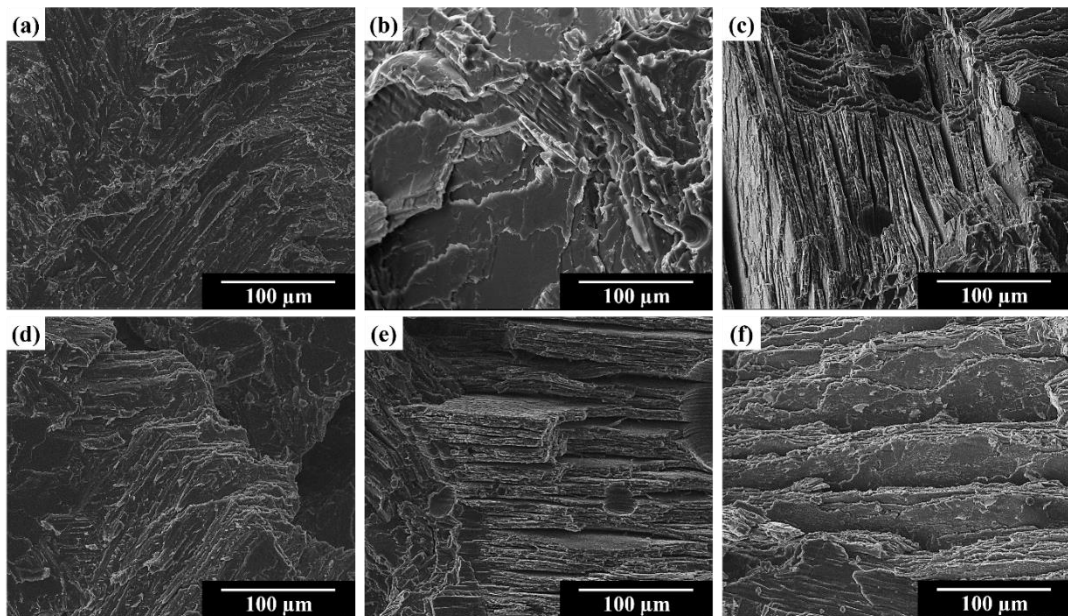


Figure 4.39: SEM images of fracture surfaces of XY -direction HT2 samples after tensile tests at; (a) Room temperature, (b) 700 °C, (c) 800 °C and Z-direction HT2 samples after tensile tests at; (d) Room temperature, (e) 700 °C, (f) 800 °C tensile test specimens.

Following the heat treatment at 1400 °C, the microstructure of the samples changed to fully lamellar, and consequently, the fractured surface texture differed from the other samples. The fracture surface of the HT2 processed XY- and Z-direction samples tested at room temperature is shown in Figure 4.40 and Figure 4.41, respectively. EDS analyses were performed on both sides of a crack in the XY- and Z-direction, as illustrated in SEM images in Figure 4.40 (b) and Figure 4.41 (b), respectively. It was found that the chemical composition on both sides of the crack was similar in the HT2 processed XY building direction. In the EDS measurement of the crack of the HT2 processed XY-direction sample, the aluminum content was found to be 32.37 ± 0.71 wt.% and 32.01 ± 0.97 wt.% on the left (marked as 1) and right (marked as 2), respectively, as shown in Figure 4.40 (c) and (d). On the contrary, in the EDS analyses presented for the HT2 processed Z-direction sample in Figure 4.41 (c) and (d), the aluminum content slightly differed from each other, with values of 30.10 ± 1.08 wt.% and 27.79 ± 0.96 wt.%, respectively.

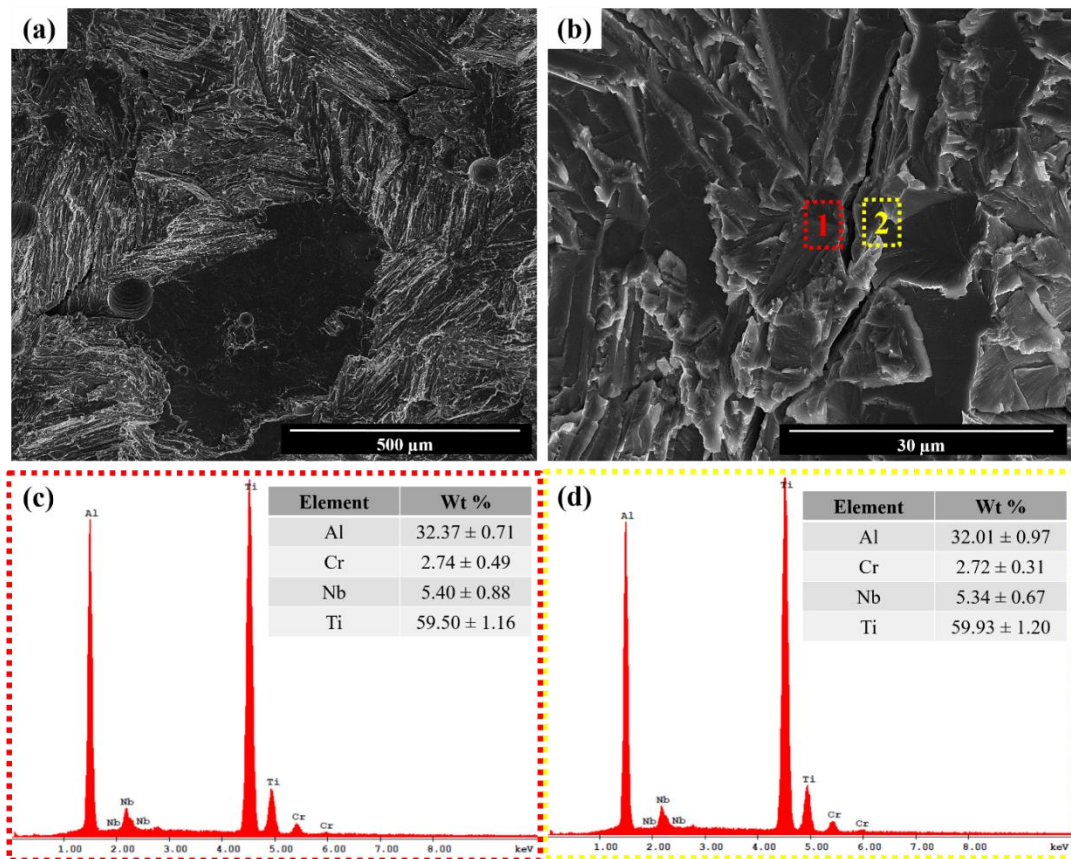


Figure 4.40: SEM images of the fracture surface from room temperature tensile tests on the HT2 processed XY-direction specimen at; (a) 250x, (b) 5000x magnification, along with EDS analysis for (c) the left side (marked as 1) and (d) the right side (marked as 2) of the crack.

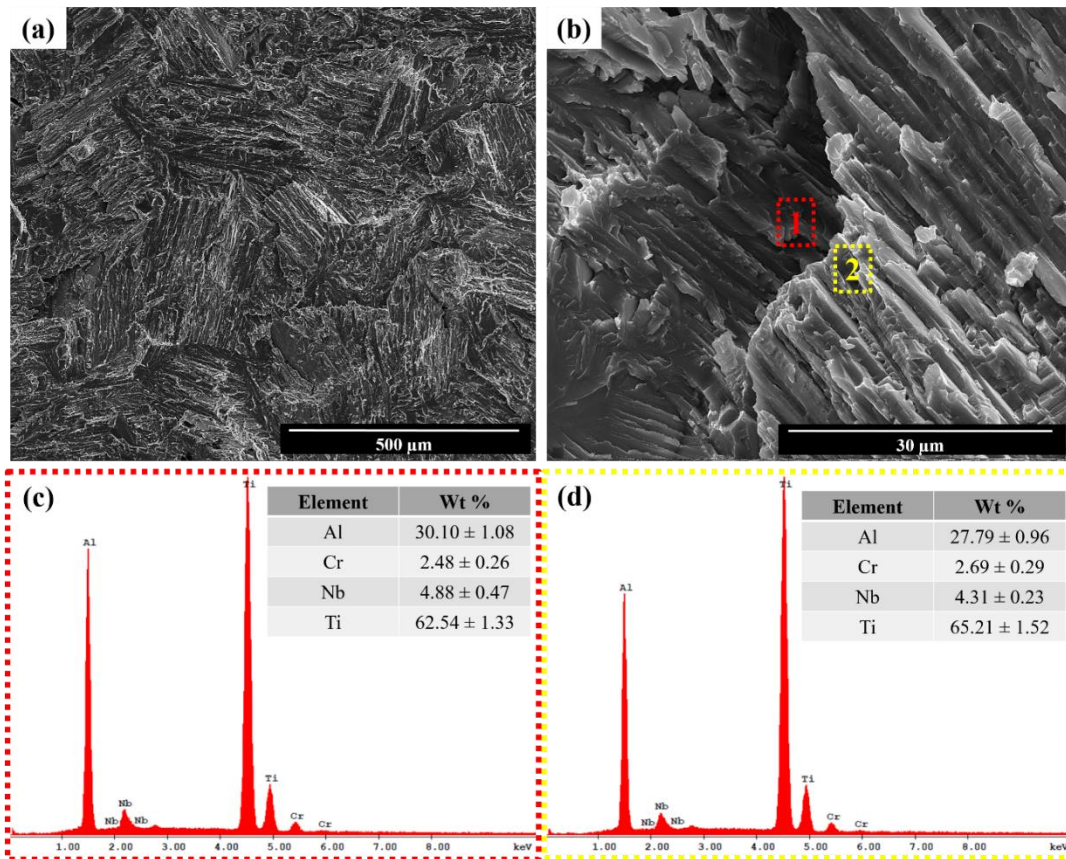


Figure 4.41: SEM images of the fracture surface from room temperature tensile tests on the HT2 processed Z-direction specimen at; (a) 250x, (b) 5000x magnification, along with EDS analysis for (c) the left side (marked as 1) and (d) the right side (marked as 2) of the crack.

In Figure 4.42, optical microscope images depict the cross-sectional views of fracture surfaces from room temperature tensile tests on HT2 processed samples in the XY- and Z-directions. Comparing YS and El.% values, the XY-direction exhibits slightly higher performance (YS: 372.50 ± 2.12 MPa, El.%: $2.09 \pm 0.01\%$) compared to the Z-direction (YS: 362.00 ± 2.12 MPa, El.%: $1.73 \pm 0.10\%$) at room temperature. In the fracture surface images shown in Figure 4.42 (a) – (h), a distinctive behavior is observed—unlike the as-built, hot isostatic pressing (HIPed), and HT1 samples—where the crack propagates similarly in both XY- and Z-directions, cutting fine $\alpha_2 + \gamma$ grains vertically. As detailed in Chapter 0, the heat

treatment at 1400 °C results in the dissolution of the duplex microstructure in the Ti48Al2Cr2Nb sample's α phase. Subsequent slow cooling facilitates the formation of $\alpha_2 + \gamma$ lamellae within primary α grains, eliminating microstructural anisotropy in the XY- and Z-direction samples. Consequently, a comparable fracture mechanism is observed in both directions, demonstrating the impact of the heat treatment on the microstructure.

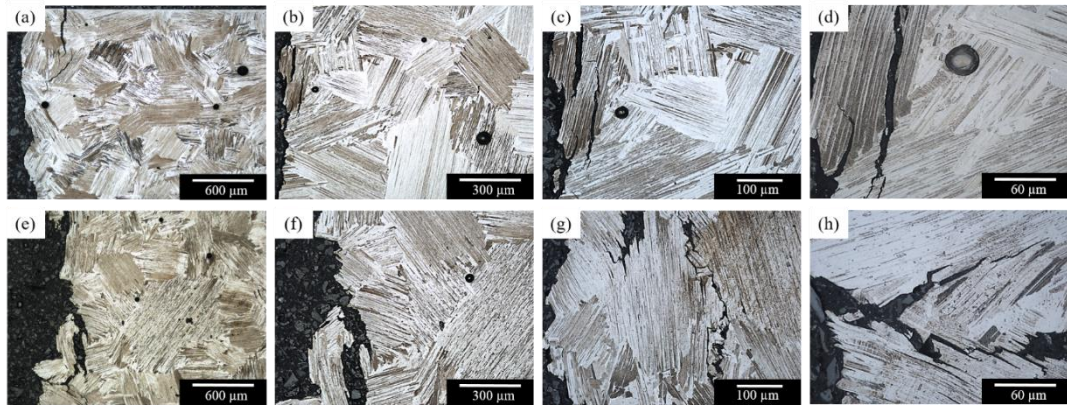


Figure 4.42: Cross section optical micrographs of room temperature tensile test fracture surfaces for PBF-EB fabricated Ti48Al2Cr2Nb HT2 processed samples in XY-direction at; (a) 50x, (b) 100x, (c) 200x, (d) 500x magnifications and in Z-direction at; (a) 50x, (b) 100x, (c) 200x, (d) 500x magnifications.

Figure 4.43 presents optical micrographs capturing the cross-sectional views of fracture surfaces from HT2 processed samples after undergoing tensile tests at 700 and 800 °C. The microstructure of fracture surfaces in the XY-direction samples at 700 °C (Figure 4.43 (a) and (b)) closely resembles that of Z-direction samples depicted in Figure 4.43 (e) and (f). Additionally, comparable grain elongation is evident in both XY- and Z-direction samples as the test temperature increases to 800 °C, as shown in Figure 4.43 (c), (d), (g), and (h). Despite the temperature rise to 800 °C, the average elongation at this temperature remains distinct for XY ($4.38 \pm 0.88\%$) and Z ($3.75 \pm 0.00\%$) direction samples. Notably, there is no discernible ductile transition even at 800 °C for any of the samples due to the fully lamellar

microstructure and Nb microsegregation as detailed in Chapter 3.7.2.4. This consistency in the tensile test results aligns with the absence of elongated grains observed in Figure 4.43 (c), (d), and (g), (h).

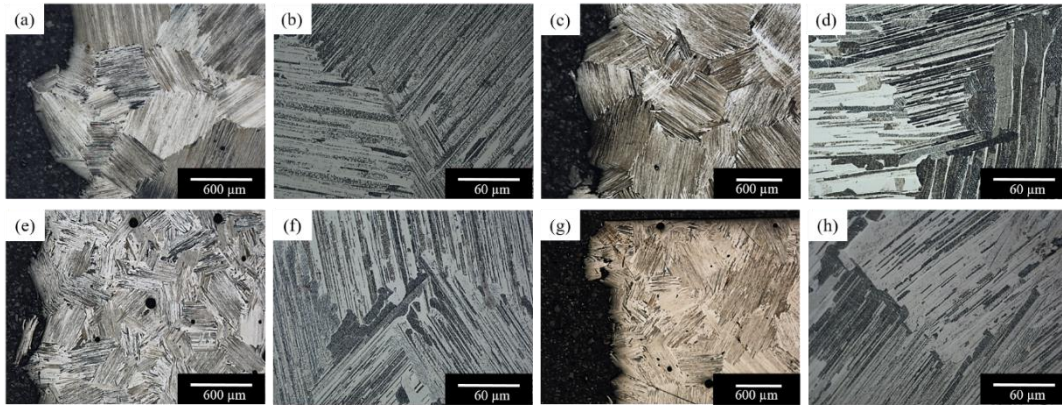


Figure 4.43: Cross-sectional optical micrographs of PBF-EB fabricated Ti48Al2Cr2Nb HT2 processed samples in XY-direction for; (a) 700 °C tensile test fracture surface at 50x, (b) 700 °C tensile test fracture surface at 500x, (c) 800 °C tensile test fracture surface at 50x, (d) 800 °C tensile test fracture surface at 500x and in Z-direction for; (e) 700 °C tensile test fracture surface at 50x, (f) 700 °C tensile test fracture surface at 500x, (g) 800 °C tensile test fracture surface at 50x, (h) of 800 °C tensile test fracture surface at 500x.

4.7.2.5 Overview of Tensile Tests

The temperature dependent ultimate tensile strength, yield strength, and elongation values are presented in the column graphs illustrated in Figure 4.44. Additionally, stress-strain curves obtained at 25 °C, 700 °C, and 800 °C are shown in Figure 4.45 for both XY and Z built direction samples. The average UTS and YS of the as-built material in XY-direction at room temperature were 636.87 ± 42.43 MPa and 560.63 ± 33.85 MPa, respectively. The average elongation value of this sample at room temperature was $1.67 \pm 0.53\%$. At 800 °C, the average UTS and yield strength of the XY samples were 568.64 ± 3.68 MPa and 437.61 ± 1.5 MPa,

respectively, with an elongation value of $54.17 \pm 4.39\%$. Comparing the results between $700\text{ }^{\circ}\text{C}$ and $800\text{ }^{\circ}\text{C}$, the elongation value increased by approximately 22 times while the yield strength decreased by 8% and the UTS decreased by 0.5%. It was determined that the PBF-EB as-built Ti48Al2Cr2Nb material undergoes a ductile transition between $700\text{-}800\text{ }^{\circ}\text{C}$, which is consistent with the transformation temperature reported as $750\text{ }^{\circ}\text{C}$ in other studies [1], [28].

However, the as-built Ti48Al2Cr2Nb samples manufactured in the Z-direction exhibited premature failure with inconsistent results. This means that some samples failed before reaching the yield point and exhibited an extremely brittle behavior throughout the testing. The average ultimate tensile strength (UTS) and yield strength (YS) for XY-direction samples were $636.87 \pm 42.43\text{ MPa}$ and $560.63 \pm 33.85\text{ MPa}$, respectively, with an elongation percentage (El.%) of $1.67 \pm 0.53\%$. In contrast, Z-direction samples experienced premature failure, displaying an average UTS of $501.50 \pm 122.75\text{ MPa}$ with a very low amount of elongation.

In the Z-direction samples, the alignment of the γ -bands was perpendicular to the loading direction. It was found that the orientation of γ bands perpendicular to the tensile testing direction in the Z sample, as shown in Figure 4.6 (b) and (d), caused crack initiation. The examinations have revealed that during PBF-EB production, γ colonies tend to coarsen due to the influence of high process temperatures. Simultaneously, the α_2 phase present in the fine regions exerts a pinning effect on the γ grains, inhibiting their growth. As a result, a sandwich-like structural development comprised of coarse γ bands and fine regions has evolved in the Z-direction sample. Furthermore, a difference in aluminum content of approximately ~1wt.% has occurred between the coarse γ bands and the fine region. The ~98 HV0.1 hardness difference between the coarse and fine regions led to the initiation of fracture at the interface between the less resistant γ phase and the fine region. The difference in chemical composition (presented in Figure 4.7) and hardness (illustrated in

Figure 4.18) between the coarse γ bands and fine lamellae regions contributes to early fracture in PBF-EB fabricated Z-direction as-built sample. The high dislocation density and internal strain, as revealed by the Grain Orientation Spread (GOS) and Kernel Average Misorientation (KAM) values in Figure 4.16, also contributed to the brittleness of the as-built samples.

Previous studies have also demonstrated the mechanical behavior differences between the XY- and Z-directions of the PBF-EB processed Ti48Al2Cr2Nb alloy. Todai et al. suggests that as-built samples oriented at a 45° angle with the build platform exhibit optimal tensile ductility and strength combination with respect to XY- and Z-direction. This orientation is associated with γ phase banding that is perpendicular to the production direction [23]. Lin et al., has found a difference of 30 MPa in the yield strengths between the XY- and Z-directions in samples that have been subjected to a heat treatment at 1260 °C to obtain a duplex microstructure. It should be noted that tensile testing has not been performed on the as-built samples in this study [196].

In the tensile tests conducted at room temperature, presented in Figure 4.45 (a), for the HIPed XY alloy, the UTS and YS were found to be 561.03 ± 28.23 MPa and 504.96 ± 17.39 MPa, respectively, while the tensile elongation was $2.19 \pm 0.45\%$. After the application of HIP treatment, it was observed that the samples in the Z-direction did not undergo premature fracture, as observed in the as-built samples. The UTS and YS for the Z-direction HIPed samples were 551.81 ± 13.76 MPa and 514.49 ± 6.1 MPa, respectively while the tensile elongation was $2.29 \pm 0.13\%$. The disparity in UTS between the XY- and Z-direction HIPed samples was only 9.22 MPa and a similar difference of 9.53 MPa was observed in the yield strength at room temperature. Furthermore, there was a slight change of 0.1% in tensile elongation when the tests were performed for the Z-direction samples at room temperature. For samples produced in both XY- and Z-directions, the tensile and yield strengths experienced drastic alteration of 65.18 MPa and 65.42 MPa, respectively, for the HT1 samples. It was found that the duplex-like microstructure in the as-built sample persisted after the HIP and HT1 processes, see Figure 4.9. After the HT1, γ banding continued in the Z-direction sample while banding almost vanished in both the XY- and Z-directions of HIPed sample. It was observed that in the HIPed sample, the Z-direction exhibited randomly distributed equiaxed coarse γ colonies instead of banding. It was determined that the elimination of banding due to HIP resulted in similar mechanical behavior in both the XY- and Z-directions. These results indicate that the HIP treatment was a highly effective secondary treatment method to reduce the dependence on the build direction in the mechanical properties of PBF-EB manufactured Ti48Al2Cr2Nb material. It helped to reduce the anisotropy and improve the homogeneity of the mechanical properties between the XY- and Z-direction samples. Seifi et al. have also been reported that HIP is an effective method for reducing the variation in compression test results among the samples, resulting in a yield strength difference of 5 MPa [21].

In the tensile tests conducted on the XY-direction HT1 samples at room temperature (Figure 4.45 (a)), the UTS was measured as 598.18 ± 1.22 MPa and the YS was 540.00 ± 4.24 MPa. The El.% was found to be $2.50 \pm 0.00\%$. The

average UTS of the Z-direction HT1 processed samples was 532.25 ± 32.42 MPa and the YS was 474.58 ± 2.23 MPa. The El.% measured for these samples was $2.40 \pm 1.32\%$. It can be observed in Figure 4.44 (a) that the UTS of HT1 and HIPed samples in the XY-direction decreases by 8.7% and 4.4% respectively when the test temperature was raised to 700 °C from room temperature. Similarly, in Figure 4.44 (b) it is shown that the YS decreased by 15.2% for HT1 and 10.2% for HIPed samples in the XY-direction at 700 °C compared to room temperature tests. At 800 °C, the UTS decreased by 16.4% for HT1 and 5.9% for HIPed samples in the XY-direction compared to room temperature tests. Additionally, it was found that the YS of HT1 and HIPed XY-direction samples decreased by 30.4% and 17.1% respectively at 800 °C compared to room temperature tests. Furthermore, the El.% values of HT1 and HIPed samples at 700 °C increased by 1.25% and 0.94% respectively compared to room temperature tests. At 800 °C, the tensile elongation was 10.8 times higher for HT1 samples and 15.8 times higher for HIPed samples in the XY-direction compared to room temperature tests. These results indicate that the HIPed and HT1 samples exhibit a ductile behavior at 800 °C in XY-direction, as similar phenomena have been observed in the as-built sample.

There was a 2.7% decrease for HIP and a 3% decrease in UTS for HT1 at 700 °C when the tensile test results of the Z-direction samples were compared to room temperature tests in Figure 4.44 (a). The YS of Z-direction samples decreased by 3.5% for HT1 and 13.2% for HIP at 700 °C compared to room temperature as presented in Figure 4.44 (b). At 800 °C, the UTS of Z-direction samples decreased by 3.1% for HT1 and 6.6% for HIPed conditions compared to room temperature tests (Figure 4.44 (a)). When the yield strengths of HT1 and HIPed samples in the Z-direction were examined at 800 °C (Figure 4.44 (b) and (f)), there was a decrease of 16.8% for HT1 and 24.2% for HIP compared to room temperature. In HT1 and HIPed Z-direction samples, the El.% increased by 0.1% and 1.46%, respectively, at 700 °C and it was 5.2 and 7.9 times higher, respectively, at 800 °C compared to room temperature. These results indicate that the Z-direction samples also exhibit increased ductility at 800 °C. The elongation at 800 °C for both HT1 and HIP-

treated samples in the Z-direction was only half of that observed in the XY-direction.

The HT2 resulted in a significant decrease in UTS and YS for both XY- and Z-direction samples compared to the all other samples as shown in Figure 4.44. The decrease in strength was attributed to the fully lamellar microstructure observed in Figure 4.9 after HT2. The UTS decreased by 10.6% for XY-direction and 3.9% for Z-direction samples at 700 °C compared to room temperature tests, as shown in Figure 4.44 (a). However, the El.% increased by 1.04% for XY-direction and 2.02% for Z-direction samples at 700 °C compared to room temperature tests, as illustrated in Figure 4.44 (c). At 800 °C, both XY- and Z-direction samples experienced a decrease in UTS. Similarly, the YS decreased by 20.7% for XY-direction and 21.4% for Z-direction samples at 800 °C. However, the tensile elongation increased to 4.38% for XY-direction and to 3.75% for Z-direction samples at 800 °C. The increase in tensile elongation at elevated temperatures was relatively small compared to other samples, indicating that the HT2 sample did not reach the ductile transition at 800 °C. It was found that the fully lamellar microstructure within the coarse primary α grains and the randomly distributed Nb microsegregation achieved after the HT2 (shown in Figure 4.11) can contribute to the preservation of brittleness at higher temperatures. This was contrary to the statements for as-built, HIPed and HT1 conditions suggesting a ductile behavior at 800 °C. It can be concluded that the HT2 processed Ti48Al2Cr2Nb material is suitable for higher temperature applications due to its high temperature resistance, despite its lower strength compared to other samples.

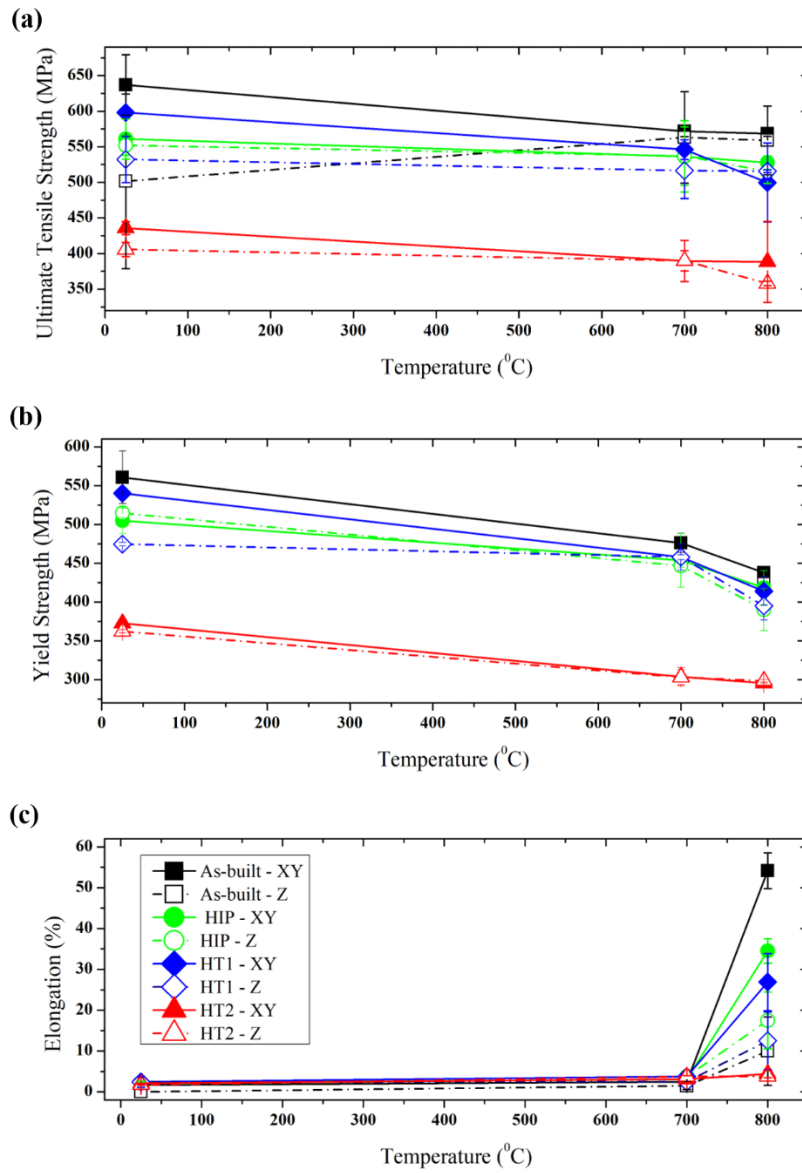


Figure 4.44: Temperature dependent line graphs of; (a) UTS, (b) YS, (c) El.% for; as-built, HIPed, HT1 and HT2 processed samples in both XY- and Z-directions.

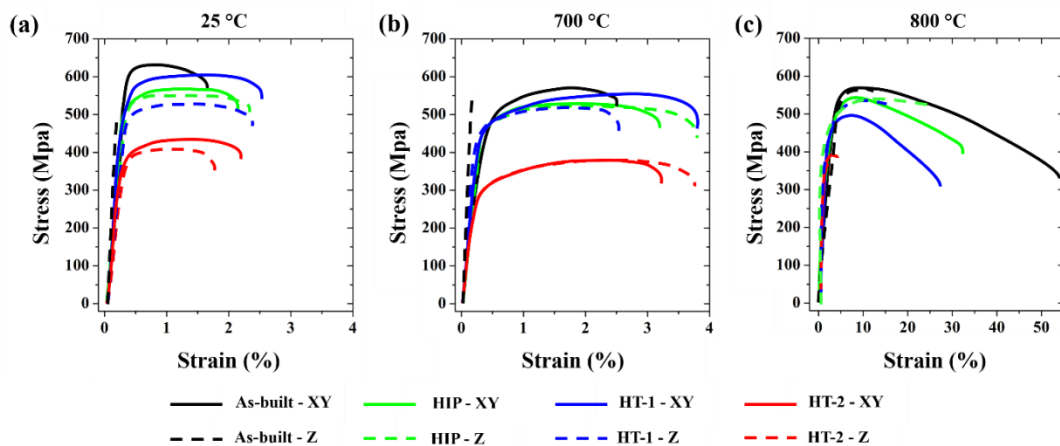


Figure 4.45: Stress-strain curves obtained at; (a) 25 °C, (b) 700 °C, (c) 800 °C for; as-built, HIPed, HT1 and HT2 processed samples in both XY- and Z-directions.

To analyse the effect of 100 MPa pressure on anisotropic behavior in tensile characteristics, a deeper analysis was performed comparing HIP and HT1 where both processes were performed at 1200 °C. It was found that the UTS and YS values in the XY-direction of the HT1 processed sample were greater, while they were lower in the Z-direction when the tensile tests of the HT1 processed and HIPed samples were compared each other. The distribution of bands in both the XY- and Z-directions following annealing heat treatment was the principal cause of anisotropy in mechanical properties as discussed earlier. Graphs in Figure 4.46 were plotted to demonstrate anisotropy in the mechanical properties. Figure 4.46 (a) provides the ratio of Z-direction UTS and YS values to the XY-direction. The same ratio is presented for El.% in Figure 4.46 (b). In both graphs, the examination of the XY/Z ratio's deviation from 1 aimed to detail the dependence of mechanical properties on the manufacturing direction. The XY/Z ratio for the HIP sample was nearly 1 in both room temperature and 700 °C tensile tests, demonstrating that anisotropy was almost completely eliminated after HIP. On the other hand, after the HT1 process the XY-direction UTS, YS, and El.% values were higher than the Z-direction in both room temperature and 700 °C tensile testing indicating a higher anisotropy. At 800 °C, all samples ductility fractured with exhibiting an entirely

different fracture character than at room temperature and 700 °C. As a result of this, the influence of anisotropy was not evaluated for the 800 °C testing.

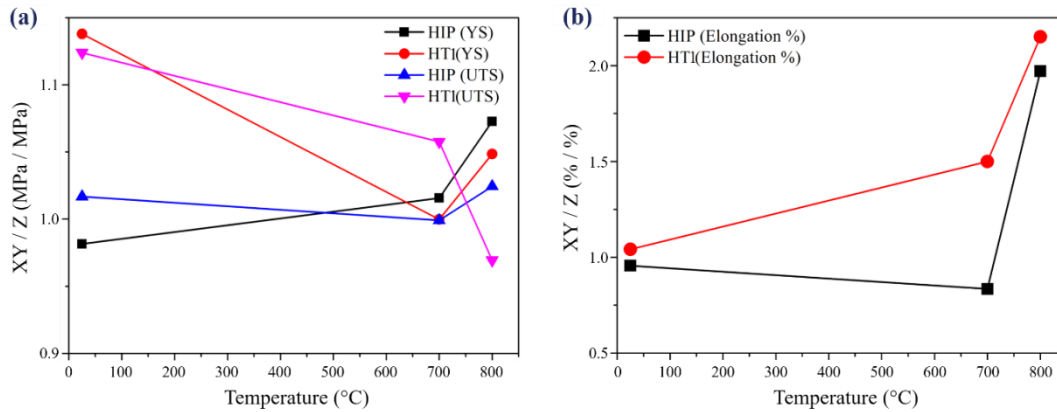


Figure 4.46: Mechanical property anisotropy diagrams of XY/Z ratio for; (a) XY_{UTS}/Z_{UTS} and XY_{YS}/Z_{YS} and (b) $XY_{El.\%}/Z_{El.\%}$.

4.7.2.6 Overview of Fracture Surfaces

The analysis of fracture surfaces was conducted comprehensively for the samples tested at room temperature, 700, and 800 °C. The fracture surface of the samples tested at room temperature are presented in the previous sections. Accordingly, it was observed that the fracture surfaces obtained from the room temperature tensile tests were relatively flat and the fractures occurred perpendicular to the direction of the tensile test. This indicates that the fractures exhibited a highly brittle behavior independent of the secondary thermal treatment applied. The fracture surfaces of the as-built samples in the XY- and Z-directions, shown in Figure 4.21 and Figure 4.22 respectively, exhibit traces of crack initiation and catastrophic fracture. Both XY- and Z-direction samples show highly flat fracture surfaces with the occurrence of transgranular cracks. In the as-built XY-direction sample presented in Figure 4.21 (b), the aluminum content difference on both sides of the microcrack was

found to be an average of 9.68 wt.% based on EDS measurements. On the other hand, the aluminum difference in the microcrack of the as-built Z-direction sample shown in Figure 4.22 (b) was determined to be an average of 11.85 wt.%. This finding confirms, as illustrated in Figure 4.24, that the cracks propagate through the chemical composition difference between the γ grains and the fine grains. The exceptional brittleness observed in the Z-direction sample is attributed to the aluminum difference at the interface of the coarse γ bands and the fine region, which extend perpendicular to the direction of the tensile test.

In the HIPed samples, shown in Figure 4.28 and Figure 4.29 for the XY- and Z-directions respectively, the formation of coarse γ colonies is observed on the fracture surfaces. However, in the HIPed sample, unlike the as-built and HT1 samples, the γ colonies in the Z-direction sample were almost randomly distributed throughout the microstructure instead of banding at regular intervals (Figure 4.9 (d)). As shown in Figure 4.28 (c) and Figure 4.29 for the high-magnification microcracks of the HIPed sample in the XY- and Z-directions, respectively, cleavage occurs between the γ grains. The aluminum content on both sides of the microcrack tips differs by 2.68 wt.% for the XY-direction and 2.77 wt.% for the Z-direction. The EBSD phase map in Figure 4.12 (b) demonstrates the distribution of the α_2 phase along the γ grain boundaries. The presence of α_2 grains at the grain boundaries of the coarse γ grains is responsible for the cleavage on the fracture surfaces.

The fracture surfaces of the HT1 XY- and Z-direction samples tested at room temperature are illustrated in Figure 4.34 and Figure 4.35, respectively. In both HT1 samples, fracture initiation sites were observed clearly, indicating catastrophic failure similar to the as-built samples. EDS analyses were conducted on both sides of a crack for the HT1 samples. It was found that the chemical composition on two sides of the crack was similar for both HT1 building directions. The aluminum content was determined to be 27.42 ± 0.72 wt.% and 28.16 ± 0.93 wt.% on two sides of the microcrack in the HT1 XY-direction sample. Similarly, in the HT1 Z-direction sample, the aluminum content was measured as 28.07 ± 0.64 wt.% and

28.47 ± 0.59 wt.%. The HT1 heat treatment resulted in chemical homogenization, which effectively inhibited the rapid propagation of the crack especially in the as-built Z-direction sample.

After the HT2 annealing heat treatment, the microstructure of the samples transformed into a fully lamellar structure, as observed in Figure 4.9 (g) and (h). Consequently, the fractured surface texture of the HT2 processed XY- and Z-direction samples exhibited distinct characteristics with showing crack initiation from alternating lamellae which was different from the fracture behavior observed in the other samples. The fracture surfaces of the HT2 samples appeared extremely flat as shown in Figure 4.40 and Figure 4.41 for XY- and Z-direction samples, respectively. Fracture surfaces revealed translamellar fractures across the lamellae, accompanied by concurrent interface delamination. EDS analyses were performed on both sides of a crack in the HT2 XY- and Z-direction samples. The EDS measurement of the crack in the HT2 XY-direction sample revealed an average aluminum content of 32.37 ± 0.71 wt.% and 32.01 ± 0.97 wt.% on each side of the crack. In contrast, the aluminum content slightly differed between the two sides of the crack in the HT2 processed Z-direction sample, with average values of 30.10 ± 1.08 wt.% and 27.79 ± 0.96 wt.%.

Fracture surfaces obtained from the 800 °C tensile tests of the samples are shown in Figure 4.47. The areas where microcracks occurred on the fracture surfaces were also examined at higher magnifications and EDS measurements were conducted on both sides of the microcracks. As a beginning, all samples except HT2 fractured in a cup and cone formation when the as-built, HIPed and HT1 samples were tested at 800 °C. The fracture surfaces of the 800 °C tensile tests are shown in Figure 4.47, where all the samples exhibited microvoid coalescence, indicating plastic deformation except for the HT2 sample. In particular, in the the XY-direction as-built, HIPed and HT1 samples, as shown in Figure 4.47 (a), (c), and (e) respectively, irregular-shaped micro cavities were observed on both sides of the microcracks. In the Z-direction as-built, HIPed and HT1 samples, as shown in Figure 4.47 (b), (d), and (f) respectively, the presence of γ cleavage was noticeable

besides the ductile fracture. The reason for the Z-direction as-built, HIPed and HT1 samples exhibiting lower elongation compared to the XY-direction at 800 °C, as previously illustrated in Figure 4.44 (c), was found to be the separation of γ colonies between each other during the tensile tests. The fracture surfaces of the HT2 samples, shown in Figure 4.47 (g) and (h), exhibited notable differences compared to all other samples, featuring very flat surfaces at 800 °C in both the XY- and Z-directions. On these fracture surfaces, traces of the fully lamellar microstructure (seen in Figure 4.9 (g) and (h)) that emerged after the HT2 heat treatment were clearly visible. The tensile tests conducted on the HT2 specimens at 800 °C resulted in a tensile elongation of $4.38 \pm 0.88\%$ in the XY-direction and $3.75 \pm 0.00\%$ in the Z-direction with demonstrating the brittle behavior of the material even at 800°.

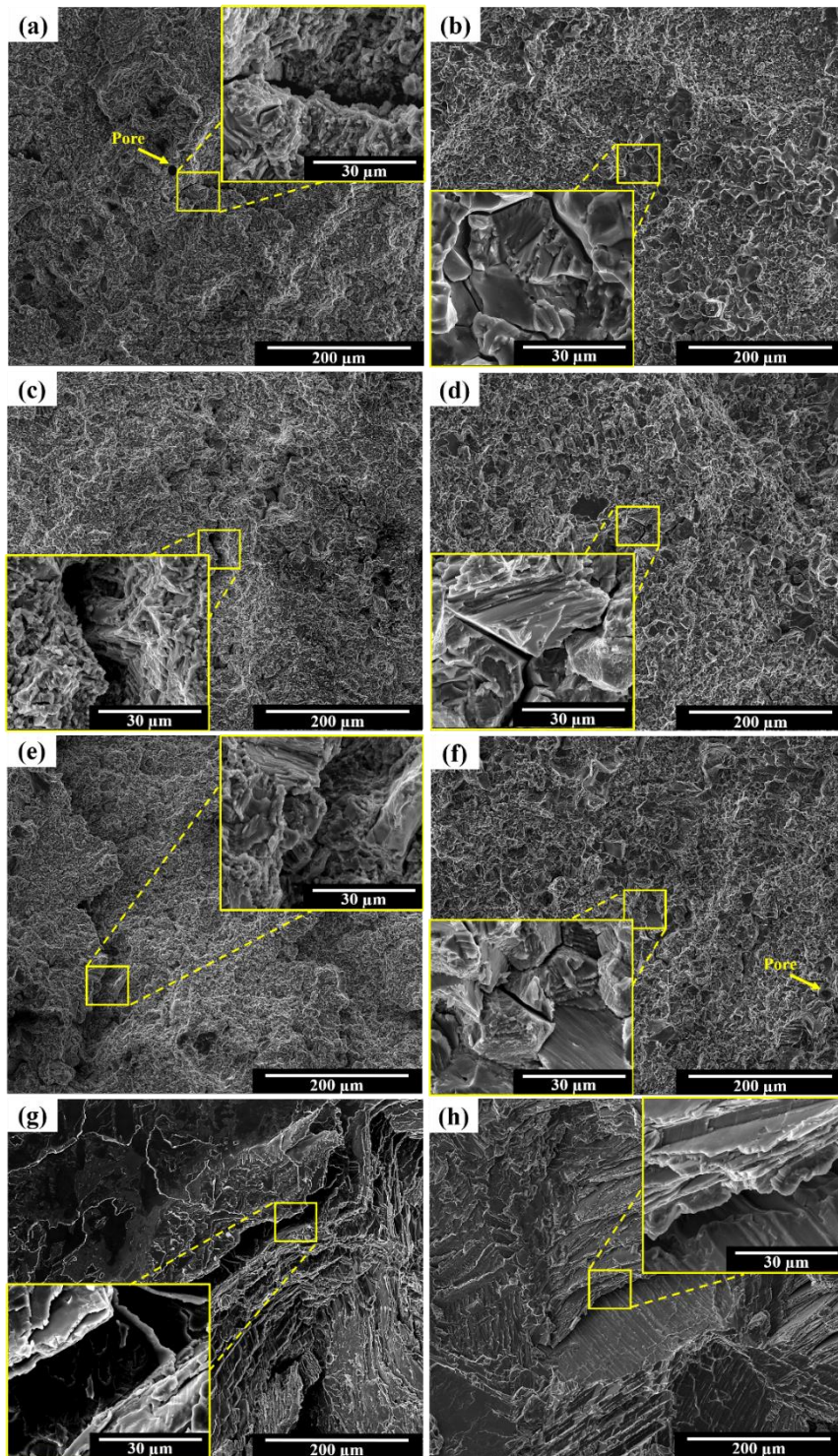


Figure 4.47: SEM images obtained from 800 °C tensile tests of the fracture surfaces of; (a) as-built sample in XY-, (b) as-built sample in Z-, (c) HIPed sample in XY-, (d) HIPed sample in Z-, (e) HT1 sample in XY-, (f) HT1 sample in Z-, (g) as-built sample in XY-, (h) HT2 sample in XY-, (h) HT2 sample in Z-directions.

4.8 Thermodynamic Modelling Studies

The Ti-Al binary and Nb/Cr modified Ti-Al-Cr-Nb quaternary phase systems are shown in Figure 4.48 (a) and (b), respectively. To investigate the effect of pressure on phase transformations, an additional 100 MPa was introduced to the system with providing the relevant diagrams for Ti-Al binary and Ti-Al-Cr-Nb quaternary phase systems illustrated in Figure 4.48 (c) and (d), respectively. To ensure consistency between experimental data and modeling studies, the Ti, Al, Cr, and Nb ratios presented in Table 4.1 were introduced into the ThermoCalc software. As shown in the phase diagrams in Figure 4.48, the introduction of 100 MPa HIP pressure increases the eutectoid temperature of the Ti-Al binary system from 1121.19 °C to 1141.48 °C in Figure 4.48 (a) and (c), respectively and the temperature of the Ti-Al-Cr-Nb quaternary phase system from 1123.91 °C to 1134.54 °C in Figure 4.48 (b) and (d) respectively, compared to the standard pressure condition. The Nb/Cr modified TiAl alloy containing 33.06 wt.% Al undergoes $L \rightarrow L + \beta \rightarrow L + \alpha \rightarrow \alpha \rightarrow \alpha + \gamma \rightarrow \gamma + \beta \rightarrow \gamma + \beta + \alpha_2$ phase transformations under standard pressure, while it enters a single γ region under 100 MPa pressure, exhibiting $L \rightarrow L + \beta \rightarrow L + \alpha \rightarrow \alpha \rightarrow \alpha + \gamma \rightarrow \gamma + \beta \rightarrow \gamma \rightarrow \gamma + \beta \rightarrow \gamma + \beta + \alpha_2$ transformations.

The Ti-Al binary system containing 33.06 wt.% Al consisted of γ and α_2 phases at RT, while at 1200 °C and 1400 °C, it composed of binary γ , α and single α , respectively as seen in Figure 4.48 (a) and (c). The modelling studies revealed that the Nb/Cr modified Ti-Al system consisted of γ , β and α_2 phases at room temperature at both standard and 100 MPa pressure, even though the XRD patterns and EBSD phase maps, illustrated in Figure 4.4 and Figure 4.12, respectively, only showed γ and α_2 phases for as-built, HIPed, HT1 and HT2 processed samples. γ , β and α_2 phases have been detected based on ThermoCalc modelling investigations in another study but they did not find a β phase in the XRD patterns or the EBSD analysis [193]. In Figures 3.6 (b) and (d), when the β phase at room temperature was investigated in detail, it was discovered that the software suggested the

presence of the Cr element only in the β phase, but not in the γ and α_2 phases. The inconsistency between the modelling and experimental data for the Nb/Cr modified Ti-Al system indicates a discrepancy although it is known that the Cr element has a β -stabilizing effect in titanium alloys [299]. The phase system at 1200 °C corresponds to the intersection zone of the $\alpha + \beta + \gamma$, $\alpha + \gamma$, and $\gamma + \beta$ transformations in Figure 4.48 (b) and (d). The system was close to the $\alpha + \gamma$ region in Figure 4.48 (b) while it was in the $\gamma + \beta$ region in Figure 4.48 (d) with the increasing transition temperature due to the impact of 100 MPa. The phase system at 1400 °C corresponds to the single α phase region in Figure 4.48 (b) and (d).

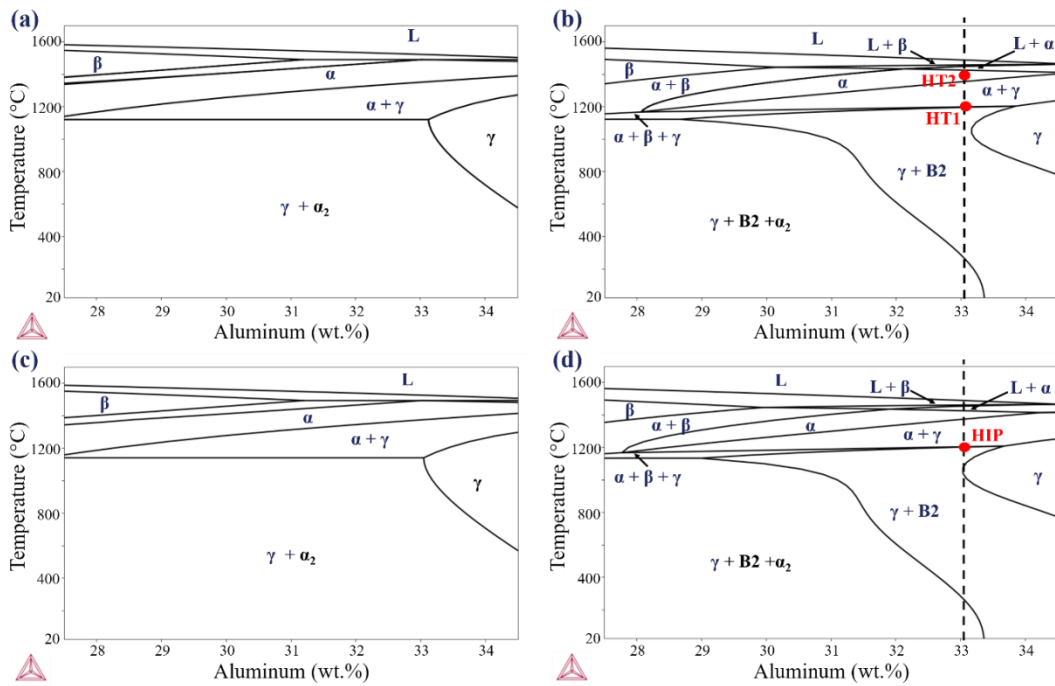


Figure 4.48: Binary and quaternary phase diagrams of; (a) Ti-Al binary and (b) Nb/Cr modified Ti–Al–Cr–Nb quaternary phase systems. Binary and quaternary phase diagrams at 100 MPa for; (c) Ti-Al binary and (d) Nb/Cr modified Ti–Al–Cr–Nb quaternary phase systems.

When examining the phase ratios in Table 4.9, it is evident that both the Ti-Al and Ti48Al2Cr2Nb systems exhibit no significant variations in phase constituents at

room temperature under a pressure of 100 MPa. The effect of pressure becomes more pronounced at 1200 °C. In the binary system at 1200 °C and standard atmospheric pressure, the amount of γ phase was calculated to be 88.8%, whereas under 100 MPa pressure, the γ phase content increased to 93.6%. In both cases of the binary system at 1200 °C, only α phase was present apart from γ . With the introduction of Nb/Cr, the system at 1200 °C, occurring in the " $\alpha + \beta + \gamma$," " $\alpha + \gamma$," and " $\gamma + \beta$ " triple intersection region, became more complex. It was found that at 1200 °C in the quaternary system, the pressure of 100 MPa favours the formation of γ similarly to the binary system. At standard atmospheric pressure, the γ phase content was 86.6%, while under 100 MPa pressure, it increased to 98.0% at 1200 °C for quaternary systems. Another difference for both quaternary systems at 1200 °C was the phase constituent other than γ . The Ti48Al2Cr2Nb alloy at 1200 °C contains 13.4% α in standard atmosphere, whereas under 100 MPa pressure, it was determined to contain 2.0% β . Modeling at 1400 °C revealed that both binary and quaternary systems, under standard atmosphere and 100 MPa pressure, include 100.0% α phase.

Table 4.9: Eutectoid temperature and phase constituent versus temperature relationship in TiAl and Ti48Al2Cr2Nb systems calculated in ThermoCalc Software.

	Eutectoid Temperature	Phase Constituents at RT	Phase Constituents at 1200 °C	Phase Constituents at 1400 °C
Ti-Al at standard pressure	1121.19 °C	γ : 84.8% α_2 : 15.2%	γ : 88.8% α : 11.2%	α : 100.0%
Ti-Al at 100 MPa pressure	1141.48 °C	γ : 84.9% α_2 : 15.1%	γ : 93.6% α : 6.4%	α : 100.0%
Ti48Al2Cr2Nb at standard pressure	1123.91 °C	γ : 87.3% α_2 : 1.4% β : 11.3%	γ : 86.6% α : 13.4%	α : 100.0%
Ti48Al2Cr2Nb at 100 MPa pressure	1134.54 °C	γ : 87.3% α_2 : 1.4% β : 11.3%	γ : 98.0% β : 2.0%	α : 100.0%

4.9 Electron Beam Powder Bed Fusion Double-Scan Studies

In Chapter 4.5, the microstructure analysis of as-built Ti48Al2Cr2Nb produced through PBF-EB fabrication revealed the presence of spherical pores. These pores are attributed to gases entrapped during the gas atomization process used for powder production. When electron beams during PBF-EB fabrication melt the powders, the trapped gases are released, leading to porosity. Figure 4.8 and Figure 4.9 demonstrate that heat treatments alone are insufficient for pore removal. Even with optimized PBF-EB process parameters, complete elimination of pores is unattainable. Figure 4.8 (b) and Figure 4.9 (b) emphasise the importance of using technologies such as HIP to efficiently remove pores generated during PBF-EB fabrication..

In Chapter 4.7.2, it was observed that Z-direction samples exhibited premature failure with considerable variability in room temperature results in the as-built condition. Subsequent application of heat treatments and HIP allowed the identification of yielding points in Z-direction samples. The anisotropy in mechanical properties between the XY- and Z-directions was found to be lower in HIPed samples compared to heat-treated samples (see Figure 4.46). These findings emphasize the necessity of subjecting PBF-EB-produced Ti48Al2Cr2Nb alloy to HIP for critical applications like aviation engines. However, the high operational costs associated with HIP contribute to an increased overall cost of Ti48Al2Cr2Nb parts produced via PBF-EB. Additionally, each supplementary operation extends the transition time from design to final part in industrial applications.

In this part of the study, the objective was to diminish the as-built material's porosity using the PBF-EB process and to effectively acquire tensile test data in the Z-direction. Selective rescanning of specific regions within the samples was conducted as a secondary step, employing distinct process parameters after each layer was exposed to electron beams during PBF-EB fabrication. This technique, referred to as "double-scan," aimed to remelt designated areas of each layer and reheat specific regions. The assumption is that this approach will reduce overall

operation time and cost by mitigating the necessity for secondary processes like HIP. Additionally, the potential exists to generate 'microstructural gradient materials' by rescanning specific sections of the components. This innovative approach seeks to broaden the application range of the Ti48Al2Cr2Nb alloy produced via PBF-EB.

A total of 75 cylindrical-shaped tensile specimens were fabricated in the Z-direction, utilizing three distinct built strategies illustrated in Figure 4.49. To ensure consistent and reliable tensile test results, 24 sample groups, with a minimum of 3 samples each employing different scanning strategies, were manufactured. Each Z-direction tensile specimen was designed with a diameter of 18 mm and a height of 110 mm. To achieve a homogeneous distribution on the built platform, specimens were randomly arranged, as depicted in Figure 4.49. A 10 mm section from the top of all 110 mm Z-direction cylinders was removed using wire-EDM. The removed parts of the samples, measuring 18 mm in diameter and 10 mm in height, were employed for microstructure examinations, while the remaining samples, with a height of 100 mm, were utilized for tensile tests. Tensile tests adhered to the methodologies outlined in Chapter 3.6.2.

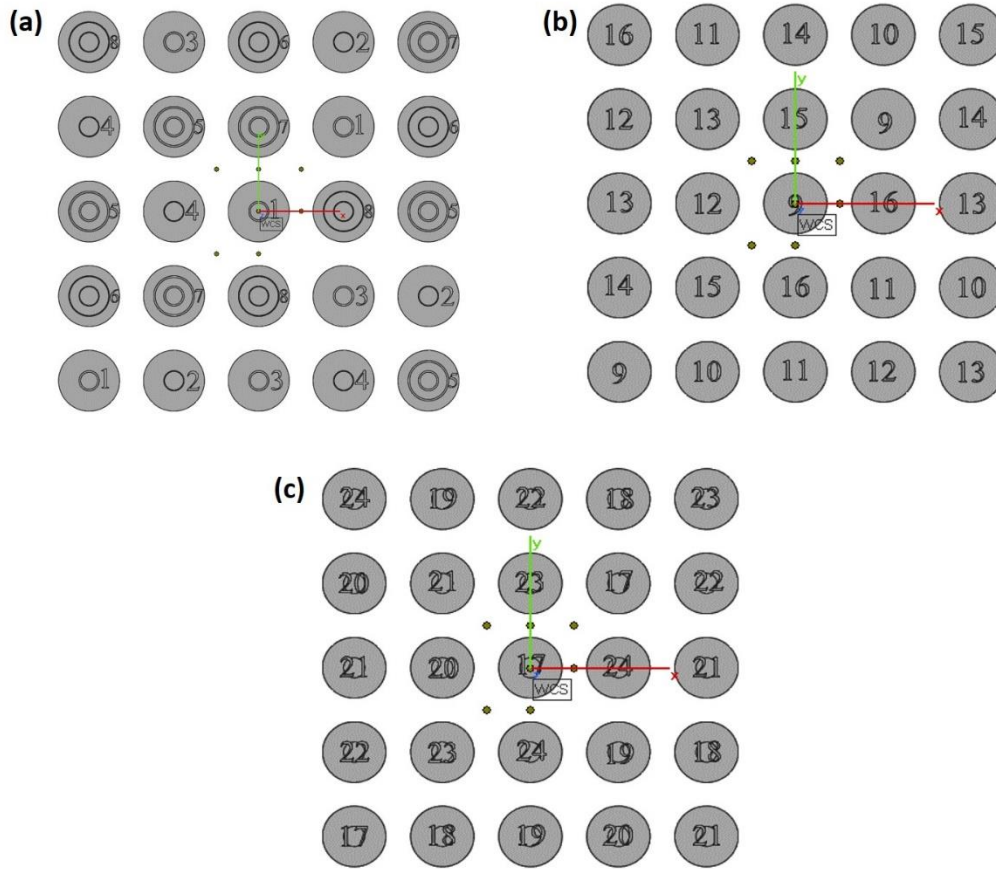


Figure 4.49: Top view of Z-direction double-scan tensile specimens; (a) partial overlap #1, (b) complete overlap and (c) partial overlap #2.

The initial scans for all samples were conducted using the PBF-EB process parameters outlined in Table 3.5. However, distinct secondary scanning parameters and performed areas were applied, as detailed in Table 4.10. In the Partial Overlap #1 PBF-EB production group, depicted in Figure 4.49 (a), the inner circle or outer ring was initially scanned. For this group, 1 and 0.5 mm regions between the inner circle and the outer ring were double-scanned at the same speed as the first melted areas. The relatively low overlap in the production of these samples, as shown in Figure 4.49 (a), resulted in secondary melting occurring in a narrow area. Nevertheless, a second preheating was achieved across the entire diameter of the 18

mm sample. This approach aimed to establish a transitional microstructure between the initially melted areas and subsequent ones, as well as the overlap region.

In the fabrication of Double-Scan Complete Overlap samples, illustrated in Figure 4.49 (b), the effect of a secondary hatch exposure with varying scan speeds along the 18 mm diameter was executed. Specifically, Sample 09 intentionally underwent no double-scan exposure after the initial scan to facilitate a comparison between standard PBF-EB production and the double-scan manufacturing strategy. The Double-Scan Complete Overlap study incorporated a variation in scanning speed during the secondary exposure for all samples, resulting in different applied area energies (E_A), as calculated in Equation 1.3. This approach allowed the observation of whether porosity in the samples could be effectively mitigated with distinct area energies. The primary objective with the Double-Scan Complete Overlap samples was to identify the most suitable scanning speed for the overlap region.

In the Double Scan Partial Overlap #2 study, illustrated in Figure 4.49 (c), the entire surface of the 18 mm diameter sample was initially produced, followed by a second scan of either the inner circle or the outer ring at varying speeds. This approach was designed to achieve a transitional microstructure in the inner and outer regions subjected to the second scan and preheating. Additionally, the study aimed to identify the most appropriate scanning speed for the partially applied secondary scanning.

Table 4.10: Double-scan parameters.

GROUP	SAMPLE NO	OVERLAP DIAMETER (mm)	SCAN STRATEGY	DOUBLE SCAN SPEED (mm/s)
Double-Scan Partial Overlap #1 (Figure 4.49 (a))	1	1	Inner circle scanned first, outer ring scanned last	1600
	2	0.5	Inner circle scanned first, outer ring scanned last	1600
	3	1	Outer ring scanned first, inner circle scanned last	1600
	4	0.5	Outer ring scanned first, inner circle scanned last	1600
	5	1	Inner circle scanned first, middle ring scanned second, outer ring scanned last	1600
	6	0.5	Inner circle scanned first, middle ring scanned second, outer ring scanned last	1600
	7	1	Outer ring scanned first, middle ring scanned second, inner circle scanned last	1600
	8	0.5	Outer ring scanned first, middle ring scanned second, inner circle scanned last	1600
Double-Scan Complete Overlap (Figure 4.49 (b))	9	no overlap	no double scan	no double scan
	10	18	Complete double scan	1600
	11	18	Complete double scan	2400
	12	18	Complete double scan	3200
	13	18	Complete double scan	4000
	14	18	Complete double scan	4800
	15	18	Complete double scan	5600
	16	18	Complete double scan	6400
Double Scan Partial Overlap #2 (Figure 4.49 (c))	17	6	Inner circle double scanned	1600
	18	12	Outer ring double scanned	1600
	19	6	Inner circle double scanned	3200
	20	12	Outer ring double scanned	3200
	21	6	Inner circle double scanned	4800
	22	12	Outer ring double scanned	4800
	23	6	Inner circle double scanned	6400
	24	12	Outer ring double scanned	6400

4.9.1 Double Scan Partial Overlap #1 Studies

Initially, the inner circle with a diameter of 6 mm at the center of Sample 01 was scanned using the PBF-EB parameters specified in Table 3.5, as depicted in Figure

4.50. Subsequently, after completing the production of the inner circle, the outer ring with outer and inner diameters of 18 and 5 mm, respectively, was produced using the same parameters. Figure 4.50 (a) and (b) illustrate that the overlap region, scanned for the second time, is distinctly separated from the inner circle and outer ring. Detailed examinations at higher magnifications (Figure 4.50 (c) and (d)) revealed that the overlap region exhibited finer grains compared to other areas of the sample. However, investigations indicated that the thickness of the overlap zone, nominally 1 mm, is approximately 0.3 mm. This phenomenon resulted from partial grain growth in the region adjacent to the inner circle, influenced by heat during the subsequent scanning of the outer region.

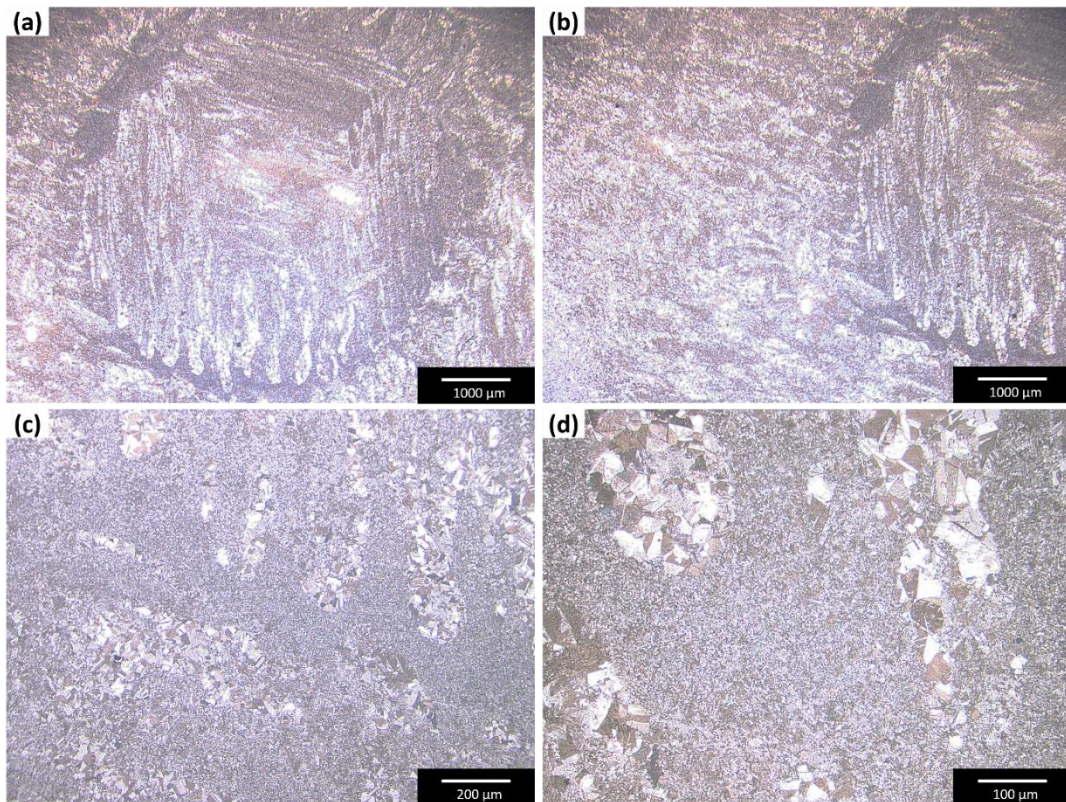


Figure 4.50: Optical micrographs of 01st sample that shows; (a) inner circle at 50x, (b) overlap region at 50x, (c) overlap region at 200x and (d) overlap region at 500x magnifications.

For Sample 02, the outer ring was produced following the scanning of the inner circle, similar to Sample 01. However, in contrast to Sample 01, the inner diameter of the outer ring for Sample 02 was 5.5 mm, and the thickness of the overlap area was reduced to 0.5 mm. Figure 4.51 (a) and (b) reveal lack-of-fusion defects and pores in the overlap region. Additionally, the microstructural transition in the overlap region is less clearly observable in the images presented in Figure 4.51 (c) and (d), which depict larger magnifications.

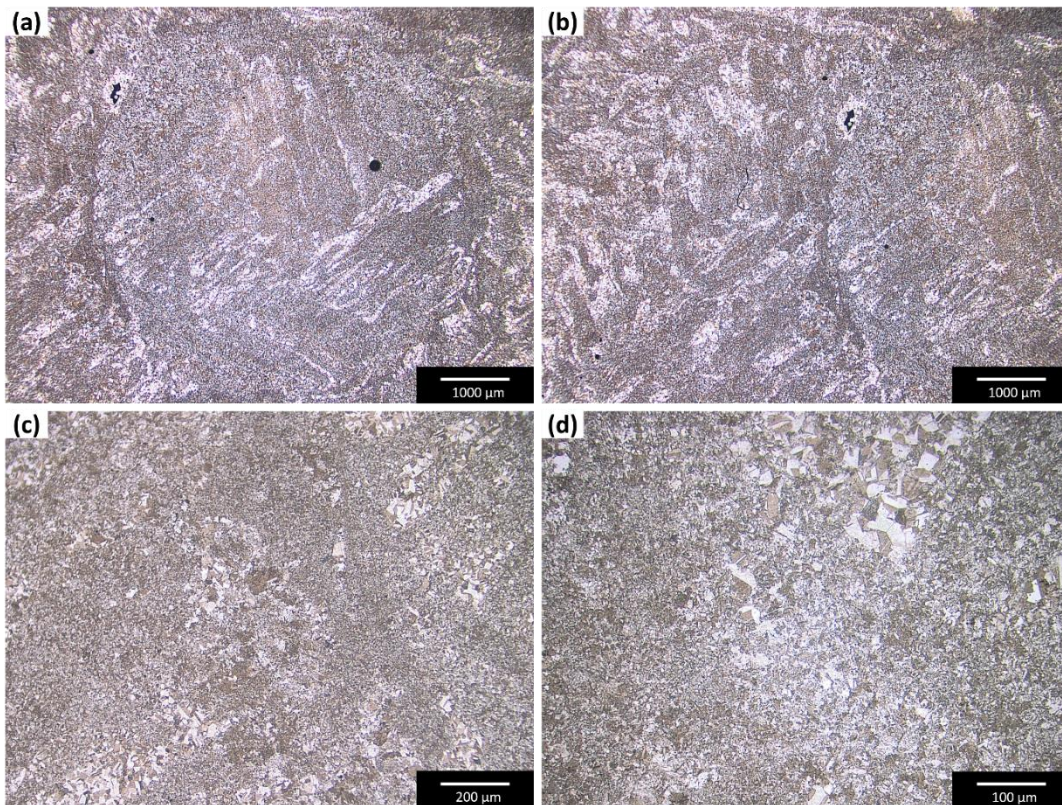


Figure 4.51: Optical micrographs of 02nd sample that shows; (a) inner circle at 50x, (b) overlap region at 50x, (c) overlap region at 200x and (d) overlap region at 500x magnifications.

Sample 03 followed a different scanning order, where the outer ring was produced first, followed by the fabrication of the inner circle. This is in contrast to Samples

01 and 02, where the inner circle was scanned first. The microstructure of Sample 03 is depicted in Figure 4.52. In this sample, manufactured with an outside-inside production principle, the thickness of the overlap region was adjusted to be 1 mm. While the microstructures in Figure 4.52 (a) and (b) exhibit the presence of an inner circle with a diameter of approximately 6 mm, no apparent microstructural transition is observed in the overlap region. Moreover, Figure 4.52 (c) and (d), with larger magnifications, reveal an absence of defects such as lack of fusion and pores in the overlap region.

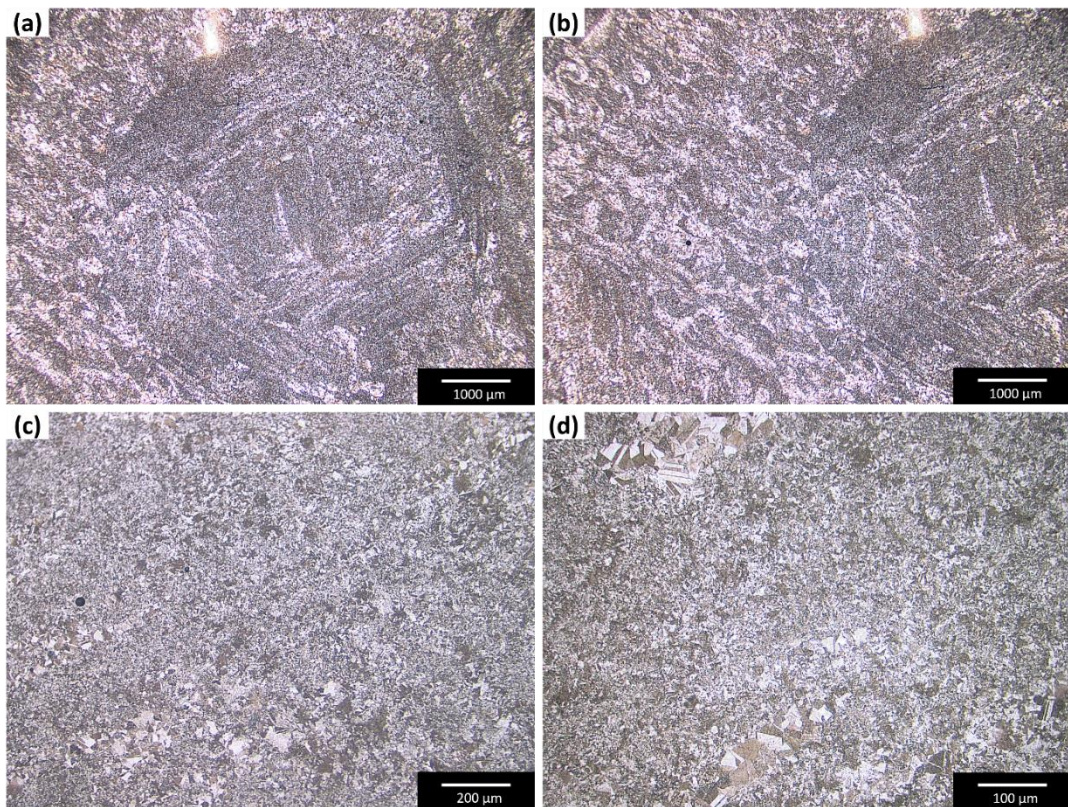


Figure 4.52: Optical micrographs of 03rd sample that shows; (a) inner circle at 50x, (b) overlap region at 50x, (c) overlap region at 200x and (d) overlap region at 500x magnifications.

In Sample 04, produced with an outside-to-inside order, the thickness of the overlap region between the outer ring and the inner circle was set at 0.5 mm. In the microstructures shown in Figure 4.53 (a) and (b), pores are notably present, particularly in the overlap region. However, the amount of unmelted region is less compared to Sample 02, which also had a 0.5 mm overlap region thickness. This difference can be attributed to the fact that in Sample 02, the inner circle, produced first, shrank after solidification, and the 0.5 mm thick overlap was insufficient to melt some locations. Since the outer ring is produced first in the outside-to-inside production order in Sample 04, the effect of shrinkage is less pronounced between the outer and inner regions. Additionally, no distinct transition region is observed in the microstructures of the overlap region presented in Figure 4.53 (c) and (d).

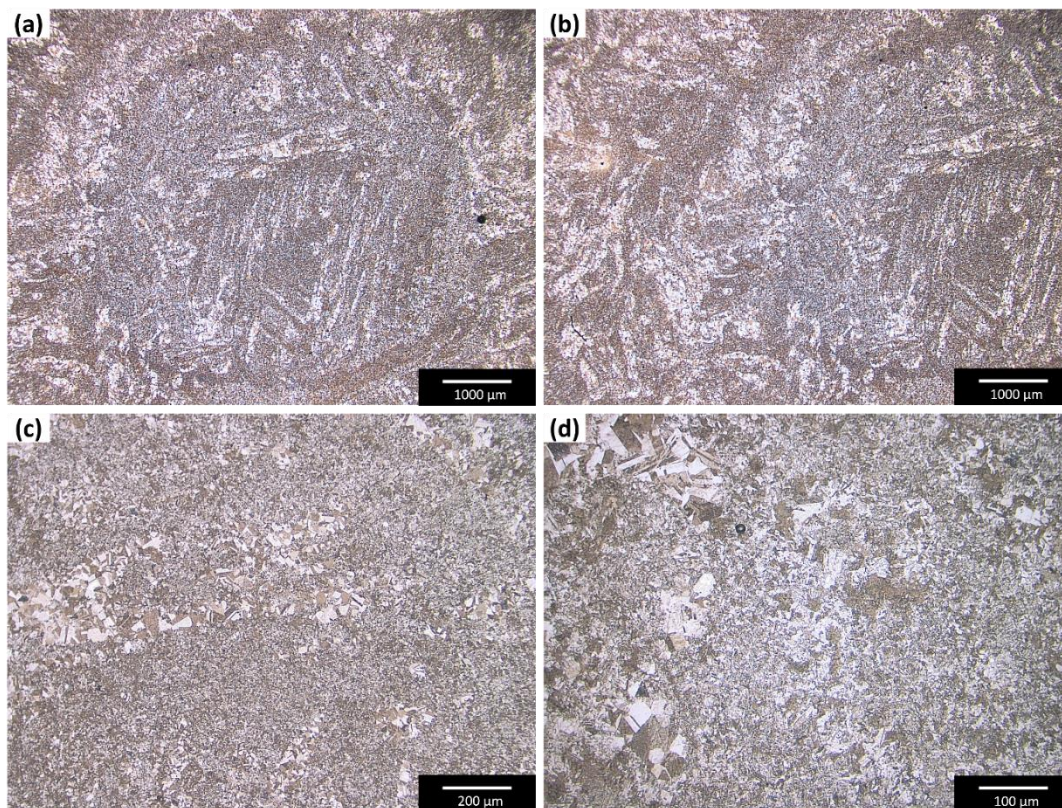


Figure 4.53: Optical micrographs of 04th sample that shows; (a) inner circle at 50x, (b) overlap region at 50x, (c) overlap region at 200x and (d) overlap region at 500x magnifications.

Sample 05 was manufactured by dividing it into three distinct regions, each with a 1 mm overlap thickness between the inner circle, middle ring, and outer ring. The manufacturing sequence involved producing the inner circle first, followed by the middle ring, and finally the outer ring. The inner circle had a diameter of 6 mm, the outer diameter of the middle ring was set to 12 mm with an inner diameter of 5 mm, resulting in a 1 mm overlap region with the inner circle. The outer ring had an outer diameter of 18 mm, an inner diameter of 11 mm, and a 1 mm overlap region with the middle ring. Figure 4.54 (a) illustrates the overlap region between the inner circle and the middle ring, while Figure 4.54 (b) represents the region between the inner circle and the middle ring and between the middle ring and the outer ring. In Figure 4.54 (c) and (d), the microstructural transition in the overlap region is shown at larger magnifications. The production of Sample 05 demonstrated that it is possible to achieve a clear microstructural transition with a 1 mm overlap thickness in fabrications conducted in the inside-outside manufacturing sequence. It's noteworthy that the number of pores was at its minimum within the Double-Scan Partial Overlap #01 study for Sample 05.

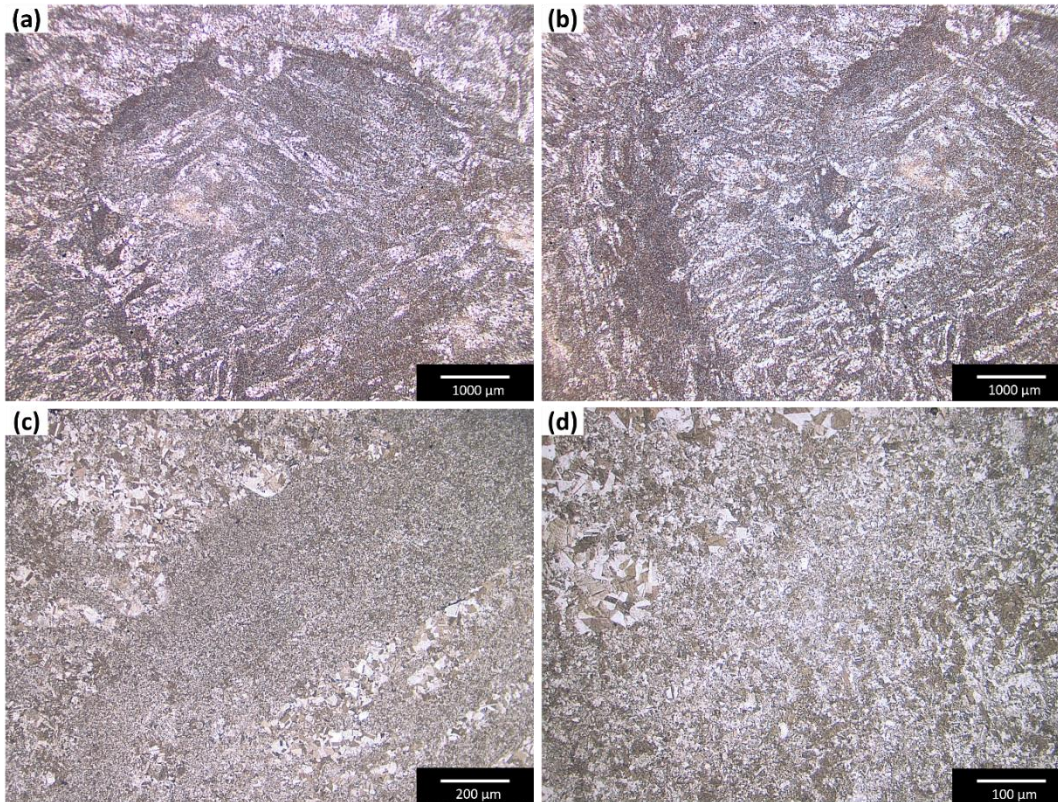


Figure 4.54: Optical micrographs of 05th sample that shows; (a) inner circle at 50x, (b) overlap region and middle ring at 50x, (c) overlap region at 200x and (d) overlap region at 500x magnifications.

Sample 06, like Sample 05, was composed of three distinct regions and manufactured in the inside-outside production order. The only difference was the reduced overlap area thickness of 0.5 mm in Sample 06. The inner circle had a thickness of 6 mm, the outer diameter of the middle ring was 12 mm with an inner diameter of 5.5 mm, and the outer diameter of the outer ring was 18 mm with an inner diameter of 11.5 mm. Figure 4.55 (a) and (b) display overlap regions between the inner circle-middle ring and middle ring-outer ring, though not as distinctly as in Figure 4.54 (a) and (b). Optical microscope images in Figure 4.55 (c) and (d), taken from the overlap regions and showing larger magnifications, reveal the absence of a clear microstructural transition in these regions. Additionally, pores were identified in the overlap areas of Sample 06. In contrast to Sample 05, the

sample with the highest number of pores in this study was Sample 06. This suggests that the 0.5 mm overlap thickness was insufficient, and the number of pores increased as the overlap thickness decreased.

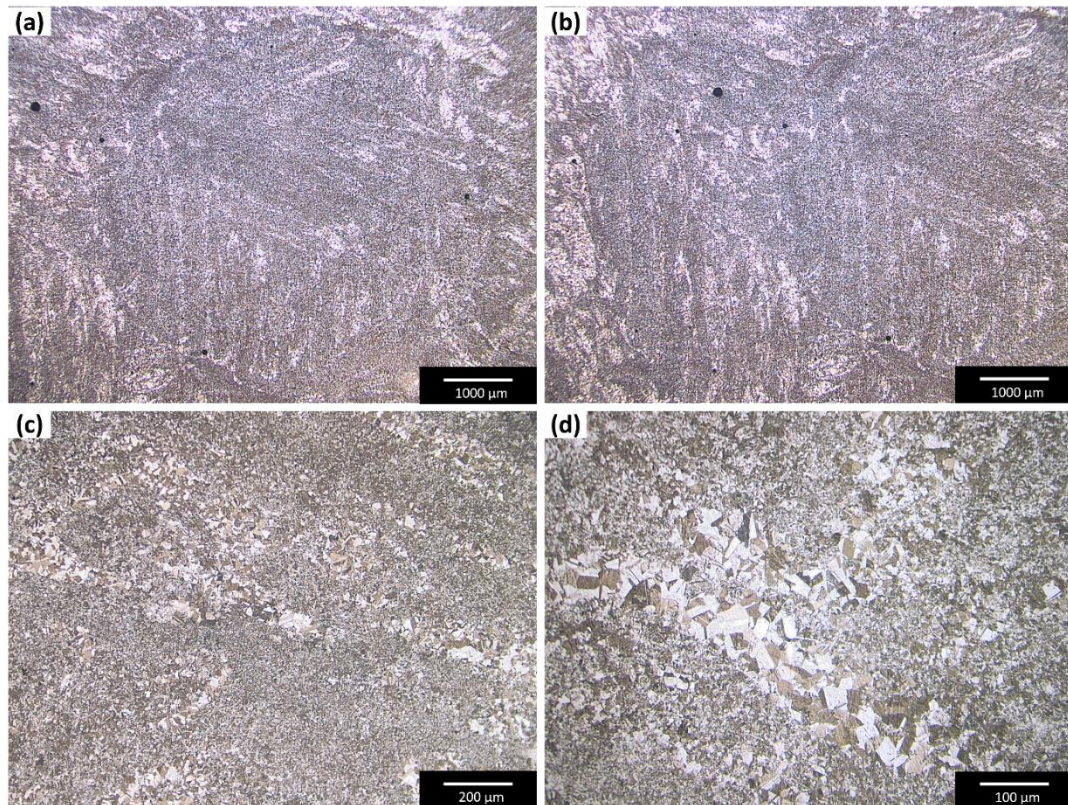


Figure 4.55: Optical micrographs of 06th sample that shows; (a) inner circle at 50x, (b) overlap region and middle ring at 50x, (c) overlap region at 200x and (d) overlap region at 500x magnifications.

Sample 07, produced in the outside-to-inside production order, comprised three regions with a 1 mm overlap thickness between each region. Figure 4.56 (a) illustrates the transition zone between the inner circle and the middle ring, while Figure 4.56 (b) displays both the overlap between the inner circle and the middle ring and the overlap between the middle ring and the outer ring. Although the regions separated by overlap are clearly visible at lower magnifications, no

microstructural transition was observed at 200x and 500x magnifications, as presented in Figure 4.56 (c) and (d), respectively. Additionally, due to the 1 mm overlap thickness, no unmelted region was observed between the regions.

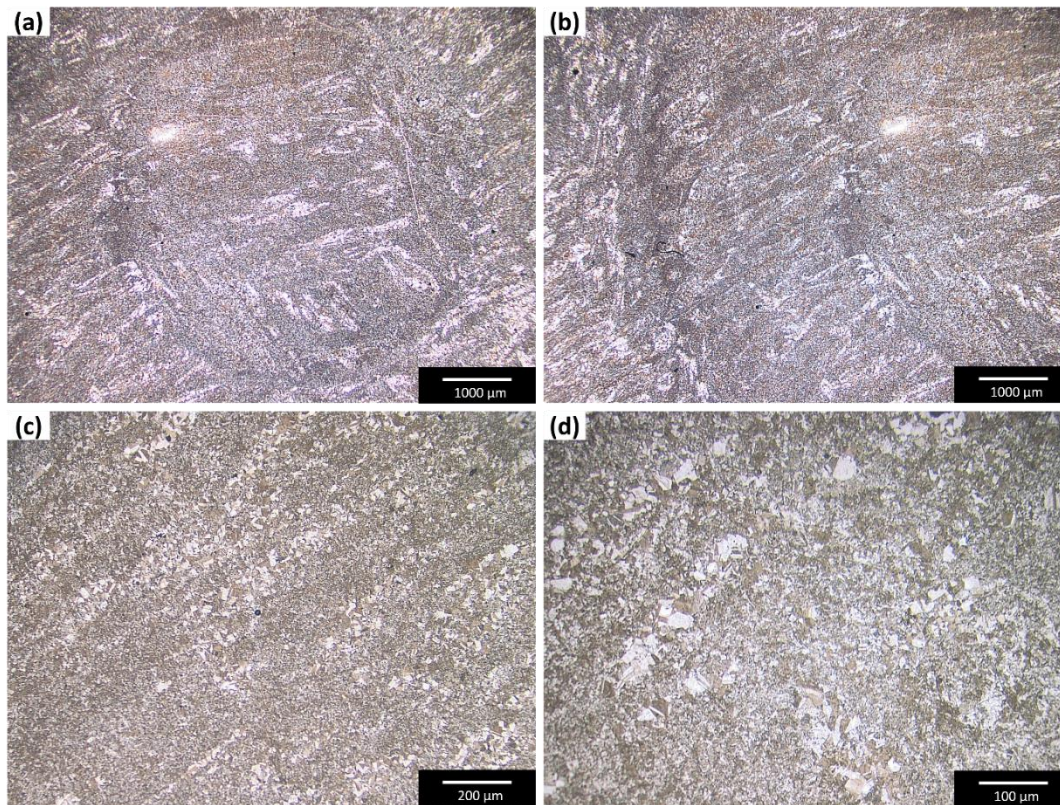


Figure 4.56: Optical micrographs of 07th sample that shows; (a) inner circle at 50x, (b) overlap region and middle ring at 50x, (c) overlap region at 200x and (d) overlap region at 500x magnifications.

Sample 08 was composed of three regions—inner circle, middle ring, and outer ring—with a 0.5 mm overlap thickness between each zone. It was manufactured in the outside-to-inside production order. Similar to all samples with a 0.5 mm overlap thickness in the Double Scan Partial Overlap #1 study, pores were present in the overlap areas. Additionally, a clear transition between the regions was not observed due to the inadequacy of the 0.5 mm overlap in creating a microstructural

transition region. Figure 4.57 (a) and (b) depict the inner circle and middle ring, while Figure 4.57 (c) and (d) show larger magnifications of the transition zones.

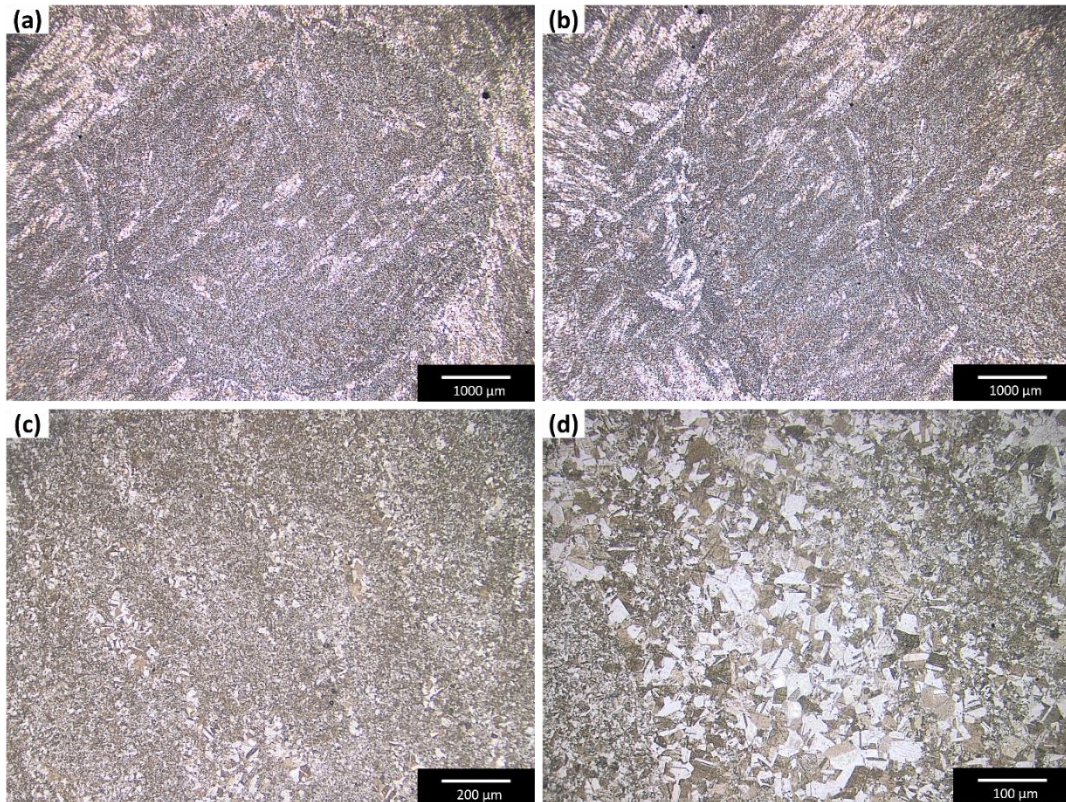


Figure 4.57: Optical micrographs of 08th sample that shows; (a) inner circle at 50x, (b) overlap region and middle ring at 50x, (c) overlap region at 200x and (d) overlap region at 500x magnifications.

The room temperature tensile test results for the Double Scan Partial Overlap #1 samples are provided in Table 4.11. It is evident that both the tensile and yield strength of "DS05" were higher than the other samples, attributed to its inner-to-outer division into three regions scanning strategy with a 1 mm overlap thickness.

The overall observations from the examination of the Double Scan Partial Overlap #1 study are as follows:

- i. Smaller grains were achieved in the overlap region formed by remelting for the second time.
- ii. The transitional microstructure became more apparent as the overlap region widened from 0.5 mm to 1 mm.
- iii. The distinction of the transition zone was less prominent when the outer ring was produced first. It was noted that the transition region became clearer when the inner circle was produced first. During PBF-EB production, the outer ring experiences faster cooling due to the colder surrounding powders in the powder bed. Conversely, when the inner circle is produced later, the cooling rate is lower, leading to grain growth.
- iv. Defects such as lack of fusion and porosity were observed when the thickness of the overlap region was reduced from 1 mm to 0.5 mm. More defects were particularly found in samples where the inner region was produced first. It was concluded that a 0.5 mm overlap was insufficient, resulting from the shrinkage of the melted Ti48Al2Cr2Nb material during cooling after solidification.

Table 4.11: Room temperature tensile test results of the double scan partial overlap #1 samples.

Sample No	E (GPa)	UTS (MPa)	0.2% YS (MPa)	Elongation (%)	RA (%)
DS01-2	148.00	560.00	515.00	3.00	3.00
DS01-3	146.00	535.00	-	2.20	2.00
DS01 Average	147.00	547.50	515.00	2.60	2.50
DS02-1	147.00	590.00	545.00	1.80	3.00
DS02-2	160.00	-	-	1.00	1.00
DS02-3	161.00	570.00	525.00	2.20	1.40
DS02 Average	156.00	580.00	535.00	1.67	1.80
DS03-1	147.00	595.00	550.00	1.60	1.40
DS03-2	143.00	-	-	2.80	1.60
DS03-3	158.00	555.00	550.00	2.20	2.00
DS03 Average	149.33	575.00	550.00	2.20	1.67
DS04-1	131.00	530.00	530.00	2.20	1.00
DS04-2	130.00	515.00	515.00	2.60	2.00
DS04-3	170.00	-	-	2.60	1.00
DS04 Average	143.67	522.50	522.50	2.47	1.33
DS05-1	180.00	-	-	1.80	0.80
DS05-2	151.00	505.00	495.00	2.80	3.00
DS05-3	155.00	735.00	685.00	2.80	3.00
DS05-4	138.00	505.00	494.00	1.80	0.40
DS05-5	129.00	720.00	720.00	1.20	1.40
DS05 Average	150.60	616.25	598.50	2.08	1.72
DS06-1	154.00	540.00	535.00	1.60	1.40
DS06-2	136.00	530.00	525.00	2.20	2.00
DS06-3	147.00	-	-	1.80	0.80
DS06 Average	145.67	535.00	530.00	1.87	1.40
DS07-2	131.00	565.00	525.00	2.60	1.40
DS07-3	149.00	570.00	565.00	1.80	1.00
DS07 Average	140.00	567.50	545.00	2.20	1.20
DS08-1	146.00	535.00	505.00	2.60	1.40
DS08-2	132.00	515.00	505.00	2.80	1.00
DS08-3	150.00	535.00	535.00	1.60	1.20
DS08 Average	142.67	528.33	515.00	2.33	1.20

4.9.2 Double Scan Complete Overlap Studies

Sample 09, presented in Figure 4.58, was produced without double-scan and served as a control group. The PBF-EB process parameters outlined in Table 3.5 were employed in the production of this sample, and no second scanning was performed on any region afterward. The microstructure and mechanical properties of samples produced in the same manner as Sample 09 were detailed in Chapter 4.5.1 and 4.7.2.1, respectively.

In the absence of double-scan, the pores formed in the microstructure are clearly visible in Figure 4.58 (a) at 50x magnification. The duplex-like microstructure, composed of γ/α_2 lamellae + fine equiaxed γ separated by a coarse γ colonies with the typical PBF-EB Ti48Al2Cr2Nb structure, is presented in Figure 4.58 (b), (c), and (d) at 200x, 500x, and 1000x magnifications, respectively.

The average maximum pore values reported in the Double-Scan Complete Overlap Study were determined through pore ratio measurements based on image processing of optical microscope images captured from the area where pores on the as-polished surface were most concentrated. The as-polished surface of each sample was examined at 50x magnification, and pore values were derived from the average of measurements taken from five different regions. The primary objective of scanning the entire 18 mm diameter for the second time in this study was to diminish the need for secondary processes such as HIP by reducing the quantity of pores present in the single-scanned sample. The porosity amount of sample 09 was measured to be 0.649%.

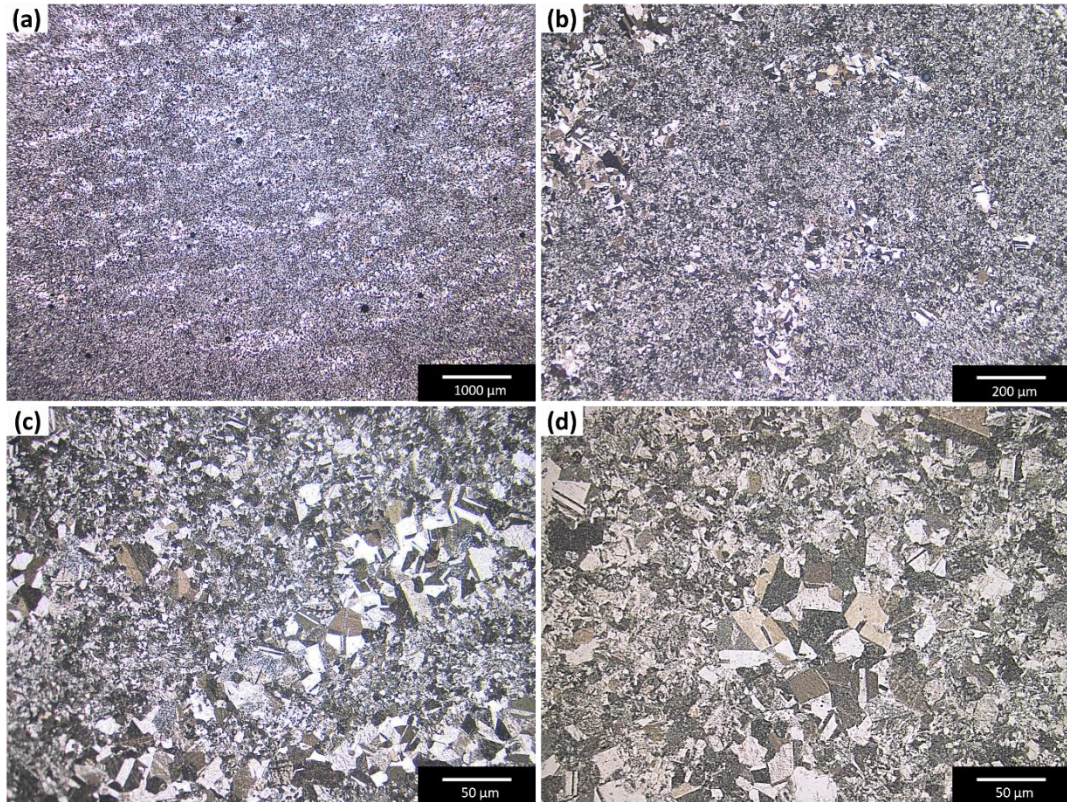


Figure 4.58: Optical micrographs of 09th sample at; (a) 50x, (b) 200x, (c) 500x, (d) 1000x magnifications.

Optical microscope images of Sample 10 are presented in Figure 4.59. The same PBF-EB parameters as specified in Table 3.5 were applied during the second scan when producing the 10th sample. Consequently, a double-scan was conducted over the entire diameter of the sample at the same scanning speed (1600 mm/s) as the first scan. Upon examining the microstructure displayed in Figure 4.59, it was observed that finer equiaxed grains were present compared to Sample 09. The maximum pore content of Sample 10 was determined to be 0.257%. As evident in Figure 4.59 (a), which shows the microstructure of Sample 10 at 50x magnification, the quantity of pores was significantly lower than the sample without double-scan. The pore value obtained in the 10th sample represented the lowest amount of pores found in the Double-Scan Complete Overlap Study.

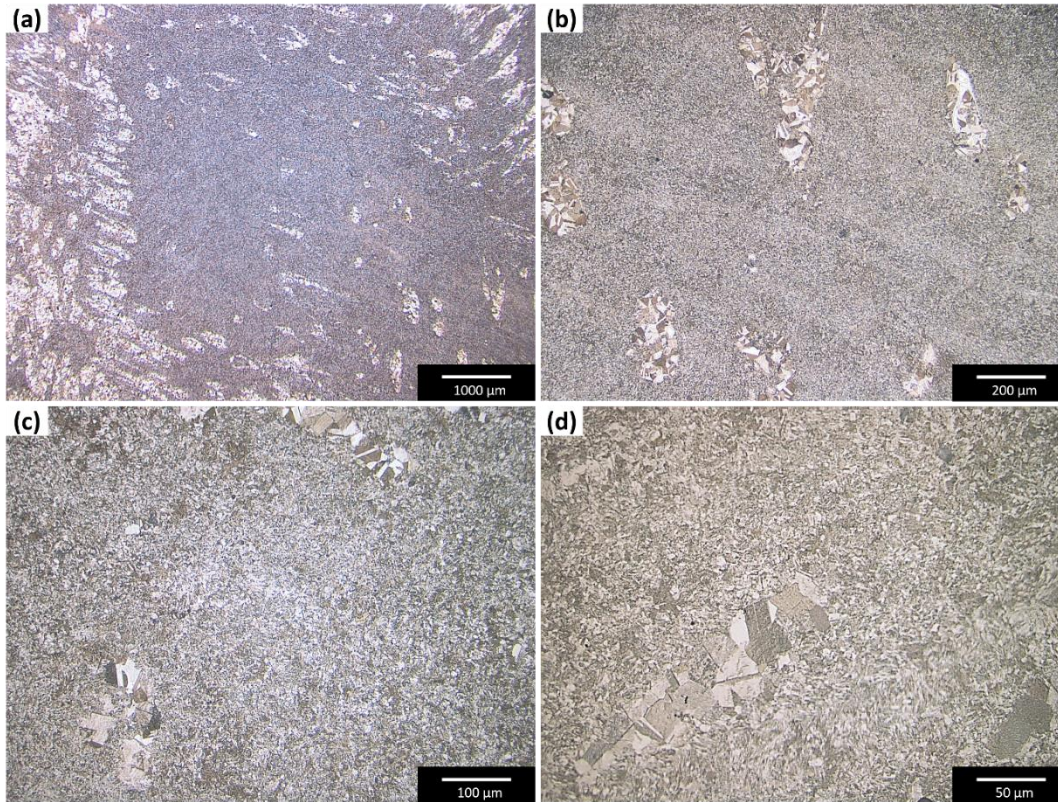


Figure 4.59: Optical micrographs of 10th sample at; (a) 50x, (b) 200x, (c) 500x, (d) 1000x magnifications.

During the second scanning of Sample number 11, a 50% faster exposure of the electron beams was executed compared to the first scanning. The double-scan area energy was also reduced by 50%, as the scanning speed was increased by 50% to 2400 mm/s. The microstructures shown in Figure 4.60 revealed coarser γ grains compared to Sample number 10, although finer grains were observed than in Sample number 09. Moreover, a slight amount of spherical-shaped pores were found in the microstructures illustrated in Figure 4.60 (a). The maximum porosity of the 11th sample was determined to be 0.385%, slightly higher than that of the 10th sample.

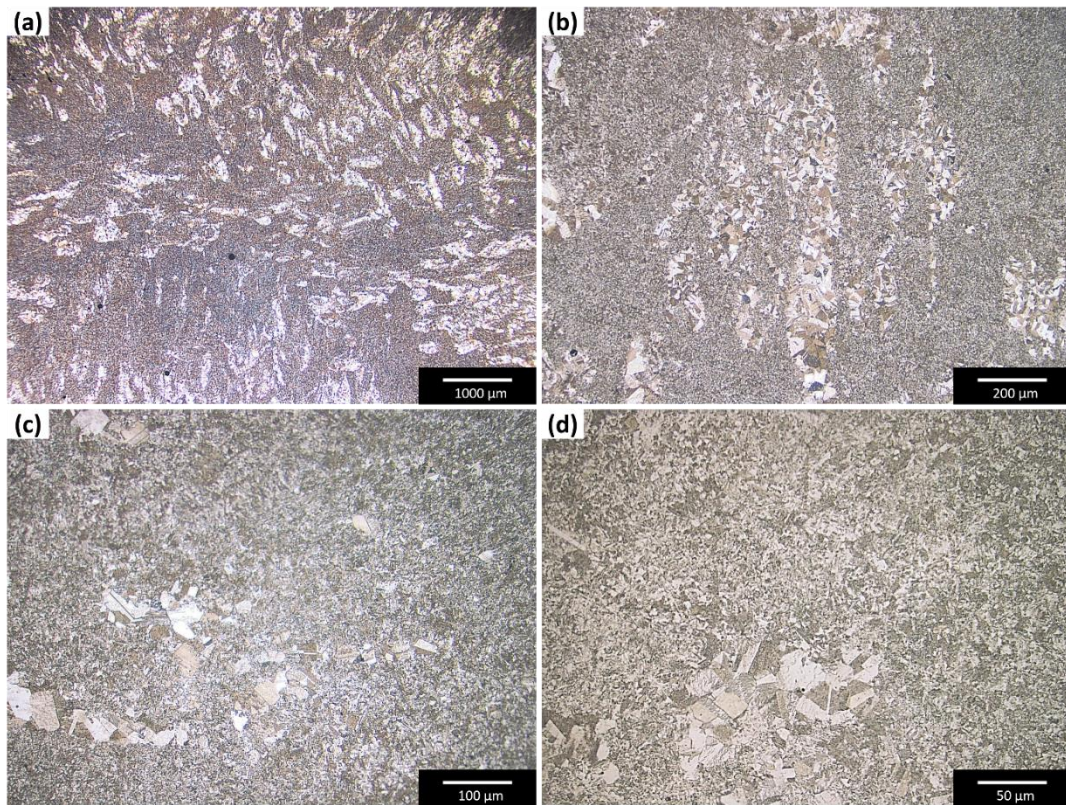


Figure 4.60: Optical micrographs of 11th sample at; (a) 50x, (b) 200x, (c) 500x, (d) 1000x magnifications.

During the second scan of Sample 12, depicted in Figure 4.61, the scan speed was doubled (3200 mm/s) in comparison to the initial scan. This adjustment aimed to reduce the area energy by half and expedite the overall production process. However, akin to Sample 11, there were fewer coarse γ colonies formed compared to the sample produced without double-scan. Additionally, the quantity of finer grains was observed to be less than in Sample 10. The pore content of Sample 12 was measured at 0.545% from the as-polished surfaces.

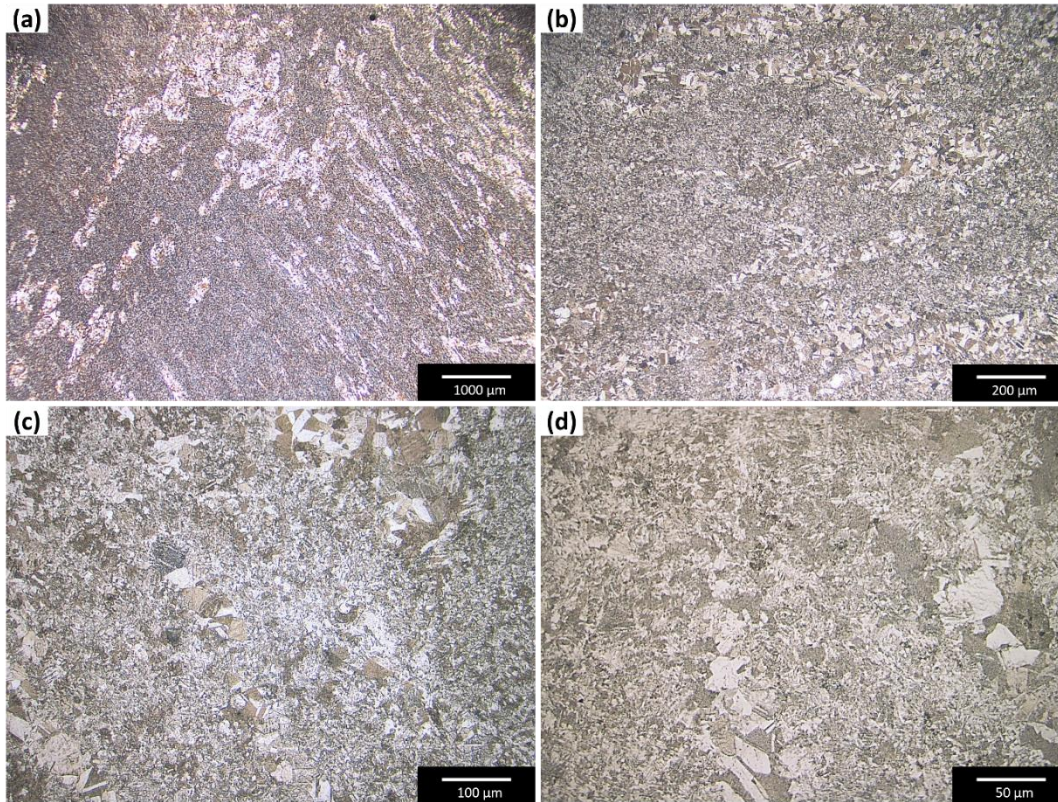


Figure 4.61: Optical micrographs of 12th sample at; (a) 50x, (b) 200x, (c) 500x, (d) 1000x magnifications.

Figure 4.62 (a) – (b), (c) – (d), (e) – (f), (g) – (h) illustrate the microstructures of Samples 13, 14, 15, and 16, respectively. Optical microscope images did not reveal discernible differences between these samples. In terms of secondary exposure, no visible alteration in the microstructure was observed when the scanning speed was 2.5 times or higher. This observation was attributed to the insufficient area energy of the second scan to remelt the material when the scanning speed decreased by more than 2.5 times. The pore contents for Samples 13, 14, 15, and 16 were determined to be 0.539%, 0.599%, 0.641%, and 0.582%, respectively.

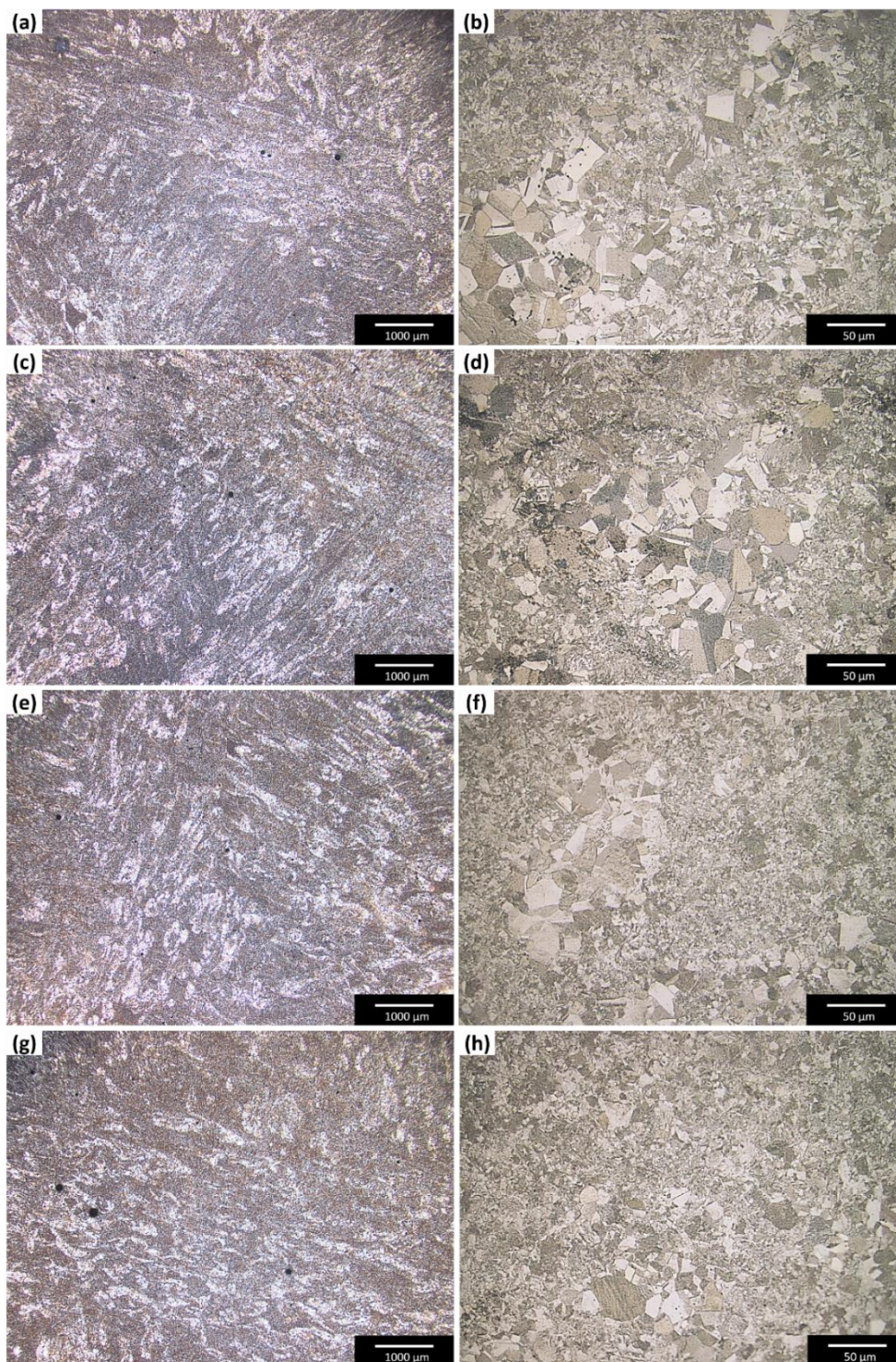


Figure 4.62: Optical micrographs of; (a) 13th sample at 50x, (b) 13th sample at 1000x, (c) 14th sample at 50x, (d) 14th sample at 1000x, (e) 15th sample at 50x, (f) 15th sample at 1000x, (g) 16th sample at 50x, (h) 16th sample at 1000x magnifications.

The room temperature tensile test results for the Double Complete Overlap samples are provided in

Table 4.12. Despite two DS10-1 samples being scrapped during machining and DS10-3 failed during tensile tests, both the tensile and yield strength of DS10-2 were higher than the other complete overlap samples. The DS10 samples underwent a complete double scan with the same scan parameters as the first scan. This likely contributed to a reduction in microspores and an enhancement in mechanical behavior.

The following conclusions were drawn from the Double Scan Complete Overlap study:

- i. A decrease in the speed of the secondary scanning corresponded to a reduction in the amount of pores. Sample 10, with the slowest scanning speed at 1600 mm/s, exhibited the least porosity (0.257%).
- ii. Sample number 09, where no second scanning was applied, displayed large pores, with a maximum porosity of 0.649%.
- iii. Significant reductions in pore amounts were observed only in the 10th and 11th samples compared to the 09th sample. Pore contents for samples 12 - 16 ranged between 0.539% and 0.641%.
- iv. All samples exhibited a duplex-like microstructure composed of fine (γ/α_2 lamellae and equiaxed γ) and coarse γ colonies. However, it was observed that the amount of coarse colonies decreased with a decrease in the second scanning speed and an increase in the area energy.
- v. Microstructural refinement was achievable by adjusting the second scanning process parameters such as scan speed.

Table 4.12: Room temperature tensile test results of the complete overlap samples.

Sample No	E (GPa)	UTS (MPa)	0.2% YS (MPa)	Elongation (%)	RA (%)
DS09-1	150.00	-	-	1.60	1.00
DS09-2	147.00	530.00	491.00	1.80	2.00
DS09-3	152.00	505.00	477.00	2.80	1.40
DS09 Average	149.67	517.50	484.00	2.07	1.47
DS10-2	147.00	660.00	650.00	1.00	2.00
DS10-3	153.00	-	-	2.20	1.00
DS10 Average	150.00	660.00	650.00	1.60	1.50
DS11-2	145.00	492.00	-	1.00	1.40
DS11-3	133.00	560.00	-	1.20	1.40
DS11 Average	139.00	526.00	-	1.10	1.40
DS12-1	142.00	600.00	575.00	1.60	1.40
DS12-2	147.00	625.00	565.00	1.60	3.00
DS12-3	144.00	570.00	555.00	1.20	1.00
DS12 Average	144.33	598.33	565.00	1.47	1.80
DS13-2	161.00	530.00	-	1.20	1.40
DS13-4	151.00	600.00	540.00	1.20	3.00
DS13 Average	156.00	565.00	540.00	1.20	2.20
DS14-1	142.00	600.00	555.00	2.60	1.00
DS14-2	131.00	535.00	520.00	1.80	1.40
DS14-3	145.00	545.00	530.00	2.60	2.40
DS14 Average	139.33	560.00	535.00	2.33	1.60
DS15-1	151.00	540.00	525.00	2.80	1.40
DS15-2	146.00	540.00	-	1.60	1.40
DS15-3	149.00	520.00	510.00	3.00	2.00
DS15 Average	148.67	533.33	517.50	2.47	1.60
DS16-2	151.00	565.00	500.00	2.20	1.40
DS16-3	156.00	540.00	505.00	2.20	2.00
DS16 Average	153.50	552.50	502.50	2.20	1.70

4.9.3 Double Scan Partial Overlap #2 Studies

Optical microscope images of the 17th sample are displayed in Figure 4.63. Following the completion of the first scan over the entire 18 mm diameter of the sample, only the inner circle with a diameter of 6 mm at the center was subjected to a second scan with the same process parameters outlined in Table 3.5. The trace of the inner circle, with a diameter of 6 mm, is distinctly visible in Figure 4.63 (a). In Figure 4.63 (b), the transition region of the inner circle is illustrated, comprising extremely fine grains, contrasted with the outer ring, which consists of coarse γ colonies and fine γ/α_2 lamellae. Figure 4.63 (c) illustrates the microstructure of the inner ring, while Figure 4.63 (d) represents the microstructure of the outer ring, which was not exposed to electron beams for the second time. Thus, a discernible microstructural contrast was identified between the outer ring and the inner circle in a double-scan experiment with a second scan exclusively targeting the inner circle.

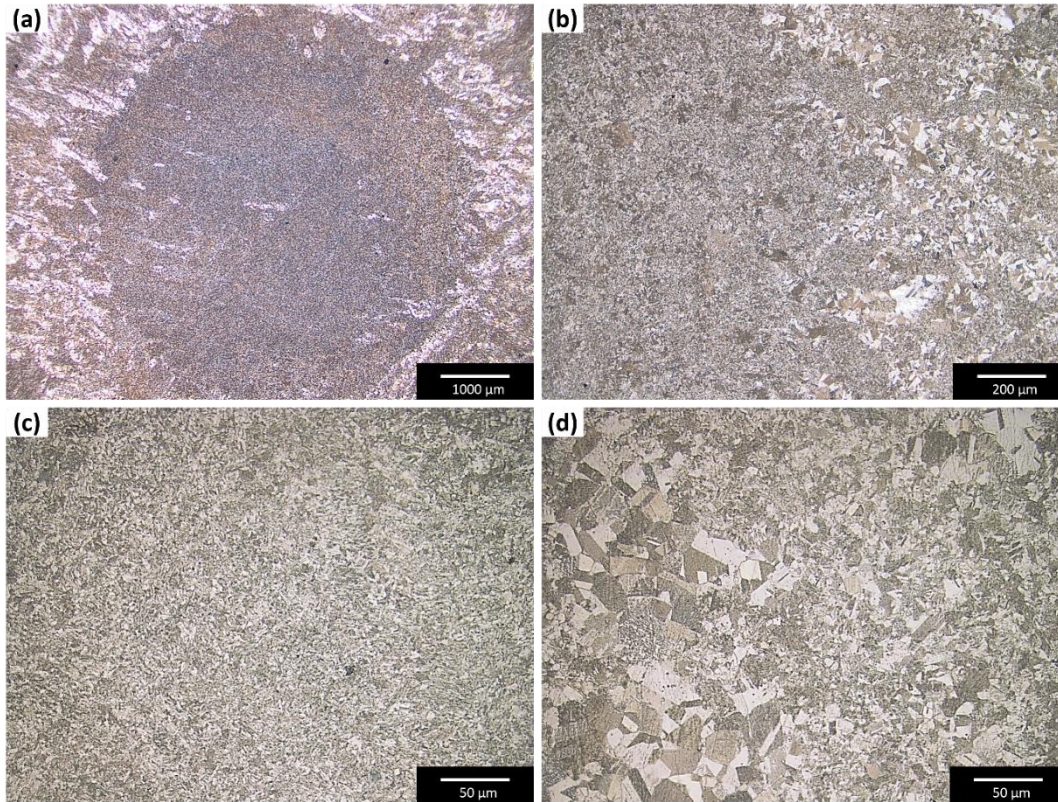


Figure 4.63: Optical micrographs of 17th sample that shows; (a) inner circle at 50x, (b) overlap region at 50x, (c) inner circle at 1000x and (d) outer ring at 1000x magnifications.

Initially, the entire diameter of 18 mm was produced, followed by a second scan specifically targeting the outer ring with an outer diameter of 18 mm and an inner diameter of 6 mm to manufacture the 18th sample, utilizing the process parameters outlined in Table 3.5. Figure 4.64 (a) and (b) reveal that no microstructural transition zone was formed when only the outer ring was subjected to a second scan, even though the same second scan speed as the 17th sample was employed. Additionally, no microstructural alterations were observed between the inner circle and outer ring, as illustrated in Figure 4.64 (c) and (d), respectively.

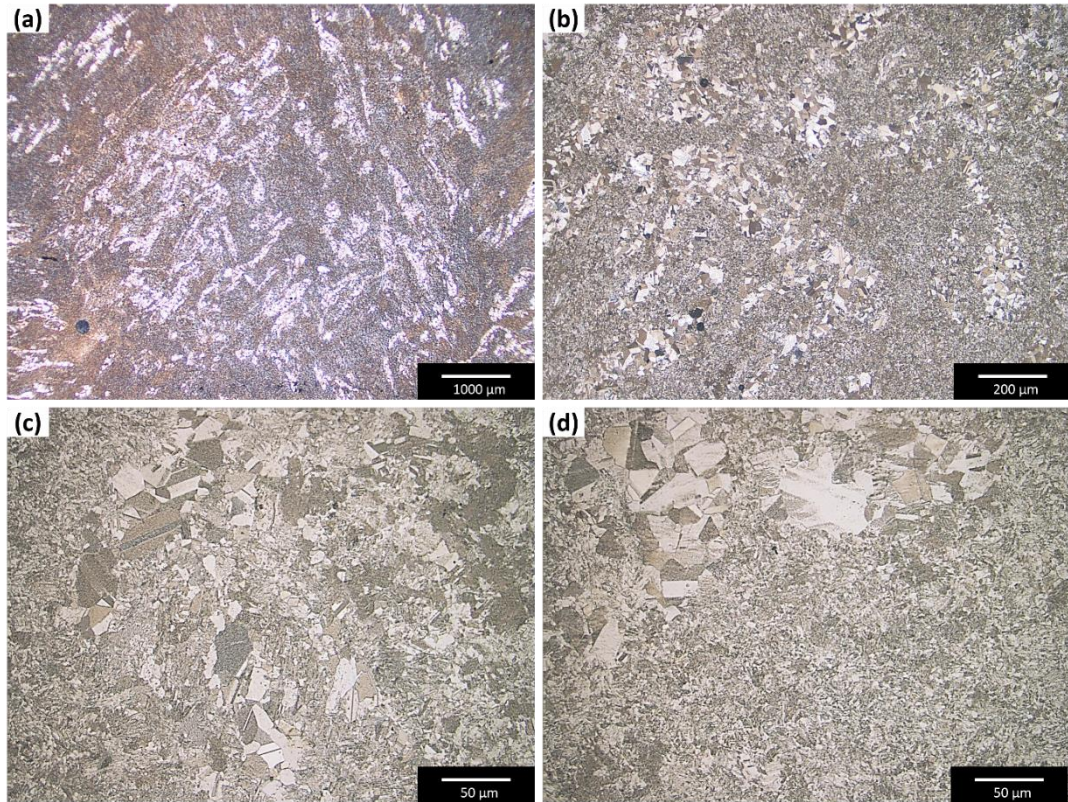


Figure 4.64: Optical micrographs of 18th sample that shows; (a) inner circle at 50x, (b) overlap region at 50x, (c) inner circle at 1000x and (d) outer ring at 1000x magnifications.

When the second scan speed of the inner circle was doubled for the fabrication of the 19th sample, no transition zones were observed in the microstructures shown in Figure 4.65 (a) and (b). Additionally, there was no apparent difference between the microstructures of the inner circle and outer ring, as depicted in Figure 4.65 (c) and (d), respectively. The same scenario was observed in Sample 20, where the scanning speed of the outer ring was doubled (Figure 4.66). No microstructural transitions were identified in either the outer ring or the inner circle of the 20th sample.

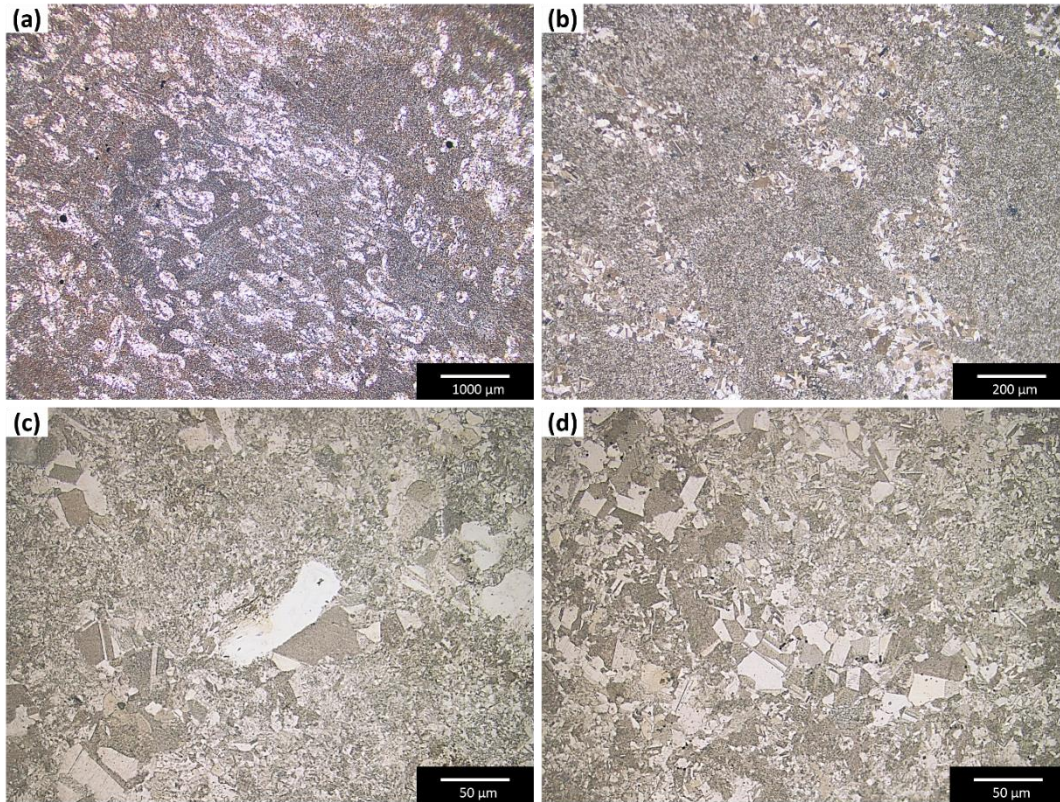


Figure 4.65: Optical micrographs of 19th sample that shows; (a) inner circle at 50x, (b) overlap region at 50x, (c) inner circle at 1000x and (d) outer ring at 1000x magnifications.

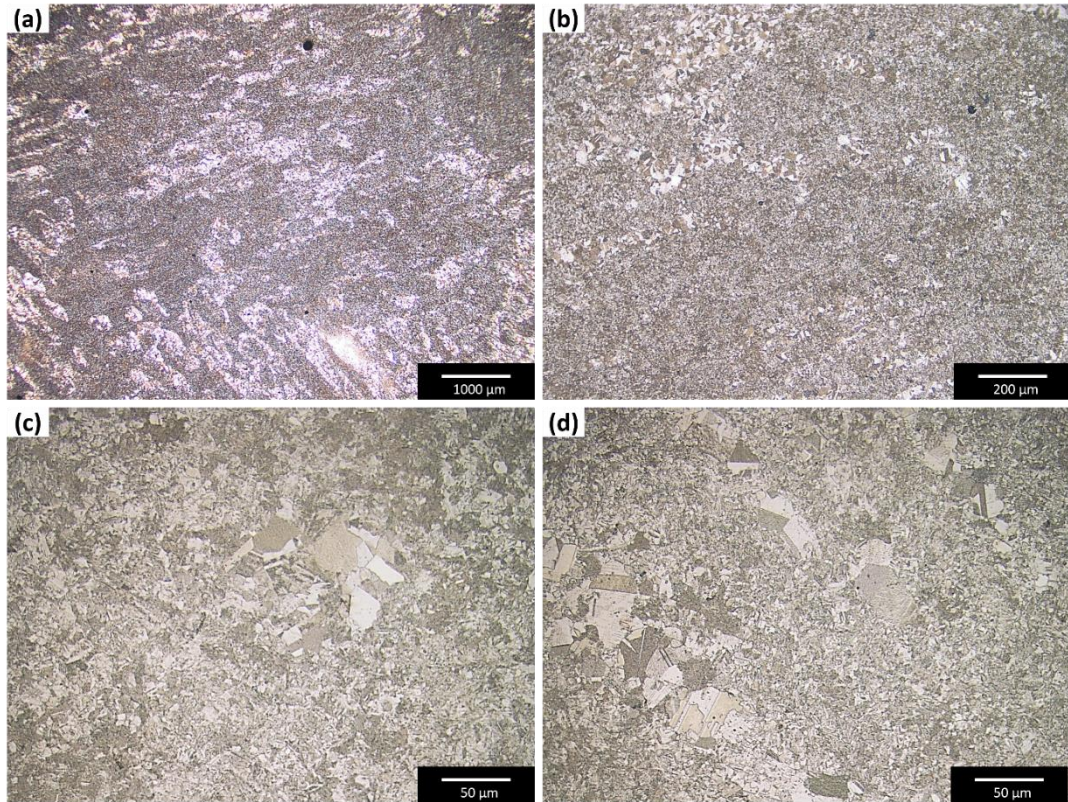


Figure 4.66: Optical micrographs of 20th sample that shows; (a) inner circle at 50x, (b) overlap region at 50x, (c) inner circle at 1000x and (d) outer ring at 1000x magnifications.

Figure 4.67 (a) – (b), (c) – (d), (e) – (f), and (g) – (h) display the microstructures of samples 21, 22, 23, and 24, respectively. While the images at 50x magnification in Figure 4.67 show the inner circle of the samples, the images at 1000x magnification represent the overlap regions of each sample. Therefore, the inner circle is depicted in Figure 4.67 (b) and (d), while the outer ring is illustrated in Figure 4.67 (d) and (h). However, it was not feasible to discern the differences between these samples by scrutinizing the optical microscope images. No visible alterations were observed in the microstructures when the second scanning speed was 3 times and above. This observation is attributed to the insufficient area energy of the second scan to remelt the material as the scanning speed decreased by more than 3 times.

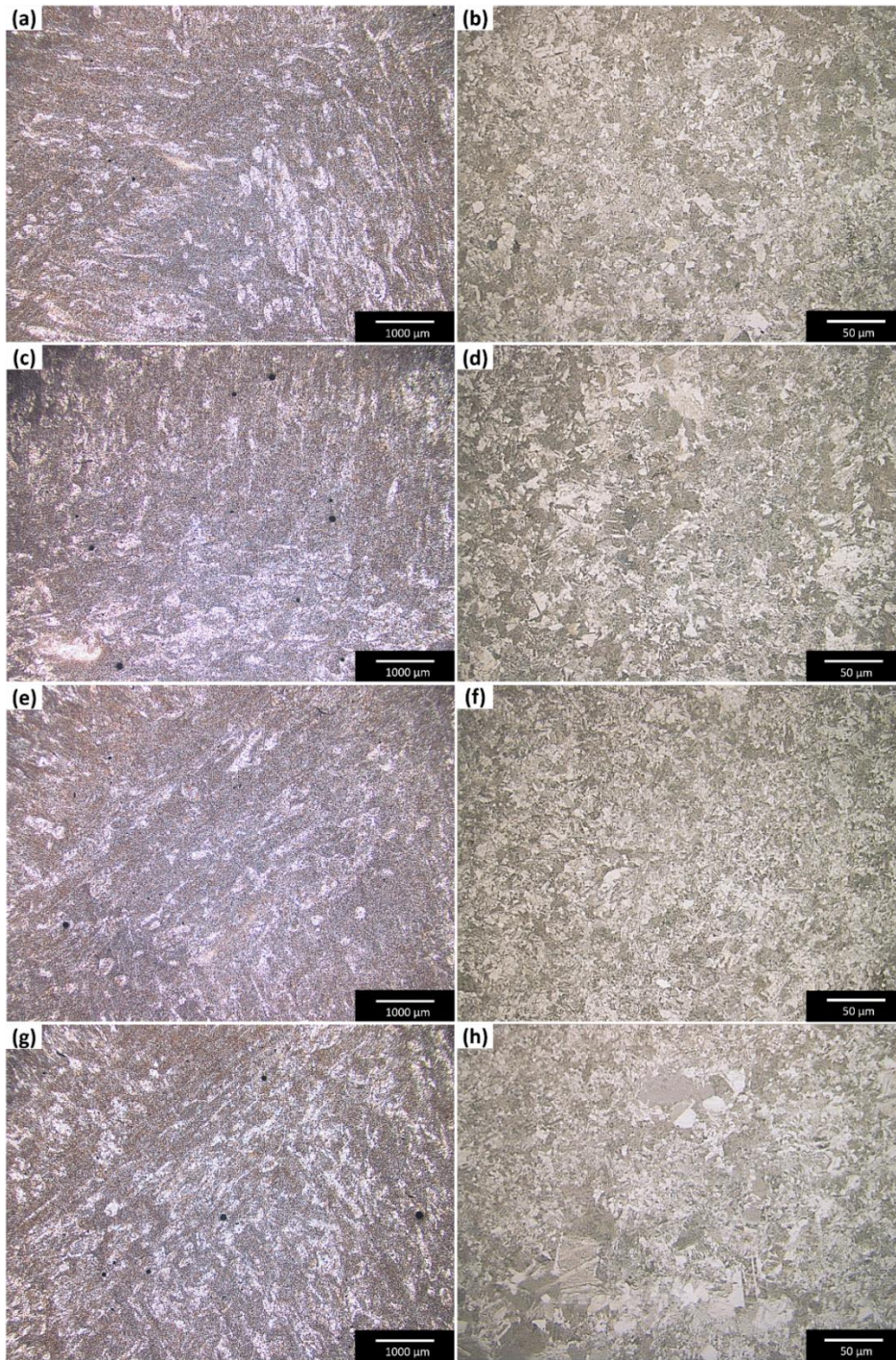


Figure 4.67: Optical micrographs of; (a) inner circle of 21st sample at 50x, (b) inner circle of 21st sample at 1000x, (c) inner circle of 22nd sample at 50x, (d) outer ring of 22nd sample at 1000x, (e) inner circle of 23rd sample at 50x, (f) inner circle of 23rd sample at 1000x, (g) inner circle of 24th sample at 50x, (h) outer ring of 24th sample at 1000x.

The room temperature tensile test results for the Double Scan Partial Overlap #2 samples are presented in

Table 4.13. It is evident that both the tensile and yield strength of DS17 were the highest among all double scan samples. This is likely attributed to its high-energy inner circle double-scan strategy with a 6 mm overlap thickness.

The following conclusions were drawn from the evaluation of the Double Scan Partial Overlap #2 study:

- i. Finer grains were observed to form when only the inner circle with a 6 mm diameter was subjected to electron beam exposure for the second time.
- ii. No microstructural transition zone was observed when the outer ring was chosen as the overlap region.
- iii. Scanning the inner circle alone was not only sufficient to create the microstructural transition zone but also necessary to perform the second scan with a certain energy density. A microstructural transition was observed when the second scan was conducted with the same electron beam speed as the first scan (1600 mm/s), while the same was not adequate when scanning the outer ring for the second time.

Table 4.13: Room temperature tensile test results of the double scan partial overlap #2 samples.

Sample No	E (GPa)	UTS (MPa)	0.2% YS (MPa)	Elongation (%)	RA (%)
DS17-1	132.00	760.00	710.00	1.80	1.00
DS17-2	118.00	730.00	720.00	1.60	2.40
DS17-3	140.00	745.00	710.00	0.60	1.40
DS17 Average	130.00	745.00	713.33	1.33	1.60
DS18-1	132.00	575.00	570.00	2.80	2.00
DS18-2	151.00	-	-	2.60	1.00
DS18-3	145.00	575.00	550.00	2.60	1.40
DS18 Average	142.67	575.00	560.00	2.67	1.47
DS19-1	150.00	520.00	-	2.20	1.60
DS19-2	172.00	580.00	-	1.80	1.40
DS19 Average	161.00	550.00	-	2.00	1.50
DS20-1	152.00	540.00	540.00	1.00	1.40
DS20-2	143.00	560.00	530.00	2.20	2.00
DS20-3	144.00	545.00	-	1.80	1.00
DS20 Average	146.33	548.33	535.00	1.67	1.47
DS21-1	142.00	525.00	-	2.20	0.40
DS21-2	174.00	545.00	545.00	2.60	1.00
DS21-3	162.00	550.00	545.00	2.20	2.00
DS21-4	156.00	540.00	-	1.80	1.20
DS21 Average	158.50	540.00	545.00	2.20	1.15
DS22-1	175.00	535.00	-	2.60	1.00
DS22-2	178.00	535.00	530.00	2.20	1.40
DS22-3	140.00	555.00	550.00	3.00	1.00
DS22 Average	164.33	541.67	540.00	2.60	1.13
DS23-1	161.00	570.00	545.00	1.00	2.00
DS23-2	172.00	510.00	-	1.00	2.00
DS23-3	150.00	555.00	545.00	1.00	0.40
DS23 Average	161.00	545.00	545.00	1.00	1.47
DS24-1	158.00	545.00	535.00	1.00	3.00
DS24-2	141.00	520.00	510.00	0.60	2.00
DS24-3	158.00	515.00	515.00	1.00	1.40
DS24 Average	152.33	526.67	520.00	0.87	2.13

4.9.4 Overview of Double-Scan Studies

Evaluations were conducted on 24 distinct samples comprising PBF-EB scanning strategies in the double-scan study. The studies were subdivided into three groups for the production of microstructure and tensile samples through the application of secondary scans. Given that the primary objective of this study was to mitigate premature failure in the PBF-EB as-built sample along the production direction, tests were exclusively carried out on Z-direction tensile samples. Table 4.14 presents the top three specimens with the highest mechanical strength according to tensile tests in the entire double-scan study.

No premature failure was observed in the DS09 specimens produced as a reference sample. However, precise data could not be obtained as the as-built Z specimen failed before reaching the yielding point during the tensile tests in Chapter 4.7.2.1. DS09 samples were manufactured with the PBF-EB parameters outlined in Table 3.5 and did not undergo any double scan. In comparison to the as-built Z samples in Chapter 4.7.2.1, DS09 samples produced with the same PBF-EB process parameters and scanning strategy exhibited superior strength values. As explained in Chapter 3.2, preheating with lower energy density is applied before the samples are melted during PBF-EB production. Therefore, secondary preheating is applied to the samples remelted by double scanning and also to the surrounding areas of the sample. Although no secondary melting or preheating is applied to DS09, it is possible that DS09 has been influenced by heat, leading to a change in its microstructure as if it has been heat-treated due to the preheating applied to the neighboring samples. DS09 results are not included in Table 4.14 as they do not represent standard PBF-EB production from a single-step preheat and melt scan strategy.

Table 4.14: Room temperature tensile test results for samples that have highest strength values in double-scan studies.

Sample Name	Test Temperature	E (GPa)	UTS (MPa)	0.2% YS (MPa)	Elongation (%)	RA (%)
DS05	RT	150.60	616.25	598.50	2.08	1.72
DS10	RT	150.00	660.00	650.00	1.60	1.50
DS17	RT	130.00	745.00	713.33	1.33	1.60

Figure 4.68 and Figure 4.69 depict the cross-sections parallel to the build direction (and parallel to the tensile test direction) microstructures of the as-built sample alongside DS05, 10, and 17 specimens. As elucidated in Chapter 4.5.1, in the parallel to the build direction section of the as-built sample, the γ bands align perpendicular to the manufacturing direction, as well as the tensile test direction. The studies revealed differences in both the aluminum content (see Chapter 4.5.1) and the hardness (see Chapter 4.7.1) of the γ bands compared to the fine region. During the tensile tests explained in Chapter 4.7.2.1, it was observed that the as-built samples produced in the Z-direction ruptured from the interface of the coarse γ bands and the fine region.

In the double-scan study, an observation was made that the banding composed of coarse γ grains decreased when examining the microstructures parallel to the tensile direction of the first three samples with the highest strength at 50x (Figure 4.68) and 200x (Figure 4.69). Consequently, the strength values for DS05, 10, and 17 samples were higher than those of the other double-scanned samples.

The DS05 sample, as illustrated in Figure 4.68 (b) and Figure 4.69 (b), was produced by dividing it into three separate regions, as outlined in Chapter 4.9.1. A 1mm thick double-scan was applied between the three regions, with the entire surface preheated before each double-scan. Figure 3.4 illustrates that the temperature of the sample surface increased above 1060 °C due to the applied preheating during each double-scan. Consequently, it was observed that the γ bands of the DS05 sample were homogeneously distributed compared to the as-built condition. Additionally, grain coarsening was noted due to the three stepped

preheating during the electron beam scanning of three stepped melting in DS05 samples.

In the production of the DS10 sample, as depicted in Figure 4.68 (c) and Figure 4.69 (c), the entire surface of the 18 mm diameter sample was initially scanned, as detailed in Chapter 4.9.2. Subsequently, a double-scan was performed with a scan speed of 1600 mm/s across the entire surface. Examination of the DS10 sample at 50x magnification revealed a reduction in the γ banding but still present in the structure (Figure 4.68). Additionally, it was observed that γ colonies were coarsened, similar to DS05. The analysis conducted on the DS10 sample indicated that the second scanning of the entire surface in PBF-EB production increased strength but did not address the premature failure issue.

In the production of the DS17 sample, as illustrated in Figure 4.68 and Figure 4.69 (d), after initially producing the entire 18 mm surface, the 6 mm diameter center of the sample was double-scanned using the same PBF-EB parameters, as explained in Chapter 4.9.3. Microstructure images from the double-scan part of the sample revealed the removal of γ banding. Examinations indicated that there was no coarsening in the DS17 sample, distinguishing it from the other samples. Consequently, as presented in Table 4.14, the strength values for DS17 were superior to all other samples.

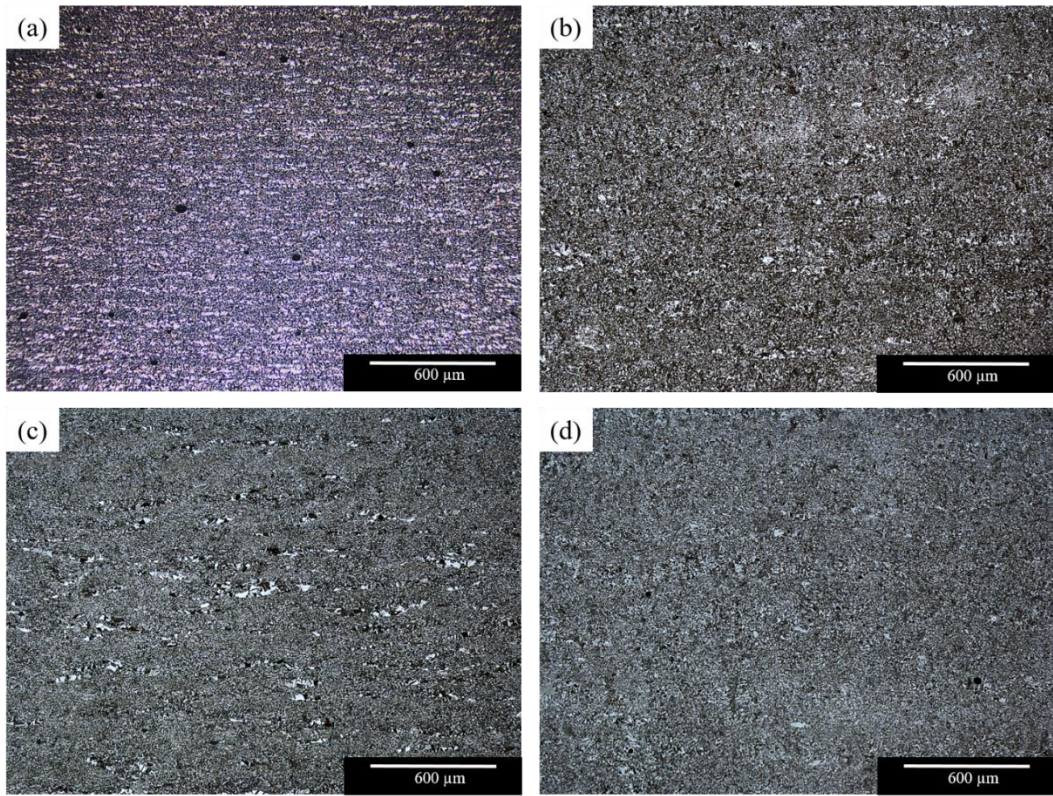


Figure 4.68: Optical microscopy images in parallel to build direction of; (a) as-built, (b) DS05, (c) DS10, (d) DS17 samples at 50x magnification.

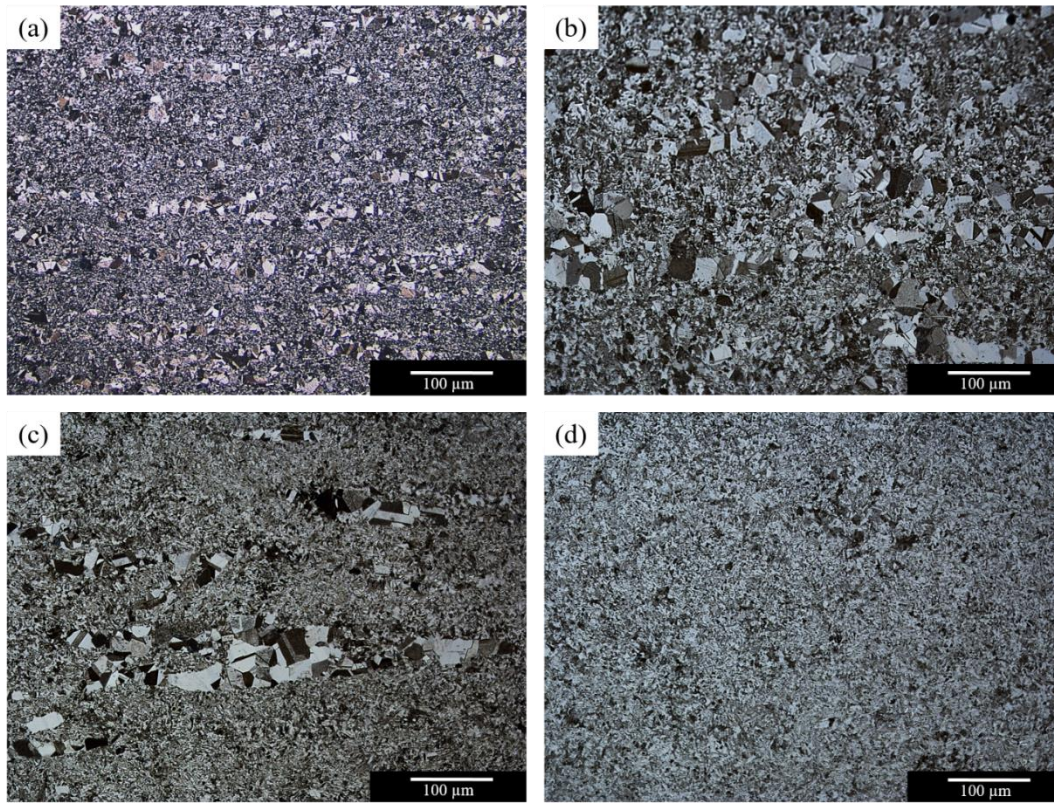


Figure 4.69: Optical microscopy images in Z-direction of; (a) as-built, (b) DS05, (c) DS10, (d) DS17 samples at 200x magnification.

It is well-established that aluminum evaporation occurs during PBF-EB production conducted under vacuum conditions. This phenomenon is expected to be more prevalent in double-scan samples compared to as-built samples. There is a hypothesis suggesting that the evaporation may be most significant in DS17 samples, particularly where γ banding has been completely eliminated. To gain a more thorough understanding, further examinations of double-scan samples are recommended, utilizing SEM (Scanning Electron Microscopy), EDS (Energy Dispersive Spectroscopy), and EBSD (Electron Backscatter Diffraction) analyses. These advanced techniques can provide detailed insights into the microstructure and elemental composition of the samples, shedding light on the effects of the double-scan process and potential aluminum evaporation.

CHAPTER 5

CONCLUSION

The main objective of this study was to investigate the effect of secondary treatments on the room and elevated temperature mechanical properties of Ti48Al2Cr2Nb alloy via the interactions between the resulting microstructure, fracture behaviour and crystallographic texture. The key outcomes of the investigation can be outlined as follows:

1. The microstructures of as-built cross-sections, both perpendicular and parallel to the building direction (BD), displayed similar features. In both orientations, a duplex-like microstructure consisting of γ/α_2 lamellae, fine equiaxed γ grains, and relatively coarse equiaxed γ grains was observed. However, in the parallel-to-build direction cross-section, the as-built samples exhibited coarse γ bands aligned perpendicularly to the PBF-EB build direction and tensile load direction. This banded microstructure contributed to the initiation of severe cracks between the coarse γ colonies and the regions containing fine γ/α_2 lamellae as well as equiaxed γ grains.
2. Microhardness measurements indicated a considerable disparity of approximately ~ 98 HV0.1 between the coarse γ grains and fine γ/α_2 lamellae within the Ti48Al2Cr2Nb alloy samples. This notable difference in microhardness values led to the preferential propagation of cracks between the weaker γ grains and the stronger γ/α_2 lamellae. The significant contrast in microhardness between these regions played a pivotal role in influencing the path of crack propagation and, consequently, the overall fracture behavior of the material.

3. The examination of the cross-sections of the tensile tested samples provided more information into the crack propagation mechanism. The cracks were discovered to originate from locations with a significant difference in aluminium concentration and mechanical characteristics, notably between the coarse grains and the fine lamellar region. Cracks were initiated and propagated by the difference, which produced a zone of concentrated stress. The catastrophic nature of the fracture became apparent when the banded microstructure was orientated perpendicular to the tensile test direction.

4. The banded structure became more evident after annealing 1 (HT1) at 1200 °C due to grain coarsening, and the $\langle 001 \rangle$ texture observed in as-built samples intensified. While HIPing at 1200 °C under 100 MPa resulted in greater coarsening of the microstructure (both γ and α_2 grain sizes), it also eliminated the texture and banded structure. Annealing 2 (HT2) at 1400 °C, on the other hand, produced a substantially stronger $\langle 001 \rangle // \text{BD}$ texture, almost four times higher than that of the as-built condition.

5. The HIPing process increased the α_2 phase content from 1.7% to 3.7%, as revealed by EBSD phase mapping. In contrast, the HT1 process, which was at the same treatment temperature with HIP, did not exhibit a noticeable increase in the quantity of α_2 phase based on EBSD examination. The finer α_2 phase in the HT1 processed samples likely exerted a pinning effect, inhibiting grain growth, particularly in finer microstructure regions. Elevating the annealing temperature to 1400 °C resulted in a transformation of the microstructure from duplex-like to fully lamellar. Subsequent cooling from the 1400 °C processing temperature led to the formation of α_2 phase, reaching a content of 9.0% in the HT2 processed samples.

6. Both HIPing and HT1 processes led to a reduction in dislocation density and inherent strain, as evidenced by the decrease in the KAM number fraction and GOS values. The HT1 and HT2 processed samples achieved full recrystallization, while the recrystallization fraction in the HIPed sample was 80.5%. Grain coarsening during HIPing resulted in a higher misorientation angle, contributing to a lower recrystallization fraction. In addition, HT2 resulted in higher KAM and GOS values compared to HIPed and HT1 annealed conditions, likely due to an increased presence of α_2 lamellae hindering the recrystallization process.

7. The as-built sample exhibited high brittleness in room temperature tensile tests, exhibiting fracture without yielding in Z-direction (parallel to BD) tensile test specimens. Subsequent HIP and HT1 processes contributed to the reduction of KAM and GOS values, resulting in yield strength (YS) of 514.49 ± 6.10 MPa and 474.58 ± 21.23 MPa, respectively. The strength variation between HIPed and HT1 samples can be attributed to various factors, including the elimination of the banded structure, less intensified texture in $\langle 001 \rangle // \text{BD}$, along with higher amount of α_2 phase and twin boundary fraction in the HIPed samples. Furthermore, HT2 processed Z-direction samples exhibited a YS of 362.00 ± 2.12 MPa at room temperature, mainly due to the fully lamellar microstructure consisting of $\gamma + \alpha_2$ lamellae. The absence of a layered microstructure in HT2 samples led to a decrease in anisotropy in the mechanical properties between XY- and Z-directions.

8. The HT1 process, conducted at the same temperature as HIP, led to incomplete elimination of mechanical anisotropy, with the Z-direction displaying greater brittleness compared to the XY-direction. The γ banding observed in the Z-direction of the as-built sample remained apparent after HT1 treatment. EBSD phase mapping showed a preferential distribution of

the α_2 phase in the fine lamellar region, unlike the homogeneous distribution observed in the HIPed sample.

9. The as-built, HIPed, and HT1 processed samples, initially found to be highly brittle in room temperature tensile tests, demonstrated significant ductility and underwent plastic deformation during tensile testing at 800 °C. However, the HT2 processed sample did not exhibit ductile fracture behavior at either room temperature or high temperatures. This behavior was ascribed to the presence of Nb microsegregation in the HT2 sample. Despite a one-third decrease in yield strength compared to the as-built sample, it was observed that the material could still be utilized at 800 °C after the HT2 treatment.
10. Crack propagation in the as-built samples was localized between the banded structures with the softer and coarser γ phase region and the harder and finer γ/α_2 lamellae region characterized by a contrast in both hardness and aluminum content. This difference displayed approximately 10 wt.% variation in aluminum content between these microstructurally distinct regions. The implementation of post-processing treatments, such as HIPing or annealing, played a crucial role in minimizing the chemical composition variation across the fine and coarse regions, ultimately contributing to a reduction in catastrophic brittle fracture.
11. In addition to the effect of the secondary treatments, this study also highlighted the potential for enhancing mechanical performance, particularly in the Z-direction, through modifications in the PBF-EB fabrication strategy. The implementation of Double-Scan (DS) studies aimed to address the premature failure observed in Z-direction samples, with the objective of mitigating the sandwich-like (banded) structure

without resorting to post-processing techniques like HIP. Additionally, these studies were instrumental in reducing the as-built porosity of 0.649%. Notably, the Double-Scan samples, specifically DS05, 10, and 17, demonstrated superior yield and tensile strength compared to other samples. Furthermore, the Double-Scan samples did not exhibit premature failure, a significant improvement over the as-built samples manufactured in the Z-direction.

12. Grain refinement was evident in the rescanned overlap area of the DS05 sample. However, in other regions which were not subjected to a second-time melting, grain coarsening occurred. This coarsening was attributed to the cyclic preheating during the further scanning process for each layer.
13. The full double scanning of the entire surface in the 10th DS sample led to higher strength compared to other complete-overlap-scanned samples. However, intrinsic brittleness was not entirely eliminated, and there was a slight coarsening observed in the γ colonies, contributing to premature failure of some of the samples.
14. DS17 demonstrated the highest yield and tensile strength among the various double-scan samples. The production of DS17 resulted in no banded microstructure or coarsening. This suggests that partial double-scanning of the inner diameter of a cylinder could be an effective method for enhancing the mechanical properties of PBF-EB-produced Ti48Al2Cr2Nb alloy.

The following future studies are recommended to further investigate the effect of secondary thermal treatments and/or PBF-EB production strategy on the mechanical properties of Ti48Al2Cr2Nb alloy.

- More research is needed to understand the mechanism that prevents the ductile transition in HT2 samples at 800 °C. While HT2 treated samples exhibit favourable behavior at 800 °C, with room temperature strength ~200 MPa less than the as-built sample in the XY-direction, additional creep tests are strongly advised to assess its feasibility for elevated temperature applications.
- The occurrence of the B2 phase was calculated in thermodynamic modelling studies due to the presence of Cr. However, neither XRD nor EBSD investigations revealed the presence of the B2 phase. Further research utilising transmission electron microscopy (TEM) would be beneficial in order to detect the existence of B2 precipitates and gain a better understanding of the microstructure.
- HIP appears to be the only method capable of addressing certain drawbacks arising in PBF-EB production, such as reducing microstructural texture, eliminating porosity, and decreasing mechanical anisotropy. Therefore, it is recommended to conduct fatigue tests, especially at elevated temperatures, to further evaluate the performance and reliability of the material after HIP treatment.

PBF-EB double-scan production strategy has proven to be an excellent alternative to traditional post-thermal processes, effectively reducing porosity and increasing strength, particularly in the Z-direction. However, the potential loss of aluminum during the second-time melting on previously produced surfaces needs careful consideration. Conducting a comprehensive analysis using SEM and EBSD would provide valuable insights into the microstructure of these double-scanned samples.

REFERENCES

- [1] Appel, F., Oehring, M., & Wagner, R. (2000). Novel design concepts for gamma-base titanium aluminide alloys. *Intermetallics*, 8(9–11), 1283–1312. [https://doi.org/10.1016/S0966-9795\(00\)00036-4](https://doi.org/10.1016/S0966-9795(00)00036-4).
- [2] Murr, L. E., Gaytan, S. M., Ceylan, A., Martinez, E., Martinez, J. L., Hernandez, D. H., Machado, B. I., Ramirez, D. A., Medina, F., Collins, S., & Wicker, R. B. (2010). Characterization of titanium aluminide alloy components fabricated by additive manufacturing using electron beam melting. *Acta Materialia*, 58(5), 1887–1894. <https://doi.org/10.1016/j.actamat.2009.11.032>.
- [3] Wu, X. (2006). Review of alloy and process development of TiAl alloys. *Intermetallics*, 14(10–11), 1114–1122. <https://doi.org/10.1016/J.INTERMET.2005.10.019>.
- [4] Austin, C. M. (1993). Development and Implementation Status of Cast Titanium Aluminide. *Structural Intermetallics*, 143–150. <https://doi.org/10.4131/jshpreview.9.300>.
- [5] Yamaguchi, M., Inui, H., & Ito, K. (2000). High-temperature structural intermetallics. *Acta Materialia*, 48(1), 307–322. [https://doi.org/10.1016/S1359-6454\(99\)00301-8](https://doi.org/10.1016/S1359-6454(99)00301-8).
- [6] Murr, L. E. (2015). Metallurgy of additive manufacturing: Examples from electron beam melting. *Additive Manufacturing*, 5, 40–53. <https://doi.org/10.1016/J.ADDMA.2014.12.002>.
- [7] Fadeev, A. v, Bazhenov, V. E., & Koltygin, A. v. (2015). Improvement in the casting technology of blades for aviation gas-turbine engines made of TNM-B1 titanium aluminide alloy produced by induction crucible melting. *Russian Journal of Non-Ferrous Metals*, 56(1), 26–32. <https://doi.org/10.3103/S1067821215010071>.

- [8] Thomas, M., Raviart, J. L., & Popoff, F. (2005). Cast and PM processing development in gamma aluminides. *Intermetallics*, 13(9), 944–951. <https://doi.org/10.1016/J.INTERMET.2004.12.010>.
- [9] Lewandowski, J. J., & Seifi, M. (2016). Metal Additive Manufacturing: A Review of Mechanical Properties. *Annual Review of Materials Research*, 46(1), 151–186. <https://doi.org/10.1146/annurev-matsci-070115-032024>.
- [10] Srivastava, D. (2002). Microstructural characterization of the γ -TiAl alloy samples fabricated by direct laser fabrication rapid prototype technique. *Bulletin of Materials Science*, 25(7), 619–633. <https://doi.org/10.1007/BF02707895>.
- [11] Löber, L., Biamino, S., Ackelid, U., Sabbadini, S., Epicoco, P., Fino, P., & Eckert, J. (2011). Comparison off selective laser and electron beam melted titanium aluminides. In 2011 International Solid Freeform Fabrication Symposium. University of Texas at Austin. <http://dx.doi.org/10.26153/tsw/15316>.
- [12] Gussone, J., Hagedorn, Y. C., Gherekhloo, H., Kasperovich, G., Merzouk, T., & Hausmann, J. (2015). Microstructure of γ -titanium aluminide processed by selective laser melting at elevated temperatures. *Intermetallics*, 66, 133–140. <https://doi.org/10.1016/J.INTERMET.2015.07.005>.
- [13] Li, W., Liu, J., Wen, S., Wei, Q., Yan, C., & Shi, Y. (2016). Crystal orientation, crystallographic texture and phase evolution in the Ti–45Al–2Cr–5Nb alloy processed by selective laser melting. *Materials Characterization*, 113, 125–133. <https://doi.org/10.1016/J.MATCHAR.2016.01.012>.
- [14] Ge, W., Lin, F., & Guo, C. (2014). The effect of scan pattern on microstructure evolution and mechanical properties in electron beam melting Ti47Al2Cr2Nb. In *Solid Freeform Fabrication Proceedings* (pp. 501-13). Univ. Tex. Austin. <http://dx.doi.org/10.26153/tsw/15702>.

- [15] Schwerdtfeger, J., & Körner, C. (2014). Selective electron beam melting of Ti-48Al-2Nb-2Cr: Microstructure and aluminium loss. *Intermetallics*, 49, 29–35. <https://doi.org/10.1016/J.INTERMET.2014.01.004>.
- [16] Biamino, S., Klöden, B., Weissgärber, T. Dr.-Ing., Kieback, B., & Ackelid, U. (2014). Properties of a TiAl Turbocharger Wheel Produced by Electron Beam Melting. <https://api.semanticscholar.org/CorpusID:209545982>
- [17] Franzén, S. F., Karlsson, J., Dehoff, R. R., Ackelid, U., Rios, O., & Peter, W. H. (2011). Microstructural properties of gamma titanium aluminide manufactured by electron beam melting. Oak Ridge National Lab.(ORNL), Oak Ridge, TN (United States).
- [18] Ge, W., Guo, C., & Lin, F. (2014). Effect of Process Parameters on Microstructure of TiAl Alloy Produced by Electron Beam Selective Melting. *Procedia Engineering*, 81, 1192–1197. <https://doi.org/10.1016/J.PROENG.2014.10.096>.
- [19] McLouth, T., Chang, Y.-W., Wooten, J., & Yang, J.-M. (2015). The Effects of Electron Beam Melting on the Microstructure and Mechanical Properties of Ti-6Al-4V and Gamma-TiAl. *Microscopy and Microanalysis*, 21(S3), 1177–1178. <https://doi.org/10.1017/S1431927615006674>.
- [20] Biamino, S., Penna, A., Ackelid, U., Sabbadini, S., Tassa, O., Fino, P., Pavese, M., Gennaro, P., & Badini, C. (2011). Electron beam melting of Ti-48Al-2Cr-2Nb alloy: Microstructure and mechanical properties investigation. *Intermetallics*, 19(6), 776–781. <https://doi.org/10.1016/J.INTERMET.2010.11.017>.
- [21] Seifi, M., Salem, A. A., Satko, D. P., Ackelid, U., Semiatin, S. L., & Lewandowski, J. J. (2017). Effects of HIP on microstructural heterogeneity, defect distribution and mechanical properties of additively manufactured EBM Ti48Al2C2Nb. *Journal of Alloys and Compounds*, 729, 1118–1135. <https://doi.org/10.1016/j.jallcom.2017.09.163>.
- [22] Cho, K., Kobayashi, R., Oh, J. Y., Yasuda, H. Y., Todai, M., Nakano, T., Ikeda, A., Ueda, M., & Takeyama, M. (2018). Influence of unique layered

- microstructure on fatigue properties of Ti48Al2C2Nb alloys fabricated by electron beam melting. *Intermetallics*, 95, 1–10. <https://doi.org/10.1016/j.intermet.2018.01.009>.
- [23] Todai, M., Nakano, T., Liu, T., Yasuda, H. Y., Hagihara, K., Cho, K., Ueda, M., & Takeyama, M. (2017). Effect of building direction on the microstructure and tensile properties of Ti48Al2C2Nb alloy additively manufactured by electron beam melting. *Additive Manufacturing*, 13, 61–70. <https://doi.org/10.1016/J.ADDMA.2016.11.001>.
- [24] Seifi, M., Ghamarian, I., Samimi, P., Ackelid, U., Collins, P., & Lewandowski, J. (2016). Microstructure and Mechanical Properties of Ti-48Al-2Cr-2Nb Manufactured Via Electron Beam Melting. In *Proceedings of the 13th World Conference on Titanium* (pp. 1317–1322). Wiley. <https://doi.org/10.1002/9781119296126.ch223>.
- [25] Dimiduk, D. M., Miracle, D. B., Kim, Y. W., & Mendiratta, M. G. (1991). Recent progress on intermetallic alloys for advanced aerospace systems. *ISIJ International*, 31(10), 1223-1234. <https://doi.org/10.2355/isijinternational.31.1223>.
- [26] Baudana, G., Biamino, S., Ugues, D., Lombardi, M., Fino, P., Pavese, M., & Badini, C. (2016). Titanium aluminides for aerospace and automotive applications processed by Electron Beam Melting: Contribution of Politecnico di Torino. *Metal Powder Report*, 71(3), 193–199. <https://doi.org/10.1016/J.MPRP.2016.02.058>.
- [27] Leyens, C., & Peters, M. (Eds.). (2006). *Titanium and titanium alloys: fundamentals and applications*. Wiley-vch.
- [28] Loria, E. A. (2000). Gamma titanium aluminides as prospective structural materials. *Intermetallics*, 8(9-11), 1339-1345.
- [29] Lapin, J. (2009, May). TiAl-based alloys: Present status and future perspectives. In *Conference proceedings METAL* (Vol. 19, No. 21.5, p. 2009).

- [30] Kothari, K., Radhakrishnan, R., & Wereley, N. M. (2012). Advances in gamma titanium aluminides and their manufacturing techniques. In *Progress in Aerospace Sciences* (Vol. 55, pp. 1–16). Elsevier Ltd. <https://doi.org/10.1016/j.paerosci.2012.04.001>.
- [31] Genç, O., & Unal, R. (2022). Development of gamma titanium aluminide (γ -TiAl) alloys: A review. In *Journal of Alloys and Compounds* (Vol. 929). Elsevier Ltd. <https://doi.org/10.1016/j.jallcom.2022.167262>.
- [32] Voice, W. E., Henderson, M., Shelton, E. F. J., & Wu, X. (2005). Gamma titanium aluminide, TNB. *Intermetallics*, 13(9), 959–964. <https://doi.org/10.1016/j.intermet.2004.12.021>.
- [33] Williams, J. C. (2007). *Titanium. Engineering materials and processes*. Springer.
- [34] Soboyejo, W. O., Ye, F., & Srivatsan, T. S. (1997). The fatigue and fracture behaviour of a gamma-titanium aluminide intermetallic: Influence of ductile phase reinforcement. *Engineering fracture mechanics*, 56(3), 379-395.
- [35] Clemens, H., & Mayer, S. (2013). Design, processing, microstructure, properties, and applications of advanced intermetallic TiAl alloys. *Advanced engineering materials*, 15(4), 191-215.
- [36] Loretto, M. H., Hu, D., Huang, A. J., & Wu, X. (2005). Heat treatment of cast TiAl-based alloys. *Materials Forum*, 29, 17-20.
- [37] Kim, Y. W. (1989). Intermetallic alloys based on gamma titanium aluminide. *Jom*, 41, 24-30.
- [38] Stoloff, N. S., & Sikka, V. K. (2012). *Physical metallurgy and processing of intermetallic compounds*. Springer Science & Business Media.
- [39] Dimiduk, D. M. (1999). Gamma titanium aluminide alloys-an assessment within the competition of aerospace structural materials. In *Materials Science and Engineering* (Vol. 263).
- [40] Chen, W., & Li, Z. (2019). Additive manufacturing of titanium aluminides. In *Additive Manufacturing for the Aerospace Industry* (pp. 235–263). Elsevier Inc. <https://doi.org/10.1016/B978-0-12-814062-8.00013-3>.

- [41] B. P. Bewlay S. Nag, A. S., & Weimer, M. J. (2016). TiAl alloys in commercial aircraft engines. *Materials at High Temperatures*, 33(4–5), 549–559. <https://doi.org/10.1080/09603409.2016.1183068>.
- [42] Clemens, H., & Mayer, S. (2016). Intermetallic titanium aluminides in aerospace applications – processing, microstructure and properties. *Materials at High Temperatures*, 33(4–5), 560–570. <https://doi.org/10.1080/09603409.2016.1163792>.
- [43] Hautmann, D. (2013). Titanium aluminide—a class all by itself. *MTU Aero Engines AG*, 10(1), 24-29.
- [44] Ian Goold (2014). Rolls-Royce Advances Toward UltraFan. *Air Transport*. Available from: <https://www.ainonline.com/aviation-news/air-transport/2014-07-14/rolls-royceadvances-toward-ultrafan>.
- [45] Lasalmonie, A. (2006). Intermetallics: Why is it so difficult to introduce them in gas turbine engines? *Intermetallics*, 14(10–11), 1123–1129. <https://doi.org/10.1016/J.INTERMET.2006.01.064>.
- [46] Applications, Component Assessment, and Outlook. (2011). In *Gamma Titanium Aluminide Alloys* (pp. 729–738). John Wiley & Sons, Ltd. <https://doi.org/10.1002/9783527636204.ch19>.
- [47] *Intermetallics*, S. (2001). edited by KJ Hemker, DM Dimiduk, H. Clemens, R. Darolia, H. Iui, JM Larson, VK Sikka, M. Thomas, and JD Whittenberger,(TMS, Warrendale, PA, 2001).
- [48] Austin, C. M., & Kelly, T. J. (1995). *Gamma titanium aluminides*. TMS, Warrendale, PA, 21.
- [49] Horton, J., Baker, I., Hanada, S., Noebe, R. D., & Schwartz, D. S. (1995). High-temperature ordered intermetallic alloys VI: Part 1. *Materials Research Society symposium proceedings Volume 364* (No. CONF-941144). Materials Research Society, Pittsburgh, PA (United States).
- [50] Morris, D. G., Naka, S., & Caron, P. (2000). *Intermetallics and superalloys*. EUROMAT 99. Vol. 10. Germany.

- [51] Tetsui, T. (1999). Gamma Ti aluminides for non-aerospace applications. *Current Opinion in Solid State and Materials Science*, 4(3), 243–248. [https://doi.org/10.1016/S1359-0286\(99\)00023-6](https://doi.org/10.1016/S1359-0286(99)00023-6).
- [52] Noda, T. (1998). Application of cast gamma TiAl for automobiles. *Intermetallics*, 6(7–8), 709–713. [https://doi.org/10.1016/S0966-9795\(98\)00060-0](https://doi.org/10.1016/S0966-9795(98)00060-0).
- [53] Tetsui, T. (2002). Development of a TiAl turbocharger for passenger vehicles. *Materials Science and Engineering: A*, 329–331, 582–588. [https://doi.org/10.1016/S0921-5093\(01\)01584-2](https://doi.org/10.1016/S0921-5093(01)01584-2).
- [54] Constitution. (2011). In *Gamma Titanium Aluminide Alloys* (pp. 5–23). John Wiley & Sons, Ltd. <https://doi.org/10.1002/9783527636204.ch2>.
- [55] Murr, L. E., Gaytan, S. M., Ceylan, A., Martinez, E., Martinez, J. L., Hernandez, D. H., & Wicker, R. B. (2010). Characterization of titanium aluminide alloy components fabricated by additive manufacturing using electron beam melting. *Acta materialia*, 58(5), 1887-1894.
- [56] Djanarthany S., Viala JC., & Bouix J. (2010). An overview of monolithic titanium aluminides based on Ti₃Al and TiAl. *Materials Chemistry and Physics*, 72, no. 3, 301–319, 2001.
- [57] Schuster, J. C., & Palm, M. (2006). Reassessment of the binary aluminum-titanium phase diagram. *Journal of phase equilibria and diffusion*, 27(3), 255-277.
- [58] Witusiewicz, V. T., Bondar, A. A., Hecht, U., Rex, S., & Velikanova, T. Y. (2008). The Al–B–Nb–Ti system: III. Thermodynamic re-evaluation of the constituent binary system Al–Ti. *Journal of Alloys and Compounds*, 465(1–2), 64–77. <https://doi.org/10.1016/J.JALLCOM.2007.10.061>.
- [59] Grytsiv, A., Rogl, P., Schmidt, H., & Giester, G. (2003). Constitution of the ternary system Al-Ru-Ti (aluminum-ruthenium-titanium). *Journal of phase equilibria*, 24, 511-527.
- [60] Raghavan, V. (2005). Al-Ti (aluminum-titanium). *Journal of Phase Equilibria and Diffusion*, 26(2), 171.

- [61] Ohnuma, I., Fujita, Y., Mitsui, H., Ishikawa, K., Kainuma, R., & Ishida, K. (2000). Phase equilibria in the Ti–Al binary system. *Acta Materialia*, 48(12), 3113–3123. [https://doi.org/10.1016/S1359-6454\(00\)00118-X](https://doi.org/10.1016/S1359-6454(00)00118-X).
- [62] Kattner, U. R., Lin, J. C., & Chang, Y. A. (1992). Thermodynamic assessment and calculation of the Ti–Al system. *Metallurgical Transactions A*, 23, 2081–2090.
- [63] Kim, Y. Y. (1992). Microstructural evolution and mechanical properties of a forged gamma titanium aluminide alloy. *Acta metallurgica et materialia*, 40(6), 1121–1134.
- [64] Yamabe, Y., Takeyama, M., & Kikuchi, M. (1995). Microstructure evolution through solid-solid phase transformations in gamma titanium aluminides. *TMS Annual Meeting*, 111–129.
- [65] Okamoto, H., & Massalski, T. B. (1990). *Binary alloy phase diagrams*. ASM International, Materials Park, OH, USA, 12.
- [66] Duan, B., Yang, Y., He, S., Feng, Q., Mao, L., Zhang, X., Jiao, L., Lu, X., Chen, G., & Li, C. (2022). History and development of γ -TiAl alloys and the effect of alloying elements on their phase transformations. *Journal of Alloys and Compounds*, 909, 164811. <https://doi.org/10.1016/J.JALLCOM.2022.164811>.
- [67] McCullough, C., Valencia, J. J., Levi, C. G., & Mehrabian, R. (1989). Phase equilibria and solidification in Ti–Al alloys. *Acta Metallurgica*, 37(5), 1321–1336. [https://doi.org/10.1016/0001-6160\(89\)90162-4](https://doi.org/10.1016/0001-6160(89)90162-4).
- [68] Singh, A. K., Muraleedharan, K., & Banerjee, D. (2003). Solidification structure in a cast γ alloy. *Scripta Materialia*, 48(6), 767–772. [https://doi.org/10.1016/S1359-6462\(02\)00558-4](https://doi.org/10.1016/S1359-6462(02)00558-4).
- [69] Beranoagirre, A., Olvera, D., López de Lacalle, L. N., & Urbicain, G. (2011, January). Drilling of intermetallic alloys gamma TiAl. In *AIP Conference Proceedings* (Vol. 1315, No. 1, pp. 1023–1028). American Institute of Physics.

- [70] Biswas, K., & Samal, S. (2012). Solidification of Peritectic Alloys. In *Solidification of Containerless Undercooled Melts* (pp. 509–541). John Wiley & Sons, Ltd. <https://doi.org/10.1002/9783527647903.ch23>.
- [71] Johnson, D. R., Inui, H., & Yamaguchi, M. (1998). Crystal growth of TiAl alloys. *Intermetallics*, 6(7–8), 647–652. [https://doi.org/10.1016/S0966-9795\(98\)00056-9](https://doi.org/10.1016/S0966-9795(98)00056-9).
- [72] Herlach, D. M. (Ed.). (2006). *Solidification and crystallization*. John Wiley & Sons.
- [73] McCullough, C., Valencia, J. J., Levi, C. G., & Mehrabian, R. (1990). Microstructural analysis of rapidly solidified Ti–Al–X powders. *Materials Science and Engineering: A*, 124(1), 83–101. [https://doi.org/10.1016/0921-5093\(90\)90337-3](https://doi.org/10.1016/0921-5093(90)90337-3).
- [74] Nishida, M., Tateyama, T., Tomoshige, R., Morita, K., & Chiba, A. (1992). Electron microscopy studies of Ti - 47 at. % Al powder produced by plasma rotating electrode process. *Scripta Metallurgica et Materialia*, 27(3), 335–340. [https://doi.org/10.1016/0956-716X\(92\)90522-G](https://doi.org/10.1016/0956-716X(92)90522-G).
- [75] Dey, S. R., Hazotte, A., & Bouzy, E. (2009). Crystallography and phase transformation mechanisms in TiAl-based alloys – A synthesis. *Intermetallics*, 17(12), 1052–1064. <https://doi.org/10.1016/J.INTERMET.2009.05.013>.
- [76] Hill, D., Banerjee, R., Huber, D., Tiley, J., & Fraser, H. L. (2005). Formation of equiaxed alpha in TiB reinforced Ti alloy composites. *Scripta Materialia*, 52(5), 387–392. <https://doi.org/10.1016/J.SCRIPTAMAT.2004.10.019>.
- [77] Blackburn, M. J. (1970). Some Aspects Of Phase Transformations In Titanium Alloys. *The Science, Technology and Application of Titanium*, 633–643. <https://doi.org/10.1016/B978-0-08-006564-9.50071-3>.
- [78] Li, X., Fan, J., Su, Y., Liu, D., Guo, J., & Fu, H. (2012). Lamellar orientation and growth direction of α phase in directionally solidified Ti-

- 46Al-0.5W-0.5Si alloy. *Intermetallics*, 27, 38–45.
<https://doi.org/10.1016/J.INTERMET.2012.01.010>.
- [79] Saari, H., Beddoes, J., Seo, D. Y., & Zhao, L. (2005). Development of directionally solidified γ -TiAl structures. *Intermetallics*, 13(9), 937–943.
<https://doi.org/10.1016/J.INTERMET.2004.12.006>.
- [80] Ding, X. F., Lin, J. P., Zhang, L. Q., Su, Y. Q., Wang, H. L., & Chen, G. L. (2011). Lamellar orientation control in a Ti–46Al–5Nb alloy by directional solidification. *Scripta Materialia*, 65(1), 61–64.
<https://doi.org/10.1016/J.SCRIPTAMAT.2011.02.011>.
- [81] Ding, X. F., Lin, J. P., Zhang, L. Q., Su, Y. Q., & Chen, G. L. (2012). Microstructural control of TiAl–Nb alloys by directional solidification. *Acta Materialia*, 60(2), 498–506.
<https://doi.org/10.1016/J.ACTAMAT.2011.10.009>.
- [82] Umakoshi, Y., Nakano, T., & Yamane, T. (1992). The effect of orientation and lamellar structure on the plastic behaviour of TiAl crystals. *Materials Science and Engineering: A*, 152(1–2), 81–88.
[https://doi.org/10.1016/0921-5093\(92\)90050-B](https://doi.org/10.1016/0921-5093(92)90050-B).
- [83] Aaronson, H. I., & Vasudevan, V. K. (2002). General discussion session of the symposium on “The mechanisms of the massive transformation”. *Metallurgical and Materials Transactions A*, 33, 2445–2470.
- [84] Cha, L., Scheu, C., Clemens, H., Chladil, H. F., Dehm, G., Gerling, R., & Bartels, A. (2008). Nanometer-scaled lamellar microstructures in Ti–45Al–7.5Nb–(0; 0.5)C alloys and their influence on hardness. *Intermetallics*, 16(7), 868–875. <https://doi.org/10.1016/J.INTERMET.2008.03.009>.
- [85] Yamamoto, Y., Takeyama, M., & Matsuo, T. (2002). Stability of lamellar microstructure consisting of γ/γ interfaces in Ti–48Al–8Nb single crystal at elevated temperatures. *Materials Science and Engineering: A*, 329–331, 631–636. [https://doi.org/10.1016/S0921-5093\(01\)01660-4](https://doi.org/10.1016/S0921-5093(01)01660-4).

- [86] Hazzledine, P. M., & Kad, B. K. (1995). Yield and fracture of lamellar $\gamma\alpha_2$ TiAl alloys. *Materials Science and Engineering: A*, 192–193(PART 1), 340–346. [https://doi.org/10.1016/0921-5093\(94\)03216-5](https://doi.org/10.1016/0921-5093(94)03216-5).
- [87] Ding, X. F., Zhao, Y. Q., Zuo, J. B., Feng, X., Nan, H., Liang, Y. F., & Su, Y. Q. (2020). Chemical composition analysis on industrial scale ingots and castings of TiAl alloys. *China Foundry*, 17, 441-446.
- [88] Appel, F., Clemens, H., & Fischer, F. D. (2016). Modeling concepts for intermetallic titanium aluminides. *Progress in Materials Science*, 81, 55–124. <https://doi.org/10.1016/J.PMATSCI.2016.01.001>.
- [89] Nathal, M. V., Darolia, R., Liu, C. T., Martin, P. L., Miracle, D. B., Wagner, R., & Yamaguchi, M. (1997). *Structural intermetallics*. TMS: Warrendale, PA, USA, 157.
- [90] Kainuma, R., Fujita, Y., Mitsui, H., Ohnuma, I., & Ishida, K. (2000). Phase equilibria among α (hcp), β (bcc) and γ (L10) phases in Ti–Al base ternary alloys. *Intermetallics*, 8(8), 855–867. [https://doi.org/10.1016/S0966-9795\(00\)00015-7](https://doi.org/10.1016/S0966-9795(00)00015-7).
- [91] Brotzu, A., Felli, F., & Pilone, D. (2014). Effect of alloying elements on the behaviour of TiAl-based alloys. *Intermetallics*, 54, 176–180. <https://doi.org/10.1016/J.INTERMET.2014.06.007>.
- [92] Huang, S. C. (1989). Titanium aluminum alloys modified by chromium and niobium and method of preparation. Patent Number US 4879092.
- [93] Huang, S. C., & Hall, E. L. (1991). Plastic deformation and fracture of binary TiAl-base alloys. *Metallurgical Transactions A*, 22, 427-439.
- [94] Cotton, J. D., Noebe, R. D., Kaufman, M. J., Darolia, R., Lewandowski, J. J., Liu, C. T., & Nathal, M. V. (1993). *Structural Intermetallics*. TMS, Warrendale, PA, 513-522.
- [95] Alloy Design. (2011). In *Gamma Titanium Aluminide Alloys* (pp. 465–478). John Wiley & Sons, Ltd. <https://doi.org/10.1002/9783527636204.ch13>.

- [96] Paul, J. D. H., Appel, F., & Wagner, R. (1998). The compression behaviour of niobium alloyed γ -titanium aluminides. *Acta Materialia*, 46(4), 1075–1085. [https://doi.org/10.1016/S1359-6454\(97\)00332-7](https://doi.org/10.1016/S1359-6454(97)00332-7).
- [97] Pilone, D., Felli, F., & Brotzu, A. (2013). High temperature oxidation behaviour of TiAl–Cr–Nb–Mo alloys. *Intermetallics*, 43, 131–137. <https://doi.org/10.1016/J.INTERMET.2013.07.023>.
- [98] Wang, F., Tang, Z., & Wu, W. (1997). Effect of chromium on the oxidation resistance of TiAl intermetallics. *Oxidation of metals*, 48, 381-390.
- [99] Sun, F. S., Cao, C. X., Yan, M. G., & Kim, S. E. (2001). Alloying mechanism of beta stabilizers in a TiAl alloy. *Metallurgical and Materials Transactions A*, 32, 1573-1589.
- [100] Doi, H., Hashimoto, K., Kasahara, K., & Tsujimoto, T. (1990). Site determination of third elements in TiAl compound by X-ray diffractometry. *Materials Transactions, JIM*, 31(11), 975-982.
- [101] Huang, S. C., & Hall, E. L. (1991). The effects of Cr additions to binary TiAl-base alloys. *Metallurgical Transactions A*, 22, 2619-2627.
- [102] S. K. Varma R. Mahapatra, C. H. A. C., & Corral, E. (2007). Influence of Processing on Microstructures of Ti-44Al-11Nb Alloy. *Materials and Manufacturing Processes*, 14(6), 821–835. <https://doi.org/10.1080/10426919908914875>.
- [103] Dong, C., Jiao, Z., Yu, H., Zhou, H., Kong, F., & Chen, Y. (2017). Effect of dwell condition on fatigue behaviour of a high-Nb TiAl alloy at 750 °C. *Intermetallics*, 91, 1–7. <https://doi.org/10.1016/J.INTERMET.2017.07.006>.
- [104] Jiang, H., Hirohata, M., Lu, Y., & Imanari, H. (2002). Effect of Nb on the high temperature oxidation of Ti–(0–50 at.%)Al. *Scripta Materialia*, 46(9), 639–643. [https://doi.org/10.1016/S1359-6462\(02\)00042-8](https://doi.org/10.1016/S1359-6462(02)00042-8).
- [105] Kim, S. W., Hong, J. K., Na, Y. S., Yeom, J. T., & Kim, S. E. (2014). Development of TiAl alloys with excellent mechanical properties and oxidation resistance. *Materials & Design (1980-2015)*, 54, 814–819. <https://doi.org/10.1016/J.MATDES.2013.08.083>.

- [106]Vojtěch, D., Popela, T., Kubásek, J., Maixner, J., & Novák, P. (2011). Comparison of Nb- and Ta-effectiveness for improvement of the cyclic oxidation resistance of TiAl-based intermetallics. *Intermetallics*, 19(4), 493–501. <https://doi.org/10.1016/J.INTERMET.2010.11.025>.
- [107]Pérez, P., Haanappel, V. A. C., & Stroosnijder, M. F. (2000). The effect of niobium on the oxidation behaviour of titanium in N₂/20% O₂ atmospheres. *Materials Science and Engineering: A*, 284(1–2), 126–137. [https://doi.org/10.1016/S0921-5093\(00\)00754-1](https://doi.org/10.1016/S0921-5093(00)00754-1).
- [108]Yang, R., Cui, Y. Y., Dong, L. M., & Jia, Q. (2003). Alloy development and shell mould casting of gamma TiAl. *Journal of Materials Processing Technology*, 135(2–3), 179–188. [https://doi.org/10.1016/S0924-0136\(02\)00873-7](https://doi.org/10.1016/S0924-0136(02)00873-7).
- [109]Stucke, M. A., Dimiduk, D. M., & Hazzledine, P. M. (1993). High Temperature Ordered Intermetallic Alloys V: MRS Symp. Proc.
- [110]Hodge, A. M., Hsiung, L. M., & Nieh, T. G. (2004). Creep of nearly lamellar TiAl alloy containing W. *Scripta Materialia*, 51(5), 411–415. <https://doi.org/10.1016/J.SCRIPTAMAT.2004.05.005>.
- [111]Hu, D. (2016). Role of boron in TiAl alloy development: a review. *Rare Metals*, 35(1), 1-14.
- [112]Hu, D. (2002). Effect of boron addition on tensile ductility in lamellar TiAl alloys. *Intermetallics*, 10(9), 851–858. [https://doi.org/10.1016/S0966-9795\(02\)00087-0](https://doi.org/10.1016/S0966-9795(02)00087-0).
- [113]Bryant, J. D., Christodoulou, L., & Maisano, J. R. (1990). Effect of TiB₂ additions on the colony size of near gamma titanium aluminides. *Scripta Metallurgica et Materialia*, 24(1), 33–38. [https://doi.org/10.1016/0956-716X\(90\)90562-U](https://doi.org/10.1016/0956-716X(90)90562-U).
- [114]Wang, Q., Ding, H., Zhang, H., Chen, R., Guo, J., & Fu, H. (2017). Variations of microstructure and tensile property of γ -TiAl alloys with 0–0.5 at% C additives. *Materials Science and Engineering: A*, 700, 198–208. <https://doi.org/10.1016/J.MSEA.2017.06.019>.

- [115]Appel, F., Fischer, F. D., & Clemens, H. (2007). Precipitation twinning. *Acta Materialia*, 55(14), 4915–4923. <https://doi.org/10.1016/J.ACTAMAT.2007.05.007>.
- [116]Worth, B. D., Jones, J. W., & Allison, J. E. (1995). Creep deformation in near- γ TiAl: Part 1. the influence of microstructure on creep deformation in Ti-49Al-1V. *Metallurgical and Materials Transactions A*, 26, 2947-2959.
- [117]Perdrix, F., Trichet, M. F., Bonnentien, J. L., Cornet, M., & Bigot, J. (2001). Relationships between interstitial content, microstructure and mechanical properties in fully lamellar Ti-48Al alloys, with special reference to carbon. *Intermetallics*, 9(9), 807–815. [https://doi.org/10.1016/S0966-9795\(01\)00066-8](https://doi.org/10.1016/S0966-9795(01)00066-8).
- [118]Maki, K., Shioda, M., Sayashi, M., Shimizu, T., & Isobe, S. (1992). Effect of silicon and niobium on oxidation resistance of TiAl intermetallics. *High Temperature Aluminides and Intermetallics*, 591–596. <https://doi.org/10.1016/B978-1-85166-822-9.50093-5>.
- [119]Tsuyama, S., Mitao, S., & Minakawa, K. (1992). Alloy modification of γ -base titanium aluminide for improved oxidation resistance, creep strength and fracture toughness. 451–456. <https://doi.org/10.1016/B978-1-85166-822-9.50073-X>.
- [120]Noda, T., Okabe, M., Isobe, S., & Sayashi, M. (1995). Silicide precipitation strengthened TiAl. *Materials Science and Engineering: A*, 192–193(PART 2), 774–779. [https://doi.org/10.1016/0921-5093\(94\)03313-7](https://doi.org/10.1016/0921-5093(94)03313-7).
- [121]Taniguchi, S., Juso, H., & Shibata, T. (1996). Improvement in high-temperature oxidation resistance of TiAl by addition of 0.2 mass% Zr. *Materials transactions, JIM*, 37(3), 245-251.
- [122]JIANG, H. ren, WANG, Z. lei, MA, W. shuai, FENG, X. ran, DONG, Z. qiang, ZHANG, L., & LIU, Y. (2008). Effects of Nb and Si on high temperature oxidation of TiAl. *Transactions of Nonferrous Metals Society of China*, 18(3), 512–517. [https://doi.org/10.1016/S1003-6326\(08\)60090-4](https://doi.org/10.1016/S1003-6326(08)60090-4).

- [123]Kim, Y.-W. (1994). Ordered intermetallic alloys, part III: Gamma titanium aluminides. *JOM*, 46(7), 30–39. <https://doi.org/10.1007/BF03220745>.
- [124]Mercer, C., Lou, J., & Soboyejo, W. O. (2000). An investigation of fatigue crack growth in a cast lamellar Ti-48Al-2Cr-2Nb alloy. *Materials Science and Engineering: A*, 284(1–2), 235–245. [https://doi.org/10.1016/S0921-5093\(00\)00702-4](https://doi.org/10.1016/S0921-5093(00)00702-4).
- [125]Kumpfert, J., Kim, Y. W., & Dimiduk, D. M. (1995). Effect of microstructure on fatigue and tensile properties of the gamma TiAl alloy Ti-46.5Al-3.0Nb-2.1Cr-0.2W. *Materials Science and Engineering: A*, 192–193(PART 1), 465–473. [https://doi.org/10.1016/0921-5093\(94\)03263-7](https://doi.org/10.1016/0921-5093(94)03263-7).
- [126]Herrmann, D., & Appel, F. (2009). Diffusion bonding of γ (TiAl) alloys: influence of composition, microstructure, and mechanical properties. *Metallurgical and Materials Transactions A*, 40, 1881-1902.
- [127]Clemens, H., Chladil, H. F., Wallgram, W., Zickler, G. A., Gerling, R., Liss, K. D., Kremmer, S., Güther, V., & Smarsly, W. (2008). In and ex situ investigations of the β -phase in a Nb and Mo containing γ -TiAl based alloy. *Intermetallics*, 16(6), 827–833. <https://doi.org/10.1016/J.INTERMET.2008.03.008>.
- [128]Hu, D., Jiang, H., & Wu, X. (2009). Microstructure and tensile properties of cast Ti-44Al-4Nb-4Hf-0.1Si-0.1B alloy with refined lamellar microstructures. *Intermetallics*, 17(9), 744–748. <https://doi.org/10.1016/J.INTERMET.2009.03.002>.
- [129]Niu, H. Z., Su, Y. J., Zhang, Y. S., Zhang, D. L., Lu, J. W., Zhang, W., & Zhang, P. X. (2015). Microstructural evolution and mechanical properties of a β -solidifying γ -TiAl alloy densified by spark plasma sintering. *Intermetallics*, 66, 96–102. <https://doi.org/10.1016/J.INTERMET.2015.07.003>.
- [130]Huang, S. C. (1989). Titanium aluminum alloys modified by chromium and niobium and method of preparation. Patent NumberUS 4879092.

- [131] Clemens, H., Rumberg, I., Schretter, P., & Schwantes, S. (1994). Characterization of Ti₄₈Al₂Cr sheet material. *Intermetallics*, 2(3), 179–184. [https://doi.org/10.1016/0966-9795\(94\)90056-6](https://doi.org/10.1016/0966-9795(94)90056-6).
- [132] Koeppe, C., Bartels, A., Seeger, J., & Mecking, H. (1993). General aspects of the thermomechanical. *Metallurgical Transactions A*, 24, 1795-1806.
- [133] Frommeyer, G., Wunderlich, W., Kremser, Th., & Liu, Z. G. (1992). Strength properties and enhanced plasticity of intermetallic Ti–Al–(CrSi) alloys. *High Temperature Aluminides and Intermetallics*, 166–172. <https://doi.org/10.1016/B978-1-85166-822-9.50030-3>.
- [134] Kelly, T., Juhas, M., & Huang, S. (1993). Effect of a B₂/gamma structure on the tensile properties of the cast gamma titanium aluminide Ti₄₈Al₂Cr₂Nb. *Scripta Metallurgica Et Materialia*, 29, 1409-1414. [https://doi.org/10.1016/0956-716X\(93\)90328-P](https://doi.org/10.1016/0956-716X(93)90328-P).
- [135] George, E. P., Yamaguchi, M., Kumar, K. S., & Liu, C. T. (1994). Ordered Intermetallics. *Annual Review of Materials Science*, 24(1), 409–451. <https://doi.org/10.1146/annurev.ms.24.080194.002205>.
- [136] Kourtis, L. (2017). Electron Beam Melting of Titanium Aluminides; Process Development and Material Properties Optimisation (Doctoral dissertation, University of Sheffield).
- [137] Herzig, C., Przeorski, T., Friesel, M., Hisker, F., & Divinski, S. (2001). Tracer solute diffusion of Nb, Zr, Cr, Fe, and Ni in γ -TiAl: effect of preferential site occupation. *Intermetallics*, 9(6), 461–472. [https://doi.org/10.1016/S0966-9795\(01\)00025-5](https://doi.org/10.1016/S0966-9795(01)00025-5).
- [138] Appel, F., Clemens, H., & Oehring, M. (2000). Recent advances in development and processing of titanium aluminide alloys. *MRS Online Proceedings Library (OPL)*, 646.
- [139] Jin, Y., Wang, J. N., Yang, J., & Wang, Y. (2004). Microstructure refinement of cast TiAl alloys by β solidification. *Scripta Materialia*, 51(2), 113–117. <https://doi.org/10.1016/J.SCRIPTAMAT.2004.03.044>.

- [140]Huang, Z. W. (2008). Ordered ω phases in a 4Zr–4Nb-containing TiAl-based alloy. *Acta Materialia*, 56(8), 1689–1700. <https://doi.org/10.1016/J.ACTAMAT.2007.12.013>.
- [141]Tetsui, T., Shindo, K., Kobayashi, S., & Takeyama, M. (2003). Strengthening a high-strength TiAl alloy by hot-forging. *Intermetallics*, 11(4), 299–306. [https://doi.org/10.1016/S0966-9795\(02\)00245-5](https://doi.org/10.1016/S0966-9795(02)00245-5).
- [142]Kim, Y. W., Kim, S. L., Dimiduk, D., & Woodward, C. (1995). Gamma Titanium Aluminides, eds. YW Kim, D. Morris, R. Yang, and C. Leyens (TMS, Warrendale, PA, 2008) p, 215.
- [143]Wu, X., & Hu, D. (2005). Microstructural refinement in cast TiAl alloys by solid state transformations. *Scripta Materialia*, 52(8), 731–734. <https://doi.org/10.1016/J.SCRIPTAMAT.2004.12.021>.
- [144]Kumagai, T., Abe, E., Takeyama, M., & Nakamura, M. (1997). Microstructural evolution of massively transformed γ -TiAl during isothermal aging. *Scripta Materialia*, 36(5), 523–529. [https://doi.org/10.1016/S1359-6462\(96\)00416-2](https://doi.org/10.1016/S1359-6462(96)00416-2).
- [145]Hu, D., Huang, A. J., Novovic, D., & Wu, X. (2006). The effect of boron and alpha grain size on the massive transformation in Ti–46Al–8Nb–xB alloys. *Intermetallics*, 14(7), 818–825. <https://doi.org/10.1016/J.INTERMET.2005.12.003>.
- [146]Huang, A., Loretto, M. H., Hu, D., Liu, K., & Wu, X. (2006). The role of oxygen content and cooling rate on transformations in TiAl-based alloys. *Intermetallics*, 14(7), 838–847. <https://doi.org/10.1016/J.INTERMET.2005.12.006>.
- [147]Hu, D., Huang, A., Loretto, M. H., & Wu, X. (2007). Designing TiAl alloys to transform massively during slow cooling. In *Proc. of 11th World Conf. of Titanium* (Vol. 2, p. 1317).
- [148]Froes, F. H., Suryanarayana, C., & Eliezer, D. (1991). *Production, Characteristics, and Commercialization of Titanium Aluminides*. ISIJ

International, 31(10), 1235–1248.
<https://doi.org/10.2355/isijinternational.31.1235>.

- [149] Aguilar, J., Schievenbusch, A., & Kättlitz, O. (2011). Investment casting technology for production of TiAl low pressure turbine blades – Process engineering and parameter analysis. *Intermetallics*, 19(6), 757–761. <https://doi.org/10.1016/J.INTERMET.2010.11.014>.
- [150] Ingot Production and Component Casting. (2011). In *Gamma Titanium Aluminide Alloys* (pp. 479–519). John Wiley & Sons, Ltd. <https://doi.org/10.1002/9783527636204.ch14>.
- [151] Gélébart, L., Bornert, M., Bretheau, T., Caldemaison, D., Crépin, J., & Zaoui, A. (2004). Lamellar grains distribution and plastic strain heterogeneities in TiAl cast samples. *Experiments and modelling. Matériaux & Techniques*, 92(1-2), 69-76. <https://doi.org/10.1051/mattech:2004008>.
- [152] Yamaguchi, M., & Inui, H. (1993). TiAl compounds for structural applications. 127–142.
- [153] Thomas, F., Contreras, J., Bilbao, G., Invarardi, L., & Thomas, J. (1999). An improved technique for isolating pig islets: The importance of tensegrity in islet long-term culture viability. *Transplantation Proceedings*, 31(1–2), 633–634. [https://doi.org/10.1016/S0041-1345\(98\)01590-5](https://doi.org/10.1016/S0041-1345(98)01590-5).
- [154] Hofmann, U., & Blum, W. (1999). Microstructural evolution during high temperature deformation of lamellar Ti48Al–2Nb–2Cr. *Intermetallics*, 7(3–4), 351–361. [https://doi.org/10.1016/S0966-9795\(98\)00097-1](https://doi.org/10.1016/S0966-9795(98)00097-1).
- [155] Appel, F., & Oehring, M. (2003). γ -Titanium Aluminide Alloys: Alloy Design and Properties. In *Titanium and Titanium Alloys* (pp. 89–152). John Wiley & Sons, Ltd. <https://doi.org/10.1002/3527602119.ch4>
- [156] Wrought Processing. (2011). In *Gamma Titanium Aluminide Alloys* (pp. 573–682). John Wiley & Sons, Ltd. <https://doi.org/10.1002/9783527636204.ch16>.

- [157] Powder Metallurgy. (2011). In *Gamma Titanium Aluminide Alloys* (pp. 521–572). John Wiley & Sons, Ltd. <https://doi.org/10.1002/9783527636204.ch15>.
- [158] Lagos, M. A., Agote, I., San Juan, J. M., & Hennicke, J. (2014). Fabrication of TiAl alloys by alternative powder methods. TMS Annual Meeting, 2014-February, 77–82. <https://doi.org/10.1002/9781118998489.ch11>.
- [159] Froes, F. H., Suryanarayana, C., & Eliezer, D. (1992). Review Synthesis, properties and applications of titanium aluminides. In *JOURNAL OF MATERIALS SCIENCE* (Vol. 27).
- [160] Bilgin, G. M. (2017). Optimization of the mechanical properties of Ti-6Al-4V alloy produced by three dimensional additive manufacturing using thermochemical processes [M.S. - Master of Science]. Middle East Technical University.
- [161] Karimi, P., Keshavarz, M. K., Sadeghi, E., Habibnejad, M., & Vlasea, M. (2023). Interplay of process, microstructure, and mechanical performance in electron beam-powder bed fusion of Ti48Al2Nb2Cr. *Additive Manufacturing*, 77, 103811. <https://doi.org/10.1016/J.ADDMA.2023.103811>.
- [162] Emiralioğlu, A., & Ünal, R. (2022). Additive manufacturing of gamma titanium aluminide alloys: a review. In *Journal of Materials Science* (Vol. 57, Issue 7, pp. 4441–4466). Springer. <https://doi.org/10.1007/s10853-022-06896-4>.
- [163] Gibson, I., Rosen, D. W., Stucker, B., Khorasani, M., Rosen, D., Stucker, B., & Khorasani, M. (2021). *Additive manufacturing technologies* (Vol. 3, pp. 125-171). Cham, Switzerland: Springer. <https://doi.org/10.1007/978-3-030-56127-7>.
- [164] Dutta, B., & Froes, F. H. (Sam). (2017). The Additive Manufacturing (AM) of titanium alloys. *Metal Powder Report*, 72(2), 96–106. <https://doi.org/10.1016/J.MPRP.2016.12.062>.

- [165]Ding, D., Pan, Z., Cuiuri, D., & Li, H. (2015). Wire-feed additive manufacturing of metal components: technologies, developments and future interests. *The International Journal of Advanced Manufacturing Technology*, 81, 465-481.
- [166]Cai, X., Dong, B., Yin, X., Lin, S., Fan, C., & Yang, C. (2020). Wire arc additive manufacturing of titanium aluminide alloys using two-wire TOP-TIG welding: Processing, microstructures, and mechanical properties. *Additive Manufacturing*, 35, 101344. <https://doi.org/10.1016/J.ADDMA.2020.101344>.
- [167]Wang, J., Luo, Q., Wang, H., Wu, Y., Cheng, X., & Tang, H. (2020). Microstructure characteristics and failure mechanisms of Ti-48Al-2Nb-2Cr titanium aluminide intermetallic alloy fabricated by directed energy deposition technique. *Additive Manufacturing*, 32, 101007. <https://doi.org/10.1016/J.ADDMA.2019.101007>.
- [168]Srivastava, D., Hu, D., Chang, I. T. H., & Loretto, M. H. (1999). The influence of thermal processing route on the microstructure of some TiAl-based alloys. *Intermetallics*, 7(10), 1107–1112. [https://doi.org/10.1016/S0966-9795\(99\)00029-1](https://doi.org/10.1016/S0966-9795(99)00029-1).
- [169]Moll, J. H., Whitney, E., Yolton, C. F., & Habel, U. (1999). Laser forming of gamma titanium aluminide. *Gamma titanium aluminides*, 255-263.
- [170]Srivastava, D., Chang, I. T. H., & Loretto, M. H. (2001). The effect of process parameters and heat treatment on the microstructure of direct laser fabricated TiAl alloy samples. *Intermetallics*, 9(12), 1003–1013. [https://doi.org/10.1016/S0966-9795\(01\)00063-2](https://doi.org/10.1016/S0966-9795(01)00063-2).
- [171]Thomas, M., Malot, T., & Aubry, P. (2017). Laser Metal Deposition of the Intermetallic TiAl Alloy. *Metallurgical and Materials Transactions A*, 48(6), 3143–3158. <https://doi.org/10.1007/s11661-017-4042-9>.
- [172]Zhang, X. D., Brice, C., Mahaffey, D. W., Zhang, H., Schwendner, K., Evans, D. J., & Fraser, H. L. (2001). Characterization of laser-deposited

- TiAl alloys. *Scripta Materialia*, 44(10), 2419–2424. [https://doi.org/10.1016/S1359-6462\(01\)00915-0](https://doi.org/10.1016/S1359-6462(01)00915-0).
- [173] Liu, Y. C., Guo, Z. Q., Wang, T., Xu, D. S., Song, G. S., Yang, G. C., & Zhou, Y. H. (2001). Directional growth of metastable phase γ in laser-remelted Ti–Al. *Journal of Materials Processing Technology*, 108(3), 394–397. [https://doi.org/10.1016/S0924-0136\(00\)00851-7](https://doi.org/10.1016/S0924-0136(00)00851-7).
- [174] Qu, H. P., & Wang, H. M. (2007). Microstructure and mechanical properties of laser melting deposited γ -TiAl intermetallic alloys. *Materials Science and Engineering: A*, 466(1–2), 187–194. <https://doi.org/10.1016/J.MSEA.2007.02.073>.
- [175] Qu, H. P., Li, P., Zhang, S. Q., Li, A., & Wang, H. M. (2010). The effects of heat treatment on the microstructure and mechanical property of laser melting deposition γ -TiAl intermetallic alloys. *Materials & Design*, 31(4), 2201–2210. <https://doi.org/10.1016/J.MATDES.2009.10.045>.
- [176] Shen, C., Liss, K. D., Reid, M., Pan, Z., Ma, Y., Li, X., & Li, H. (2019). In-situ neutron diffraction characterization on the phase evolution of γ -TiAl alloy during the wire-arc additive manufacturing process. *Journal of Alloys and Compounds*, 778, 280–287. <https://doi.org/10.1016/J.JALLCOM.2018.11.150>.
- [177] Wang, J., Pan, Z., Wei, L., He, S., Cuiuri, D., & Li, H. (2019). Introduction of ternary alloying element in wire arc additive manufacturing of titanium aluminide intermetallic. *Additive Manufacturing*, 27, 236–245. <https://doi.org/10.1016/J.ADDMA.2019.03.014>.
- [178] Wang, L., Zhang, Y., Hua, X., Shen, C., Li, F., Huang, Y., Ding, Y., Zhang, P., Lu, Q., Zhang, T., & Shang, J. (2021). Twin-wire plasma arc additive manufacturing of the Ti–45Al titanium aluminide: Processing, microstructures and mechanical properties. *Intermetallics*, 136, 107277. <https://doi.org/10.1016/J.INTERMET.2021.107277>.
- [179] Ma, Y., Cuiuri, D., Li, H., Pan, Z., & Shen, C. (2016). The effect of postproduction heat treatment on γ -TiAl alloys produced by the GTAW-

- based additive manufacturing process. *Materials Science and Engineering: A*, 657, 86–95. <https://doi.org/10.1016/J.MSEA.2016.01.060>.
- [180]Löber, L., Petters, R., Kühn, U., & Eckert, J. (2011, September). Selective laser melting of titaniumaluminides. In 4th International Workshop on Titanium Aluminides.
- [181]Löber, L., Schimansky, F. P., Kühn, U., Pyczak, F., & Eckert, J. (2014). Selective laser melting of a beta-solidifying TNM-B1 titanium aluminide alloy. *Journal of Materials Processing Technology*, 214(9), 1852–1860. <https://doi.org/10.1016/J.JMATPROTEC.2014.04.002>.
- [182]Shi, X., Ma, S., Liu, C., & Wu, Q. (2017). Parameter optimization for Ti-47Al-2Cr-2Nb in selective laser melting based on geometric characteristics of single scan tracks. *Optics & Laser Technology*, 90, 71–79. <https://doi.org/10.1016/J.OPTLASTEC.2016.11.002>.
- [183]Li, W., Liu, J., Zhou, Y., Li, S., Wen, S., Wei, Q., Yan, C., & Shi, Y. (2016). Effect of laser scanning speed on a Ti-45Al-2Cr-5Nb alloy processed by selective laser melting: Microstructure, phase and mechanical properties. *Journal of Alloys and Compounds*, 688, 626–636. <https://doi.org/10.1016/J.JALLCOM.2016.07.206>.
- [184]Sankar, G. S., Karthik, G. M., Mohammad, A., Kumar, R., & Janaki Ram, G. D. (2019). Friction Welding of Electron Beam Melted γ -TiAl Alloy Ti-48Al-2Cr-2Nb. *Transactions of the Indian Institute of Metals*, 72(1), 35–46. <https://doi.org/10.1007/s12666-018-1458-x>.
- [185]Dzogbewu, T. C. (2020). Additive manufacturing of TiAl-based alloys. *Manufacturing Review*, 7, 35.
- [186]Cormier, D., Harrysson, O., Mahale, T., & West, H. (2007). Freeform Fabrication of Titanium Aluminide via Electron Beam Melting Using Prealloyed and Blended Powders. *Research Letters in Materials Science*, 2007, 034737. <https://doi.org/10.1155/2007/34737>.
- [187]Mohammad, A., Alahmari, A. M., Mohammed, M. K., Renganayagalu, R. K., & Moiduddin, K. (2017). Effect of energy input on microstructure and

mechanical properties of titanium aluminide alloy fabricated by the additive manufacturing process of electron beam melting. *Materials*, 10(2), 211. <https://doi.org/10.3390/ma10020211>.

- [188]Chen, Y., Yue, H., Wang, X., Xiao, S., Kong, F., Cheng, X., & Peng, H. (2018). Selective electron beam melting of TiAl alloy: Microstructure evolution, phase transformation and microhardness. *Materials Characterization*, 142, 584–592. <https://doi.org/10.1016/j.matchar.2018.06.027>.
- [189]Yue, H., Peng, H., Li, R., Gao, R., Wang, X., & Chen, Y. (2021). High-temperature microstructure stability and fracture toughness of TiAl alloy prepared via electron beam smelting and selective electron beam melting. *Intermetallics*, 136, 107259. <https://doi.org/10.1016/J.INTERMET.2021.107259>.
- [190]Kim, Y. K., Youn, S. J., Kim, S. W., Hong, J., & Lee, K. A. (2019). High-temperature creep behaviour of gamma Ti-48Al-2Cr-2Nb alloy additively manufactured by electron beam melting. *Materials Science and Engineering: A*, 763, 138138. <https://doi.org/10.1016/J.MSEA.2019.138138>.
- [191]Yue, H., Peng, H., Li, R., Qi, K., Zhang, L., Lin, J., & Su, Y. (2021). Effect of heat treatment on the microstructure and anisotropy of tensile properties of TiAl alloy produced via selective electron beam melting. *Materials Science and Engineering: A*, 803, 140473. <https://doi.org/10.1016/j.msea.2020.140473>.
- [192]Mohammad, A., Al-Ahmari, A. M., Balla, V. K., Das, M., Datta, S., Yadav, D., & Janaki Ram, G. D. (2017). In vitro wear, corrosion and biocompatibility of electron beam melted γ -TiAl. *Materials & Design*, 133, 186–194. <https://doi.org/10.1016/j.matdes.2017.07.065>.
- [193]Cakmak, E., Nandwana, P., Shin, D., Yamamoto, Y., Gussev, M. N., Sen, I., Seren, M. H., Watkins, T. R., & Haynes, J. A. (2019). A comprehensive study on the fabrication and characterization of Ti-48Al-2Cr-2Nb

- preforms manufactured using electron beam melting. *Materialia*, 6, 100284. <https://doi.org/10.1016/j.mtla.2019.100284>.
- [194]Chen, W., Yang, Y., Liu, L., Chen, Z., & Liu, D. (2017). Microstructure control and tensile properties of EBM γ -TiAl. *Aeronaut Manuf Technol*.
- [195]Soliman, H. A., & Elbestawi, M. (2022). Titanium aluminides processing by additive manufacturing – a review. In *International Journal of Advanced Manufacturing Technology* (Vol. 119, Issues 9–10, pp. 5583–5614). Springer Science and Business Media Deutschland GmbH. <https://doi.org/10.1007/s00170-022-08728-w>.
- [196]Lin, B., Chen, W., Yang, Y., Wu, F., & Li, Z. (2020). Anisotropy of microstructure and tensile properties of Ti–48Al–2Cr–2Nb fabricated by electron beam melting. *Journal of Alloys and Compounds*, 830. <https://doi.org/10.1016/j.jallcom.2020.154684>.
- [197]Reith, M., Franke, M., Schloffer, M., & Körner, C. (2020). Processing 4th generation titanium aluminides via electron beam based additive manufacturing – characterization of microstructure and mechanical properties. *Materialia*, 14, 100902. <https://doi.org/10.1016/J.MTLA.2020.100902>.
- [198]Pradeep, G. V. K., Duraiselvam, M., Prasad, K. S., & Mohammad, A. (2020). Tribological Behaviour of Additive Manufactured γ -TiAl by Electron Beam Melting. *Transactions of the Indian Institute of Metals*, 73(6), 1661–1667. <https://doi.org/10.1007/s12666-020-01950-8>.
- [199]Doubenskaia, M., Domashenkov, A., Smurov, I., & Petrovskiy, P. (2018). Study of Selective Laser Melting of intermetallic TiAl powder using integral analysis. *International Journal of Machine Tools and Manufacture*, 129, 1–14. <https://doi.org/10.1016/J.IJMACHTOOLS.2018.02.003>.
- [200]Vogelpoth, A., Schleifenbaum, J. H., & Rittinghaus, S. (2019, June). Laser additive manufacturing of titanium aluminides for turbomachinery applications. In *Turbo Expo: Power for Land, Sea, and Air* (Vol. 58677, p.

- V006T24A011). American Society of Mechanical Engineers.
<https://doi.org/10.1115/GT2019-90947>.
- [201]Yang, Y., Wen, S., Wei, Q., Li, W., Liu, J., & Shi, Y. (2017). Effect of scan line spacing on texture, phase and nanohardness of TiAl/TiB₂ metal matrix composites fabricated by selective laser melting. *Journal of Alloys and Compounds*, 728, 803–814.
<https://doi.org/10.1016/J.JALLCOM.2017.09.053>.
- [202]Choron, D., Naveos, S., Thomas, M., Petit, J., & Boisselier, D. (2020). Direct Laser Additive Manufacturing of TiAl Intermetallic Compound by Powder Directed Energy Deposition (DED). *MATEC Web Conf.*, 321.
<https://doi.org/10.1051/mateconf/202032103020>.
- [203]Balla, V. K., Das, M., Mohammad, A., & Al-Ahmari, A. M. (2016). Additive Manufacturing of γ -TiAl: Processing, Microstructure, and Properties. *Advanced engineering materials*, 18(7), 1208-1215.
<https://doi.org/10.1002/adem.201500588>.
- [204]Huang, D., Tan, Q., Zhou, Y., Yin, Y., Wang, F., Wu, T., Yang, X., Fan, Z., Liu, Y., Zhang, J., Huang, H., Yan, M., & Zhang, M. X. (2021). The significant impact of grain refiner on γ -TiAl intermetallic fabricated by laser-based additive manufacturing. *Additive Manufacturing*, 46, 102172.
<https://doi.org/10.1016/J.ADDMA.2021.102172>.
- [205]Wang, J., Pan, Z., Ma, Y., Lu, Y., Shen, C., Cuiuri, D., & Li, H. (2018). Characterization of wire arc additively manufactured titanium aluminide functionally graded material: Microstructure, mechanical properties and oxidation behaviour. *Materials Science and Engineering: A*, 734, 110–119.
<https://doi.org/10.1016/J.MSEA.2018.07.097>.
- [206]Wang, L., Zhang, Y., Hua, X., Shen, C., Li, F., Huang, Y., & Ding, Y. (2021). Fabrication of γ -TiAl intermetallic alloy using the twin-wire plasma arc additive manufacturing process: Microstructure evolution and mechanical properties. *Materials Science and Engineering: A*, 812, 141056.
<https://doi.org/10.1016/J.MSEA.2021.141056>.

- [207]Ma, Y., Cuiuri, D., Hoye, N., Li, H., & Pan, Z. (2015). The effect of location on the microstructure and mechanical properties of titanium aluminides produced by additive layer manufacturing using in-situ alloying and gas tungsten arc welding. *Materials Science and Engineering: A*, 631, 230–240. <https://doi.org/10.1016/J.MSEA.2015.02.051>.
- [208]Najmon, J., Raeisi, S., & Tovar, A. (2019). Review of additive manufacturing technologies and applications in the aerospace industry. *Additive Manufacturing for the Aerospace Industry*. <https://doi.org/10.1016/B978-0-12-814062-8.00002-9>.
- [209]Metal AM Magazine, Unrealised potential: The story and status of Electron Beam Powder Bed Fusion. <https://www.metal-am.com/articles/unrealised-potential-the-story-and-status-of-electron-beam-powder-bed-fusion-3d-printing/>. (accessed 19 December 2023).
- [210]Yang, L., Hsu, K., Baughman, B., Godfrey, D., Medina, F., Menon, M., & Wiener, S. (2017). Additive manufacturing of metals: the technology, materials, design and production. DOI10.1007/978-3-319-55128-9.
- [211]Ampower Report, Additive Manufacturing Market. <https://additive-manufacturing-report.com/additive-manufacturing-market/#001>. (accessed 19 December 2023).
- [212]Wohlers, T., Campbell, I., Diegel, O., Huff, R., & Kowen, J. (2020). Wohlers Report 2020: 3D Printing and Additive Manufacturing Global State of the Industry, Wohlers Associates.
- [213]Donets, E. (1998). Historical review of electron beam ion sources (invited). *Review of Scientific Instruments*, 69, 614-619. <https://doi.org/10.1063/1.1148642>.
- [214]English, C. L., Tewari, S. K., & Abbott, D. H. (2010). An overview of Ni base additive fabrication technologies for aerospace applications. *Superalloy 718 and Derivatives*, 397-412.

- [215]Autodesk, Electron Beam Melting Is Just as Metal as It Sounds. <https://www.autodesk.com/redshift/electron-beam-melting/> (accessed 13 December 2023).
- [216]The Engineer, Rolls-Royce breaks additive record with printed Trent-XWB bearing. <https://www.theengineer.co.uk/content/news/rolls-royce-breaks-additive-record-with-printed-trent-xwb-bearing/>. (accessed 13 December 2023).
- [217]Aerospace Manufacturing and Design, EBM technology expedites A&D projects. <https://www.aerospacemanufacturinganddesign.com/article/amd0314-3d-titanium-components/>. (accessed 13 December 2023).
- [218]Sinha, A., Swain, B., Behera, A., Mallick, P., Samal, S., M, V., & Behera, A. (2022). A Review on the Processing of Aero-Turbine Blade Using 3D Print Techniques. *Journal of Manufacturing and Materials Processing*. <https://doi.org/10.3390/jmmp6010016>.
- [219]Blakey-Milner, B., Gradl, P., Snedden, G., Brooks, M., Pitot, J., Lopez, E., Leary, M., Berto, F., & du Plessis, A. (2021). Metal additive manufacturing in aerospace: A review. *Materials & Design*, 209, 110008. <https://doi.org/10.1016/J.MATDES.2021.110008>.
- [220]Gong, X., Anderson, T., & Chou, K. (2012, June). Review on powder-based electron beam additive manufacturing technology. In *International Symposium on Flexible Automation* (Vol. 45110, pp. 507-515). American Society of Mechanical Engineers. <https://doi.org/10.1115/ISFA2012-7256>.
- [221]Liu, B., Wildman, R., Tuck, C., Ashcroft, I., & Hague, R. (2011). Investigation the effect of particle size distribution on processing parameters optimisation in selective laser melting process. In *2011 International Solid Freeform Fabrication Symposium*. University of Texas at Austin. <http://dx.doi.org/10.26153/tsw/15290>.
- [222]Stanford, M. K., DellaCorte, C., & Eylon, D. (2003, January). Particle size effects on flow properties of Ps304 plasma spray feedstock powder blend.

- In 27th Annual Cocoa Beach Conference on Advanced Ceramics and Composites: A: Ceramic Engineering and Science Proceedings (pp. 577-585). Hoboken, NJ, USA: John Wiley & Sons, Inc. <https://doi.org/10.1002/9780470294802.ch82>.
- [223] Yang, S., & Evans, J. R. G. (2007). Metering and dispensing of powder; the quest for new solid freeforming techniques. *Powder Technology*, 178(1), 56–72. <https://doi.org/10.1016/J.POWTEC.2007.04.004>.
- [224] Van der Schueren B., & Kruth, J. P. (1995). Powder deposition in selective metal powder sintering. *Rapid Prototyping Journal*, 1(3), 23–31. <https://doi.org/10.1108/13552549510094241>.
- [225] Berretta, S., Ghita, O., Evans, K. E., Anderson, A., & Newman, C. (2013). Size, shape and flow of powders for use in Selective Laser Sintering (SLS). *High Value Manufacturing: Advanced Research in Virtual and Rapid Prototyping*, 49.
- [226] Galati, M., & Iuliano, L. (2018). A literature review of powder-based electron beam melting focusing on numerical simulations. *Additive Manufacturing*, 19, 1–20. <https://doi.org/10.1016/J.ADDMA.2017.11.001>.
- [227] Milberg, J., & Sigl, M. (2008). Electron beam sintering of metal powder. *Production Engineering*, 2(2), 117–122. <https://doi.org/10.1007/s11740-008-0088-2>.
- [228] Sigl, M., Lutzmann, S., & Zaeh, M. F. (2006, September). Transient physical effects in electron beam sintering. In 2006 International Solid Freeform Fabrication Symposium. <http://dx.doi.org/10.26153/tsw/7154>.
- [229] Qi, H. B., Yan, Y. N., Lin, F., He, W., & Zhang, R. J. (2006). Direct metal part forming of 316L stainless steel powder by electron beam selective melting. *Proceedings of the Institution of Mechanical Engineers, Part B: Journal of Engineering Manufacture*, 220(11), 1845–1853. <https://doi.org/10.1243/09544054JEM438>.
- [230] Rafi, H. K., Karthik, N. v, Gong, H., Starr, T. L., & Stucker, B. E. (2013). Microstructures and Mechanical Properties of Ti6Al4V Parts Fabricated by

Selective Laser Melting and Electron Beam Melting. *Journal of Materials Engineering and Performance*, 22(12), 3872–3883. <https://doi.org/10.1007/s11665-013-0658-0>.

- [231]Strondl, A., Lyckfeldt, O., Brodin, H., & Ackelid, U. (2015). Characterization and Control of Powder Properties for Additive Manufacturing. *JOM*, 67(3), 549–554. <https://doi.org/10.1007/s11837-015-1304-0>.
- [232]Zhong, C., Chen, J., Linnenbrink, S., Gasser, A., Sui, S., & Poprawe, R. (2016). A comparative study of Inconel 718 formed by High Deposition Rate Laser Metal Deposition with GA powder and PREP powder. *Materials & Design*, 107, 386–392. <https://doi.org/10.1016/J.MATDES.2016.06.037>.
- [233]Xie, X., Li, N., Liu, W., Huang, S., He, X., Yu, Q., ... & Hou, X. (2022). Research Progress of Refractory High Entropy Alloys: A Review. *Chinese Journal of Mechanical Engineering*, 35(1), 142.
- [234]Taneva, E., Kusnoto, B., & Evans, C. A. (2015). 3D scanning, imaging, and printing in orthodontics. *Issues in contemporary orthodontics*, 148(5), 862-7. <https://doi.org/10.5772/60010>.
- [235]Yim, S., Bian, H., Aoyagi, K., Yanagihara, K., Kitamura, S. ichi, Manabe, H., Daino, Y., Hayasaka, Y., Yamanaka, K., & Chiba, A. (2022). Ball-milling treatment of gas-atomized Ti48Al2Cr2Nb powder and its effect on preventing smoking during electron beam powder bed fusion building process. *Additive Manufacturing*, 51, 102634. <https://doi.org/10.1016/J.ADDMA.2022.102634>.
- [236]Shen, N., & Chou, K. (2012, June). Thermal modeling of electron beam additive manufacturing process: powder sintering effects. In *International Manufacturing Science and Engineering Conference (Vol. 54990, pp. 287-295)*. American Society of Mechanical Engineers. <https://doi.org/10.1115/MSEC2012-7253>.
- [237]Chiba, A., Daino, Y., Aoyagi, K., & Yamanaka, K. (2021). Smoke suppression in electron beam melting of Inconel 718 alloy powder based on

- insulator–metal transition of surface oxide film by mechanical stimulation. *Materials*, 14(16), 4662. <https://doi.org/10.3390/ma14164662>.
- [238] Joe, H. E., Yun, H., Jo, S. H., Jun, M. B., & Min, B. K. (2018). A review on optical fiber sensors for environmental monitoring. *International journal of precision engineering and manufacturing-green technology*, 5, 173-191.
- [239] Reith, M., Franke, M., & Körner, C. (2023). Impact of the acceleration voltage on the processing of γ -TiAl via electron beam powder bed fusion. *Progress in Additive Manufacturing*. <https://doi.org/10.1007/s40964-023-00499-4>.
- [240] Sonkamble, V., & Phafat, N. (2023). A current review on electron beam assisted additive manufacturing technology: recent trends and advances in materials design. *Discover Mechanical Engineering*, 2(1). <https://doi.org/10.1007/s44245-022-00008-x>.
- [241] Grand View Research, Metal 3D Printing Market Size, Share & Trends Analysis Report By Component. <https://www.grandviewresearch.com/industry-analysis/metal-3d-printing-market>. (accessed 19 December 2023).
- [242] Stavropoulos, P., & Foteinopoulos, P. (2018). Modelling of additive manufacturing processes: a review and classification. *Manufacturing Review*, 5, 2. <https://doi.org/10.1051/mfreview/2017014>.
- [243] Wimler, D., Lindemann, J., Reith, M., Kirchner, A., Allen, M., Vargas, W. G., Franke, M., Klöden, B., Weißgärber, T., Güther, V., Schloffer, M., Clemens, H., & Mayer, S. (2021). Designing advanced intermetallic titanium aluminide alloys for additive manufacturing. *Intermetallics*, 131, 107109. <https://doi.org/10.1016/J.INTERMET.2021.107109>.
- [244] Silvestri, A. T., Foglia, S., Borrelli, R., Franchitti, S., Pirozzi, C., & Astarita, A. (2020). Electron beam melting of Ti6Al4V: Role of the process parameters under the same energy density. *Journal of Manufacturing Processes*, 60, 162–179. <https://doi.org/10.1016/J.JMAPRO.2020.10.065>.

- [245]Moritz, J., Teschke, M., Marquardt, A., Stepien, L., López, E., Brückner, F., & Leyens, C. (2021). Electron beam powder bed fusion of γ -titanium aluminide: Effect of processing parameters on part density, surface characteristics, and aluminum content. *Metals*, 11(7), 1093. <https://doi.org/10.3390/met11071093>.
- [246]Yue, H., Peng, H., Li, R., Su, Y., Zhao, Y., Qi, K., & Chen, Y. (2020). Selective electron beam melting of TiAl alloy: metallurgical defects, tensile property, and determination of process window. *Advanced Engineering Materials*, 22(8), 2000194. <https://doi.org/10.1002/adem.202000194>.
- [247]Wei, H. L., Mukherjee, T., Zhang, W., Zuback, J. S., Knapp, G. L., De, A., & DebRoy, T. (2021). Mechanistic models for additive manufacturing of metallic components. *Progress in Materials Science*, 116, 100703. <https://doi.org/10.1016/J.PMATSCI.2020.100703>.
- [248]Gui, Y., Aoyagi, K., Bian, H., & Chiba, A. (2022). Detection, classification and prediction of internal defects from surface morphology data of metal parts fabricated by powder bed fusion type additive manufacturing using an electron beam. *Additive Manufacturing*, 54, 102736. <https://doi.org/10.1016/J.ADDMA.2022.102736>.
- [249]DebRoy, T., Wei, H. L., Zuback, J. S., Mukherjee, T., Elmer, J. W., Milewski, J. O., Beese, A. M., Wilson-Heid, A., De, A., & Zhang, W. (2018). Additive manufacturing of metallic components – Process, structure and properties. *Progress in Materials Science*, 92, 112–224. <https://doi.org/10.1016/J.PMATSCI.2017.10.001>.
- [250]Juechter, V., Scharowsky, T., Singer, R. F., & Körner, C. (2014). Processing window and evaporation phenomena for Ti–6Al–4V produced by selective electron beam melting. *Acta Materialia*, 76, 252–258. <https://doi.org/10.1016/J.ACTAMAT.2014.05.037>.
- [251]Reith, M., Breuning, C., Franke, M., & Körner, C. (2022). Impact of the power-dependent beam diameter during electron beam additive

- manufacturing: A case study with γ -TiAl. *Applied Sciences*, 12(21), 11300. <https://doi.org/10.3390/app122111300>.
- [252]Moritz, J., Teschke, M., Marquardt, A., Stepien, L., López, E., Brueckner, F., & Leyens, C. (2023). Influence of Electron Beam Powder Bed Fusion Process Parameters at Constant Volumetric Energy Density on Surface Topography and Microstructural Homogeneity of a Titanium Aluminide Alloy. *Advanced Engineering Materials*, 2201871. <https://doi.org/10.1002/adem.202201871>.
- [253]Körner, C. (2016). Additive manufacturing of metallic components by selective electron beam melting — a review. *International Materials Reviews*, 61(5), 361–377. <https://doi.org/10.1080/09506608.2016.1176289>.
- [254]Mandil, G., Le, V. T., Paris, H., & Suard, M. (2016). Building new entities from existing titanium part by electron beam melting: microstructures and mechanical properties. *The International Journal of Advanced Manufacturing Technology*, 85(5), 1835–1846. <https://doi.org/10.1007/s00170-015-8049-3>.
- [255]He, W., Jia, W., Liu, H., Tang, H., Kang, X., & Huang, Y. (2011). Research on Preheating of Titanium Alloy Powder in Electron Beam Melting Technology. *Rare Metal Materials and Engineering*, 40(12), 2072–2075. [https://doi.org/10.1016/S1875-5372\(12\)60014-9](https://doi.org/10.1016/S1875-5372(12)60014-9).
- [256]Tang, H. P., Qian, M., Liu, N., Zhang, X. Z., Yang, G. Y., & Wang, J. (2015). Effect of Powder Reuse Times on Additive Manufacturing of Ti-6Al-4V by Selective Electron Beam Melting. *JOM*, 67(3), 555–563. <https://doi.org/10.1007/s11837-015-1300-4>.
- [257]Attar, E. (2011). Simulation of selective electron beam melting processes. Friedrich-Alexander-Universitaet Erlangen-Nuernberg (Germany).
- [258]Karlsson, J., Snis, A., Engqvist, H., & Lausmaa, J. (2013). Characterization and comparison of materials produced by Electron Beam Melting (EBM) of two different Ti–6Al–4V powder fractions. *Journal of Materials Processing*

Technology, 213(12), 2109–2118.
<https://doi.org/10.1016/J.JMATPROTEC.2013.06.010>.

- [259]Wang, P., Sin, W. J., Nai, M. L. S., & Wei, J. (2017). Effects of processing parameters on surface roughness of additive manufactured Ti-6Al-4V via electron beam melting. *Materials*, 10(10), 1121.
<https://doi.org/10.3390/ma10101121>.
- [260]Tammas-Williams, S., Zhao, H., Léonard, F., Derguti, F., Todd, I., & Prangnell, P. B. (2015). XCT analysis of the influence of melt strategies on defect population in Ti-6Al-4V components manufactured by Selective Electron Beam Melting. *Materials Characterization*, 102, 47–61.
<https://doi.org/10.1016/J.MATCHAR.2015.02.008>.
- [261]Smith, C. J., Derguti, F., Hernandez Nava, E., Thomas, M., Tammas-Williams, S., Gulizia, S., Fraser, D., & Todd, I. (2016). Dimensional accuracy of Electron Beam Melting (EBM) additive manufacture with regard to weight optimized truss structures. *Journal of Materials Processing Technology*, 229, 128–138.
<https://doi.org/10.1016/J.JMATPROTEC.2015.08.028>.
- [262]Puebla, K., Murr, L. E., Gaytan, S. M., Martinez, E., Medina, F., & Wicker, R. B. (2012). Effect of melt scan rate on microstructure and macrostructure for electron beam melting of Ti-6Al-4V. DOI:10.4236/msa.2012.35038.
- [263]Gong, X., Lydon, J., Cooper, K., & Chou, K. (2014). Beam speed effects on Ti-6Al-4V microstructures in electron beam additive manufacturing. *Journal of Materials Research*, 29(17), 1951-1959.
doi:10.1557/jmr.2014.125.
- [264]Morita, T., Tsuda, C., & Nakano, T. (2017). Influences of scanning speed and short-time heat treatment on fundamental properties of Ti-6Al-4V alloy produced by EBM method. *Materials Science and Engineering: A*, 704, 246–251. <https://doi.org/10.1016/J.MSEA.2017.08.020>.

- [265]A. Kirchner B. Klöden, J. L. T. W., & Kieback, B. (2015). Process window for electron beam melting of Ti-6Al-4V. *Powder Metallurgy*, 58(4), 246–249. <https://doi.org/10.1179/0032589915Z.000000000244>.
- [266]Rausch, A. M., Markl, M., & Körner, C. (2019). Predictive simulation of process windows for powder bed fusion additive manufacturing: Influence of the powder size distribution. *Computers & Mathematics with Applications*, 78(7), 2351–2359. <https://doi.org/10.1016/J.CAMWA.2018.06.029>.
- [267]Abdeen, D. H., & Palmer, B. R. (2016). Effect of processing parameters of electron beam melting machine on properties of Ti-6Al-4V parts. *Rapid Prototyping Journal*, 22(3), 609–620. <https://doi.org/10.1108/RPJ-09-2014-0105>.
- [268]Helmer, H., Körner, C., & Singer, R. (2014). Additive manufacturing of nickel-based superalloy Inconel 718 by selective electron beam melting: Processing window and microstructure. *Journal of Materials Research*, 29(17), 1987-1996. doi:10.1557/jmr.2014.192.
- [269]Hrabe, N., & Quinn, T. (2013). Effects of processing on microstructure and mechanical properties of a titanium alloy (Ti-6Al-4V) fabricated using electron beam melting (EBM), Part 2: Energy input, orientation, and location. *Materials Science and Engineering: A*, 573, 271–277. <https://doi.org/10.1016/J.MSEA.2013.02.065>.
- [270]ASTM B822-20, Standard Test Method for Particle Size Distribution of Metal Powders and Related Compounds by Light Scattering, ASTM International, West Conshohocken, PA, 2020, DOI: 10.1520/B0822-20.
- [271]ASTM F3049-14, Standard Guide for Characterizing Properties of Metal Powders Used for Additive Manufacturing Processes, ASTM International, West Conshohocken, PA, 2014, DOI: 10.1520/F3049-14.
- [272]ASTM B212-17, Standard Test Method for Apparent Density of Free-Flowing Metal Powders Using the Hall Flowmeter Funnel, ASTM International, West Conshohocken, PA, 2017, DOI: 10.1520/B0212-17.

- [273]ASTM B527-20, Standard Test Method for Tap Density of Metal Powders and Compounds, ASTM International, West Conshohocken, PA, 2020, DOI: 10.1520/B0527-20.
- [274]Liu, B., Wildman, R., Tuck, C., Ashcroft, I., & Hague, R. (2011). Investigation the effect of particle size distribution on processing parameters optimisation in selective laser melting process. Additive manufacturing research group, Loughborough University, 227-238.
- [275]Bumiller, M., Carson, J., & Prescott, J. (2002, July). A preliminary investigation concerning the effect of particle shape on a powder's flow properties. In World congress on particle technology (Vol. 4, pp. 21-25). Sydney Australia.
- [276]ASTM B213-20, Standard Test Methods for Flow Rate of Metal Powders Using the Hall Flowmeter Funnel, ASTM International, West Conshohocken, PA, 2020, DOI: 10.1520/B0213-20.
- [277]Ian Gibson, I. G. (2015). Additive Manufacturing Technologies 3D Printing, Rapid Prototyping, and Direct Digital Manufacturing.
- [278]Arcam EBM A2X. GE Additive. <https://www.ge.com/additive/additive-manufacturing/machines/ebm-machines/arcam-ebm-a2x>. (accessed 21 January 2021).
- [279]Fang, T. Y., & Wang, W. H. (1998). Microstructural features of thermochemical processing in a Ti-6Al-4V alloy. *Materials chemistry and Physics*, 56(1), 35-47.
- [280]Doğu, M. N., Esen, Z., Davut, K., Tan, E., Gümüş, B., & Dericioğlu, A. F. (2020). Microstructural and texture evolution during thermo-hydrogen processing of Ti6Al4V alloys produced by electron beam melting. *Materials Characterization*, 168, 110549.
- [281]Pushilina, N., Syrtanov, M., Kashkarov, E., Murashkina, T., Kudiiarov, V., Laptev, R., & Koptyug, A. (2018). Influence of manufacturing parameters on microstructure and hydrogen sorption behaviour of electron beam melted titanium Ti-6Al-4V alloy. *Materials*, 11(5), 763.

- [282]Pushilina, N., Panin, A., Syrtanov, M., Kashkarov, E., Kudiiarov, V., Perevalova, O., & Koptuyug, A. (2018). Hydrogen-induced phase transformation and microstructure evolution for Ti-6Al-4V parts produced by electron beam melting. *Metals*, 8(5), 301.
- [283]Dunstan, M. K., Paramore, J. D., Butler, B. G., & Fang, Z. Z. (2020). The uses and applications of hydrogen processing for titanium additive manufacturing. In *MATEC Web of Conferences* (Vol. 321, p. 03003). EDP Sciences.
- [284]Bilgin, G. M. (2017). Optimization of the mechanical properties of Ti-6Al-4V alloy produced by three dimensional additive manufacturing using thermochemical processes (Doctoral dissertation, MS thesis, Dept. Metal. & Mat. Eng., Middle East Tech. Univ, Ankara, Turkey, 2017.[Online]. Available: <http://etd.lib.metu.edu.tr/upload/12620708/index.pdf>).
- [285]Zhao, J., Ding, H., Zhong, Y., & Lee, C. S. (2010). Effect of thermo hydrogen treatment on lattice defects and microstructure refinement of Ti6Al4V alloy. *international journal of hydrogen energy*, 35(12), 6448-6454.
- [286]Bilgin, G. M., Esen, Z., Akin, Ş. K., & Dericioglu, A. F. (2017). Optimization of the mechanical properties of Ti-6Al-4V alloy fabricated by selective laser melting using thermohydrogen processes. *Materials Science and Engineering: A*, 700, 574-582.
- [287]ASTM B311-17, Standard Test Method for Density of Powder Metallurgy (PM) Materials Containing Less Than Two Percent Porosity, ASTM International, West Conshohocken, PA, 2017, DOI: 10.1520/B0311-17
- [288]Bunge, H.J., 1982. Introduction, *Texture Analysis in Materials Science*, pp. 1–2, <https://doi.org/10.1016/b978-0-408-10642-9.50006-4>.
- [289]ASTM E8/E8M-16, Standard Test Methods for Tension Testing of Metallic Materials, ASTM International, West Conshohocken, PA, 2016, DOI: 10.1520/E0008_E0008M-16.

- [290]ASTM E21-17, Standard Test Methods for Elevated Temperature Tension Tests of Metallic Materials, West Conshohocken, PA, 2019, DOI: 10.1520/E0021-17.
- [291]Djanarthany S., Viala JC., & Bouix J. (2010). An overview of monolithic titanium aluminides based on Ti₃Al and TiAl. *Materials Chemistry and Physics*, 72, no. 3, 301–319, 2001.
- [292]Schuster, J. C., & Palm, M. (2006). Reassessment of the binary aluminum-titanium phase diagram. *Journal of phase equilibria and diffusion*, 27(3), 255-277.
- [293]Kaplanskii, Y. Y., Levashov, E. A., Korotitskiy, A. V., Loginov, P. A., Sentyurina, Z. A., & Mazalov, A. B. (2020). Influence of aging and HIP treatment on the structure and properties of NiAl-based turbine blades manufactured by laser powder bed fusion. *Additive Manufacturing*, 31, 100999.
- [294]Yoshioka, Y., Saito, D., Takaku, R., Itou, S., Sato, I., Ishibashi, K., & Sakai, Y. (2010). Development, reliability evaluation and service experiences of gas turbine blade life regeneration technology. *Transactions of the Indian Institute of Metals*, 63(2), 289-295.
- [295]VanDrunen, G., Liburdi, J., Wallace, W., & Terada, T. (1979). Hot isostatic processing of IN-738 turbine blades. In *AGARD Advan. Fabric. Processes* 12 p (SEE N79-23236 14-31).
- [296]Juechter, V., & Körner, C. (2016). Creep properties of Ti₄₈Al₂C₂Nb produced by selective electron beam melting. In *Key Engineering Materials* (Vol. 704, pp. 190-196). Trans Tech Publications Ltd.
- [297]Moore, P. O. (Ed.). (2012). *Nondestructive testing handbook*. American Society for Nondestructive Testing.
- [298]ASTM E539-19, Standard Test Method for Analysis of Titanium Alloys by Wavelength Dispersive X-Ray Fluorescence Spectrometry, ASTM International, West Conshohocken, PA, 2019, DOI: 10.1520/E0539-19

- [299]Lütjering, G., & Williams, J. C. (2007). *Titanium Engineering Materials and Processes*, Springer.
- [300]Jin, Z., & Gray, G. T. (1998). On deformation twins and twin-related lamellae in TiAl. *Journal of Materials Science*, 33(1), 77–83. <https://doi.org/10.1023/A:1004389428278>.
- [301]Zong, Y., Wen, D., Liu, Z., & Shan, D. (2016). γ -Phase transformation, dynamic recrystallization and texture of a forged TiAl-based alloy based on plane strain compression at elevated temperature. *Materials & Design*, 91, 321–330. <https://doi.org/10.1016/J.MATDES.2015.11.120>.
- [302]Holland, S., Wang, X., Chen, J., Cai, W., Yan, F., & Li, L. (2019). Multiscale characterization of microstructures and mechanical properties of Inconel 718 fabricated by selective laser melting. *Journal of Alloys and Compounds*, 784, 182–194. <https://doi.org/10.1016/J.JALLCOM.2018.12.380>.
- [303]Aota, L. S., Bajaj, P., Zilnyk, K. D., Ponge, D., & Sandim, H. R. Z. (2021). The origin of abnormal grain growth upon thermomechanical processing of laser powder-bed fusion alloys. *Materialia*, 20, 101243.
- [304]Suwas, S., & Ray, R. K. (2014). *Crystallographic texture of materials* (pp. 108-173). London: Springer.
- [305]Knörlein, J., Franke, M. M., Schloffer, M., & Körner, C. (2022). In-situ aluminum control for titanium aluminide via electron beam powder bed fusion to realize a dual microstructure. *Additive Manufacturing*, 59, 103132.
- [306]Wartbichler, R., Clemens, H., & Mayer, S. (2019). Electron Beam Melting of a β -Solidifying Intermetallic Titanium Aluminide Alloy. *Advanced Engineering Materials*, 21(12), 1900800. <https://doi.org/10.1002/adem.201900800>.
- [307]Al-Bermani, S. S., Blackmore, M. L., Zhang, W., & Todd, I. (2010). The origin of microstructural diversity, texture, and mechanical properties in

electron beam melted Ti-6Al-4V. Metallurgical and materials transactions a, 41, 3422-3434.

- [308]Galarraga, H., Warren, R. J., Lados, D. A., Dehoff, R. R., Kirka, M. M., & Nandwana, P. (2017). Effects of heat treatments on microstructure and properties of Ti-6Al-4V ELI alloy fabricated by electron beam melting (PBF-EB). *Materials Science and Engineering: A*, 685, 417-428.
- [309]Youn, S. J., Kim, Y. K., Kim, S. W., & Lee, K. A. (2020). Elevated temperature compressive deformation behaviours of γ -TiAl-based Ti-48Al-2Cr-2Nb alloy additively manufactured by electron beam melting. *Intermetallics*, 124, 106859.
- [310]Gottstein, G. (2004). *Physical foundations of materials science (Vol. 3)*. Berlin: Springer.
- [311]Xu, X. J., Lin, J. P., Teng, Z. K., Wang, Y. L., & Chen, G. L. (2007). On the microsegregation of Ti-45Al-(8-9) Nb-(W, B, Y) alloy. *Materials letters*, 61(2), 369-373.
- [312]Haanappel, V. A. C., Clemens, H., & Stroosnijder, M. F. (2002). The high temperature oxidation behaviour of high and low alloyed TiAl-based intermetallics. *Intermetallics*, 10(3),293-305.

APPENDICES

A. Coefficient of Thermal Expansion of Electron Beam Powder Bed Fusion Fabricated Ti48Al2Cr2Nb

Table A.5.1: Coefficient of thermal expansion of PBF-EB fabricated
Ti48Al2Cr2Nb.

Temperature (°C)	XY Average	XY Extrapolated	Z Average	Z Extrapolated
	CTE ($10^{-6}/K$)			
30	6.32220	9.83221	6.30209	9.89618
40	7.97353	9.87459	8.00628	9.93491
50	8.63398	9.91698	8.66893	9.97364
60	9.10029	9.95936	9.13123	10.01236
70	9.36921	10.00174	9.39278	10.05109
80	9.57046	10.04412	9.58958	10.08982
90	9.72301	10.08651	9.73855	10.12855
100	9.84217	10.12889	9.85358	10.16727
110	9.96860	10.17127	9.97671	10.20600
120	10.06250	10.21366	10.07215	10.24473
130	10.14435	10.25604	10.15822	10.28345
140	10.22467	10.29842	10.23663	10.32218
150	10.28972	10.34080	10.30142	10.36091
160	10.35222	10.38319	10.36328	10.39964
170	10.41208	10.42557	10.42368	10.43836
180	10.46817	10.46795	10.47723	10.47709
190	10.52365	10.51034	10.53145	10.51582
200	10.56892	10.55272	10.57058	10.55454
210	10.58935	10.59510	10.58712	10.59327
220	10.62700	10.63748	10.62102	10.63200
230	10.67028	10.67028	10.66417	10.66417
240	10.71318	10.71318	10.70788	10.70788
250	10.75463	10.75463	10.75082	10.75082
260	10.79650	10.79650	10.79430	10.79430
270	10.83287	10.83287	10.83293	10.83293
280	10.86867	10.86867	10.86842	10.86842
290	10.90913	10.90913	10.90943	10.90943
300	10.94497	10.94497	10.94597	10.94597
310	10.97863	10.97863	10.98003	10.98003
320	11.01117	11.01117	11.01182	11.01182
330	11.04092	11.04092	11.04118	11.04118

340	11.06937	11.06937	11.06988	11.06988
350	11.09580	11.09580	11.09633	11.09633
360	11.12570	11.12570	11.12618	11.12618
370	11.15315	11.15315	11.15427	11.15427
380	11.18028	11.18028	11.18162	11.18162
390	11.20703	11.20703	11.20885	11.20885
400	11.23452	11.23452	11.23553	11.23553
410	11.26025	11.26025	11.26160	11.26160
420	11.28537	11.28537	11.28693	11.28693
430	11.31078	11.31078	11.31228	11.31228
440	11.33457	11.33457	11.33637	11.33637
450	11.35827	11.35827	11.35998	11.35998
460	11.38215	11.38215	11.38333	11.38333
470	11.40225	11.40225	11.40397	11.40397
480	11.42655	11.42655	11.42823	11.42823
490	11.44888	11.44888	11.45033	11.45033
500	11.47118	11.47118	11.47295	11.47295
510	11.49737	11.49737	11.49958	11.49958
520	11.52188	11.52188	11.52368	11.52368
530	11.54603	11.54603	11.54813	11.54813
540	11.56947	11.56947	11.57158	11.57158
550	11.59267	11.59267	11.59460	11.59460
560	11.61698	11.61698	11.61927	11.61927
570	11.64190	11.64190	11.64355	11.64355
580	11.66497	11.66497	11.66633	11.66633
590	11.68733	11.68733	11.68835	11.68835
600	11.70960	11.70960	11.71005	11.71005
610	11.73545	11.73545	11.73553	11.73553
620	11.76072	11.76072	11.76045	11.76045
630	11.78768	11.78768	11.78653	11.78653
640	11.81557	11.81557	11.81395	11.81395
650	11.84453	11.84453	11.84260	11.84260
660	11.87302	11.87302	11.87097	11.87097
670	11.90222	11.90222	11.90022	11.90022
680	11.93210	11.93210	11.92973	11.92973
690	11.96225	11.96225	11.95977	11.95977
700	11.99097	11.99097	11.98833	11.98833
710	12.01892	12.01892	12.01612	12.01612
720	12.04710	12.04710	12.04352	12.04352
730	12.07717	12.07717	12.07363	12.07363
740	12.10815	12.10815	12.10398	12.10398
750	12.14108	12.14108	12.13615	12.13615

760	12.17347	12.17347	12.16800	12.16800
770	12.20550	12.20550	12.19930	12.19930
780	12.23773	12.23773	12.23098	12.23098
790	12.27058	12.27058	12.26358	12.26358
800	12.30312	12.30312	12.29563	12.29563
810	12.33750	12.33750	12.32990	12.32990
820	12.37132	12.37132	12.36393	12.36393
830	12.40552	12.40552	12.39782	12.39782
840	12.43977	12.43977	12.43222	12.43222
850	12.47563	12.47563	12.46807	12.46807
860	12.51282	12.51282	12.50510	12.50510
870	12.55037	12.55037	12.54275	12.54275
880	12.58795	12.58795	12.58037	12.58037
890	12.62568	12.62568	12.61797	12.61797
900	12.66383	12.66383	12.65580	12.65580
910	12.70238	12.70238	12.69383	12.69383
920	12.74122	12.74122	12.73225	12.73225
930	12.78025	12.78025	12.77072	12.77072
940	12.82055	12.82055	12.81037	12.81037
950	12.86093	12.86093	12.85000	12.85000
960	12.90158	12.90158	12.89028	12.89028
970	12.94245	12.94245	12.93130	12.93130
980	12.98305	12.98305	12.97220	12.97220
990	13.02167	13.02167	13.01152	13.01152
1000	13.06268	13.06268	13.05288	13.05288

CURRICULUM VITAE

Surname, Name: Bilgin, Güney Mert

EDUCATION

Degree	Institution	Year of Graduation
MS	Middle East Technical University Metallurgical and Materials Engineering	2017
BS	Yıldız Technical University Metallurgical and Materials Engineering	2014
High School	Ümitköy Anadolu High School, Ankara	2009

FOREIGN LANGUAGES

Advanced English, Intermediate Italian

PUBLICATIONS

1. Ozer, M., Yılmaz, O., Subasi, L., Gunaydin, A., Bilgin, G. M., Zulić, S., & Kaufman, J. (2024). Enhancement of surface characteristics of additively manufactured γ -TiAl and IN939 alloys after laser shock processing. *Optics & Laser Technology*, 170, 110330.
2. Isik, M., Yildiz, M., Secer, R. O., Sen, C., Bilgin, G. M., Orhangul, A., & Koc, B. (2023). Fabrication of Electron Beam Melted Titanium Aluminide: The Effects of Machining Parameters and Heat Treatment on Surface Roughness and Hardness. *Metals*, 13(12), 1952.
3. Demirtas, H., Cebi, A., Aslan, M. T., Yılmaz, O., Nesli, S., Subasi, L., Gunaydin, A., Bilgin, G. M., Orhangul, Akin & Akbulut, G. (2023). Electrochemical machining of additively manufactured γ -TiAl parts: post-processing technique to reduce surface roughness. *The International Journal of Advanced Manufacturing Technology*, 1-11.
4. Doğu, M. N., Ozer, S., Yalçın, M. A., Davut, K., Bilgin, G. M., Obeidi, M. A., & Brabazon, D. (2023). Effect of solution heat treatment on the microstructure and

crystallographic texture of IN939 fabricated by powder bed fusion-laser beam. *Journal of Materials Research and Technology*, 24, 8909-8923.

5. Ozer, S., Bilgin, G. M., Davut, K., Esen, Z., & Dericioglu, A. F. (2022). Effect of post fabrication aging treatment on the microstructure, crystallographic texture and elevated temperature mechanical properties of IN718 alloy fabricated by selective laser melting. *Journal of Materials Processing Technology*, 306, 117622.

6. Demirtas, H., Yilmaz, O., Subasi, L., Gunaydin, A., Bilgin, G. M., Orhangul, A., & Nesli, S. (2021). Surface quality improvement using electro chemical machining process for γ -TiAl parts produced by electron beam melting. *Procedia CIRP*, 102, 240-245.

7. Bilgin, G. M., Esen, Z., Akın, Ş. K., & Dericioglu, A. F. (2017). Optimization of the mechanical properties of Ti-6Al-4V alloy fabricated by selective laser melting using thermohydrogen processes. *Materials Science and Engineering: A*, 700, 574-582.

Swimming, Travelling, Football, Playing Trumpet, Latin Dances